3D conformal antennas for radar applications

Luc Fourtinon

IMT Atlantique
Bretagne-Pays de la Loire
École Mines-Télécom

UNIVERSITE BRETAGNE LOIRE

THÈSE / IMT Atlantique

sous le sceau de l'Université Bretagne Loire

pour obtenir le grade de

DOCTEUR D'IMT Atlantique

Et en cotutelle avec Cranfield University

Spécialité : Electronique

École Doctorale Mathématiques et STIC

Présentée par

Luc Fourtinon

Préparée dans le département Micro-ondes

Laboratoire Labsticc

3D Conformal Antennas for Radar Applications

Thèse soutenue le 15 décembre 2017

devant le jury composé de :

Eric Rius
Professeur des universités, Université de Bretagne Occidentale / président

Michèle Lalande
Professeure des universités, XLIM – Université de Limoges / rapporteur

Laurent Ferro-Famil
Professeur des universités, IETR – Université de Rennes 1 / rapporteur

Yves Quéré
Maître de conférences, Université de Bretagne Occidentale / examinateur

Guillaume Lesueur
Ingénieur, Thales Optronique / examinateur

Philippe Pouliguen
Responsable scientifique, DGA-MI – Bruz / examinateur

Alessio Balleri
Professeur, Cranfield university / co-directeur de thèse

Christian Person
Professeur, IMT Atlantique / directeur de thèse

Thomas Merlet
Innovation Manager, Thales Optronique – Elancourt / invité

Patrick Pottier
Ingénieur R&D, DGA-MI – Bruz / invité

N° d'ordre : 2017IMTA0060

Sous le sceau de l'Université de Bretagne Loire

IMT-Atlantique

En habilitation conjointe avec l'Université de Bretagne Occidentale

Ecole Doctorale – SICMA

3D CONFORMAL ANTENNAS FOR RADAR APPLICATIONS

Thèse de Doctorat

Mention : STIC – Science et Technologies Information Communication

Présentée par **Luc Fourtinon**

Département : Micro-ondes

Laboratoire : Lab-STICC Pôle: DIM

Directeur de thèse : Christian PERSON

Soutenue le 15 Décembre 2017

Jury :

Mme. Michèle Lalande – Professeure, XLIM (Rapporteur)
M. Laurent Ferro Famil – Professeur, IETR (Rapporteur)
M. Eric Rius – Professeur, Université de Brest (Président du jury)
M. Christian Person – Professeur, IMT-Atlantique (Directeur de thèse)
M. Alessio Balleri – Maitre de conférence, Université de Cranfield (Directeur de thèse)
M. Yves Quéré – Maitre de conférence, Université de Brest (Examinateur)
M. Philippe Pouliguen – DGA (Examinateur)
M. Guillaume Lesueur – Thalès (Examinateur)
M. Thomas Merlet – Thalès (Invité)

CRANFIELD UNIVERSITY

L. FOURTINON

3D CONFORMAL ANTENNAS FOR RADAR APPLICATIONS

CRANFIELD DEFENSE AND SECURITY
Centre for Electronic Warfare, Information and Cyber

PhD
Academic Year: 2014–2018

Supervisor: Dr A. Balleri
January 2018

CRANFIELD UNIVERSITY

CRANFIELD DEFENSE AND SECURITY
Centre for Electronic Warfare, Information and Cyber

PhD

Academic Year: 2014–2018

L. FOURTINON

3D conformal antennas for radar applications

Supervisor: Dr A. Balleri
January 2018

This thesis is submitted in partial fulfilment of the requirements for the degree of PhD.

Acknowledgements

I am very thankful to my thesis director from IMT-Atlantique: Prof. Christian Person for its supervision throughout the years. I also owe a lot to my Cranfield supervisor, Dr. Alessio Balleri, for its constant dedication, motivation and energy during my time in Cranfield University, in the United Kingdom. I also want to express sincere thanks to Dr. Yves Quéré for its close supervision during my stay, as I was working in the University of Brest, in France.

I would like to express my sincere gratitude to my examiners from IMT-Atlantique: Prof. Michèle Lalande and Prof. Laurent Ferro Famil for their questions and corrections. I also would like to show deep appreciations to Dr. Philippe Pouliguen, Dr. Thomas Merlet, Dr. Guillaume Lesueur and Prof. Eric Rius for their support and advices during the years. I would like to acknowledge the interest and help of my Cranfield examiners: Dr. Fabiola Gersone and Dr. Derek Bray.

The contributions in this work would not have been possible without the help and support of my friends in France. I would like to express my considerations to: Sarra, Younes, Denis, Adrien, Ruben, Vinod, Norbert, Christophe, Nathan, Vassidiki, Mira, Mohammad, Nathalie and Letitia. I spent wonderful moments with them and they allowed me to improve not only scientifically but also personally. I also would like to thank Dr. Annaig Martin-Guennou for its priceless help at the beginning of my doctorate.

The scheme of my doctorate offered me the chance to discover and work in the United Kingdom. Many persons that are now my friends have helped to smoother my difficulties and transform this experience into a successful story. I would like to profoundly thank: Krasin, Akhil, Federico, Alejandro, Sebastian, Nasiytah, Carole, Hugo, Damien, Eddie, Monica, Giovanna, Fabiola, Axel, Gareth, Ray, Leon and Amélie. Also, a special thank to Özgün for the joyful moments, this experience would not have been the same without you.

Enfin, je voudrais témoigner ma gratitude envers mes parents ainsi que ma soeur pour être toujours présents et pour leur amour.

Contents

Abstract

Embedded below the radome of a missile, existing RF-seekers use a mechanical rotating antenna to steer the radiating beam in the direction of a target. Latest research is looking at replacing the mechanical antenna components of the RF-seeker with a novel 3D conformal antenna array that can steer the beam electronically. 3D antennas may offer significant advantages, such as faster beamsteering and better coverage but, at the same time, introduce new challenges resulting from a much more complex radiation pattern than that of 2D antennas.

Thanks to the mechanical system removal, the new RF-seeker has a wider available space for the design of a new 3D conformal antenna. To take best benefits of this space, different array shapes are studied, hence the impact of the position, orientation and conformation of the elements is assessed on the antenna performance in terms of directivity, ellipticity and polarisation. To facilitate this study of 3D conformal arrays, a Matlab program has been developed to compute the polarisation pattern of a given array in all directions.

One of the task of the RF-seeker consists in estimating the position of a given target to correct the missile trajectory accordingly. Thus, the impact of the array shape on the error between the measured direction of arrival of the target echo and its true value is addressed. The Cramer-Rao lower bound is used to evaluate the theoretical minimum error. The model assumes that each element receives independently and allows therefore to analyse the potential of active 3D conformal arrays. Finally, the phase monopulse estimator is studied for 3D conformal arrays whose quadrants do not have the same characteristics. A new estimator more adapted to non-identical quadrants is also proposed.

Keywords: conformal, 3D, phased arrays, AESA, polarisation, cross-polarisation, ellipticity, monopulse, maximum likelihood estimator, Cramer-Rao lower bound

Résumé

Embarqué sous le radôme du missile, les autodirecteurs existants utilisent une rotation mécanique du plan d´antenne pour balayer le faisceau en direction d´une cible. Les recherches actuelles examinent le remplacement des composantes mécaniques de rotation de l´antenne par un nouveau réseau d´antennes 3D conformes à balayage électronique. Les antennes 3D conformes pourraient offrir des avantages significatifs, tels qu´un balayage plus rapide et une meilleure couverture angulaire mais qui pourraient aussi offrir de nouveaux challenges résultant d´un diagramme de rayonnement plus complexes en 3D qu´en 2D.

Le nouvel autodirecteur s´affranchit du système mécanique de rotation ce qui libère de l'espace pour le design d´une nouvelle antenne 3D conforme. Pour tirer le meilleur parti de cet espace, différentes formes de réseaux sont étudiées, ainsi l'impact de la position, de l'orientation et de la conformation des éléments est établi sur les performances de l´antenne, en termes de directivité, ellipticité et de polarisation. Pour faciliter cette étude de réseaux 3D conformes, un programme Matlab a été développé, il permet de générer rapidement le diagramme de rayonnement en polarisation d´un réseau donné dans toutes les directions.

L´une des tâches de l´autodirecteur consiste à estimer la position d´une cible donnée afin de corriger la trajectoire du missile. Ainsi, l´impact de la forme du réseau sur l´erreur entre la direction d´arrivée mesurée de l'écho de la cible et sa vraie valeur est analysé. La borne inférieure de Cramer-Rao est utilisée pour calculer l´erreur minimum théorique. Ce modèle suppose que chaque élément est alimenté séparément et permet ainsi d´évaluer le potentiel des réseaux 3D conformes actifs. Finalement, l´estimateur du monopulse en phase est étudié pour des réseaux 3D conformes dont les quadrants n´auraient pas les mêmes caractéristiques. Un nouvel estimateur, plus adapté à des quadrants non identiques, est aussi proposé.

Mots-clés: antenne conforme, antenne réseau à commande de phase, polarisation, polarisation croisée, ellipticité, monopulse, maximum de vraisemblance, borne inférieure de Cramer-Rao

Preface

The missile innovation state fund

The needs to renew and keep missiles at the cutting edge of technology are motivated by France and the UK ministry of defence. This effort to jointly build a new generation of missiles is one of the point of the Lancaster House treaty, under which the French and UK governments have set a research fund called Materials and Components for Missiles, Innovation and Technology Partnership (MCM-ITP).

The missile innovation trends consist in enhancing the lethality and accuracy of the weapon at a reduced cost. All the components of the missile are targeted for improvement.

The domain dedicated to the RF-seeker research is managed by Thales Optronic SAS in Elancourt, France.

The laboratory project

A team of the Lab-STICC laboratory has applied several times for this state fund to work on the RF-seeker. It started in 2014 and the team has grown over the years. The projects Pyrana, Cobra, Lizard and now Dragon have investigated the subject as shown in Figure 1. The global objective of these projects is to design and develop a new generation of RF-seeker. The antenna shape has been studied as well as the technological aspect for the antenna manufacturing. Respective to those projects, this PhD is more fundamental.

Later on, new PhDs have been dedicated to the processing part with a study on targets classification and a study on the multiple beam analysis which is a step towards a multifunction RF-seeker. More recently a PhD started on the transmission and reception modules to improve the component integration.

This shows that the PhD brick is interlocked into a whole project with multiple interconnections and the complexity of the seeker system.

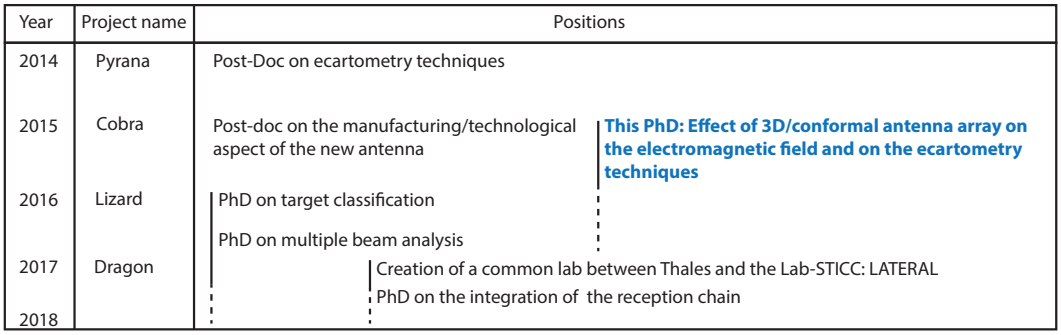

Figure 1: Project organisation

General introduction

This effort to continuously increase the weapon lethality is conducted by countries for deterrence, intimidation and the protection of their inhabitants. For guided weapons, the cumulated global missiles and missile defense systems market for the next 10 years is valued at US$384 billions from USA media sources [Cision PR Newswire, 2017] [Jane's by IHS Markit, 2014]. The innovation efforts are therefore strongly motivated for defence as well as for economical reasons. The French and UK governments are collaborating through the MCM-ITP funding for missile innovation. Hence, this thesis is nested into this innovation problem with the study of a new generation of RF-seekers.

Current RF-seekers steer their beams using a mechanical system that rotates the antenna plane. This mechanical system has various drawbacks: it is bulky, fragile and expensive. The rotating system undergoes strong vibrations as the missile usually travels at several times the speed of sound. Hence, it is expensive to build a reliable system. The mechanical system also limits the field of view by limiting the steering angle.

Planar active electronically steered arrays (AESA) are mature today thanks to the development of integrated transmit/receive modules and are currently used for aircraft, in the Rafale for example. Hence, it seems natural to use them for missiles. Existing AESA antennas are built with planar structures, as the beam is steered away from the antenna axis, its performance decreases which limits the field of view and the target signal detection. It is therefore not necessarily advantageous to switch to a planar AESA antenna in missiles. Nonetheless, the mechanical system removal offers more space that brings new degrees of freedom for the antenna design. A possible solution would be to conform the radiating elements to increase the coverage and the gain.

The effects of 3D and conformal antennas on the radiation performance are explored in term of directivity and polarisation. For the current planar RF-seekers, the radiating elements are aligned and parallel which simplifies the study of the electric field. For 3D conformal antennas where the elements have different orientations the polarisation is more complex. In this sense, the position and orientation of the elements are investigated, as well as the degree of curvature on the polarisation. The performance criteria

of some specific antenna arrays are also studied and compared with its current planar mechanically steered counterpart.

The RF-seeker role is not only to detect the target echo but also to estimate its direction of arrival. After processing an estimation, the command unit modifies the missile trajectory accordingly. Specific direction of arrival techniques have been developed for planar arrays. Replacing this current antenna by a new 3D conformal array requires therefore an investigation as to whether it is beneficial in term of estimation and whether the current direction of arrival techniques can be applied to this new technology.

To answer to these different problems, in chapter I, the context is presented in more detail. In chapter II, a literature review is carried out and the polarisation study is developed together with that of the direction of arrival estimation. In chapter III, the characteristics of the radiated field are considered as the position, orientation and degree of curvature of the array is modified. In chapter IV, the effect of the 3D and conformation is studied on the direction of arrival techniques.

List of publications:

- **Journals:**
  1. A study of 3D/conformal polarised arrays for direction of arrival, publication in process
- **First author conferences:**
  1. Directivity and ellipticity study for planar and 3D conformal RF-seeker antennas, 2017 IEEE CAMA (Conference on Antenna Measurements and Applications) in Japan
  2. Antennes 3D pour autodirecteurs: directivité et polarisation, workshop Electromagnétique et guerre électronique, Toulouse, 2017
  3. Beampattern and polarisation synthesis of 3D RF-seeker antenna arrays, SSPD (Sensor Signal Processing for Defense) in Edinburgh, 2015
- **Non first author conferences:**
  1. Etude de la polarisation d´un réseau conformé de guides à fentes fonctionnant dans la bande Ku et réalisé en technologie additive, JNM (journée Nationale Micro-ondes), in St-Malo, France, 2017
  2. Design and manufacturing of a 3-D conformal slotted waveguide antenna array in Ku-band based on Direct Metal Laser Sintering, 2016 IEEE CAMA (Conference on Antenna Measurements and Applications) in Syracuse, US

3. Optimisation d´une antenne 3D conforme d´autodirecteur : balayage électronique et polarisation, JNM (journée Nationale Micro-ondes), in Bordeaux, France, 2015
4. Simulation électromagnétique HPC de réseaux d´antennes 3D/conformes, JNM (Journée Nationale Micro-ondes), in Bordeaux, France, 2015

Chapter 1 Context

Governments and companies are pushed to innovate to improve the lethality and accuracy of their weapons to ensure their citizens security as well as to win new markets [Cision PR Newswire, 2017] [Jane's by IHS Markit, 2014]. This thesis focuses on missiles, principally on the problem of a new generation of RF-seekers.

As a starting point and in order to understand better the context of the subject, the flying scenario and the missile environment are presented. Multiple impediments and couter-measures techniques require improvement of the missile technology and more specifically the RF-seeker. Performance criteria are introduced to compare the different antenna steering techniques: both mechanical and electronic. The reasons for rejecting a planar antenna are presented and a preliminary study optimising the antenna shape is carried out. Finally the multiple challenges for the design and manufacturing of a 3D/conformal antenna are presented.

1.1 The missile and its environment

1.1.1 Overview of a missile

The following definition is found in [Siouris, 2004] for a missile: 'In general, a missile can be defined as an aerospace vehicle with varying guidance capabilities that is self-propelled through space for the purpose of inflicting damage on a designated target'. The self-propelled missile can be decomposed into a generic structure shown in Figure 1.1. An important part of the missile volume is dedicated to the propellant that guarantee the autonomy of the weapon. The jet engine technology is chosen according to the mission distance. The missile carries the lethal charge contained in the warhead, its size is chosen according to the threat. The missile is sent towards a target that can move during the missile flight, therefore to update the trajectory and steer the missile, the seeker senses the target and the processing unit allows the guidance by comparing the data received by the seeker with stored and previously analysed data.

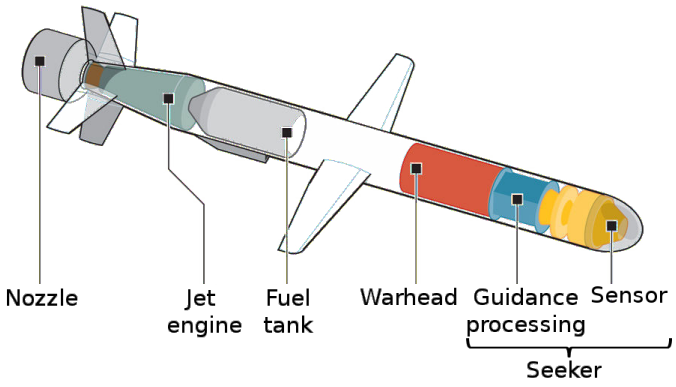

Figure 1.1: Structure of a missile

1.1.2 The missile guidance scenario

A target has been detected and classified as a threat by an aircraft or a ground station. The missile is launched and starts going up to accumulate gravity potential energy and more quickly dive on the target in the last flying phase. As it is launched, the missile knows in which direction flying since the aircraft or base has sent the last target position to the missile. Before the missile is close enough from the target to detect it, the missile uses an inertial navigational guidance: it uses its own sensors to measure its acceleration and know its position. When the time to impact is below a few tens of seconds, the homing guidance starts: the seeker switches on and sends pulses towards the target. The echo signal is processed, the new impact point is calculated and the missile trajectory is corrected. Eventually if the guidance has been effective the threat is destroyed as shown in Figure 1.2.

A homing guidance means that the missile uses its own equipment to steer its trajectory towards the target impact point [Siouris, 2004, p. 158]. Different kind of homing guidance systems exist, in this thesis, an active radar guidance is considered. In the missile context, the embedded radar is called RF-seeker, it emits electromagnetic pulses and active homing specifies that the missile sends its own pulses.

Depending on the target size, the target is not detected at the same distance. Typically, the seekers switches on a few kilometres from the target. The bigger the target, the farther the seeker can switch to the homing guidance.

To steer the missile towards a moving target, the missile command system needs to estimate the error angle between the radar beam axis and the designated target, this is called ecartometry. The error tends to be minimised during the missile travelling, it allows to track the target.

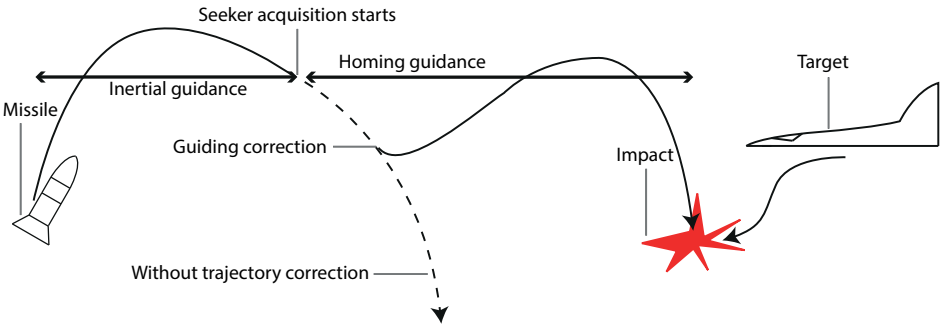

Figure 1.2: Missile trajectory

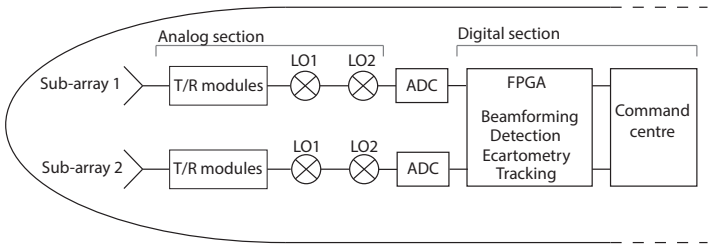

Figure 1.3: RF-seeker system

1.1.3 The missile seeker and the environment

The seeker sends an electromagnetic signal at the speed of light towards the target that reflects it. The target echo then propagates back and is sensed by the antenna. Afterwards, the processing unit analyses the received signal and estimates the new target direction with ecartometry techniques, finally the command system steers the missile accordingly. The ecartometry techniques are developed further in the chapter.

The antenna has the role to detect the echo signal and the processing unit to determine the target direction, they are complementary.

1.1.3.1 RF-seeker system

The organisation of the current RF-seeker is depicted in Figure 1.3. A signal is received by two antenna sub-array to calculate the ecartometry error. Then the signals go through transmitter and receiver modules which main goal is the signal amplification. Then the signals are mixed for transposition into baseband. The analog signals are converted into digital signals and analysed in the Field Programmable Gate Array (FPGA) module. This module carries out beamforming, detection, estimation of the target position and target tracking. Finally based on the signal analysis, the command centre adapts its decision.

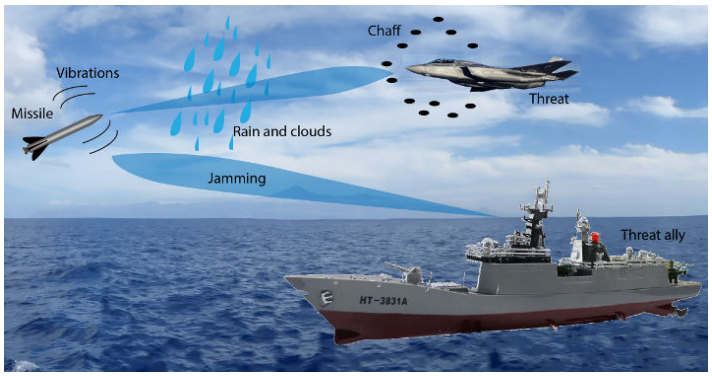

Figure 1.4: A battle-space scenario

1.1.3.2 Missile environment

In a realistic battle-space scenario, as shown in Figure 1.4, many factors impact upon the detection and estimation of the target. Firstly, the missile undergoes strong vibrations as it travels at several times the speed of sound; the seeker has to be robust enough to endure them. Secondly, natural hurdles due to the environment such as fog, clouds, rain or snow, can affect the signal strength. The target may also use counter-measure techniques to affect the missile guidance. The target carries out jamming or can use a decoy or chaffs: a cloud of metal fibre filaments that prevent target detection. Finally, the signal suffers from the noise in the receiver and various losses due to the electronic components imperfections. All of these effects have to be accounted during the seeker conception to make a more effective and resilient detection and estimation. Other factors include the low volume and weight, ease of maintenance, long storage period after which the missile should be unaltered, etc.

1.2 The performance criteria of an RF-seeker

An RF-seeker system performs well when the quantity of information extracted from a pulse is high, for example: target range, speed, angular position, type of target etc. To achieve this goal, the two radar components, the antenna and the processing unit, should be high performing. In that regard, first, definitions are provided, then, in order to understand and be able to be critical regarding the antenna and the ecartometry performance, various criteria are defined.

1.2.1 Antenna definitions

The IEEE Standard Definition of Terms for Antennas (IEEE Std 145-2013) [Antennas and Society, 2013] gives the following definition for an antenna:

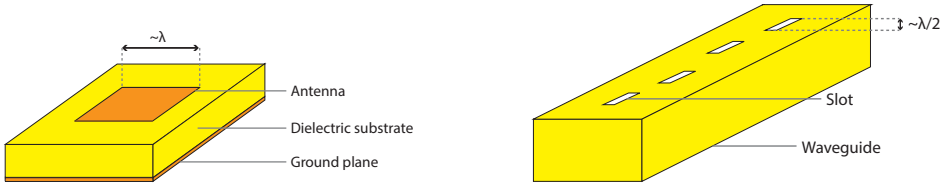

(a) Microstrip patch antenna (b) slotted waveguide

Figure 1.5: RF-seeker antenna elements

Antenna: That part of a transmitting or receiving system that is designed to radiate or to receive electromagnetic waves.

The antenna provides a transition between the electric and magnetic currents in a circuit and the electromagnetic signal in the free-space and reciprocally. It is a passive and reciprocal device, it works identically in emission and reception. Usual antennas for RF-seekers are microstrip or slot antennas, as shown in Figure 1.5.

A microstrip patch antenna consists of a metallised pattern and a metallic ground plane, separated by a dielectric substrate. The metallised pattern order of magnitude is the wavelength.

A slotted waveguide antenna is made of a metallic pipe with circular or rectangular sections, into which slots have been pierced. The slot order of magnitude is the half wavelength.

A microstrip patch antenna or a single slot; in the context of antenna arrays, these are radiating elements.

From the IEEE standards [Antennas and Society, 2013]:

Radiating element: A basic subdivision of an antenna that in itself is capable of radiating or receiving radio waves.

Radiating elements are used to improve the antenna performance and form array antennas.

Array antenna: An antenna comprised of a number of radiating elements the inputs (or outputs) of which are combined. Syn: **antenna array**.

When referring to a part of the antenna the term quadrant is used throughout this work. The definition cannot be found in the IEEE standards, therefore the author proposes the following:

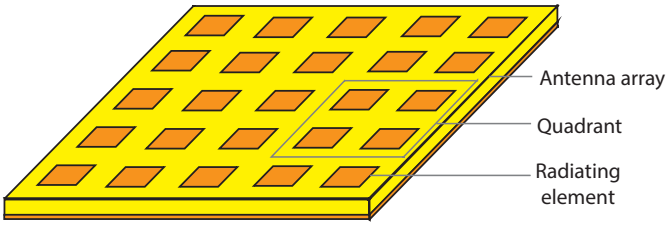

Figure 1.6: Distinction between radiating element, quadrant and antenna array

Figure 1.7: 9B-1103M Russian active radar seeker antenna

Quadrant: An intermediate sub-division of an antenna array that gathers more than one radiating element. It can be found worded as sub-array.

The word antenna can be used to refer to many different objects: e.g. radiating element or the antenna array, as shown in Figure 1.6. In this study, for simplicity, radiating elements are sometimes called elements and the antenna array array or antenna.

The example of a Russian active radar seeker antenna, consisting of an array of slot elements, is shown in Figure 1.7.

1.2.2 The link budget equation

The antenna detection is efficient when the link budget is at an optimum. The link budget equation allows the antenna to be designed depending on a given scenario. The characteristic figure of merit is the signal to noise ratio SNR, which is the received power P_R divided by the thermal noise power N in the receiver. The radar emits a power signal P_E with a gain G that propagates in the air and is reflected by the target with radar cross section σ at distance R, travels back to the radar and is intercepted by an effective area A_e, as illustrated in Figure 1.8. L accounts for the losses (precipitations,

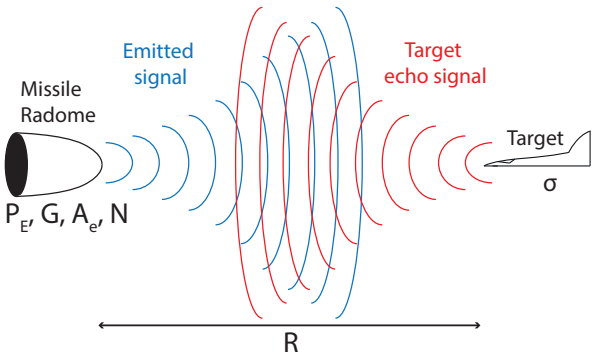

Figure 1.8: Signal travelling

P_E	G	σ	A_e	R	N
$3 \cdot 10^2$ W	20dB	cm^2 to m^2	m^2	$5 \cdot 10^2$m to 10km	-138dBW

Table 1.1: Orders of magnitude

jamming, antenna imperfections, etc.). The orders of magnitude are given in Table 1.1. The order of magnitude for the radar cross section is found in [Balanis, 2005, p. 99] and for the noise power, with an equivalent temperature of 1000K and a bandwidth of 1MHz.

$$SNR = \frac{P_R}{N} = P_E G \frac{\sigma}{4\pi R^2} \frac{A_e}{4\pi R^2} \frac{1}{L} \frac{1}{N} \tag{1.1}$$

The designer aims to improve the received power; for that purpose, using the budget link equation, the factors that can be controlled are: the emitted power, the gain and the antenna effective area, as shown in equation 1.1.

The gain characterizes the focusing of the radiated power in a given direction [Antennas and Society, 2013]:

Gain (in a given direction): The ratio of the radiation intensity in a given direction to the radiation intensity that would be produced if the power accepted by the antenna were isotropically radiated. Syn: absolute gain (of an antenna).

Radiation intensity: In a given direction, the power radiated from an antenna per unit solid angle.

Another figure of merit is the directivity which is proportional to the gain, as shown in equation 1.2.

$$G(\theta, \varphi) = \eta D(\theta, \varphi) \tag{1.2}$$

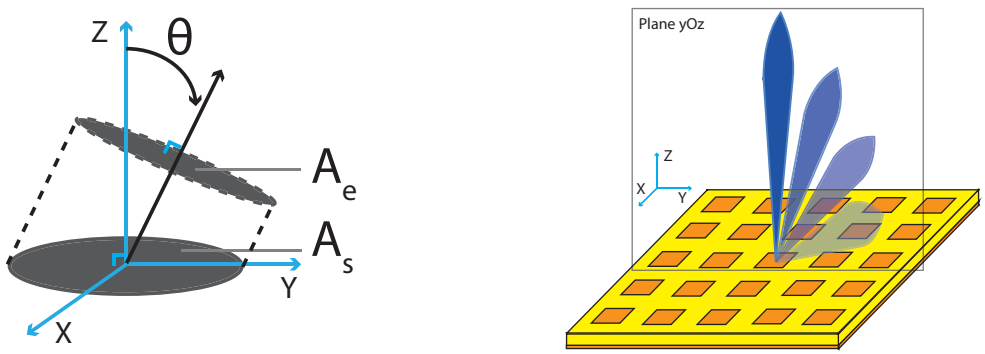

(a) The projected surface (b) Beam shape and beamsteering angle

Figure 1.9: Electronic beamsteering

Where η is antenna radiation efficiency, it is the ratio of the total power radiated by the antenna over the total input power, it is defined with impedance and polarisation matching. It accounts for the conduction and dielectric losses of the antenna itself [Balanis, 2005, p. 66]. In this thesis, the directivity is considered since in simulation antennas are considered without feeding network.

1.2.3 Relation between the directivity and the projected surface

The directivity D_0 of the antenna is proportional to its effective area as shown in equation 1.3 [Balanis, 2005, p. 93] with impedance and polarisation matching.

$$D_0 = \frac{4\pi A_e}{\eta\lambda^2} \tag{1.3}$$

For a circular planar antenna of physical surface A_s, the directivity in a given direction is proportional to the projected surface: $D(\theta) = \frac{4\pi A_s}{\eta\lambda^2}\cos\theta$, as shown in Figure 1.9a. Therefore when the direction of the main beam is steered away from its natural one the directivity decreases, as shown in Figure 1.9b.

This relation shows the interest of large antenna arrays. Increasing the number of elements, increases the effective area and at the same time increases the directivity.

In this section, the performance of an antenna has been addressed with the directivity and its relation with the surface. In the following part, the evaluation of the ecartometry performance is investigated.

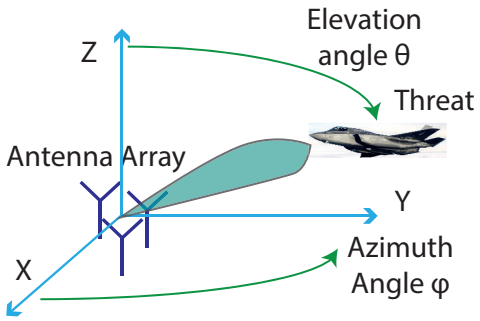

Figure 1.10: The direction of arrival angles

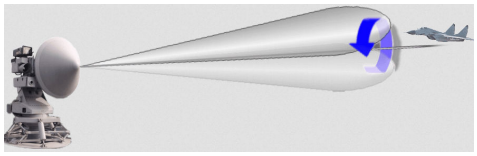

Figure 1.11: Conical scan technique

1.2.4 The ecartometry performance

Various information about the target is embedded in the signal echo: the range, the speed, the angular position and the target type. Important parameters for a seeker are the angular position: θ and φ, as shown in Figure 1.10. θ is the elevation angle, it is referenced from the axis Z. φ is the azimuthal angle, it is spinning around the axis Z and referenced from the axis X.

During its life time, the RF-seeker has two functioning phases. First the RF-seeker searches for the target, then the RF-seeker tracks it. During the tracking phase, the radar has prior information on the target angle. As the target moves, the error angle is calculated with ecartometry techniques. These include, the conical scan [Sherman and Barton, 2011, p. 4] and the monopulse technique.

The conical scan consists of rotating the beam around the target and observing the amplitude signal differences as shown in Figure 1.11. If the target does not move during a scan rotation, each signal has the same amplitude. Therefore, as the target moves, the signals can be compared and the antenna angle can be corrected. This technique is easily countermeasured and, due to the amplitude comparison, it is sensitive to the environmental conditions.

To use the monopulse technique, an antenna array emits a pulse signal towards the target. Then, in reception the array is divided in four quadrants. Comparison of the signals is realised in amplitude for the amplitude monopulse technique and in phase for the phase monopulse technique.

The phase monopulse is further detailed here, as shown in Figure 1.12a. The comparisons of the signals between quadrants A and B or C and D bring information on the

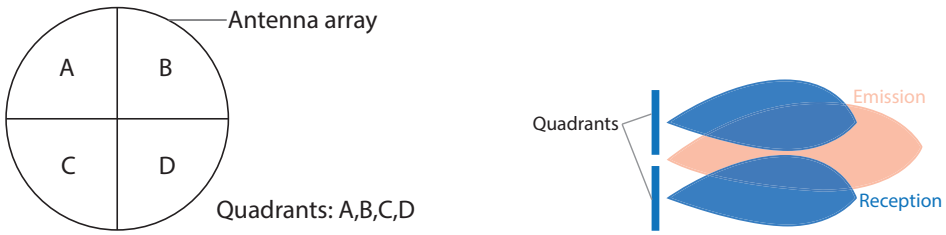

(a) The antenna and its 4 quadrants (b) Phase Monopulse

Figure 1.12: Monopulse

target azimuth. Comparisons of quadrants A and C or B and D give information on the elevation. The signal amplitude at each quadrant is the same. The phase monopulse is illustrated in Figure 1.12b.

The performance criteria for an ecartometry technique is related to an accurate estimation of the target angular position that would be robust to the perturbations of the environment and the countermeasures.

The monopulse technique can be realised analogically. Each quadrant can be made of tens of radiating elements and finally deliver one signal. It simplifies the electronic system design.

Hence, this work investigates the antenna itself and the monopulse technique. The different criteria have been introduced so that the steering techniques can be discussed further.

1.3 Comparison of the different steering techniques

According to the IEEE Standard Definition of Terms for Antennas (IEEE Std 145-2013) [Antennas and Society, 2013], beamsteering definition is:

beamsteering: Changing the direction of the major lobe of a radiation pattern.

It is also sometimes termed as beamscanning in the literature. First, the current mechanical beamsteering is discussed, then the electronic beamsteering, towards which the new generation of RF-seekers tends.

1.3.1 The current generation of RF-seeker

The current generation of RF-seeker uses a mechanical system to steer the antenna array during the tracking. The example of the RDY-2 from Thales is shown in Figure

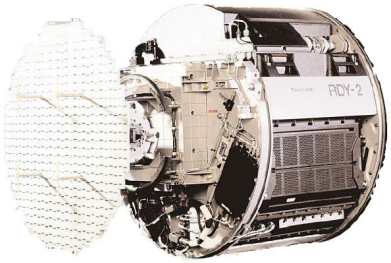

Figure 1.13: Example of a mechanically steered RF-seeker (Thales RDT-2)

1.13.

- The benefits of the planar and mechanically steered antenna include:
  - The antenna keeps the target very close to its line-of-sight due to the mechanism. The maximum of the antenna equivalent surface is projected and the maximum energy is radiated towards the target. It ensures an efficient signal detection and estimation.
  - The radiating elements of the antenna are aligned in the same orientation, therefore the antenna keeps emitting the same beam characteristic towards the target. This is convenient for facilitating the processing of the target echo.
  - The monopulse slope remains constant over the field of view.
- The limitations of the planar and mechanically steered antenna include:
  - The mechanism is a fragile component that undergoes the strong vibrations of the platform onto which the missile is held, when the plane lands or takes off. The mechanism also has to endure its own vibrations after its launch.
  - The mechanism is bulky and the planar antenna below the radome curved for aerodynamic reasons keeps an unused space, as shown in Figure 1.14. The antenna array made of metal is heavy and as it moves it could change the orientation of the missile. To prevent this effect some cumbersome elements are introduced to compensate for the array motion.
  - The RF-seeker structure itself limits the angle of rotation of the mechanical system, hence limiting the field of view by an angle of $\theta = 60°$.
  - When the antenna is steered in a particular direction, the rest of the space is not covered, from where a threat could appear (Figure 1.14).

When combined, these limitations suggest the requirements for a new RF-seeker antenna to replace the mechanical system.

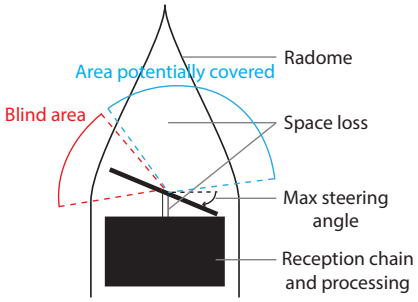

Figure 1.14: Seeker limitations

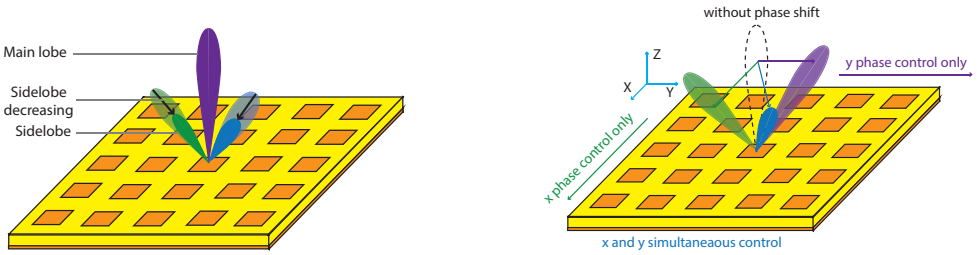

(a) Amplitude control of the beam

(b) Phase control of the beam

Figure 1.15: Amplitude and phase control of the beam

1.3.2 Degrees of freedom of the electronic steering

The phase and amplitude control of the excitation allows beamforming to be carried out. It consists of shaping the beam emitted by the antenna. Recent literature can be found about digital beamforming where the signal is digitised at each element. It allows adaptive beamforming, the beam adapts to the environmental conditions. For example, the beam can be cancelled out in the direction of a jammer and this also enables the generation of multi beams [Mailloux, 2005, p. 53–55].

First, amplitude control of the radiating elements allows low sidelobes to be kept. If the target echo is received in the sidelobe region, it induces ambiguity in the calculation of the target angle. It also reduces sidelobe clutter and chances of jamming. Therefore the sidelobe level is minimised as much as possible, as illustrated in Figure 1.15a. Second, the phase control of the radiating elements allows the antenna beam to be steered. Direction control of the beam is maintained by applying a phase shift from element to element. For a planar array, where the elements are linearly arranged in a square pattern, the phase shift along lines or rows respectively steers the beam along the line or the row. A phase combination of both allows the beam to be steered in any direction, as shown in Figure 1.15b.

An antenna with a control of the elements in amplitude and in phase has a faster

beamsteering and the potential of a more agile beam than the mechanically steered antenna. To overcome the drawbacks of the planar mechanically steered antenna, a planar electronically steered antenna is considered. Despite its advantages, some drawbacks are to be expected.

1.3.3 The limitations of the planar electronically steered array

To counteract the slowness of the mechanical beamsteering and the drawbacks of the mechanical system, the most straightforward solution would consist of using the current planar antenna with an electronic steering control. However the directivity would decrease as the projection surface of the antenna decreases following a cosine law, as shown in the section 1.2.3. This would strongly limit the field of view of the antenna; for a steering at 60°, the directivity would be halved and at 90° it would be zero, as illustrated in Figure 1.9b. By comparison, the mechanically steered array projects a constant surface in the target direction over its field of view. As a result, the planar electronically steered antenna would have a far lower directivity than the current antenna technology to be viable. Instead, to compensate for the directivity decrease and increase the received power, the emitted power can be increased, as shown in equation 1.1. However, in an embedded application this is not desirable; the missile has limited space and compensating the directivity by the emitted power would increase the battery size. The T/R modules also have constraint of power linearity; above a specific input power the amplifiers saturate and deliver a constant power to the antenna. For those two reasons, amplitude control is not considered as a feasible degree of freedom, only the directivity.

The planar electronically steered antenna has a low directivity for high steering angles. To compensate for the planar array limitations and to take benefits of the mechanical system removal, 3D conformal shapes are investigated. In the next section, using the projected surface, a study is performed to find some suitable antenna shapes.

1.4 Identification of suitable shapes

1.4.1 Objectives for the thesis

The requirements for the shape selection are exposed in this section and illustrated in Figure 1.16. The space directions around the antenna are swept by the two angles θ and φ. Along those space directions, two areas are to be distinguished.

For $\varphi = 0°$ to $360°$.

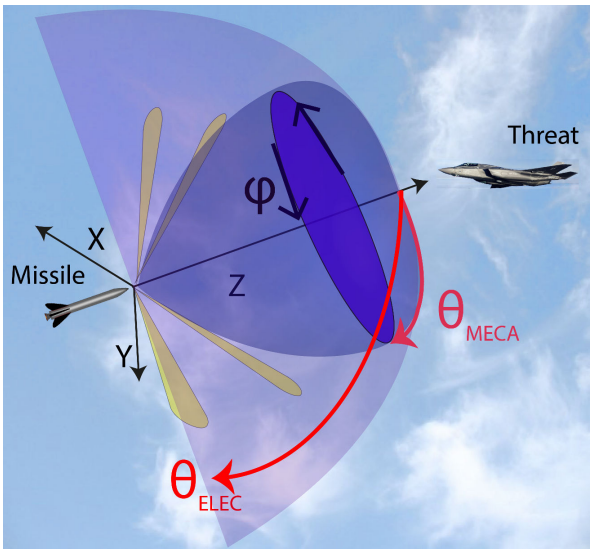

Figure 1.16: Antenna directivities

- From $\theta = 0°$ to $\theta_{MECA} = 60°$ where θ_{MECA} refers to the steering limit angle of the mechanical planar antenna. The 3D conformal antenna aims for at least identical performance than the current mechanically steered planar array.
- From $\theta = 60°$ to $\theta_{ELEC} = 90°$ where θ_{ELEC} refers to the maximum steering angle of the 3D conformal antenna. In this area, there is no relative criteria, the antenna should be as performing as possible.

The mechanically steered planar array presents constant performance along the elevation angle, the same is expected for the new antenna. In this part, performance means directivity and ecartometry accuracy. The indicative directivity level of the mechanically steered planar antenna is 25dB. In the budget link equation, the product GA_e can be changed into $G^2\frac{\lambda^2}{4\pi}$ where $G^2 = 50dB$.

The thesis will investigate whether those objectives are reachable and present the different tradeoffs induced.

1.4.2 Antenna shape study

The previous objectives show that the antenna should have a constant directivity as shown in Figure 1.16. To counteract the decrease of the field of view of the planar electronically steered antenna, some shapes that take benefits from the space below the radome and from the mechanical system removal are considered. A preliminary study of the antenna directivity is realised using the projecting surface by considering some symmetrical shapes. The synthesis of the study realised by [Josefsson and Persson, 2006] follows.

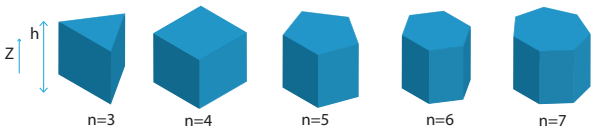

Figure 1.17: Azimuthal symmetrical shapes

First antenna shapes that produce a high and constant equivalent surface along the azimuthal angle are identified, second the study focuses on the elevation angle.

This study is preliminary in the extent that it is carried out in one azimuthal plane and one elevation plane and since it only considers the projected surface of some specific geometrical shapes.

1.4.2.1 The azimuthal study

The conditions and hypothesis of the study [Josefsson and Persson, 2006] are presented:

- The antenna shapes reviewed fit within the same given base area or volume.
- The radiating elements are assumed to be evenly distributed over the surface for simplification.
- For antennas consisting of several planar surfaces, only one planar array is active at a time. When an antenna element is not active, it is turned off.
- The azimuthal study is set in the horizontal plane $\theta = 90°$. The top and bottom planes are not accounted.
- The amplitude control is not considered in this study.

Different faceted shapes with an azimuthal periodicity are considered in this part, as shown in Figure 1.17. The height h of each shape is fixed. The extreme case with an infinite number of faces is a cylinder. The suitable number of faces n is sought.

The effect of the number of faces on the maximum steering angle, number of elements and total surface is discussed.

- If the shape has 3 faces, then each face requires a 60° steering angle to offer a 360° coverage. If the shape has 4 faces, the maximum steering angle is 45°. The maximum steering angle is therefore $\frac{\pi}{n}$ where n is the number of side faces. As the number of faces increases, the maximum steering angle decreases and the directivity decreases less in this direction.

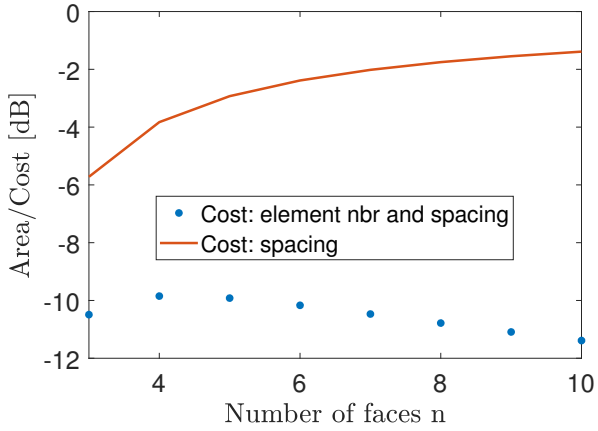

Figure 1.18: Area/cost versus the number of antenna faces; the dot curve cost: number of faces and element spacing and the line curve cost: element spacing

- If the maximum steering angle increases, the elements spacing is higher in order to avoid grating lobes. Therefore the higher the number of faces, the less dense the elements. This is the link between the number of faces and the element density.
- As described in the conditions, all the shapes are contained in the same volume, here a cylinder with a radius R. The total surface of a shape (top and bottom are not considered here) equals $2nhR\sin\frac{\pi}{n}$. The asymptotic case is a cylinder, it has an infinite number of faces and therefore the maximum surface: $2\pi Rh$. This is the link between the number of faces and the total surface cost.

The ideal antenna would have a small maximum steering angle and a high projected surface (area) for a better directivity, finally as less total surface as possible for a costless antenna with less elements. To visualise this compromise, the area for the maximum steering angle (worse case) over the cost and normalised over the total area of a face is displayed as a function of the number of faces. The cost cumulates the number of faces and the element spacing. Eventually results are a function of the maximum steering angle, number of faces and the spacing between two elements.

Among the conditions, only one surface is active at a time, in practise several surfaces would be simultaneously active, especially for a high number of faces. This case is not studied.

The best tradeoff, dot curve in Figure 1.18, is given for a shape with 4 faces where the maximum steering angle would be 45°, this means a directivity reduction of $10\log_{10}(\cos\frac{\pi}{4}) = -1.5$dB in this direction.

This result is discussed and shaded in two points. First, in practise, the 1.5dB loss is a minimum, for a real antenna it would be higher and the beam shape would also be affected. Therefore a higher number of faces would be desirable to reduce the maximum steering angle. For our application, the cost of the number of faces is not the priority,

the required performance is a high directivity. Therefore if this cost is relaxed, as shown with the line curve in Figure 1.18, then the higher the number of faces, the higher the performance.

1.4.2.2 The elevation study

The conditions in which the study is realised, are introduced:

- The antenna arrangements will fit within a base diameter 2R.
- The active surface for a curved solution is defined by a maximum local steering angle of 60°.
- All curved alternatives are rotationally symmetric.
- For the different shapes, the height is equal to their radius. It is not applicable to the plane.

The shapes considered in this part have a constant height and constant radius R: a three sided pyramid, a cone with a 90° angle, a hyperboloid with an ellipticity 1.1, a paraboloid, a half-sphere and a closed cylinder. The performance related to the effective area A_e (projected surface in a steered direction) is studied versus the total surface of the shape A_t. The surfaces are normalised over the squared radius to ensure a consistent study. The maximum steering angle is fixed to 60°, which also fixes the element spacing. The results are shown in Figure 1.19.

The ideal shape would have a maximised effective area for a maximised directivity and a minimum total surface.

The cylinder has the highest minimum effective area and the highest maximum effective area which means the best directivity over the elevation angles. The cylinder also gives a high total area which means a more expensive antenna. The hyperboloid presents similar results for a much reduced total area. The total surface is, however, not a strong constraint, therefore the closed cylinder is considered to be the best option.

The total surface cost is not a constraint in this project. If this condition is relaxed, the results are as shown in Figure 1.20 where the effective area is plotted as a function of the elevation angle.

Results show that the plane offers the best effective area until 45° but also presents the most limited coverage. The coverage is limited to 60° which is the maximum steering angle in Figure 1.20. A steering angle of 60° produces a reduction of $10\log_{10}(\cos\frac{\pi}{3}) = -3.01dB$ in directivity, which means an emitted power divided by 2.

One of the specifications of the antenna design is to maintain a constant directivity over the field of view. In that regard, the half-sphere shape performs the best, its

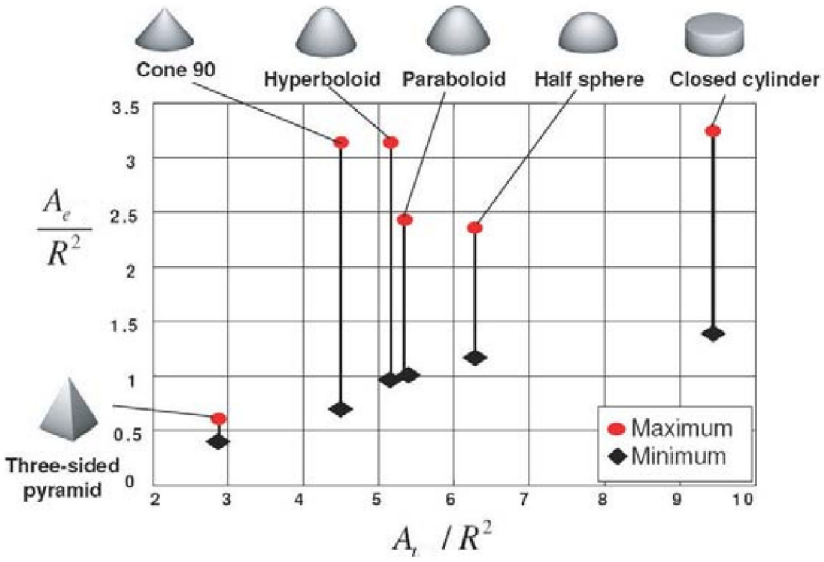

Figure 1.19: Normalised performance versus the total surface [Josefsson and Persson, 2006]

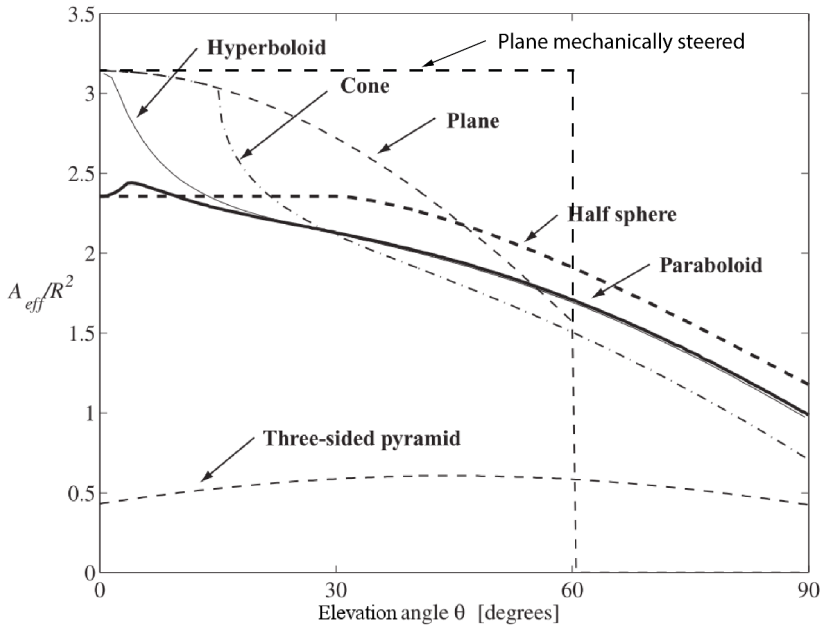

Figure 1.20: Normalised performance versus the elevation angle [Josefsson and Persson, 2006]

effective area is constant until 30°. For that reason the hyperboloid and cone are not relevant for our study. One could wonder how the cylinder performs, in Figure 1.19, its planar top would give similar results as the plane until 60°, then the side face would offer a higher coverage than the planar array.

In the direction $\theta = 0°$, the half-sphere does not perform as well as the plane. The hypothesis stating that the maximum steering angle is 60° reduces the active surface from the total surface. In this direction, the cone uses all its surface since the angle between its surface and horizontal is 45°. The hyperboloid also uses all its surface since the angle of its shape does not exceed 60°.

As a replacement for the planar array, the cylinder and half-sphere have good potential; the cylinder would have better performance than the plane which in Figure 1.20 performs the best up to 45°. The half-sphere provides the smaller range of projected surface as a function of the elevation angle; this is good for constant elevation performance and it also has the best projected surface after 45°.

1.4.2.3 Conclusion of the shape study

Different conclusions can be drawn from this study.

- The azimuthal study shows that a shape with a high number of faces or ideally a cylinder is convenient to decrease the number of elements and keep a high and constant directivity.

- The results of the elevation study show that the half-sphere is a suitable shape for constant elevation directivity.

- The compromise between the gain and field of view between the mechanically steered antenna and the electronically steered one has been demonstrated in Figure 1.20. The limitations of the planar electronically steered array are also confirmed.

- The geometrical shape height is kept constant in the elevation study. In practice, there is enough space offered by the mechanical system removal to set a half-sphere coupled to a cylinder. The cylinder effective area would compensate for the decrease of the half-sphere projected area for high elevation angles. If, as in the previous study, the maximum steering angle is 60°, starting from a direction angle of 30°, the cylinder antenna would present a higher directivity than the one presented in Figure 1.20 for the half-sphere alone.

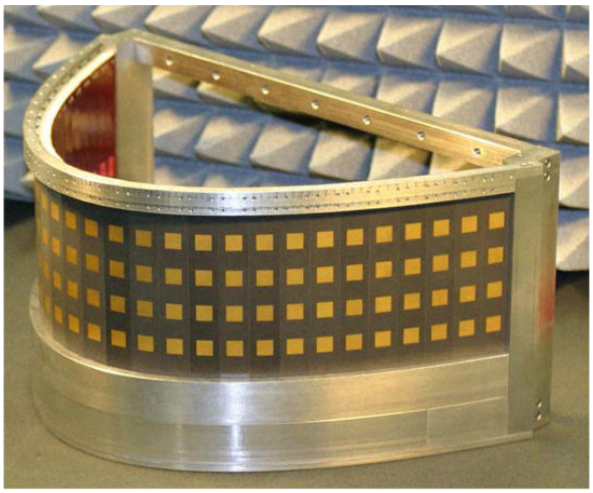

Figure 1.21: Example of a 3D conformal antenna [Bertuch et al., 2010]

1.5 Challenges of the 3D conformal electronically steered array

The previous section showed that a 3D conformal antenna has good potential to replace the mechanically steered planar antenna and also showed the array shapes that could match the directivity objectives using the projected surface. First definitions of 3D and conformation are exposed to set up the background. Second, the different challenges presented by the new antenna technology, in term of technology, design, electromagnetic field, ecartometry techniques and multi-functions, are presented.

1.5.1 Definitions of 3D and conformal

The IEEE Standard Definition of Terms for Antennas (IEEE Std 145-2013) [Antennas and Society, 2013] gives the following definition:

Conformal antenna [conformal array] An antenna [an array] that conforms to a surface whose shape is determined by consideration other than electromagnetic; for example, aerodynamic or hydrodynamic.

Applications requiring conformal antennas are various, they can be used to ensure that the antenna does not alter the aerodynamic properties of the vehicle on which they are conformed: Unmanned Aerial Vehicle (UAV) [Liu et al., 2012] or aircraft [Kanno et al., 1996] or to ensure aesthetic [de Mingo et al., 2012]. In the reference [Bertuch et al., 2010], a 3D conformal antenna is built for airborne application to demonstrate its integration and feasibility as shown in Figure 1.21. 3D conformal antennas can be

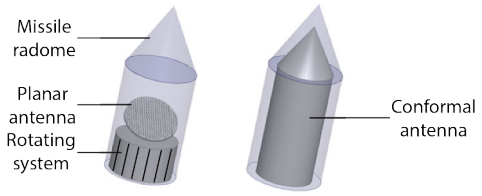

Figure 1.22: The space available below the radome

used for their flexibility for textile wearable [Mahmud and Dey, 2012]. Despite the IEEE definition, in the literature conformal antennas can be found where the design is optimised for electromagnetic purpose: for their high coverage properties such as satellite tracking [Geng et al., 2009] or for earth observation satellite [Caille et al., 2002].

There is no official definition for 3D antennas, still a lot of literature refers to this type of antenna. A definition is therefore proposed.

3D antenna [3D array] An antenna where the phase centres are not contained in a single plane and whereby its shape is determined from electromagnetic considerations.

In the case of RF-seekers, the space for the antenna is constrained by the radome shape which is the conformal aspect. There is also a new space offered by the mechanical system removal (Figure 1.22) which offers degrees of freedom to optimise the radiation pattern in directivity; this is why this antenna design is mixed, both 3D and conformal.

1.5.2 The antenna challenges

The 3D conformal antenna has a better field of view, a faster beam and the mechanical system removal decreases the production and maintenance costs. However, the realisation of the new antenna provides some challenges: technological, antenna design, guidance technique and multi-function. In this section, the different challenges are detailed.

1.5.2.1 Technological challenge

On the first hand, the technology gathers the problem of manufacturing a 3D conformal antenna, and on the second hand, increasing the active components (or Transmit/Recieve T/R modules) integration.

The additive manufacturing technology is receiving much attention in the antenna field. It consists of building a layer by layer object from bottom to top. It produces the antenna in one part which reduces the chances of discontinuities that would be obtained

with parts that are screwed together. It seems a promising technique to fabricate 3D conformal antennas as it allows to create complex shapes at a relatively low cost [Liang and Xin, 2014]. However, still little work can be found for the fabrication of large arrays. In [Guennou-Martin et al., 2016], a metal conformal slotted waveguide antenna arrays (SWAA) operating in Ku-band is presented. During the fabrication process, unexpected defects in the design are appearing. The causes of these defects have to be understood in order to be anticipated before the CAD model is generated. It is an illustration of the low maturity of the technology.

In the context of RF-seekers, the material needs to be resistant enough to endure the missile vibrations. The manufacturing process also needs to be accurate although any antenna design modifications during the manufacturing process alters the radiation pattern. This challenge goes beyond the scope of this work, thus, it is not investigated in this thesis.

A 3D conformal antenna nested below the radome of a missile would allow to embed many more elements than the mechanically steered planar array. Ideally, each element would be separately fed to achieve a multi-function antenna array, therefore, the active components needs to be highly integrated since space is very limited. In [Mancuso and Renard, 2014], the development trends of the active components are presented. A new tile architecture is described that allows to densely integrate the active components. However, complications such as overheating can appear in a dense electronic environment. This challenge is more extensively discussed in section 2.1.

1.5.2.2 Antenna design challenge

The antenna design objective is to realise a radiation pattern with strong performance to legitimate the technology change. The radar system aim is to steer the missile towards the target impact point, for that the signal to noise ratio should be as strong as possible where the only parameter accessible to the designer is the antenna gain.

The first step is to define the global shape of the antenna which has been studied in section 1.4.2. In our case the shape is designed for the best gain and as constant as possible.

The second step is the study of the position and orientation of the elements, the problem is illustrated in Figure 1.23. For the planar array, the field emitted in the direction Z is optimal since the total field has the maximum amplitude. For the conformal array, the quadrants do not have the same orientation, therefore the total field in the direction Z is weaker than the planar one, nonetheless a part of the resulting field also emits in the direction Y where the planar array cannot. Hence, a compromise exists between a sub optimal field in a specific direction but a homogeneous field over all the directions.

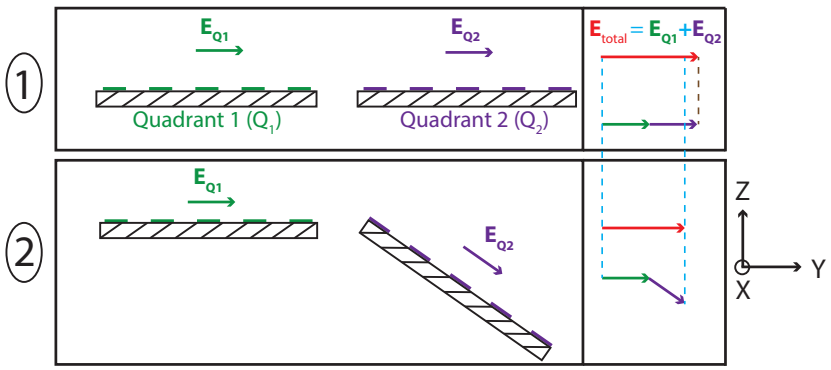

Figure 1.23: Field emitted in the direction Z: 1-Planar and 2-Conformal cases

The thesis addresses the tradeoffs produced by the different configurations of antenna arrays: position and orientation of the elements with their impact on the electromagnetic field. In the literature it is called polarisation. It is a major element of this thesis and developed further in chapters II and III.

The third step for the design of the antenna array is the radiating element type choice, as introduced earlier. The feeding of the element is also questioned, whether one or two access points are necessary.

The fourth step is the feeding network and power management. The feeding network carries the signal that has been formed by the Transmit/Receive (T/R) modules. For 3D and conformal shapes, the feeding network design is more challenging. The length of the feeding lines has to be well controlled for each element otherwise it induces a phase shift that would steer the beam direction. Consequently, if an uncontrolled phase is added to the elements it affects the beam and decreases the performance. For a conformal antenna, the space allocated for a given T/R module is reduced, however this space is constrained by the technology integration limit which limits the degree of conformation. For arrays made of hundreds of elements, if each element has a T/R module, the total cost is high. To counteract it, a solution exists in dividing the array into sub-arrays as shown in Figure 1.24. Nonetheless, the elevation and azimuthal control of the beam should be fine enough, otherwise the target tracking would be lower performing. This shows the relation and degree of freedom between the T/R modules and the feeding network and the induced compromise: precision of the beamsteering versus the cost of the system.

Finally the direction, in which the beam is focused, is studied through the beam-scheduling [Briheche et al., 2016]. The total space surrounding the antenna cannot be scanned at the same time. The scheduling consists of choosing a suitable sequence for scanning a given area.

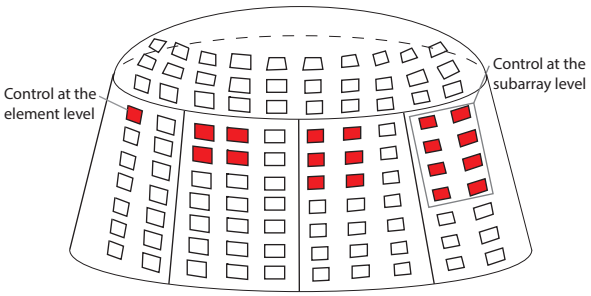

Figure 1.24: Element or sub-array feeding

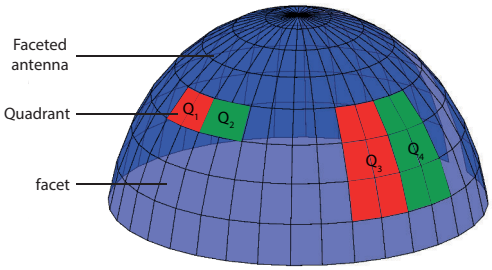

Figure 1.25: Quadrants dimensions

1.5.2.3 Ecartometry technique challenge

The RF-seeker tracks a target using ecartometry techniques and updates the target signal direction of arrival: the angles θ and φ. Those parameters are corrupted by noise which means that an error exists between the measured angles and their true values. A performing ecartometry techniques provides a close estimation from the true target angle. Consequently, one of the thesis goals is to evaluate the ability of the antenna to estimate a signal direction of arrival in each direction.

The orientation of the quadrants changes and the quadrant choice is not as trivial as for the planar antenna. An illustration of this problem is shown in Figure 1.25. A faceted half-sphere array is presented, where the target azimuthal angle is sought by carrying out monopulse, hence a choice for the quadrants dimensions should be taken. Two options are possible, first using the quadrants Q_1 and Q_2, only one facet for each quadrant, the quadrants are radiating in very close directions but the gain is small since a small surface of the antenna is used. Second, for the quadrants Q_3 and Q_4, it is the opposite, the quadrants are radiating in more diverging directions but their gains are higher although it is not usual to carry out ecartometry for non planar quadrants.

The thesis addresses the limitations and the new possibilities induced by the new antenna shape from an ecartometry perspective as well as a study of the quadrant dimensions.

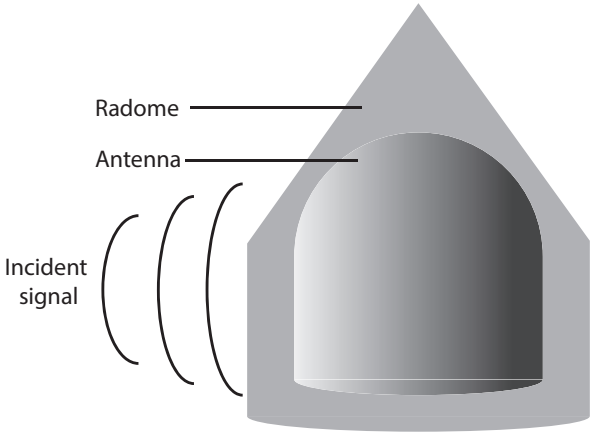

Figure 1.26: The antenna shadowing

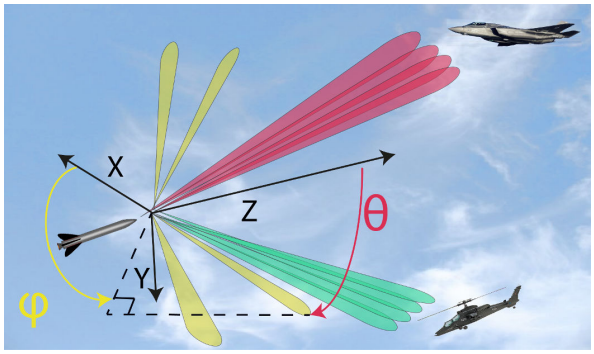

Figure 1.27: Multi-beam antenna

1.5.2.4 Multi-function challenge

Although a signal coming from a given direction illuminates the 3D/conformal antenna, a part of the antenna remains in the shadow. This is illustrated in Figure 1.26.

The antenna surface that stays in the shadow can be used for other applications. It can be used to search and track targets in other directions, this would lead to multi-target tracking. To make this technology mature, the multi-beam has to be developed, as shown in Figure 1.27.

1.6 Conclusion

The limitations of the current planar RF-seeker technology have been addressed. Furthermore, a preliminary study to identify suitable array shapes have been realised using the projected surface. As a result the cylinder and a compound made of a cylinder and a half-sphere present a high and constant projected surface over the field of view which would potentially bring high directivity performance.

The different challenges to reach a mature technology have been outlined. The thesis focuses on the antenna design and the ecartometry. The objective can be summarised as: design the new antenna such as the target detection and estimation is at least as good as, in terms of performance, the planar mechanically steered antenna. To fulfil this task, three objectives can be identified:

- The study of suitable 3D/conformal arrays is carried out to understand the trade-offs produced by the conformation.
- A method to evaluate the estimation accuracy of an antenna array is found and that can also allow comparison of arrays with each other.
- The impact of the 3D conformal on the phase monopulse is studied and the suitable quadrants dimensions are determined.

Chapter 2 From planar to 3D conformal RF-seekers

A review of the AESA antenna is carried out in order to understand how they evolved and how much their technology is advanced. Then, the specific problematic of the electromagnetic field for 3D conformal arrays are introduced. A state of the art of the control of the fields at the radiating element level as well as the array level is realised. Finally the antenna contributions of this thesis are presented.

The direction of arrival estimation is also introduced with the presentation of the estimators and the problematic. Afterwards, a literature review is realised to identify some gaps for the direction of arrival estimation related to 3D conformal arrays. Finally the contributions are exposed.

2.1 Active Electronically Scanned Antennas (AESA)

Active electronically scanned antennas consist of arrays of a few hundreds of radiating elements which beam is controlled electronically. Defense and aerospace companies are investing to replace the mechanically steered antennas by AESA antennas since the later ones offer more agility and accuracy. Those antennas are used in various applications: ground, naval or airborne. Today research trends are focused on the cost reduction, integration and performance improvement.

2.1.1 AESA progression and examples

In the 90s, the electronically steered antennas were passive, the entire array had one signal source and the beamsteering was realised in reception only. The passive naval radar TRS-3D from Airbus Defense and Space and the first version of the Thales airborne radar RBE-2 illustrate it. The TRS-3D radar is shown in Figure 2.1a. It has 16 rows of 46 radiating elements. It controls its beam electronically in elevation

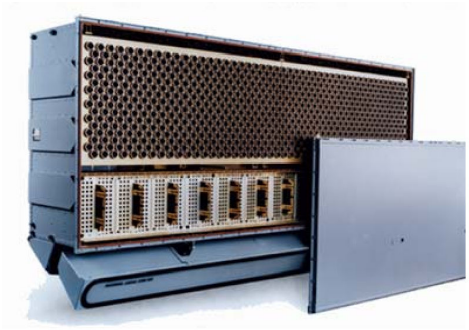

(a) Airbus Defense and Space radar: TRS-3D [Bil and Holpp, 2015]

(b) The Rafale plane [Hushkit, 2015]

(c) TRS-4D [Bil and Holpp, 2015]

Figure 2.1: Old and modern AESA

and mechanically in azimuth. It is used for air and sea target surveillance and target acquisition.

All versions of those radars built after 2000 use active electronic steering (Figure 2.1c). Each radiating element or sub-array is fed independently. The TRS-4D has a 3D tracking capacity of 1000 targets [Airbus Defense and Space, 2017], the tracking range accuracy is 15 m and the tracking range for maritime patrol aircraft goes up to 100 km. For the RBE-2, the detection range is enhanced by more than 50% and the antenna can now track a high number of targets at the same time [Hushkit, 2015].

Those radars are both multi-mode. Some of the mode of the TRS-4D are: 3D air volume surveillance with fast target alert, jammer detection, tracking and suppression, target classification, high range resolution surface surveillance.

Those two radars illustrate the number of elements that are used in today phased arrays and their computation capabilities. The evolution from passive to active radiating elements control has been possible thanks to the technology advancement and the higher computation processing for digital beamforming.

Conformal airborne AESA antennas do not exist yet. Nonetheless, to increase the coverage, multi-facet antennas can be used, the Multi-AESA Osprey Radar from Leonardo UK examplifies it [Kinghorn et al., 2016]. They have been used for search and

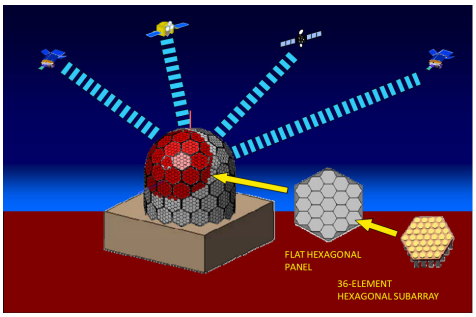

Figure 2.2: Geodesic Dome Phased Array Antenna [Ahn et al., 2010]

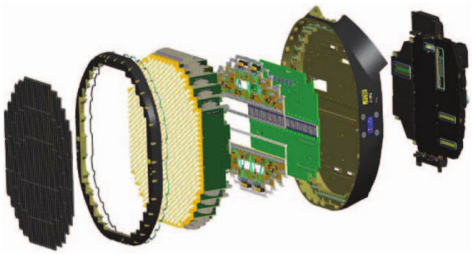

Figure 2.3: Exploded view of the Vixen 1000E AESA [Kinghorn et al., 2016]

rescue helicopters for example. For other applications such as satellite tracking, conformal AESA can be found. The Geodesic Dome Phased Array Antenna is illustrated in Figure 2.2 [Ahn et al., 2010]. It can establish up to four transmit and receive beams at the same time. The structure has 11 meters and hosts more than 60000 radiating elements. To limit the cost, the elements are arranged by sub-arrays, each 36 elements hexagonal sub-array (Figure 2.2) has one transmit and two receive ports. In total the entire structure has 3350 receiving ports. Each port signal is digitalised and processed.

The antenna can carry out different modes due to the digital beamforming: adaptive pattern control for anti-jamming or interference suppression control, direction finding with high resolution and ultra low sidelobes. The different functions expected from AESAs are similar, irrespective of the application.

The three examples introduce the capabilities of today AESA in term of multi-mode and accuracy thanks to the digital beamforming. The digital beamforming is allowed by use of active antennas and T/R modules. However, T/R modules have a cost that today research aims at decreasing. It is covered in the following section with the trends for the AESA improvements.

2.1.2 Challenges and expectations of the future AESAs

The RF electronic system of the AESA radar is made of several planks that hosts the T/R modules, power supply, control electronics and an integrated inertial measurement

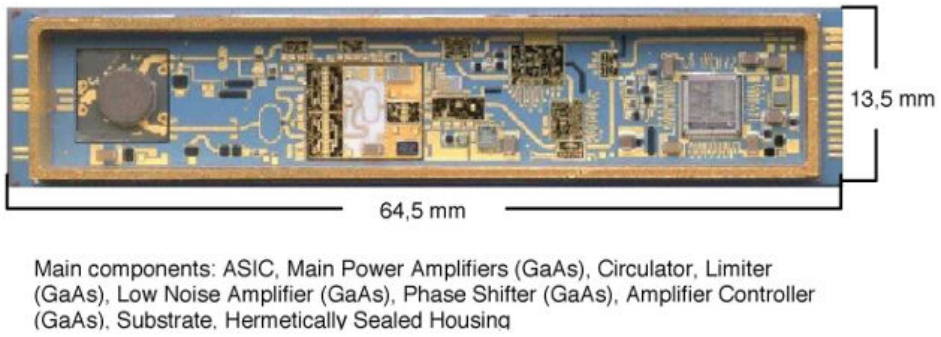

Figure 2.4: TR module [Hommel and Feldle, 2005]

unit, as illustrated in Figure 2.3 [Kinghorn et al., 2016].

The trends for the enhancement of the radar concerns the T/R module technology, the digital beamforming, the field of view and finally the co-operation among the airborne apertures [Kemkemian and Nouvel-Fiani, 2010].

Today the trends for the improvement of the T/R modules is steered by the need to reduce the cost and at the same time increase their performance. T/R modules are realised with Monolitic Microwave Integrated Circuits (MMIC) in gallium arseniure (GaAs) technology. MMICs are cheap circuits thanks to the commercial mass production. Today, T/R modules for a missile seeker cost 30 per elements [Brookner, 2008] and they are integrated enough to be put on a single chip as shown in Figure 2.4.

The technology is evolving towards gallium nitrure (GaN) which advantage is a higher power density: 3-6 W/mm for GaN versus 0.5-1.5 W/mm for GaAs [Brookner, 2008]. The GaN also has better performance in term of thermal conductiviy which allows more efficient cooling and superior voltage [Brookner, 2008] [Brookner, 2008]. The silicium germanium (SiGe) technology is also an alternative for its low cost. It does not have better performance than GaAs but it is more integrated on a single chip [Brookner, 2008].

The packaging technology is also evolving, the T/R modules used to be pluggable to ease maintenance. However the connectors increase the cost and decrease the global reliability of the system therefore the T/R modules are soldered all together on planks (Figure 2.3). Future research are looking at integrating the radiating elements, the T/R modules and the power supply all together in a 3D high dense multi-layer module [Lacomme, 2003]. The architecture is called tile for mulTI-LayEr as shown in Figure 2.5. One of the challenge of this high integration is the heat management with the power density increase.

A wide field of view is key for the aircraft survivability. However the field of view of planar AESA is limited to an elevation angle of 60° as the beam is electronically steered. To compensate this limitation, the AESA can be associated to a repositioner

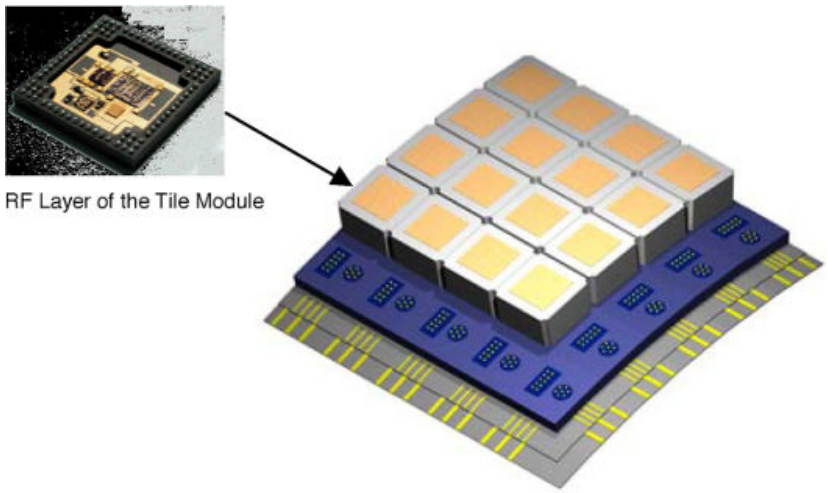

Figure 2.5: Tile technology [Hommel and Feldle, 2005]

that rotates the antenna plane. It is a solution that has been applied by Leonardo Airborne and Space Systems in the United Kingdom [Kinghorn et al., 2016]. However the RBE-2 AESA installed on the Rafale is fixed as a repositioner is not effective for a high number of targets [Hushkit, 2015]. An AESA coupled to a mechanical system is therefore not the optimal solution which rises the need for conformal airborne AESA antennas.

The active electronically scanned elements allow to increase the control of the pattern. The use of the SiGe technology allows to increase the integration and add the analog to digital converters (ADC) on a chip which means that more information needs to be processed at the same time. The choice of the digital architecture to process more data and decrease the time to decision is another challenge [Ahn et al., 2010].

Current research is also looking at limiting the cost of RF-seekers antennas and at the same time increasing its accuracy. Hence, conformal antennas are explored to take benefits of the space offered by the mechanical system removal to ensure a constant directivity as a function of the steering angle.

The field emitted by conformal antennas is more complex to study than for planar antennas. The problematic risen by conformal antennas is illustrated in the next section.

2.2 Electromagnetic field and problematic of conformal antennas

The study of the electromagnetic field is related to the polarisation. The polarisation is defined in the three next sections.

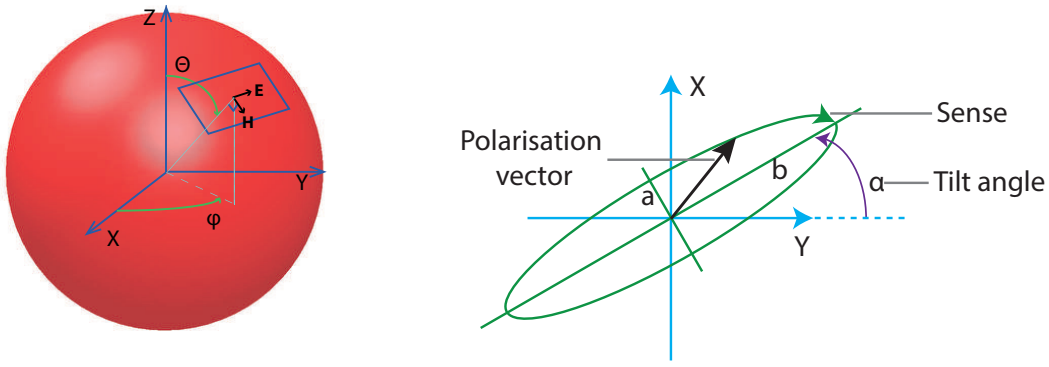

(a) The radiation sphere

(b) The polarisation state parameters

Figure 2.6

2.2.1 Electromagnetic field and polarisation

When an antenna radiates an electromagnetic signal as illustrated in Figure 2.6a, in the Fraunhofer region, beyond the minimal distance $\frac{2D^2}{\lambda}$ where D is the longest antenna dimension, the field is approximated as a plane wave in a given direction. The far field electric field can be expressed as shown in equation 2.1 which is solution of the propagation equation.

$$\mathbf{E}(\mathbf{r},t) = \frac{\|\mathbf{E}_1\|}{r} e^{j(2\pi f_0 t - \mathbf{k}\cdot\mathbf{r})}\mathbf{p} \tag{2.1}$$

Where $\mathbf{E}$ is the complex electric field, r the distance from the antenna phase centre, $\|\mathbf{E}_1\| = r\|\mathbf{E}\|$, $\mathbf{E}_1$ is the amplitude of the field independent of the distance from the antenna and $\mathbf{p} = \frac{\mathbf{E}_1}{\|\mathbf{E}_1\|}$ is the unitary polarisation vector. f_0 is the frequency and $\mathbf{k}$ is the wave vector.

In the far field, the electromagnetic wave consists of an electric $\mathbf{E}$ and magnetic $\mathbf{H}$ fields which are orthogonal and which amplitudes are proportional: $\|\mathbf{E}\| = \eta_0\|\mathbf{H}\|$, η_0 is the void impedance. Since in all directions the electric and magnetic fields are orthogonal, the antenna field is totally described by one of each, in the thesis, the electric field is considered.

The distribution of the electric field is characterised by the directivity. Their relation is shown in equation 2.2.

$$\begin{aligned} U &= \frac{r^2}{2}\,\mathrm{Re}(\mathbf{E}\times\mathbf{H}^*) = \frac{r^2}{2\eta_0}\|\mathbf{E}\|^2 \\ D(\theta,\varphi) &= \frac{U(\theta,\varphi)}{U_0} = \frac{4\pi\|\mathbf{E}(\theta,\varphi)\|^2}{\int\int_{\theta,\varphi}\|\mathbf{E}(\theta,\varphi)\|^2\sin\theta\partial\theta\partial\varphi} \end{aligned} \tag{2.2}$$

U is the radiation intensity and characterises the distribution of the field and is independent of the distance r. The directivity is the normalisation of the radiation intensity.

As an electric signal travels in the free-space, the trajectory of the tip of the polarisation vector describes an ellipse as a function of time. Two parameters are necessary to describe it: the tilt angle which is the main axis orientation of the ellipse and the axial ratio $\frac{a}{b}$. It is illustrated in Figure 2.6b. Extreme cases of the ellipse produce linear and circular polarisation, details are given in section 2.2.2.

2.2.2 The polarisation state

In a given direction and position, depending on the phase of the electric field, different trajectories are covered producing: linear, circular and elliptical polarisation.

- Linear polarisation: at every instant of time the electric field is always oriented along the same straight line. The **E** field is linear if it respects one of the two conditions:
  - Only one component
  - Two orthogonal linear components that are in time phase or 180° out of phase $\delta\phi = \phi_y - \phi_x = n\pi$
    An illustration is shown in Figure 2.7a where the wave propagates along the axis Z.
- Circular polarisation: the electric field vector tip follows a circle path as a function of time. The **E** field vector is circular if it respects the two conditions:
  - Two orthogonal components
  - The components must have the same magnitude and a time-phase difference between both which is odd multiples of $\frac{\pi}{2}$.
    An illustration is shown in Figure 2.7b.
- Elliptical polarisation corresponds to the intermediate states. The electric field vector follows an elliptical path as a function of time.

The electric field is described by a polarisation vector that describes its state and the directivity that characterises the amplitude. To be easily understood, this polarisation vector needs to be projected in a coordinate system. Its choice is discussed in the next section.

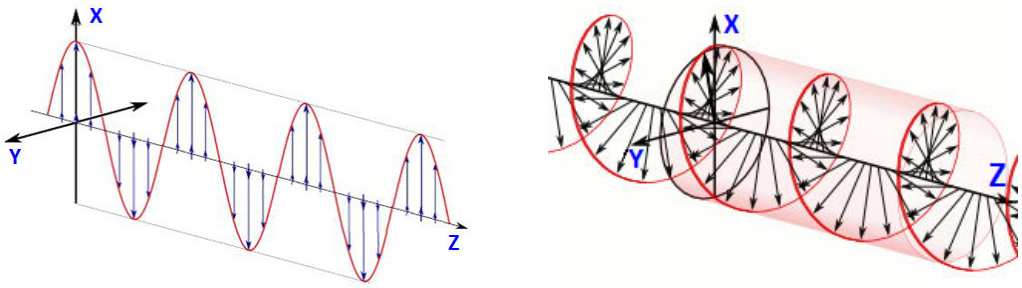

(a) Linear polarisation (b) Circular polarisation

Figure 2.7: Specific cases of polarisation state

2.2.3 The polarisation representations

The antenna radiates a complex vector field in all the directions. To facilitate its analysis, it is usually projected in a coordinate system which components are called co-polarisation and cross-polarisation components, that are written co-pol and cross-pol for brevity.

From the IEEE Standard Definition of Terms for Antennas (IEEE Std 145-2013):

Co-polarisation That polarization that the antenna is intended to radiate [receive]. See: polarization pattern, NOTE 1 and NOTE 2.

Cross-polarisation In a specified plane containing the reference polarization ellipse, the polarization orthogonal to a specified reference polarization.

The co-pol and cross-pol components are orthogonal to each other, therefore the coordinate system carrying the components should also be orthogonal.

In conclusion, it has been seen that the electric field is described by a vectors field, each vector is associated to a polarisation state. To facilitate their study, the polarisation used to be projected in an orthogonal system which components are called co-pol and cross-polar components. In the next section, the problematic of the polarisation and directivity for conformal arrays are presented.

2.2.4 Problematic of the electric field for conformal antennas

2.2.4.1 Azimuthal tradeoffs

As described in this section 1.4.1, the azimuthal directivity should be constant, the best directivity in all the directions is also sought. This leads to a tradeoff.

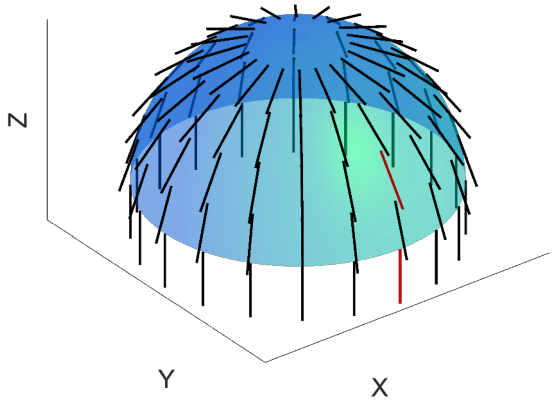

Figure 2.8: HZ dipoles covering a half-sphere antenna

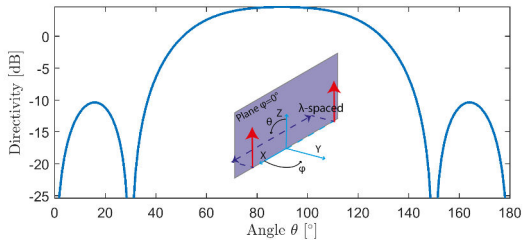

(a) 2 Hertzian dipoles z-orientated

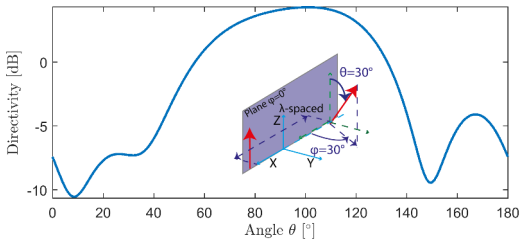

(b) 2 Hertzian dipoles one along z and one $\theta = 30°$ and $\phi = 30°$

Figure 2.9: Electric field for aligned and non aligned elements

In the following scenario where 100 Hertzian dipoles are covering a half-sphere antenna shape, radiating elements are not parallel except in the horizontal plane at the bottom of the half-sphere, as shown in Figure 2.8. Let us consider two elements taken along θ and observe the effect of their different orientation.

If the elements are kept parallel a higher directivity level is achieved in the direction $\theta = 90°$ as interferences are summing constructively, as shown in Figure 2.9a, where the maximum directivity is 4.6dB and the beamwidth is 78°. However if the elements are not aligned, as it would be produced for 3D conformal arrays, one of the elements may be rotated, as shown in Figure 2.9b. Then a beamwidth of 84° is achieved for a lower maximum directivity, its maximum is now 4.3dB.

This example shows the first problematic regarding the directivity: the tradeoff between the level of directivity and the beamwidth. In some extent, the beamwidth represents the coverage of the array.

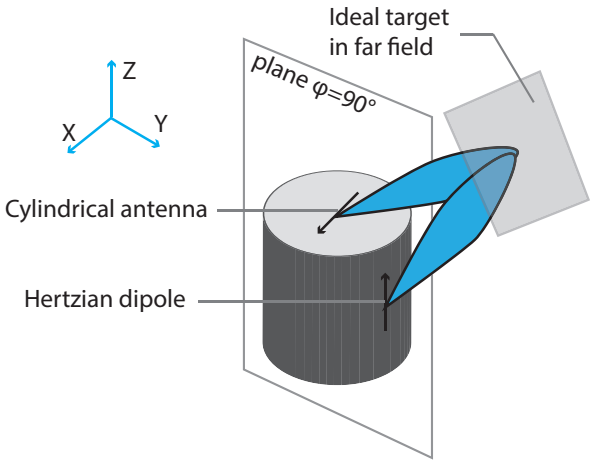

(a) Cylindrical antenna

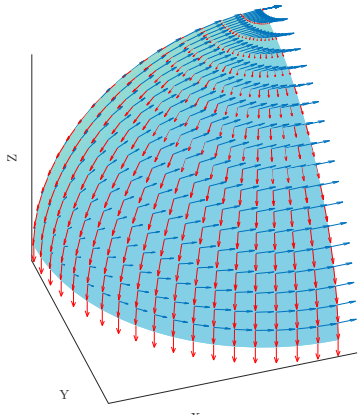

(b) Cylindrical antenna and its vector fields: vertical element (red) and horizontal element (blue)

Figure 2.10: Polarisation matching scenario and vectors field

2.2.4.2 Polarisation matching

The polarisation matching problematic is theoretically set with the following scenario. A cylindrical antenna made of two Hertzian dipoles, one on the top surface and one on the side are tracking an ideal reflector target placed at $\theta = 45°$, in the plane $\varphi = 90°$, so that both elements track the target from the same angle, as shown in Figure 2.10a. This angle is chosen to ensure that each antenna receives the signal from the other one. The reflector is ideal in the sense that it has no effect on the signal, the signal keeps same characteristic after reflection than before. In this configuration, the tracking is inefficient since antennas are blind for each other due to the orthogonality of their polarisation vectors.

The vector field of each antenna element is given in Figure 2.10b. The vectors field are calculated for each element positioned at the coordinate system origin. Changing the position of the element to be in the cylinder situation would induce a phase on the electric field that would not affect the field vectors directions, only the sense, since the elements have a linear polarisation state. In the $\varphi = 90°$ plane, along the axis Y, the vectors are orthogonal which means that the radiating elements are emitting in each other cross-polar component which makes the antennas blind to each other as well.

The link budget equation 1.1 has been set supposing a perfect matching polarisation, instead if the polarisation is accounted, the SNR is proportional to the square of the scalar product of each antenna polarisation vector $\mathbf{p}_1$ and $\mathbf{p}_2$.

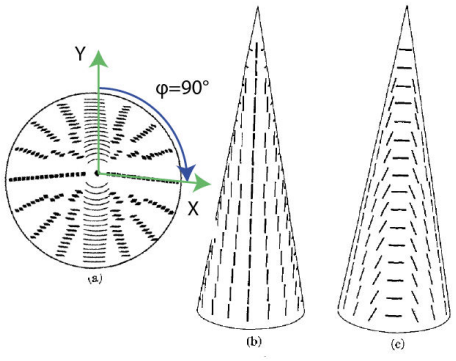

Figure 2.11: Conical array, (a) View from the axial direction. (b) Side view, (c) Side view rotated 90° from (b)

$$SNR = SNR_{MP} \|\mathbf{p}_1 \cdot \mathbf{p}_2\|^2 \tag{2.3}$$

Where SNR_{MP} is the signal to noise ratio in the case of a matching polarisation. In the cylinder situation, the final SNR is zero due to the orthogonality of the polarisation vectors.

As a conclusion, on a 3D conformal shape, where the elements have different orientations, in some cases, the polarisation of the elements could be orthogonal which would make the radiating elements of different quadrants blind for each other in the worse case and mismatched which brings a performance decrease in other cases.

To make an antenna array effective the polarisation of the elements should be matched. One of the solution could be to rotate the elements. In [Kummer, 1974], the author optimises the orientation of slots elements on a conical shape so as to have the best performance in the z-direction. This is realised by progressively rotating the elements as shown in Figure 2.11. The elements along the axis X are vertical, away from this axis, the elements are progressively tilted and are horizontally oriented along the axis Y.

This is a solution to counteract the problematic described by the HZ dipole on the cylinder. However in the case of the conical array, the elements orientation is only optimised for one specific direction. In the horizontal planes, the rotation makes the elements orthogonal and therefore fully mismatched to each other. In this thesis there should not be any privileged direction.

2.2.4.3 Polarisation state deviation

The third problematic of the polarisation concerns the deviation of the polarisation vector from an intended polarisation state. A radiating element radiates a specific

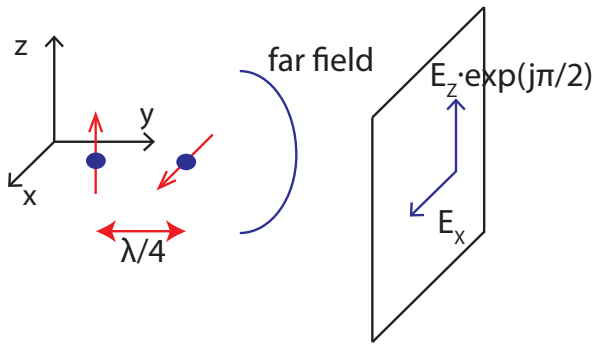

Figure 2.12: Illustration of the polarisation state deviation

polarisation state: linear, circular or elliptical, then as the elements are used in a conformal array the resulting polarisation can be different from that of the element.

The effect of the element orientation diversity on the polarisation state is explored using 2 orthogonal Hertzian dipole elements aligned along the axis Y and $\frac{\lambda}{4}$ spaced as shown in Figure 2.12. The far field in the axis Y has circular polarisation resulting from two orthogonal components with equal amplitude and $\frac{\pi}{2}$ delayed. For any distance between the elements different from a multiple of $\frac{\lambda}{4}$, $\frac{\lambda}{2}$ or λ, the resulting polarisation state would be elliptic, not linear. It illustrates the polarisation state problematic when conformal antennas are used such as the half-sphere array (Figure 2.8).

2.2.4.4 Conclusion

The thesis will address the directivity and polarisation challenges for conformal arrays. The elements have to be arranged so that first the directivity is optimal, second the polarisation from a quadrant to another is matched and third the polarisation remains linear as much as possible. A literature review is carried out on the polarisation control at the element level, then at the array level to understand how the previously exposed problematic are handled in the literature.

2.3 Antenna literature review

2.3.1 Radiating element performance review

In the literature review, the patch antennas are considered since they are low profile elements, corresponding to the need of highly integrated AESA antennas.

In the budget link antenna to target, the SNR is affected by the orientation of the elements due to the array conformation. To improve it, the radiation characteristics of the planar patch element and the conformal patch element are investigated, the

following points are studied:

- The radiation characteristics, in term of directivity and polarisation
- The radiation characteristics of conformal patches, in term of directivity and polarisation
- The polarisation purity study approach and the impact of the conformation

Improving the directivity of an antenna array can start by improving the directivity of each radiating elements. Several methods have been found to improve the directivity performance of the patch element. They consist in tuning the patch metallic shape or the substrate.

Small improvement of 0.14dB has been found using exponential shapes for two of the four sides of a square patch, as shown in Figure 2.13a. Fractal shapes have shown better enhancement of the directivity using Koch Island shapes, as shown in Figure 2.13b, however the frequency of use is not the fundamental one. In [Borja et al., 2000], the fundamental is at 1.11GHz and a performance improvement of 4dB is found at 3.52GHz. Nonetheless the patch is cumbersome for array use with a width of 1.38λ at 3.52GHz. In [Anguera et al., 2001] a bow-tie fractal of the second order with a 0.54λ size, as shown in Figure 2.13c, has 5dB of improvement over the original bow-tie element. The directivity improvement is obtained by comparison of the original and the tuned element (with and without fractals) which results in different resonance frequencies. This comparison is consequently not fair. The improvement should be taken from the original radiating element whithout fractals designed at the new frequency.

Directivity improvement is also achieved using photonic bandgap substrate as illustrated in Figure 2.13d ; it is a periodic structure that allows to eliminate unwanted resonating modes such as surface modes. In [Qiu and He, 2001], the periodic structure consists in air holes drilled in the substrate. They increase the directivity by 6dB although it produces a slight frequency shift and weaken the physical strength of the structure which could be critical for missile as the vibrations encountered are very strong when travelling at supersonic speed. Very promising publications have also been found using superstrate which consists in a dielectrique bonded to the patch or separated from it above the radiating patch as shown in Figure 2.13d. In [Qiu and He, 2001], directivity performance close from the maximum theoretical directivity have been observed with a photonic bandgap superstrate where reaching the maximum would mean that the patch behaves like an aperture. Nonetheless those structures seem too cumbersome and not really applicable for conformal shapes. Still the radome itself could play the role of the superstrate [Boutayeb et al., 2010] [Deepti Das et al., 2008].

As a result, the patch design used for the array will remain simple as most methods have too critical drawbacks for our application.

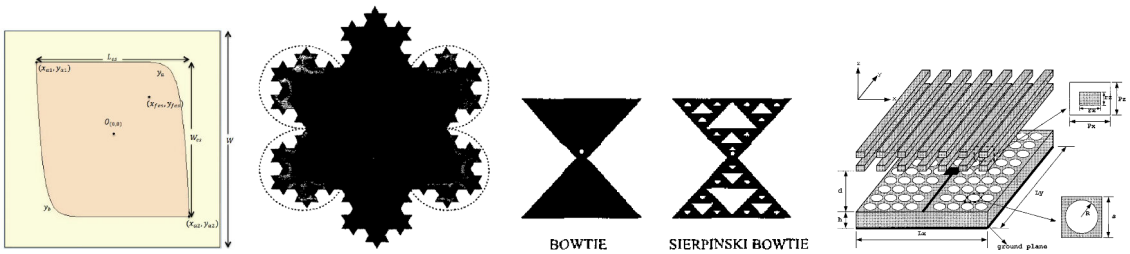

(a) exponential-square patch (b) Koch island patch (c) Fractal bow-tie patch (d) Photonic bandgap patch

Figure 2.13: Patch element illustration for directivity enhancement

The polarisation is projected on two orthogonal components: the co-pol and the cross-pol. The cross-polar is the non-intended component, a review is realised to identify what causes the cross-pol and how to lower it while keeping a constant co-pol component to maintain the directivity constant. This challenge emphasises the bound between the polarisation and the directivity.

In [Kumar and Guha, 2014], the author eliminates higher order mode resonance identified as a source of cross-polarisation. The first higher order mode resonance is concentrated at the corner of the patch and close to the non-radiating edges. Therefore the ground plane is defected with straight bracket shapes, as shown in Figure 2.14a, to improve the radiation symmetry. However ground plane defection has the drawback to generate back radiation towards T/R modules. This method is therefore not suitable, instead methods tuning the patch surface exists, in the same paper, the author observes that the co-pol to cross-pol difference decreases as the patch width to length ratio increases, finally a square shape patch is optimised for low cross-pol level. In the same direction, in [Ghosh et al., 2015], a defected patch surface is conceived to remove the first higher order resonance. The patch defect has an arc shape which radius is optimised and that removes the corners, as shown in Figure 2.14b, results are shown in Figure 2.15 where a reduction of the cross-pol component can be observed in the E and H planes while the co-pol component remains constant.

In [Mahmoud and Al-Ajmi, 2008], modifications affect the substrate to improve the polarisation purity of a circular patch. The author optimises the position of 2 metallic pins in the substrate to cancel surface waves for linear polarisation and carry out the same work for 4 pins for circular polarisation, as shown in Figure 2.16a. The interest of using pins in the antenna design is realised theoretically, using the cavity model which does not account for the pins couplings. Instead, in [Bilotti and Vegni, 2010], the author goes farther and uses the four metallic probes as feeding ports, each fed with a 90° phase (Figure 2.16b), with a similar arrangement to cancel surface wave and improve the polarisation purity, the result is that mutual couplings between the probes

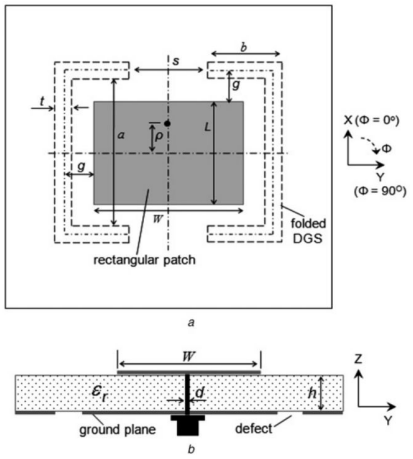

(a) Rectangular patch with defected ground plane

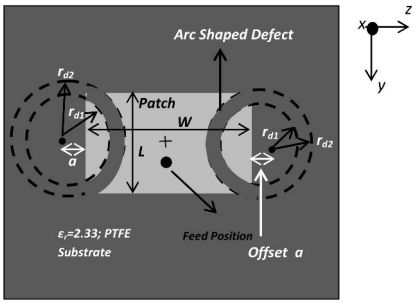

(b) Rectangular patch with defected surface

Figure 2.14: Patch element illustration for polarisation purity enhancement

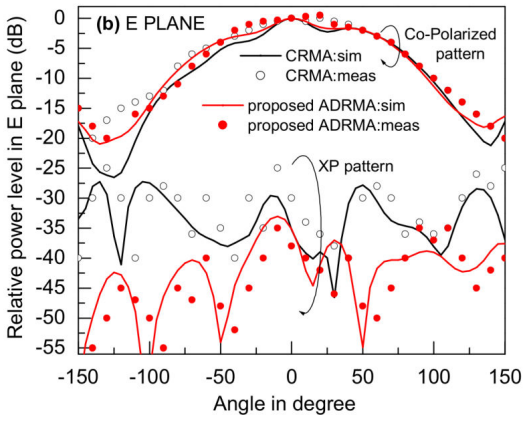

(a) E plane

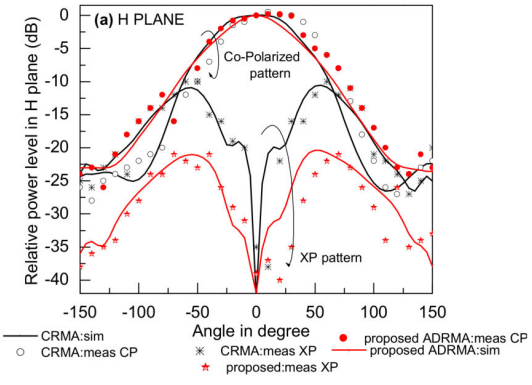

(b) H plane

Figure 2.15: Comparison between the Conventional Defected Microstrip Antenna (CDMA) and the Arc Defected Rectangular Microstrip Antenna (ADRMA)

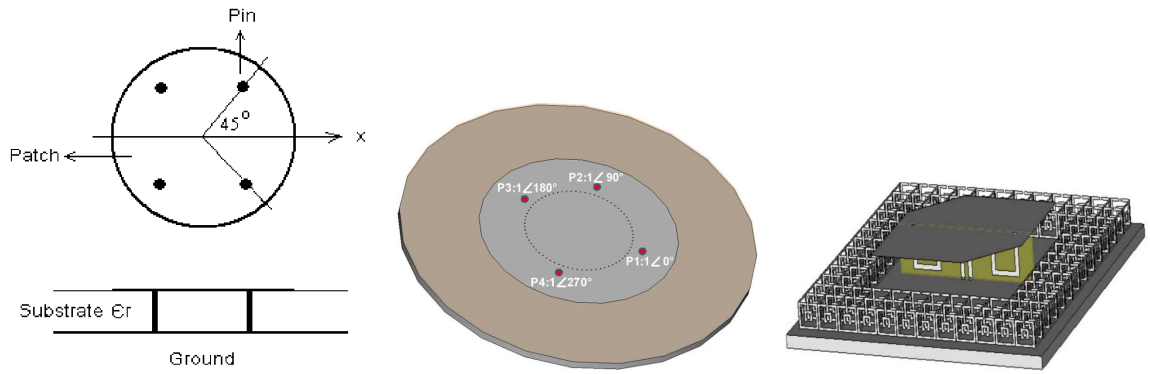

(a) Circular patch with metallic pins (b) Four pins circular antenna (c) Rectangular patch with metamaterial

Figure 2.16: Patch element illustration for polarisation purity enhancement

does not alter the adaptation and decreases the cross-pol. Despite the polarisation purity enhancement, multiplying the feeding ports may increase the feeding system complexity. The author also studies how to trap the surface waves generated by a rectangular patch. The patch has truncated corner and is set above a meander line, it is surrounded by a metamaterial made of split ring resonators to capture the surface waves and decrease the cross-polarisation, as shown in Figure 2.16c. As a result, it prevents couplings if the elements would be used in an array. Nonetheless this technique makes the radiating element too bulky for use in an array.

As a result the cross-pol component is caused by higher order resonance mode or surface wave propagation. When used in an array, it generates couplings between the radiating elements which would lower the global performance. The cross-pol can be decreased by working on the surface of rectangular patches, the substrate and even on the ground plane. Among those techniques, the defected patch surface is the best compromise for constant gain while the cross-pol component is decreased. Nevertheless, techniques that would both improve the gain and the polarisation purity would be more desirable.

In the literature, techniques allying both polarisation purity and gain enhancement can be found by using multi-layer structures. In [Mastrangeli et al., 2013] a superstrate technique is used. In [Wang et al., 2009] a multi-layer structure of stacked patches is presented. It is possible to find various publications on multi-layer structure including aperture coupled patches [Tsao et al., 1988]. This technique offers strong polarisation purity [Mao et al., 2016] as the field of the feeding probe is filtered by an aperture cut in a metallic plane located between the feeding line and the patch and can be easily coupled to the gain enhancement techniques [Coccioli et al., 1999]. However this technique has the drawback to induce back radiations, to counteract this effect an additional metallic layer should be set below the structure which would unfortunately

remove the original simplicity of the patch design. Multi-layer patches are techniques that would fit with the future trends of tile AESA antennas for high integration.

Techniques to improve the radiation performance of patch antennas seems promising. For conformal antennas the modification of the patch shape also modifies the radiations, whether it can be coupled to a performance improvement is investigated.

The radiating element is aimed to be conformed on a simply or doubly curved surface on the conformal antenna. Patch conformation with study of polarisation purity are non existent which leaves a large gap for future research. Publications with study of the directivity enhancement and conformation are rare. In [Swaisaenyakorn et al., 2016] 4 rectangular patches are conformed on a PVC pipe and aperture coupled for gain improvement, the structure offers a 360 coverage. In [Baviskar et al., 2016], a conformal patch antenna that produces a high coverage and a reduced gain is coupled to a metamaterial lens to counteract this gain reduction, as shown in Figure 2.17a. This publication is interesting as the metamaterial does not follow the curvature of the conformal antenna which means that the radome could be used for radiation enhancement.

Literature is prolific for the polarisation and directivity enhancement of planar patch antennas. The cross-pol is due to higher mode of resonance and surface waves, by reducing this component, it prevents the radiating elements to have couplings when organised in arrays which can be source of blind angles and impedance mismatching [Pozar and Schaubert, 1984]. Techniques for reduced cross-pol component consists in modifying the ground, patch itself or the substrate. The use of metamaterial substrate are also very promising for radiation enhancement. Finally, for conformal patches the literature is limited to show the impact of conformation on the polarisation purity.

Radiating elements have been tuned to reduce the cross-pol component that could alter the performance when used in an array. The methodology to improve the polarisation of a conformal array is reviewed in the next section.

2.3.2 Polarisation and methodology of analysis of conformal arrays

2.3.2.1 Problematic

In a conformal array, the choice of co-pol and cross-pol components varies from an element to another as their orientations change. For a scenario involving two orthogonal Z and X oriented Hertzian dipoles as shown in Figure 2.10a, the co-pol component of each HZ dipole is different as shown in Figure 2.10b since the electric fields of both elements are not collinear in all the directions. In this scenario, even though ideal elements without cross-polar are considered, it does not prevent the array to be

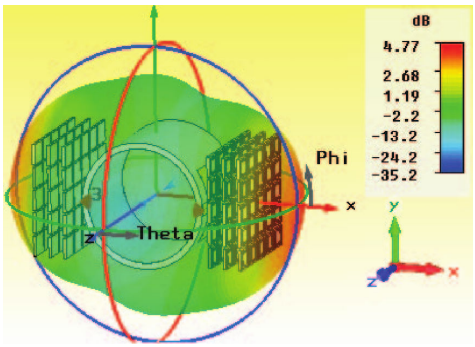

(a) Conformal antenna coupled to metamaterial lens

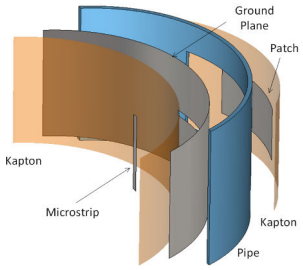

(b) Eectangular patch antenna aperture coupled and conformed on a PVC pipe

Figure 2.17

Figure 2.18: Wullenweber antenna next to Augusta in Germania

cross-pol free. In the following literature review, for an array made of several tens or hundreds elements with different orientations, the choice of the global co-pol and cross-pol coordinate system is investigated. The degrees of freedom on which the authors play for polarisation purity enhancement and their methodology for polarisation are analysed.

2.3.2.2 Literature review

The first conformal circular antenna called Wullenweber has been built during World War II for a complete azimuthal beamsteering, as shown in Figure 2.18. It was developed by the German navy communication command for direction finding of emitters. The antenna was a hundred meters of diameter. It illustrates the need to enhance the fied of view. This example could be discussed whether it is really a conformal antenna array since the phase centres of all the elements are located in the same plane.

Literature concerning the polarisation of 3D conformal antennas are publications that carry out pattern synthesis. The traditional synthesis methods used for linear

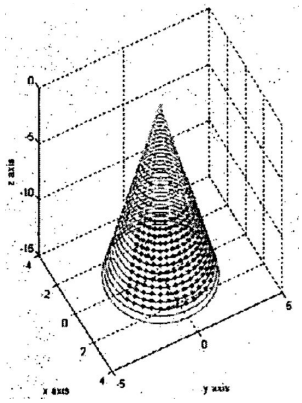

Figure 2.19: 3D cone with slot elements [Morton and Pasala, 2004]

and planar arrays are not valid as there is no factorised element factor. Publications aim at optimising an array to reach given performance using a developed algorithm. Many different methods can be found in the literature numerical and analytical methods. The numerical methods are numerous, among them interpolation technique [Yang et al., 2010], space mapping technique [Ouyang et al., 2010], non-linear optimisation method [Banach and Cunningham, 1988], intersection approach [Mazzarella and Panariello, 1993], least squares methods [Vaskelainen, 1997a], simulated annealing technique [Ferreira and Ares, 1997], adaptive array theory [Zhou and Ingram, 1999], and particle swarm optimisation [Liu et al., 2008] can be found. The numerical methods work for any kind of array, their weakness is their slowness. Analytical techniques are more specific but faster [Song, 2008], [Q. Wang, 1974]. Finally as a first answer to the methodology approach, authors develop their own program with different optimisation techniques. In the next paragraph, the details of a few relevant papers for the thesis are given.

For airborne and missile application, Dr. Morton and Dr. Pasala [Morton and Pasala, 2004] propose to optimise the directivity of a 3D cone covered with slots as illustrated in Figure 2.19. To steer the beam in the desired direction, the author carries out beamsteering in the elevation plane and switch on and off the elements in the azimuth direction. The author has shown that the curvature of the array introduces strong side-lobes from the elements which boresight is to far from the aimed direction. That is why the author makes an optimisation and switches off the elements that are too far from boresight to reduce the sidelobes. It makes a strong difference on the radiation pattern as shown in Figures 2.20a and 2.20b. In this paper, the polarisation is not studied and the on or off law applied to the side-lobes remains limiting, it is an apodisation technique with a coarse control of the element excitation.

In [Comisso and Vescovo, 2013], the authors present a fast iterative method to optimise the co-pol and cross-pol patterns of antenna arrays using a spherical coordinate system and reduce the dynamic range ratio of the excitation. This emphasize on the

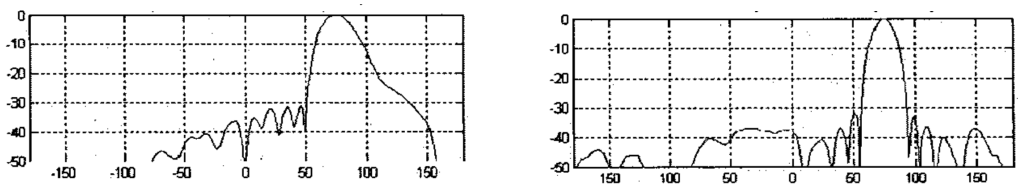

(a) Power as a function of the azimuthal angles, scanned from symmetric center

(b) Power as a function of the azimuthal angles, switched array

Figure 2.20: Fast iterative polarisation optimisation [Comisso and Vescovo, 2013]

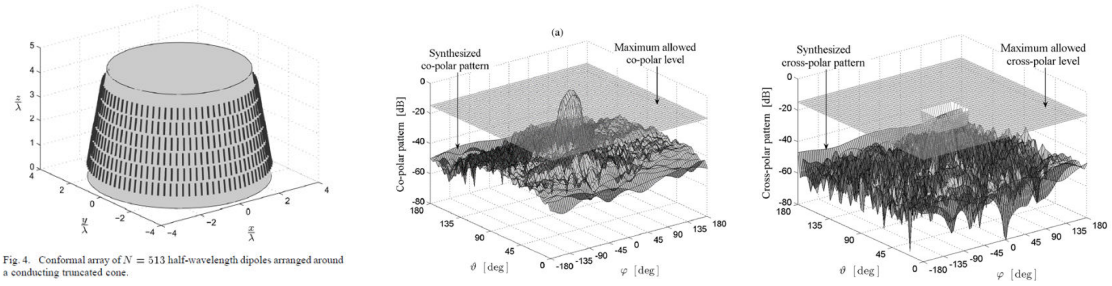

(a) Truncated cone with 513 dipoles elements

(b) co-pol pattern

(c) cross-pol pattern

Figure 2.21

excitation is interesting for the future array feeding network that may be built. The structure used as an example is a truncated cone of dipoles, as shown in Figure 2.21a, this later shape is interesting for airborne embedded antennas. The objective is to lower the sidelobe levels of the cross-pol component and keep a reasonable dynamic range ratio. However as raised by the author it would be illusory to lower much the cross-pol level without drastically decreasing the co-pol component. A result of the co-pol and cross-polar optimisation is shown in Figures 2.21b and 2.21c.

The objective patterns for the co-pol component is a maximum of -15dB for the sidelobes region and for the cross-pol component -25dB in the main lobe region and -15dB elsewhere. Results in Figures 2.21b and 2.21c show that the synthesised pattern reaches the objectives after optimising the element excitation.

However such simple radiating elements limits the control of the polarisation, that's why papers also investigate patch elements which allow dual-polarisation. In [Dohmen et al., 2007], the authors consider a sphere covered with dual-fed patch elements, as shown in Figure 2.22a.

The dual feeding of the patch effectively allows a better control of the polarisation. Excitations α_n and β_n of each feeding point control the magnitude of both projections of the E field. This yields control of the $\mathbf{E}_n$ field direction, as shown in Figure 2.22b.

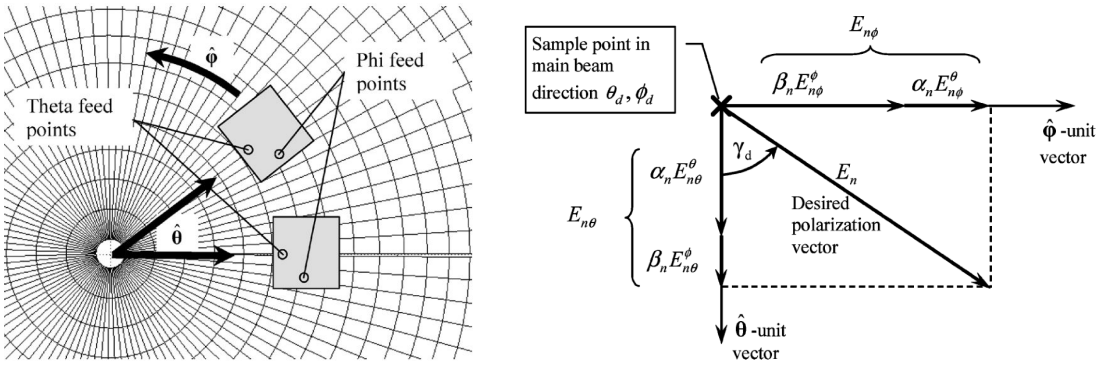

(a) Dual-fed patches (b) Control of the polarisation direction

Figure 2.22: Dual-fed patch in a spherical array

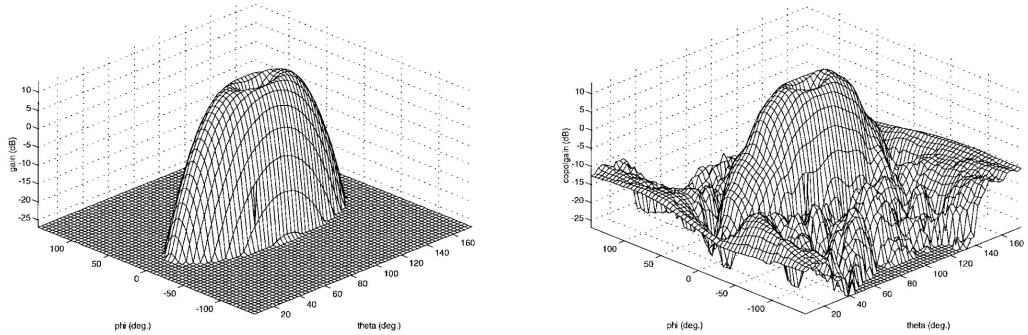

(a) Desired pattern (b) Achieved pattern

Figure 2.23: Generation of a difference pattern [Vaskelainen, 1997b]

In the literature, some authors choose to optimise the elements excitation to obtain a difference pattern; those works can directly be applied for monopulse. In [Vaskelainen, 1997b], the author studies the difference pattern generated by a sphere of modelled patches emitting circular polarisation. The desired pattern and the achieved patterns are shown in Figures 2.23a and 2.23b. Parameters investigated by the authors include the effect of the excitation type: left or right handed circular polarisation only or both on the cross-pol level. The use of both polarisations lowers the cross-pol but slightly decreases the fit with the desired **E** field.

[Dinnichert, 2000] generates both sum and difference patterns of a paraboloid with 162 dual-polarised patches for low cross-pol and low sidelobes without mentioning the polarisation coordinates system. He proposes an iterative least square method to fit a pattern with a mask where the degree of freedom is the element excitation. Such a shape is interesting for airborne antenna as its shape is close to the radome one. In [Fei-lin and Jun, 2011], a conical array is optimised for low cross-pol level and to remove the grating lobes in the context of precision-guided multi-mode seekers. Two

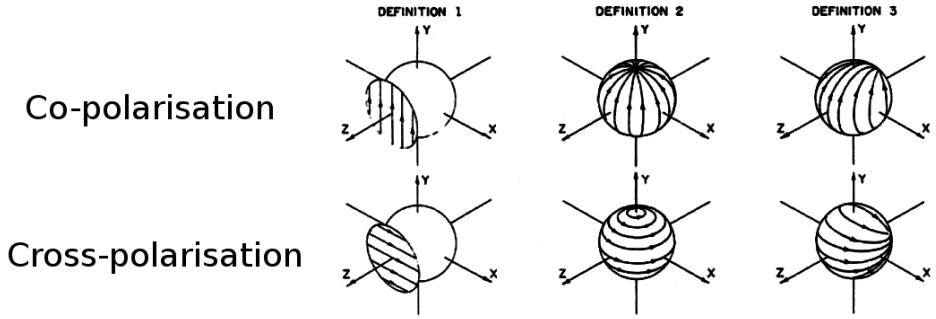

Figure 2.24: The definitions of cross polarization [Ludwig, 1973]

representations are considered to express the co-pol and cross-pol components, using the spherical coordinate system, a linear and circular representation. Results show that the circular representation has a very low cross-pol level while the linear one has strong cross-pol level. The author then produces a refinement of the array by randomly changing the spacing between the elements to cancel grating lobes.

The literature review has shown the methodology used in the literature to study the polarisation. When authors discuss the polarisation, they aim for a maximum co-pol and a minimum cross-pol. In that regard, optimisations of the elements positions or orientations are rare; instead authors set a specific array and optimise the excitation amplitude and phase. It has been found that dual-polarised elements produce a better control of the co-pol and cross-pol components level. The authors usually express the co-pol and cross-pol components in the spherical coordinate system which may be explained by the choice of azimuthal invariant arrays. [Fei-lin and Jun, 2011] discusses the choice of the polarisation representation in order to obtain a low cross-polarisation pattern.

Different definitions exist for the polarisation representation; the advantages and drawbacks of each are discussed in the next section to be able to choose the most adapted one for our application.

2.3.3 The polarisation definitions

2.3.3.1 Ludwig's definitions

In [Ludwig, 1973], he enumerates the definitions encountered. Details of each of them are given below, eventually each representation is discussed.

- Definition 1: In a Cartesian coordinate system ($\mathbf{e}_x$,$\mathbf{e}_y$,$\mathbf{e}_z$), the co-pol and cross-pol components are defined as:
  - $\mathbf{e}_{co} = \mathbf{e}_x$ and $\mathbf{e}_{cross} \perp \mathbf{e}_{co}$.

- Generally $\mathbf{e}_{co} = \alpha\mathbf{e}_x + \beta\mathbf{e}_y + \gamma\mathbf{e}_z$ and $\mathbf{e}_{cross} \perp \mathbf{e}_{co}$ where α, β and γ are reals.

- Definition 2: In a spherical coordinate system ($\mathbf{e}_\theta$,$\mathbf{e}_\varphi$) the unit vectors are tangential to the radiation surface, the co-pol and cross-pol components are defined as:
  - $\mathbf{e}_{co} = \mathbf{e}_\theta$ and $\mathbf{e}_{cross} \perp \mathbf{e}_{co}$.
  - Generally $\mathbf{e}_{co} = \alpha\mathbf{e}_\theta + \beta\mathbf{e}_\phi$ and $\mathbf{e}_{cross} \perp \mathbf{e}_{co}$.

- Definition 3: In this polarisation system, the co-pol and cross-pol components changes depending on the direction φ.
  - $\mathbf{e}_{co} = \sin\varphi\mathbf{e}_\theta + \cos\varphi\mathbf{e}_\phi$ and $\mathbf{e}_{cross} = \cos\varphi\mathbf{e}_\theta - \sin\varphi\mathbf{e}_\phi$.
  - Generally $\mathbf{e}_{ref} = \sin(\varphi - \varphi_0)\mathbf{e}_\theta + \cos(\varphi - \varphi_0)\mathbf{e}_\phi$ where φ_0 is a parameterised angle.

The different polarisation systems are illustrated in Figure 2.24.

2.3.3.2 The circular coordinate system

The circular coordinate system is not referred to by Dr. Ludwig although it is very commonly used. It uses complex unit vectors:

- Definition 4: This definition uses the unit vectors defined by the spherical coordinate system. The components are called right handed circular polarisation (RHCP) and left handed circular polarisation (LHCP).
  - $\mathbf{e}_{co} = \frac{1}{\sqrt{2}}(\mathbf{e}_\theta + j\mathbf{e}_\phi)$ and $\mathbf{e}_{cross} = \frac{1}{\sqrt{2}}(\mathbf{e}_\theta - j\mathbf{e}_\phi)$.
  - Generally $\mathbf{e}_{co} = \frac{1}{\sqrt{\alpha^2+\beta^2}}(\alpha\mathbf{e}_\theta + j\beta\mathbf{e}_\phi)$ and $\mathbf{e}_{cross} = \frac{1}{\sqrt{\alpha^2+\beta^2}}(\alpha\mathbf{e}_\theta - j\beta\mathbf{e}_\phi)$ are reals.

The polarisation definitions are illustrated, in the next section, using the electric field of the HZ dipole and the patch. The definition that produces the lower cross-pol component is discussed. The polarisation pattern of the HZ dipole and the patch antenna are given in appendix.

Illustration of the Cartesian definition

The electric field of a Z-oriented Hertzian dipole (Figure 2.25) is projected in the Cartesian coordinate system ($\mathbf{e}_X, \mathbf{e}_Y, \mathbf{e}_Z$) in each direction ($\theta, \varphi$), as shown in Figure 2.26a. The directivity pattern is superimposed onto the coordinate system.

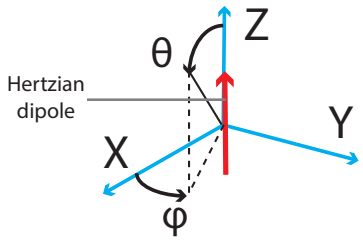

Figure 2.25: Hertzian dipole

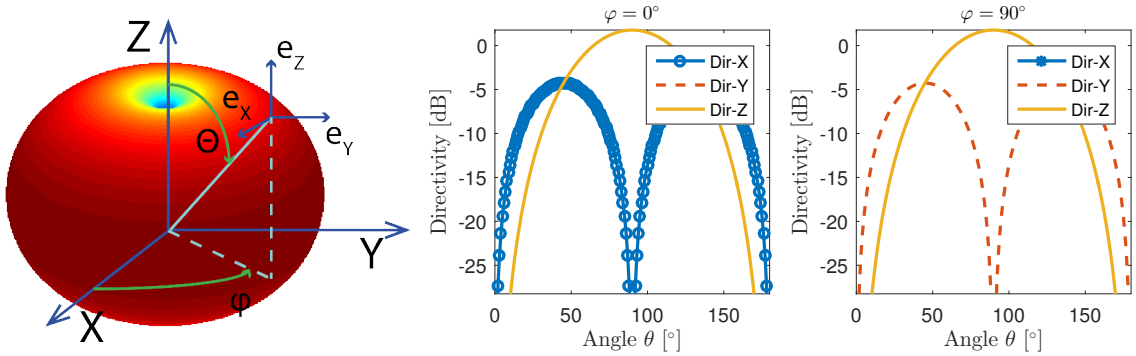

(a) Radiation sphere

(b) Co-pol (left) and cross-pol (right)

Figure 2.26: Illustration of the Cartesian definition

Results in the specific planes $\varphi = 0°$ and $\varphi = 90°$ are given in Figure 2.26b. The directivity level in each component suggests the choice of the co-pol along the vector $\mathbf{e}_Z$. There is no ambiguity, in both cut planes $\varphi = 0°$ and $\varphi = 90°$, it is maximum. The cross-pol is in a different Cartesian component depending on the plane. It is along the axis X in the plane $\varphi = 0°$ and along the axis Y in the plane $\varphi = 90°$. The scale is taken from the maximum of the total directivity $Max(Dir-X^2 + Dir-Y^2 + Dir-Z^2)$ and its minimum is 30dB below this maximum, below this level, the field is considered to be negligible, being 1000 times weaker in amplitude. In the plane $\varphi = 0°$ the component along Y and in the plane $\varphi = 90°$ the component along X are below this minimum and their impact is negligible. As a conclusion, this polarisation representation is not suitable for the dipole.

In the literature, authors often use vertical and horizontal polarisations which are specific orientations of a linearly polarised radiating element expressed in a Cartesian coordinate system.

Illustration of the spherical coordinate system

The electric field is projected in each direction (θ, φ) on the spherical unit vectors $(\mathbf{e}_r, \mathbf{e}_\theta, \mathbf{e}_\varphi)$, as shown in Figure 2.27a. Since the field is contained in a plane orthogonal

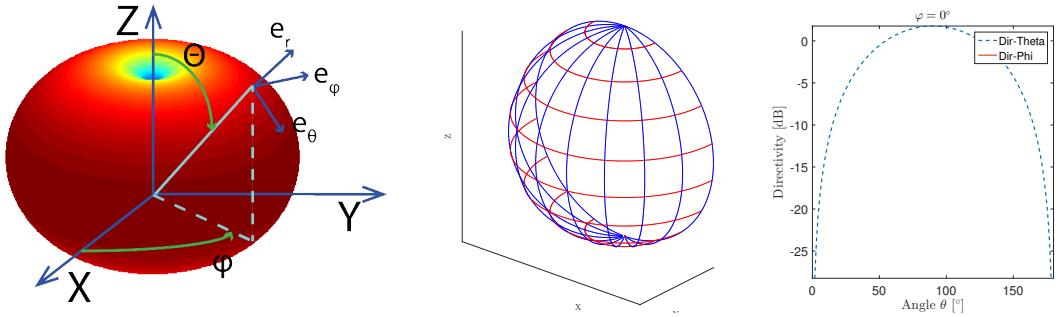

(a) Radiation sphere (b) Spherical field lines (c) Co-pol and cross-pol

Figure 2.27: Illustration of the spherical coordinate system

to the propagation direction $\mathbf{e}_r$, the components $\mathbf{e}_\theta, \mathbf{e}_\varphi$ are enough to express the electric field. The field lines are shown in Figure 2.27b, the θ lines go through the poles and the φ lines are parallel to each other and orthogonal to the axis Z. This definition only requires the use of two components compared to the Cartesian coordinate system that uses three.

The example of the HZ dipole field is shown in Figure 2.27c. The rotation invariance around the axis Z allows generalisation of the result given in a single plane φ to all the other planes. The electric field is contained in the θ component while the φ component is 30dB below the θ component. This polarisation definition therefore fits best with the Hertzian dipole.

Illustration of the mixed coordinate system

This representation of the polarisation is usually referred as the 3^{rd} Ludwig's definition. This definition consists of projecting the $\mathbf{e}_\theta$ and $\mathbf{e}_\varphi$ vectors onto the planes $\varphi = 0°$ and $\varphi = 90°$. The co-pol component changes from the $\mathbf{e}_\varphi$ to the $\mathbf{e}_\theta$ vector when the observation direction rotates around the axis Z: from the plane $\varphi = 0°$ to $\varphi = 90°$. The vector lines are represented in Figure 2.28a, they are converging in one pole.

This definition is not suitable for the Hertzian dipole, it would give $\mathbf{e}_{co} = E_1 \sin\theta \sin\varphi \mathbf{e}_\theta$ and $\mathbf{e}_{cross} = E_1 \sin\theta \cos\varphi \mathbf{e}_\theta$ where E_1 is the electric field amplitude independent of the direction. The components are the same with a $\varphi = \frac{\pi}{2}$ shift which does not allow the identification of the co-pol or cross-pol component. For an x-fed patch, this definition is convenient, as shown in Figure 2.28b. In the $\varphi = 0°$ plane the component $L3Y$ is more than 30dB below the reference component $L3X$ and in the $\varphi = 90°$ the $L3Y$ component remains dominant.

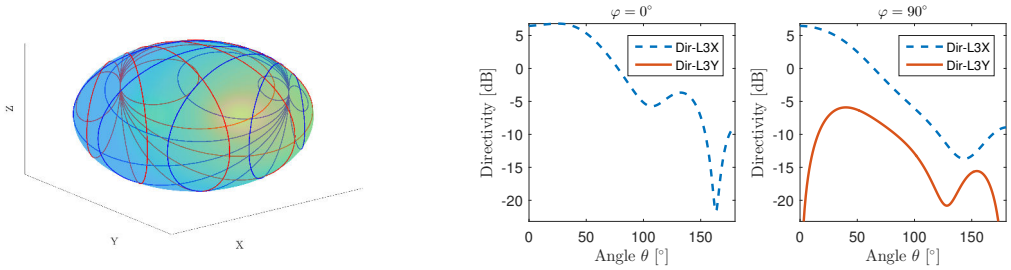

(a) 3^{rd} Ludwig's definition field lines (b) Co-pol and cross-pol

Figure 2.28: Illustration of the mixed coordinate system

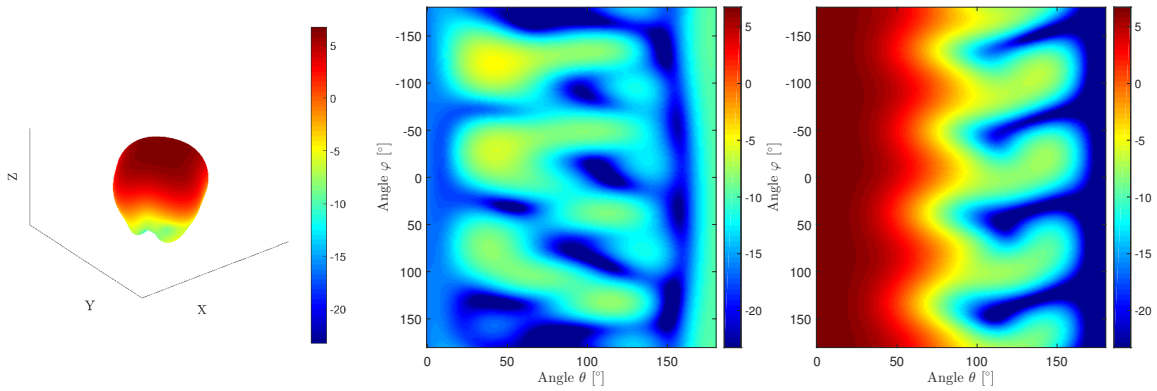

(a) Dir-Total (b) Dir-RHCP (c) Dir-LHCP

Figure 2.29: Circularly polarised patch

Illustration of the circular coordinate system

This representation is used for circular polarisation RHCP and LHCP. This polarisation is usually achieved using dual polarised radiating elements using horns and patches. The circular coordinate system is not represented since it requires a complex coordinate system. The example of a patch radiating in the Z-direction and dual-fed along the X and Y directions with a 90° phase is given in Figure 2.29.

The electric field of a patch with two access fed points with a 90° phase produces a rotating vectors field, as a result the rotating polarisation definition matches with this field. The co-pol component is LHCP.

The different definitions are now discussed in greater detail.

2.3.4 Discussion

In order to understand the different definitions, this publication [Ludwig, 1973] is firstly detailed since it is so commonly referenced by authors for polarisation. Ludwig relates the choice of the representation firstly to the source and primary field distribution, secondly to the secondary radiation pattern of reflector antennas.

A secondary radiation pattern is the reflected pattern produced by a paraboloidal antenna reflecting a horn antenna signal for example.

According to the author, the first definition (Cartesian) is convenient for source currents. For field description it is less suitable as a fields radiated by an antenna is better being described by a coordinate system that possesses only two components, that is why, definitions 2 and 3 are more suitable.

The 3^{rd} Ludwig definition is raised by the need to have a reflector antenna that would offer two orthogonal communication channels. The feeding antenna radiates a signal that is reflected on the parabola. The signal used to suffer from losses during the reflection although cross-polarisation currents are induced in the reflector. [Koffman, 1966] found a necessary and sufficient condition for zero cross polarised surface currents: $E_\theta \cos\varphi = E_\varphi \sin\varphi$. Hence if a reflector antenna respects this condition it is equivalent to saying that there is no cross-pol, according to the 3^{rd} definition, and the energy will completely contribute to the peak gain on axis. Finally, if the antenna respects the 3^{rd} Ludwig's definition the cross-pol is negligible and the antenna could offer two communication channels. This is the context in which the 3rd Ludwig's definition has been proposed.

This definition is widely used in the literature although at first it has been set for the specific case of reflector antenna and to facilitate the analysis of antenna measurement.

In this reference [Knittel, 1973], Dr. Knittel criticises Dr. Ludwig's paper for being to definite on the interest of his 3^{rd} definition for antenna patterns. Instead, he proposes: 'the cross-polarisation characteristic of an antenna should provide a measure of the deviation of the antenna polarisation from a *meaningful* nominal state. This depends on the intended use of the antenna.' To support its point, he proposes a radar antenna with linear polarisation tracking a target in ideal conditions. In this case the same antenna is used in emission and reception, hence there is no polarisation mismatch and Ludwig's definitions of cross-polarisation are not applicable. To conclude on that, he is raising the point that a definition of the cross-polarisation characterising the modification of the polarisation from linear to circular would be necessary. He also suggests that in many cases, cross-polarisation is not really relevant as it is difficult to define a meaningful one.

The essence of this talk reveals that the conditions and objectives of the study have to be well defined in order to use an appropriate definition of the polarisation. In

response to those critics, Dr. Ludwig suggests the axial ratio as a measure of the linear deviation. In the proceeding research, a similar measure of this deviation is proposed.

Each definition proposed by Dr. Ludwig is applicable to different cases found in the literature which are detailed here.

- Cartesian coordinate system: source currents, aperture antennas and planar arrays with rectangular shape.
- Spherical coordinate system: patches radiating in the X direction, dipole elements, circular arrays and azimuth periodic arrays.
- Mixed coordinate sytem: patches radiating in the Z direction, Huygens sources, 3D antennas and for comparison with measurement plots.

This paper has been released in 1973 and is still used as a reference, especially regarding the 3^{rd} definition. In publications, the definition used is not always mentioned, for example, where a single patch element is considered and polarisation patterns are presented: [Tsao et al., 1988], [Luk et al., 1998] and [Li et al., 2004]. Furthermore in other papers even though the polarisation is explicitly mentioned authors rarely explain why they choose a definition rather than another.

For the need of this thesis, the Cartesian and spherical polarisation definitions are used in order to investigate the electromagnetic properties of the field for the different arrays. The three components of the Cartesian definitions allow to finely characterise the electric field. The spherical definition is chosen as one of the objective for the antenna is to find azimuthal invariant performance which induces an azimuthal invariant shape as well. This was found in the preliminary study of the chapter 1. The 3^{rd} Ludwig definition is not used as it requires to know the azimuthal target angle to compute the representation. The circular definition RHCP and LHCP is not selected, first, since it makes difficult the understanding of the field. Second, since the interactions between a circularly polarised wave state and hydrometeors are more difficult to modelise.

2.3.4.1 Conclusion of the antenna literature review

AESA antennas with planar arrays are mature, their cost decreases and thanks to the digital beamforming they can cover different using modes. After a review of the literature, mature airborne 3D conformal AESA have not been found. One barrier for 3D conformal arrays is the technology and the polarisation since the electric field is more complex to study than for planar arrays.

It has been shown in this state of the art that the directivity and polarisation are closely related. The sources of the cross-polarisation are not studied the same whether a radiating element is considered or an array made of hundreds of elements.

The radiating element cross-polarisation is caused by higher mode resonance or surface waves that can induce couplings when used in arrays or scan blindness which means a reduced directivity. Different techniques have been reviewed to reduce the cross-pol component and increase the gain, modifying the patch surface to remove the cross-polarisation sources is the most interesting as it does not affect the co-pol one. To reduce the surface waves, metamaterial can be used to limit their propagation but it leads to bulky radiating elements. Finally, publications on the polarisation of conformal patches have not been found.

For arrays, most publications set a given array geometry and then authors realise pattern synthesis algorithms to optimise the excitation and achieve a specific radiation pattern. Dual-polarisation seems promising as it allows a higher control of the electric field. However authors do not discuss the causes of the cross-pol component.

One paper was found [Fei-lin and Jun, 2011] that discusses the choice of the polarisation representation in order to decrease the cross-pol component. This suggests that a coordinate system can be more suitable that another one to project the field and obtain a low cross-pol level. Hence, a review of the different polarisation definitions has shown that it would depend on the radiating element and the array geometry. Usually for azimuth invariant arrays, the spherical definition is chosen.

In conclusion, analysis of the co-pol and cross-pol components in relation to the coordinate system for complex arrays have not been found. Furthermore, no publications have been found studying the effect of the positions or orientations of phased arrays radiating elements on the polarisation.

2.3.5 Contributions on the 3D conformal arrays

The objective is to find a suitable array that take benefits from the available space below the radome. Different types of arrays are studied, in each case the polarisation and directivity are compared.

- A Matlab program is realised for the fast simulation of complex arrays.
- Comparison of three 3D conformal arrays, faceted: truncated faceted cone, one degree of curvature: truncated cone and two degree of curvatures: half-sphere
- The tradeoffs produced by the positions and orientations of the elements for a planar array are addressed.

- The impact of matching the elements orientations on the polarisation purity and directivity is studied.

- The sources of ellipticity as a function of the array configuration and beamsteering are explored.

The 3D and conformation of phased arrays not only has an impact on their directivity and conformation but also on their direction of arrival estimation and ecartometry. The estimators and the tool used to evaluate the estimation performance are introduced in the next section, followed by a literature review.

2.4 Introduction to the CRLB and estimators

2.4.1 The causes of the estimation: the noise and its model

The echo signal reflected on the target is sensed and measured by the antenna elements sensors. Like in various engineering fields, where signal measurements are required whether they are acoustic, optic or electric, the sensors always suffer from losses and imperfections. In the RF-seeker, the antenna transforms the electromagnetic signal into an electric signal. For every useful signal, an unwanted thermal noise is superimposed. This is due to the motion of free electron charges in the conductors and semi-conductors of the electronic components. The mean power of the noise signal is $N = kTB$ where k is the Boltzmann's constant, T is the temperature in Kelvin and B is the bandwidth of the receiver.

The thermal noise is modelled in signal processing by a white Gaussian process, white meaning that the power spectral density of the noise is uniform over the bandwidth, and Gaussian meaning that the complex amplitude of the unwanted electric signal follows a Gaussian distribution. The in-phase and quadrature components of the noise signal, w_I and w_Q, produced by the IQ detector are samples of two statistically independent Gaussian processes with zero mean and variance σ^2. The noise components at each antenna element are assumed statistically independent and identically distributed, i.e. $E\{w_i w_j\} = 0$ where $i \neq j$ and $w_i = w_{iI} + jw_{iQ}$. Many other sources of interference exist but they are not considered.

Many parameters can be extracted from the echo signal measurements: the range, the direction of arrival (angular position), the speed, the airborne type. In this thesis, the direction of arrival is considered.

2.4.2 Estimation and estimators

The measurements of the target parameters are uncertain due to the noise signal. The target parameters have therefore to be estimated and estimation is subject to an error: the error is defined as the difference between the estimate and the true value. To estimate the parameters, estimators are used. Numerous estimators exist for RF-seekers. It would therefore be convenient to have a criteria to measure their absolute estimation performance.

The geometry of the elements is also a degree of freedom. It is at first interest to know if 3D conformal arrays are really competitive for direction of arrival estimation.

The Cramer-Rao Lower Bound can fulfil this double objective.

2.4.2.1 What is the CRLB?

In the literature, the Camer-Rao Lower Bound (CRLB) is often used as a reference to compare different antenna designs but also to evaluate the efficiency of their estimator. The CRLB has therefore a double interest in this thesis.

Let us assume an unknown parameter α extracted from a noise corrupted signal modelled by a process x characterised by a Probability Density Function (PDF) p.

Provided that the first and second derivate of the PDF (equation 2.4) exist and are absolutely integrable [Van Trees, 2004]:

$$\frac{\partial \ln p(x,\alpha)}{\partial \alpha} \qquad \frac{\partial^2 \ln p(x,\alpha)}{\partial \alpha^2} \tag{2.4}$$

Then, the variance of the estimate $\hat{\theta}$ provided by any unbiased estimator respects the following condition [Kay, 1993a]:

$$var(\hat{\theta}) \geq \frac{1}{-E\left\{\frac{\partial^2 \ln p(x,\alpha)}{\partial \alpha^2}\right\}} \tag{2.5}$$

Where the right member of the inequality is called the CRLB. It provides the theoretical minimum variance for any unbiased estimator.

A first example is derived using the signal model, as shown in equation 2.6, where a real parameter α is sought, on which a white Gaussian noise w following a normal distribution $\mathcal{N}(0,\sigma^2)$, is superimposed.

$$x = \alpha + w \tag{2.6}$$

The associated PDF is shown in equation 2.7.

$$p(x;\alpha) = \frac{1}{\sqrt{2\pi\sigma^2}} e^{-\frac{1}{2\sigma^2}(x-\alpha)^2} \tag{2.7}$$

Finally using 2.5, the minimum bound is $CRLB = \sigma^2$.

One can notice that taking the second derivative of a function provides the convexity of that function. For a Gaussian distribution, its convexity is set by the inverse of its variance. Hence, in the specific case of a linear model and a Gaussian noise, the CRLB provides the variance of the PDF which is also the variance of the estimate. This is consistent with the result $CRLB = \sigma^2$.

To calculate the CRLB, the theoretical statistical expectation is applied to the inverse of the convexity of the PDF function. This operator uses an infinite serie over the different samples of the signal model which allows to achieve a closed form result without accounting for estimator processing.

The parameter that is estimated can also be part of a complex function and for n processed samples it gives: $x_n = x_{In} + jx_{Qn} = s_I(n,\alpha) + n_I(0,\sigma^2) + j(s_Q(n,\alpha) + n_Q(0,\sigma^2))$. The pdf is

$$p(x_I, x_Q; \alpha) = \frac{1}{(2\pi\sigma^2)^N} e^{-\frac{1}{2\sigma^2}\sum_n (x_{In}-s_I(n;\alpha))^2 + (x_{Qn}-s_Q(n;\alpha))^2}$$

The first derivative of the likelihood function with respect to α is derived, then the second derivative and finally the expectation is applied.

$$\begin{aligned}
\frac{\partial \ln p(x_I, x_Q;\alpha)}{\partial\alpha} &= -\frac{1}{2\sigma^2}\sum_n \frac{\partial}{\partial\alpha}\left[(x_{In}-s_I(n;\alpha))^2 + (x_{Qn}-s_Q(n;\alpha))^2\right] \\
&= \frac{1}{\sigma^2}\sum_n \left[(x_{In}-s_I(n;\alpha))\frac{\partial s_I(n;\alpha)}{\partial\alpha} + (x_{Qn}-s_Q(n;\alpha))\frac{\partial s_Q(n;\alpha)}{\partial\alpha}\right] \\
\frac{\partial^2 \ln p(x_I, x_Q;\alpha)}{\partial\alpha^2} &= \frac{1}{\sigma^2}\sum_n \left[-\left(\frac{\partial s_I(n;\alpha)}{\partial\alpha}\right)^2 + (x_{In}-s_I(n;\alpha))\frac{\partial^2 s_I(n;\alpha)}{\partial\alpha^2}\right. \\
&\qquad \left. -\left(\frac{\partial s_Q(n;\alpha)}{\partial\alpha}\right)^2 + (x_{Qn}-s_Q(n;\alpha))\frac{\partial^2 s_Q(n;\alpha)}{\partial\alpha^2}\right] \\
E\left(\frac{\partial^2 \ln p(x_I, x_Q;\alpha)}{\partial\alpha^2}\right) &= -\frac{1}{\sigma^2}\sum_n \left[\left(\frac{\partial s_I(n;\alpha)}{\partial\alpha}\right)^2 + \left(\frac{\partial s_Q(n;\alpha)}{\partial\alpha}\right)^2\right]
\end{aligned}$$

Finally the minimum variance of the parameter is:

$$var(\hat{\alpha}) \geq \frac{\sigma^2}{\sum_n \left[\left(\frac{\partial s_I(n;\alpha)}{\partial\alpha}\right)^2 + \left(\frac{\partial s_Q(n;\alpha)}{\partial\alpha}\right)^2\right]} \tag{2.8}$$

2.4.2.2 What is the Maximum Likelihood (ML) estimator?

As discussed in the previous section, to estimate as accurately as possible a signal embedded in noise, an efficient unbiased estimator is sought offering a minimum variance. Quotation from [Kay, 1993a]: 'Minimum variance unbiased estimator do not in general exist.' An alternative to that is the maximum likelihood estimator. In case the minimum variance unbiased estimator does not exist or cannot be found, the ML estimator always exist and can be calculated 'for most cases' [Kay, 1993a], this estimator is asymptotically efficient. It means that the estimator reaches the CRLB for a large number of samples. Furthermore if the minimum variance estimator exist the ML estimator will find it. Finally a closed form of the ML estimator is not always possible to derive, hence computer simulations are necessary to find it.

A generic signal model of the signal measurement is given in equation 2.9. This time the parameter α that will be estimated is a parameter of a function v.

$$x = v(\alpha) + w \tag{2.9}$$

The ML estimator is then given in equation 2.10.

$$\frac{\partial \ln p(x, \alpha)}{\partial \alpha} = 0 \tag{2.10}$$

Where $\ln p(x, \alpha)$ is called the likelihood function.

Calculating the ML estimator consists therefore in finding the maximum of the likelihood function. For a white Gaussian noise with zero mean, the maximum of the likelihood function is an estimate of the random variable mean $v(\alpha)$ from which the parameter α can be found. By averaging a large number of estimate, a close approximation of the parameter α can be found.

An estimator that leads to the true value of a random variable is called efficient. The ML estimator requires a high number of datas to reach the parameter true value, hence it is asymptotically efficient.

2.4.2.3 What is the monopulse?

The monopulse is a technique used in RF-seekers for target tracking. Various feeding techniques exist to carry out the monopulse ratio [Skolnik, 2008, sec. 9.6]. In this thesis, using an array of radiating elements, the monopulse is realised by sending a pulse with all the elements and in reception by comparing the signal received on the array quadrants. It is illustrated in the case of the phase monopulse in Figure 2.30.

(a) Monopulse in emission (b) Monopulse in reception

Figure 2.30: Monopulse emission and reception

(a) Amplitude monopulse (b) Phase monopulse

Figure 2.31: The different monopulse techniques

The theoretical definitions of the amplitude and phase monopulse from [Darricau, 1993] are:

Amplitude monopulse: Get patterns which amplitude is variable and phase is as constant as possible. It implies a same phase centre for each antenna to generate the beams (Figure 2.31a).

Phase monopulse: get patterns which phase is variable and amplitude is as constant as possible. In this case, antennas have distinct phase centres and the beams are parallel (Figure 2.31b).

The amplitude monopulse has beams oriented in different directions. A signal impinging on the quadrants is amplified by different gains which allows discrimination of the direction of arrival.

The phase monopulse has parallel beams and the quadrants phase centres are separated. The signal received by each quadrant is affected by a different phase which allows discrimination of the direction of arrival.

Here, the monopulse in phase is chosen for its robustness for RF-seeker missile application. An example is derived using two omnidirectional radiating elements of amplitude A and a target located at 10 km range for different angles from $-90°$ to $90°$, as shown in Figure 2.32. Each element receives respectively a signal $s_0 = Ae^{-j2\pi f_0 t_0}$

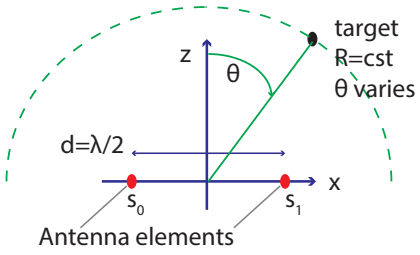

Figure 2.32: Scheme of the target and phase centres

and $s_1 = Ae^{-j2\pi f_0 t_1}$ where t_0 and t_1 are the time delay from target to the antenna phase centres.

The monopulse is realised by carrying out the ratio of the difference over the sum of the signals. If the first element s_0 receives the signal at time t_0, then the second element s_1 receives it at $t_1 = t_0 + \frac{d\sin\theta}{c}$ where $d\sin\theta$ is the path difference of the signal angle of arrival. The monopulse ratio calculation is given in equation 2.11.

$$\begin{aligned}\frac{\Delta}{\Sigma} = \frac{s_0 - s_1}{s_0 + s_1} &= \frac{Ae^{-j2\pi f_0 t_0} - Ae^{-j2\pi f_0 t_1}}{Ae^{-j2\pi f_0 t_0} + Ae^{-j2\pi f_0 t_1}} \\ &= \frac{1 - e^{-j2\pi f_0 \frac{d\sin\theta}{c}}}{1 + e^{-j2\pi f_0 \frac{d\sin\theta}{c}}} = j\tan\left(\frac{\pi d\sin\theta}{\lambda}\right)\end{aligned} \tag{2.11}$$

Where f_0 is the carrier frequency, c the speed of light, $\lambda = \frac{c}{f_0}$ the wavelength. The result is pure imaginary, during the processing, the imaginary part of the ratio is therefore computed. Finally the angle of arrival of the signal is obtained, as shown in equation 2.12.

$$\theta = \text{asin}\left(\frac{\lambda}{\pi d}\,\text{atan}\left(\text{Im}\left(\frac{\Delta}{\Sigma}\right)\right)\right) \tag{2.12}$$

The angle could also be calculated from the difference only $\Delta = s_0 - s_1$ which gives an expression for the direction of arrival angle: $\theta = \text{asin}\left(\frac{\lambda}{\pi d}\,\text{asin}\left(\frac{\|\Delta\|}{2A}\right)\right)$. However the measurements would be sensitive to the amplitude of the signal A. To counteract this dependency, the difference is normalised with respect to the emitted signal (sum signal Σ).

The cancellation of the amplitude of the incident signal is an advantage of the phase monopulse technique. It means that the angle estimation is resilient to the amplitude fluctuations of the target.

The monopulse slope $\left.\frac{\partial\frac{\Delta}{\Sigma}}{\partial\theta}\right|_{\theta=0}$ is used as a figure of merit to evaluate an array configuration; here the monopulse slope factor equals to $\frac{\pi d}{\lambda}$. The monopulse is better performing with a steep slope, as illustrated in Figure 2.33. Two arbitrary arrays produce each a different monopulse curve $\text{Im}(\frac{\Delta_1}{\Sigma_1})$ and $\text{Im}(\frac{\Delta_2}{\Sigma_2})$ where the second one is steeper

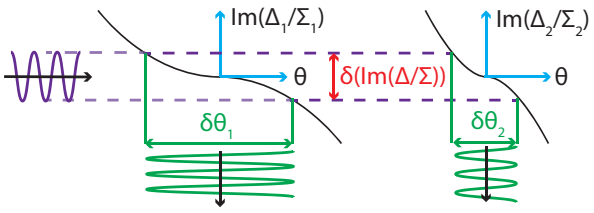

Figure 2.33: Interest of a steep slope

than the first. It is assumed that a signal embedded in noise produces a given delta of monopulse ratio $\delta(\mathrm{Im}(\frac{\Delta}{\Sigma}))$. The second configuration provides a more accurate angle estimation since the delta angle is smaller. This is demonstrated analytically for the phase monopulse in section 4.1.3.2.

The monopulse slope factor can be normalised over the beamdwidth of the total array θ_{bw}, defined as the angle for which the directivity is 3dB from the maximum directivity. This allows us to make a consistent monopulse slope factor comparison from one array configuration to another; the term normalised monopulse slope factor $k_m = \frac{\partial \frac{\Delta}{\Sigma}}{\partial \theta} \cdot \theta_{bw}\Big|_{\theta=0}$ is used. This new figure of merit k_m therefore accounts for the estimation and detection aspects.

2.4.3 Contributions on estimators

The monopulse is a technique often used to estimate the direction of arrival for planar RF-seeker arrays. A model exists to characterise the performance of the amplitude monopulse [Kanter, 1977] and to estimate a target elevation angle but not for the phase monopulse. A model is developed using the phase monopulse slope approximation, valid only for a high SNR. This model offers a closed form expression for the study of any array.

The maximum likelihood estimator is a more advanced technique that requires signals to be available at each radiating element. The pros and cons of the monopulse and the maximum likelihood estimator are addressed for a linear array with omnidirectional elements.

The effect of the number of elements and the target angle on the monopulse estimation performance are studied for omnidirectional elements using the analytical expression of the monopulse ratio.

For 3D conformal arrays and monopulse, no relevant publications can be found. The evolution of the monopulse slope factor is therefore addressed for 3D conformal arrays.

A new monopulse estimator that takes benefits of the amplitude and phase monopulse techniques and resilient to 3D and conformation is proposed.

2.4.4 Cramer-Rao Lower Bound literature review

Previous work has been carried out to obtain the lowest error variance for the direction estimation of a signal impinging on an array. As a reference the Cramer-Rao Lower Bound (CRLB) is often used to assess the efficiency of an unbiased direction of arrival estimator. [Stoica and Nehorai, 1989] develops a general model for a planar and linear array where an incident deterministic signal is embedded in white Gaussian noise. The same author in [Stoica and Nehorai, 1990] develops a model for any arbitrary array; an asymptotic CRLB expression valid when the number of elements and snapshots are sufficiently large. The bound is derived when the incident signal follows a Gaussian random law which takes into account echo variations and the result is obtained with the asymptotic maximum likelihood estimator. [Stoica et al., 2001] corrects for this lack and makes a direct derivation. Expectedly the bound increases when the signal follows a Gaussian law. In conclusion, those papers address a theoretical expression for the CRLB but do not explore the effect of the array arrangement. Furthermore the authors apply their study to omni-directional elements only and the geometry, which refers to the phase centres arrangement, remains uniform and in 1D.

An approach has been investigated using differential geometry for DOA estimation for arbitrary 1D arrays [Manikas et al., 1994] where a CRLB expression is derived but these results remain limited. Instead, examples using the CRLB to optimise the array arrangement in 2D can be found. [Ho and Vicente, 2008] finds the best configuration of an array made of omnidirectional elements although it is space constrained. The CRLB minimization is carried out through range and bearing estimation in presence of Gaussian noise in order to have isotropic performance. The estimation of those parameters can actually be decoupled and results converge towards a circular array. On the other hand, if the array constraint is removed, it has been shown that a V-shape array has better isotropic estimation accuracy than the circular array [Filik and Tuncer, 2008]. This is explained by the bigger aperture of the V-shape array which could also be seen as a drawback. Furthermore, as a part of the array arrangement study, the intersensors spacing is also an explored parameter. A bigger aperture offers better performance, hence it is interesting to have largely spaced sensors, however it has the drawback to make appearing ambiguous angles. To avoid these effects, [Tan et al., 1996] provides mathematical intersensors conditions. In [Gazzah and Abed-Meraim, 2009], the conditions are introduced as constraints to derive the CRLB and systematic searches are carried out to find the best arrangement for given estimation performance. Whether isotropic or directive array patterns are sought results are close to V-shape arrays. In those previous references, the geometry is 2D and the element type is always omni-directional.

2D arrays have been widely studied, however the technology is evolving for 3D and conformal arrays. An attempt to show the interest of a 3D array is given in [Moriya

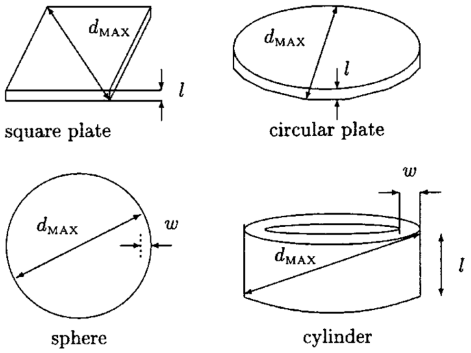

Figure 2.34: Array shapes considered for azimuthal invariant performance

et al., 2012]. The author starts considering a planar array in the xOy plane and observe the effect of moving some elements over Z. As a result, the CRLB decreases along the elevation angle whereas it remains constant along the azimuthal angle. To achieve the joint estimation of the azimuth and elevation angles with the lowest bound, constraints of symmetry need to be applied on the array. They have been explored and set in [Mirkin and Sibul, 1991] to decouple the azimuth and elevation angles of a signal embedded in white Gaussian noise. The symmetry constraints have been generalised in [Nielsen, 1994] for 3D arrays with the same scenario. For example, the author suggests that superimposed square arrays or circular arrays will fulfil the requirements. An array configuration decoupling the DOA angles also ensures that the off-diagonal elements of the CRLB are null and hence minimises the bound, it also produces isotropic performance. [Baysal and Moses, 2003] proposes an ellipse representation to visualise the deviation from invariant results for both azimuth and elevation angles and 4 methods to analytically produce the DOA angles performance invariant for omni-directional element arrays. [Dogandzic and Nehorai, 2001] derives the CRLB for array geometries (Figure 2.34) that both satisfy azimuth invariant performance and diagonal CRLB and uses its results to find the shape that leads to the lowest location error: cylindrical ring, spherical layer. Indeed, the previous publications have been carried out for 3D arrays, the use of omni-directional elements remains limiting in front of real systems.

Real antenna arrays do not have omni-directional but directive patterns although publications are very few for DOA estimation that take it into account. [Werner et al., 2016] and [Jackson et al., 2015] consider theoretical patterns as a first step. In [Werner et al., 2016], the author studies cooperative receivers with sector antennas where the patterns are derived with Gaussian shapes and [Jackson et al., 2015] studies a circular array of four patch using cardioid patterns. As a conclusion, in those publications, polarisation effect is not investigated for the CRLB and the phase centres of the radiating elements remain in a plane although directive patterns are used.

Results including 3D arrays and polarisation can be found but are rare, in [Schulz and Thomae, 2015] the author develops some expressions for the CRLB with and with-

out taking into account the polarisation using the example of an L-quad array. This study leading to different results shows the necessity to include the polarisation for real antenna DOA estimation simulation. [Liu et al., 2014] studies a linear array of orthogonal dipoles, which geometry remains limiting. In [Wan et al., 2014] joint polarisation and direction of arrival are studied. Cylindrical, spherical and conical shapes are investigated. Efforts are focused on developing a new algorithm flexible for conformal arrays rather than the polarisation effect. [Costa et al., 2012] evaluates the joint DOA and polarisation estimation performance for any fixed unknown array disposed in a conformal geometry using a different approach with calibration measurements. In [Häge and Oispuu, 2011] the author discusses the effect of the co-pol to cross-pol ratio on the estimation of the polarisation parameters but the effect on the direction of arrival is not explored.

2.4.5 Contributions on the CRLB

Previous studies addressing the CRLB expression generally use omni-directional elements and if derived more specifically for directive elements and also taking into account polarisation, the phase centres of the elements remain usually in a plane. Publications also discuss the estimation of the incident polarised signal but no effect of the cross-pol on the direction of arrival estimation can be found. The different contributions developed in this thesis are presented.

- A reception model is developed for a polarised signal impinging on an arbitrary array, this reception model is used to address the CRLB for 3D arrays.
- This model is used to demonstrate the interest of 3D and conformation for DOA estimation improvement for omnidirectional elements with uncoupled elevation and azimuthal angles. Then, to realise this study in the case of directive elements a general expression for the CRLB with Hertzian dipole voltage for any orientation is given.
- The interest of 3D and conformation is showed with directive elements in specific configurations.
- The effect of the cross-pol phase on the direction of arrival estimation performance is studied.
- All those contributions are derived analytically.

Chapter 3 Study of planar and 3D/conformal arrays

In the previous chapter, the literature review has allowed to identify some gaps on the study of the polarisation and directivity of 3D conformal antennas. In this chapter, the array arrangement, the radiating elements orientation as well as the polarisation state are studied. First the study is realised for a planar antenna, then for 3D and conformal arrays.

As shown earlier in the manuscript, the different problematic that are discussed are:

- In which extent a 3D conformal array is desirable for high and homogeneous directivity and polarisation purity performance?
- What is the effect of the elements location and orientation of an array on the directivity and polarisation?
- In which extent can the beamsteering compensate the polarisation state deviation?

By answering to the first question, whether the 3D conformal array is better than the mechanically steered array is also investigated.

In section 1.2.4, the monopulse technique for direction of arrival is described. In emission, the all array is emitting and in reception, the array is divided into different quadrants. This chapter benefits to the monopulse study as it contributes to the emission beam study. The next chapter considers the reception part. In that sense those studies are complementary.

The study starts with the inherent vectorial property of the electromagnetic waves. The wave vibrates in the free-space and describes an elliptic trajectory as a function of time. The characteristics of this trajectory are first presented using the Stokes parameters that allows to define figures of merit for the polarisation study. Then the Matlab program that allowed to study complex arrays is described. Then, studies for planar arrays and finally 3D conformal arrays are carried out.

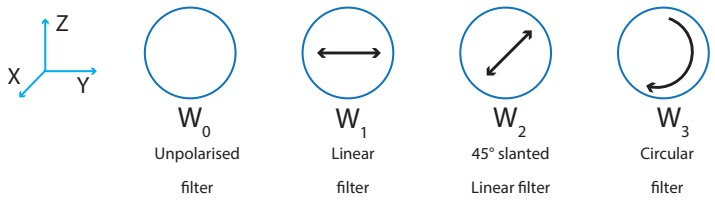

Figure 3.1: The four filters

3.1 The Stokes parameters

The Stokes parameters are used in astrophysics and optics to fully characterise an incident polarised wave, they allow to define figures of merit that facilitate the polarisation study. To define these Stokes parameters, let us consider an electromagnetic wave that goes through four filters that allow to define the four Stokes parameters, as shown in Figure 3.1.

- The first filter gives the total emitted field.
- The second filter filters the horizontal component of the field.
- The third filter filters the 45° linear component.
- The fourth filter filters the circular component

W_0,W_1,W_2 and W_3 are the time average Poyting vector or power flux density measurements obtained as output of each filter. Analytically, the Stokes parameters are defined such as:

$$\begin{bmatrix} S_0 \\ S_1 \\ S_2 \\ S_3 \end{bmatrix} = \begin{bmatrix} 2W_0 \\ 2W_1 - 2W_0 \\ 2W_2 - 2W_0 \\ 2W_3 - 2W_0 \end{bmatrix}$$

Two examples are derived to sense how the Stokes parameters are calculated, first using an unpolarised impinging wave and second using a linearly polarised impinging wave.

The power measurements and Stokes parameters are given for each case.

- For an unpolarised impinging wave:

$$\begin{bmatrix} W_0 \\ W_1 \\ W_2 \\ W_3 \end{bmatrix} = 0.5 \begin{bmatrix} 1 \\ 1 \\ 1 \\ 1 \end{bmatrix} \Longrightarrow \begin{bmatrix} S_0 \\ S_1 \\ S_2 \\ S_3 \end{bmatrix} = \begin{bmatrix} 1 \\ 0 \\ 0 \\ 0 \end{bmatrix}$$

The wave does not have any privileged direction, the trajectory of the polarisation vector does not have a fix state. Therefore each filter filters half of the impinging wave power. From the Stokes parameters it is possible to conclude that the wave is fully unpolarised.

- For a linearly polarised impinging wave:

$$\begin{bmatrix} W_0 \\ W_1 \\ W_2 \\ W_3 \end{bmatrix} = \begin{bmatrix} 0.5 \\ 1 \\ 0.5 \\ 0.5 \end{bmatrix} \Longrightarrow \begin{bmatrix} S_0 \\ S_1 \\ S_2 \\ S_3 \end{bmatrix} = \begin{bmatrix} 1 \\ 1 \\ 0 \\ 0 \end{bmatrix}$$

Half of the energy passes through the first filter by definition. Then the total power goes through the horizontal filter. By projection half of the energy is filtered by the 45° filter and same for the circular filter. The Stokes parameters confirm that the wave is horizontally polarised.

The Stokes parameters can be expressed in different coordinate systems. All the expressions are equivalent. In a general coordinate system base $(\mathbf{a}, \mathbf{b})$, the incident electric field is:

$$\mathbf{E} = E_a \mathbf{a} + E_b \mathbf{b}$$

The Stokes parameters can be addressed in different coordinate system, for example, a Cartesian system or a 45° rotated Cartesian system or a spherical system.

- In a horizontal/vertical base: $\mathbf{a} = \mathbf{U}_x$ and $\mathbf{b} = \mathbf{U}_y$
- In a (45°,135°) linear base: $\mathbf{a} = \frac{1}{\sqrt{2}}(\mathbf{U}_x + \mathbf{U}_y)$ and $\mathbf{b} = \frac{1}{\sqrt{2}}(\mathbf{U}_x - \mathbf{U}_y)$
- In a circular base: $\mathbf{a} = \frac{1}{\sqrt{2}}(\mathbf{U}_x + j \cdot \mathbf{U}_y)$ $\mathbf{b} = \frac{1}{\sqrt{2}}(\mathbf{U}_x - j \cdot \mathbf{U}_y)$

A specific coordinate system associates the ellipse parameters of a plane wave to the Stokes parameters. The ellipse parameters are: the orientation of the major axis ψ measured from the horizontal axis and the ellipticity χ, as shown in Figure 3.2. The Cartesian coordinate system uses the 3 last Stokes parameters as the vectors base from which the ellipse parameters are defined, as shown in Figure 3.3a. The ellipses produced by the different combinations of angles (ψ, χ) in all the directions of a given sphere define the Poincaré sphere, as shown in Figure 3.3b. It associates a polarisation state to each direction of a given sphere.

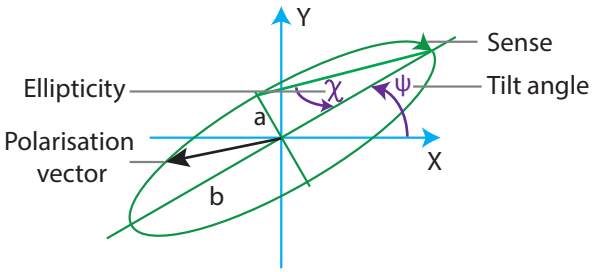

Figure 3.2: The ellipse parameters

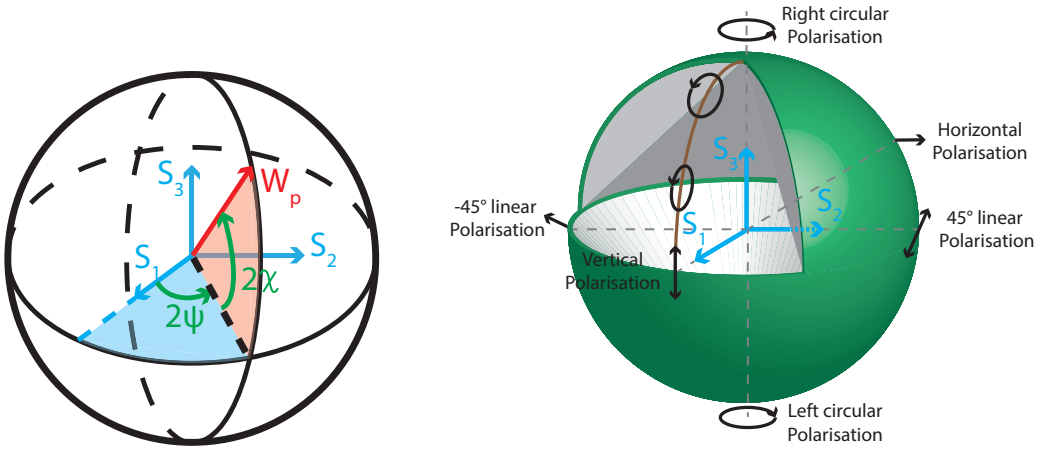

(a) The ellipse parameters

(b) The Poincaré sphere and the polarisation states

Figure 3.3

In the horizontal plane, where $\chi = 0°$, the polarisation state is linear. In the direction S_1 where $\psi = 0°$, the polarisation is vertical and in the $-S_1$ direction where $\psi = 90°$, the polarisation is horizontal. At the poles, the polarisation is circular where $\chi = 45°$. In all the directions other than the horizontal plane and the poles, the polarisation is elliptic. In the north hemisphere, the ellipses are right handed and in the south hemisphere, they are left handed.

The amplitude of each electric field component and the phase between these components, as shown in Figure 3.4, produce a specific polarisation state as outlined in section 2.2.2. There is therefore a link between the electric field characteristics and the ellipse parameters.

Considering a plane wave propagating along the axis Z, the expression of the field is $\mathbf{E} = E_{x0}e^{j\phi_{x0}}\mathbf{e}_x + E_{y0}e^{j\phi_{y0}}\mathbf{e}_y$. The phase and the ratio of the amplitude components of the electric field are $\phi = \phi_{y0} - \phi_{x0}$, $\tan\alpha = \frac{\|E_y\|}{\|E_x\|} = \frac{E_{y0}}{E_{x0}}$ and $\gamma = \frac{E_y}{E_x}$. In the following, the analytical relations between the ellipse parameters (χ, ψ) and the electric field parameters γ and (α, ϕ) are sought.

The Stokes parameters expressed in a Cartesian coordinate system are given in

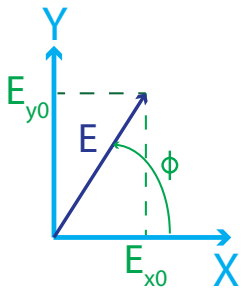

Figure 3.4: The electric field parameters

equation 3.1.

$$\begin{bmatrix} S_0 \\ S_1 \\ S_2 \\ S_3 \end{bmatrix} = \begin{bmatrix} E_x E_x^* + E_y E_y^* \\ E_x E_x^* - E_y E_y^* \\ E_x E_y^* + E_x^* E_y \\ j(E_x E_y^* - E_x^* E_y) \end{bmatrix} = \begin{bmatrix} E_{x0}^2 + E_{y0}^2 \\ E_{x0}^2 - E_{y0}^2 \\ 2\,\mathrm{Re}(E_x E_y^*) \\ -2\,\mathrm{Im}(E_x E_y^*)) \end{bmatrix} \tag{3.1}$$

The Stokes parameters expressed in the Poincaré coordinate system are given in equation 3.2.

$$\begin{bmatrix} S_0 \\ S_1 \\ S_2 \\ S_3 \end{bmatrix} = \begin{bmatrix} W_{tot} \\ W_p \cos 2\psi \cos 2\chi \\ W_p \sin 2\psi \cos 2\chi \\ W_p \sin 2\chi \end{bmatrix} \tag{3.2}$$

W_p is defined as $W_p = \sqrt{S_1^2 + S_2^2 + S_3^2}$. W_{tot} accounts for both polarised and unpolarised electric fields.

From the previous relations, the expression of the ellipse parameters are sought as a function of the electric field. Let us calculate the quotients $\frac{S_2}{S_1}$ and $\frac{S_3}{S_0}$ from equations 3.1 and 3.2 to make appearing the relations. In this development, a fully polarised wave is assumed, therefore the condition $W_{tot} = W_p$ is set. Results are given in equations 3.3 to 3.6.

$$\begin{cases} \dfrac{S_2}{S_1} = \dfrac{W_p \sin 2\psi \cos 2\chi}{W_p \cos 2\psi \cos 2\chi} = \tan 2\psi & (3.3) \\ \dfrac{S_3}{S_0} = \dfrac{W_p \sin 2\chi}{W_p} = \sin 2\chi & (3.4) \end{cases}$$

$$\begin{cases} \dfrac{S_2}{S_1} = \dfrac{2\,\mathrm{Re}(E_x \cdot E_y^*)}{E_{x0}^2 - E_{y0}^2} = \dfrac{2E_{0x}E_{0y}\cos\phi}{E_{0x}^2 - E_{0y}^2} = \dfrac{2E_{0x}E_{0y}\cos\phi}{E_{0x}^2(1-\|\gamma\|^2)} = \dfrac{2\|\gamma\|\cos\phi}{1-\|\gamma\|^2} & (3.5) \\ \dfrac{S_3}{S_0} = \dfrac{-2\,\mathrm{Im}(E_x \cdot E_y^*)}{E_{x0}^2 + E_{y0}^2} = \dfrac{2\|\gamma\|\sin\phi}{1+\|\gamma\|^2} & (3.6) \end{cases}$$

The relation between the ellipse parameters and the electric field parameters are shown in equation 3.7 using the ratio $\frac{S_3}{S_0}\frac{S_1}{S_2}$ and $\frac{S_1}{S_0}$.

$$\begin{aligned} \frac{s_3}{s_0}\frac{s_1}{s_2} &= \frac{\sin 2\chi}{\tan 2\psi} = \tan\phi\frac{1-\tan^2\alpha}{1+\tan^2\alpha} = \tan\phi\cos 2\alpha \\ \frac{s_1}{s_0} &= \cos 2\psi\cos 2\chi = \frac{1-\tan^2\alpha}{1+\tan^2\alpha} = \cos 2\alpha \end{aligned} \tag{3.7}$$

Those results allow to set a relation between the electric field parameters (α, ϕ) and the Poincaré sphere directions (ψ, χ) α, as shown in equation 3.8.

$$\begin{aligned} \cos 2\alpha &= \cos 2\psi cos2\chi \\ \tan\phi &= \frac{\tan 2\chi}{\sin 2\psi} \end{aligned} \tag{3.8}$$

If we gather the results of the equations 3.3 with 3.5 and 3.4 with 3.6 and by noticing that $2\|\gamma\|\cos\phi = 2\,\mathrm{Re}(\gamma)$ and $2\|\gamma\|\sin\phi = 2\,\mathrm{Im}(\gamma)$, the ellipse parameters can be expressed as a function of the ratio of the amplitudes, as shown in equation 3.9.

$$\begin{aligned} \chi &= \frac{1}{2}\arcsin\left(\frac{2\,\mathrm{Im}(\gamma)}{1+\|\gamma\|^2}\right) \\ \psi &= \frac{1}{2}\arctan\left(\frac{2\,\mathrm{Re}(\gamma)}{1-\|\gamma\|^2}\right) \end{aligned} \tag{3.9}$$

The Stokes parameters have been presented, they allow to introduce the ellipse parameters: χ and ψ. In this thesis, the ellipticity χ is used in order to measure and represent the polarisation state. For that purpose, the components E_θ and E_φ can be substituted to the E_x and E_y components to calculate the polarisation state in all the directions of the space.

3.2 The developed software tool

The objective of this thesis is to investigate and find suitable array topologies. The state of the art shows that for polarisation purity, the authors use a program for optimisation. In this study, the optimisation is not the aim but rather to study different

shapes to provide constraint and insight on how to design the RF-seeker antenna. A Matlab program has been developed to easily generate arrays with tens to hundreds elements. The program does not account for mutual coupling. The aim of this program is not to simulate accurately a radiation pattern but to give an idea of the performance of a given design thanks to a fast simulation. Once a design is selected as suitable it can be simulated in a finite element software to accounts for all the antenna imperfections.

3.2.1 Global description of the programs

Two Matlab programs have been successfully developed. The first one computes the radiation pattern of a 3-Dimensional antenna array that consists of HZ dipoles, for which the mathematical expression of the electric field is known. A second Matlab tool that generates the radiation pattern of arrays using more complex radiating elements has also been successfully developed. Both programs require very low processing time and generates the output plots quickly.

The first program calculates the analytical expression of a HZ dipole in a given orientation. Then a script, where the position of each element is defined, is used to compute the proper 3D path difference. This process is iterated for each element of the array and finally the total sum is carried out. The different steps are illustrated in Figure 3.5a.

The second developed software allows the user to import the radiation pattern of any element computed with a simulation software (e.g. HFSS). This allows the study of arrays consisting of complex radiating elements for which an analytical expression of the pattern is unknown. The import requires the real and imaginary parts of the X, Y and Z components of the field. The main shape of the array is selected and implemented by indicating the location of the phase centres of each element and then the elements are rotated in 3D around their phase centres to produce a specific antenna design. The array beampattern is calculated by applying the 3D path difference to each element and then by superimposing each contribution to compute the global array pattern. Finally the results are displayed either in magnitude, in directivity or using the polarisation vector. An illustration is depicted in Figure 3.5b. This tool allows the testing of complex shapes with high flexibility.

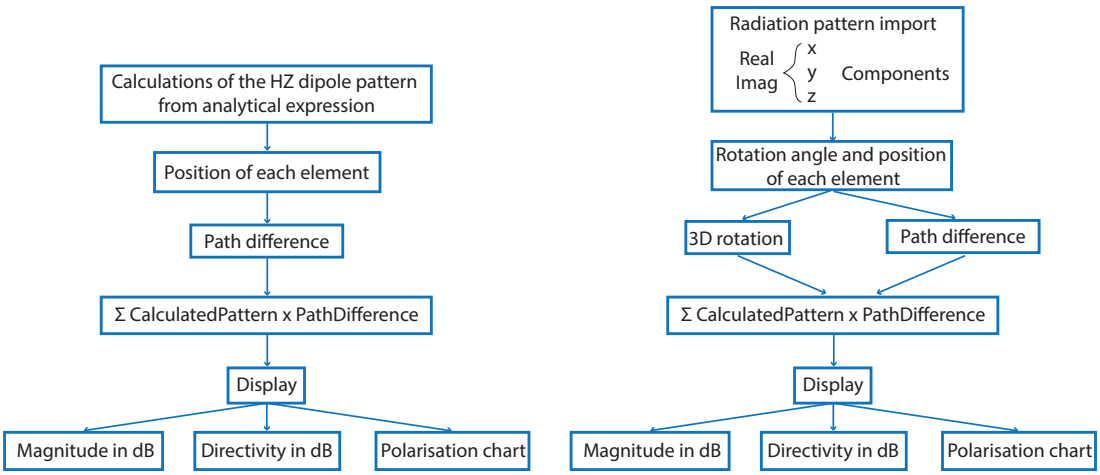

(a) 1^{st} Matlab program: analytical (b) 2^{nd} Matlab program: generic

Figure 3.5: Maps of the Matlab programs

3.2.2 Mathematical development

3.2.2.1 The HZ dipole calculation

The general expression of a HZ dipole for any orientation is sought in this section, using the potential vector A.

The potential vector can be calculated from the current sources, as shown in equation 3.10 [Balanis, 2005, p. 139]. Then the magnetic field $\mathbf{H}$ is derived, from which the electric field $\mathbf{E}$, is found, as shown in equations 3.11 and 3.12.

$$\mathbf{A} = \frac{\mu_0}{4\pi} \int_C I_0 \frac{e^{-\mathbf{k}\cdot\mathbf{r}}}{r} dl' \tag{3.10}$$

$$\mathbf{H} = \frac{1}{\mu} \nabla \times \mathbf{A} \tag{3.11}$$

$$\mathbf{E} = \frac{1}{j\omega\epsilon} \nabla \times \mathbf{H} \tag{3.12}$$

Where dl' is the infinitesimal dipole length and C the contour along which the integral is carried out. The HZ dipole is infinitesimal which produces a constant current I_0 along the element. The only term remaining in the integral is the term dl'. The general orientation of the HZ dipole is indicated by (θ', φ'); it produces a potential vector expression, as shown in Figure 3.13.

$$\mathbf{A} = \frac{\mu_0 I_0}{4\pi} \frac{e^{-j\mathbf{k}\cdot\mathbf{r}}}{r} l(\cos\varphi' \sin\theta' \mathbf{e}_x + \sin\varphi' \sin\theta' \mathbf{e}_y + \cos\theta' \mathbf{e}_z) \tag{3.13}$$

For brevity the following notations are used: $l_x = l\cos\varphi'\sin\theta'$, $l_y = l\sin\varphi'\sin\theta'$ and $l_z = l\cos\theta'$. The magnetic field is calculated from the general potential vector expression thanks to equation 3.11. The result is given in equation 3.14. The coordinate system is changed to the spherical category.

$$\begin{aligned}\mathbf{H} =& \frac{I_0}{4\pi}\frac{e^{-j\mathbf{k}\cdot\mathbf{r}}}{r}(\frac{1}{r}+jk)\,[(-l_x\sin\varphi + l_y\cos\varphi)\mathbf{e}_\theta \\ &+ (-l_x\cos\theta\cos\varphi - l_y\cos\theta\sin\varphi + l_z\sin\theta)\mathbf{e}_\varphi]\end{aligned} \tag{3.14}$$

Finally the electric field expression is given in equation 3.15.

$$\begin{aligned}\mathbf{E} =& \eta\frac{I_0}{4\pi}\frac{e^{-j\mathbf{k}\cdot\mathbf{r}}}{r}\left[\frac{2}{r}(1+\frac{1}{jkr})(l_x\cos\varphi\sin\theta + l_y\sin\varphi\sin\theta + l_z\cos\theta)\mathbf{e}_r\right. \\ &+ (jk+\frac{1}{r}+\frac{1}{jkr^2})(-l_x\cos\theta\cos\varphi - l_y\cos\theta\sin\varphi + l_z\sin\theta)\mathbf{e}_\theta \\ &\left.- (jk+\frac{1}{r}+\frac{1}{jkr^2})(-l_x\sin\varphi + l_y\cos\varphi)\mathbf{e}_\varphi\right]\end{aligned} \tag{3.15}$$

For a HZ dipole oriented along the axis Z: $l_x = l_y = 0$ and $l_z = 1$.

$$\mathbf{E} = \eta\frac{I_0}{4\pi}\frac{e^{-j\mathbf{k}\cdot\mathbf{r}}}{r}\left[\frac{2}{r}(1+\frac{1}{jkr})\cos\theta\mathbf{e}_r + (jk+\frac{1}{r}+\frac{1}{jkr^2})\sin\theta\mathbf{e}_\theta\right] \tag{3.16}$$

If the terms proportional to $\frac{1}{r^2}$ or with a higher order are neglected, it produces the expression given in section A.1 [Balanis, 2005, p. 154].

3.2.2.2 3D path difference

The path difference reference for each element is taken from the array phase centre which is also the coordinate system origin.

To understand how the 3D path difference is computed, the far field expression of a plane wave is developed in the specific case of an array made of two elements with amplitude $\|E_0\|$ and $\|E_1\|$, as shown in Figure 3.6. The resulting equation is shown in equation 3.17.

$$\mathbf{E}(r_0) = \|E_0\|\frac{e^{-j\frac{2\pi}{\lambda}r_0}}{r_0}\mathbf{p}_0 + \|E_1\|\frac{e^{-j\frac{2\pi}{\lambda}r_1}}{r_1}\mathbf{p}_1 \tag{3.17}$$

$\mathbf{p}_0$ and $\mathbf{p}_1$ are the polarisation vectors (see section 2.4.1 for details). r_0 and r_1 are the distances from the elements phase centres to the observation position and $r_1 = r_0 + \delta = r_0 + d\sin\theta$, where δ is the path difference between the elements and d is the element distance. In the denominator, the distance r_1 can be approximated as

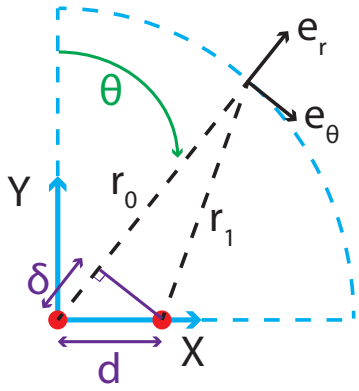

Figure 3.6: Two omnidirectional elements array

$r_1 = r_0$ since $\delta << r_0$. That said, the electric field can be written as shown in equation 3.18.

$$\mathbf{E}(\mathbf{r}_0) = \frac{e^{-j\frac{2\pi}{\lambda}r_0}}{r_0}\left(\|E_0\|\mathbf{p}_0 + \|E_1\|e^{j\frac{2\pi}{\lambda}d\sin\theta}\mathbf{p}_1\right) \tag{3.18}$$

More generally, the first element is located at $\mathbf{u}_0$ and the second one is at a position $\mathbf{u}_1$, both referenced from the coordinate system origin.

$$\mathbf{E}(\mathbf{r}_0) = \frac{e^{-j\frac{2\pi}{\lambda}r_0}}{r_0}\left(\|E_0\|e^{-j\frac{2\pi}{\lambda}\mathbf{u}_0\cdot\mathbf{e}_r}\mathbf{p}_0 + \|E_1\|e^{-j\frac{2\pi}{\lambda}\mathbf{u}_1\cdot\mathbf{e}_r}\mathbf{p}_1\right) \tag{3.19}$$

Where $\mathbf{e}_r$ is the radial vector of the spherical coordinate system.

In conclusion, in an array with N elements, the n^{th} element has the 3D path difference $e^{-j\frac{2\pi}{\lambda}\mathbf{u}_n\cdot\mathbf{e}_r}$. The term $e^{-j\frac{2\pi}{\lambda}r_0}$ is a constant phase that cancels in the radiation pattern in amplitude, and when phase is involved, the variations of phase are sought. This term is factorised and constant for all the elements, hence this term is not accounted for in this chapter.

3.2.2.3 Total array electric field

More generally, for an array with N elements where the phase centre is located at the coordinate system centre and the elements position vector is $\mathbf{u}_n$, the total field equation in the direction $\mathbf{r} = r\mathbf{e}_r$, where r is the observation point to phase centre distance, can be written as shown in equation 3.20. As mentioned earlier, the factorised phase term is not accounted here since it has no effect and the term $\frac{1}{r}$ is included in the complex electric field term E_n.

$$\mathbf{E}(\mathbf{r}) = \sum_{n=1}^{N}\|E_n\|e^{-j\frac{2\pi}{\lambda}\mathbf{u}_n\cdot\mathbf{e}_r}\mathbf{p}_n \tag{3.20}$$

3.2.2.4 Display of the total electric field

The total electric field $\|r\mathbf{E}\|$ can be displayed in magnitude or in total directivity as shown in equation 2.2 with the partial directivity $DirX$, $DirY$, $DirZ$ in the Cartesian coordinate system (equation 3.21), $Dir\theta$, $Dir\phi$ in the spherical one, $DirRHCP$, $DirLHCP$ in the circular one and $DirL3X$, $DirL3Y$ in the 3^{rd} Ludwig's system. Alternatively, using the ellipticity as shown in equation 3.9, it can be displayed using the polarisation vector. The ellipticity and the trajectory displays are gathered under the term 'polarisation charts'.

$$DirX(\theta,\varphi) = \frac{U_X(\theta,\varphi)}{U_0} = \frac{4\pi\|E_X(\theta,\varphi)\|^2}{\int\int_{\theta,\varphi}\|\mathbf{E}(\theta,\varphi)\|^2\sin\theta\partial\theta\partial\varphi} \tag{3.21}$$

The trajectory chart displays the elliptical electric field trajectory in all directions. As the plane wave travels in free-space, it is vibrating and for a given direction it describes an ellipse, caused by the time component $e^{j2\pi f_0 t}$. To simulate this effect, a phase φ_{var} varying from 0 to 2π is applied to the electric field, as shown in equation 3.22.

$$\mathbf{E} = \begin{bmatrix} 0 \\ \|E_\theta\|e^{j\varphi_{var}}\mathbf{e}_\theta \\ \|E_\varphi\|e^{j\varphi_{var}}\mathbf{e}_\varphi \end{bmatrix} \tag{3.22}$$

3.2.3 Interest of the polarisation charts and polarisation deviation

The polarisation chart is illustrated using the example of the two orthogonal HZ dipoles, as introduced in section 2.2.4.3. This example was used to understand the effect of the element orientation on the polarisation state deviation. This example is expanded further in this section.

The elements are orthogonal and their phase centres are aligned along the axis Y, they are $\frac{\lambda}{4}$ spaced; the structure is shown in Figure 3.7a.

The result of the constructive and destructive interferences is shown in Figure 3.7b with a plot of the directivity of the electric field. Results show that a null occurs at $(\theta = 45°, \varphi = 0°)$ and a maximum occurs at $(\theta = 135°, \varphi = 0°)$. However, the gain itself does not provide any insight to the polarisation state of the emitted field.

There are at least three directions in the space for which the results of the polarisation can be easily predicted.

- P1: In the Z-direction, there is a null from the vertical element and a maximum

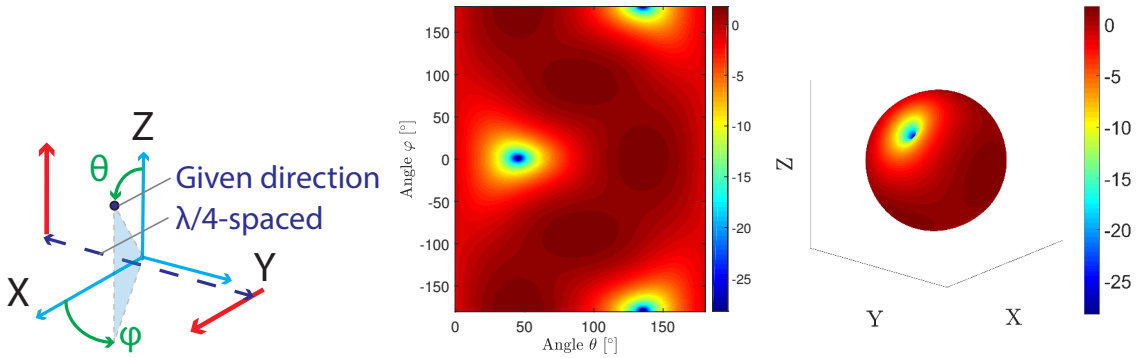

(a) Scheme of the arrangement (b) 2D total directivity pattern (dB) (c) 3D total directivity pattern (dB)

Figure 3.7: Two orthogonal Hertzian dipoles

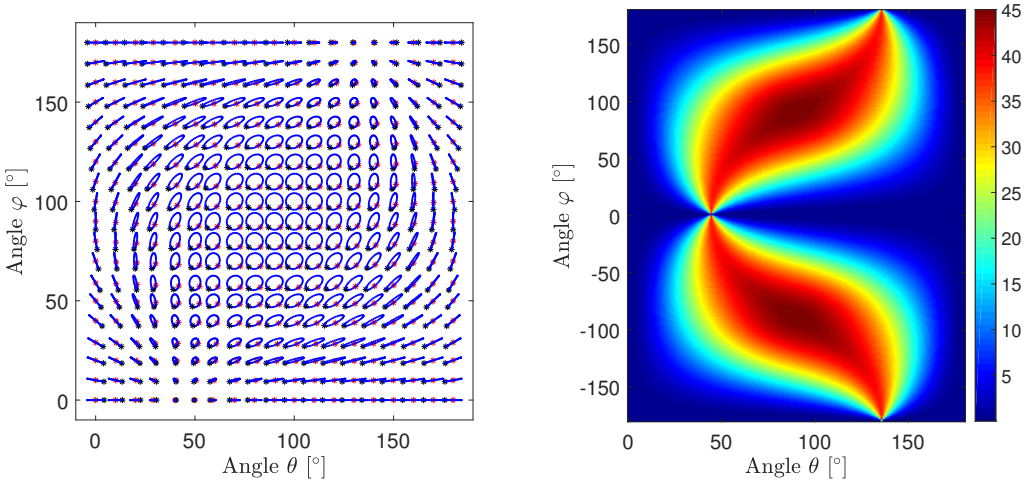

(a) Trajectory chart of the two orthogonal elements

(b) Ellipticity χ of the two orthogonal elements

Figure 3.8: Polarisation charts

value from the horizontal one along the θ-component. Hence, the result is a linear polarisation.

- P2: In the X-direction, the reasoning is reversed, there is a maximum from the vertical element and a null from the horizontal one. Hence, the polarisation is vertical linear.

- P3: In the Y-direction, there is a maximum radiated by each antenna and a phase of 90° between each component due to the $\frac{\lambda}{4}$-distance between each element. This result in a circular polarisation.

The results of the simulation for the polarisation chart are shown in Figure 3.8a.

The ellipticity of the field varies from linear to circular, as expected, passing through many different elliptic states. The field rotation directions are also indicated by the black and red dots. To set the electric field rotation sense, it is assumed that the field is studied in reception mode; from Figure 3.8a in the Y-axis direction the field is Right Handed Circular polarised (RHCP). From black to red dots, the phase is increasing from 0° to 90°, assuming a thumb going towards the reader to get a RHCP in the Y-direction. For better readability, the plot is limited to φ from 0° to 180°. A qualitative plot of the ellipticity is given in Figure 3.8b where the exact values simulated can be found. If the polarisation is linear, the value is $\chi = 0°$ and if it is circular we have $\chi = 45°$, otherwise the field is elliptic.

The simulation results are compared with the three previous predictions:

- P1: In the Z-direction ($\theta = 0°$, $\forall\varphi$), the polarisation state is linear and the value of the ellipticity is $\chi = 0°$, i.e. linear, and correct.
- P2: In the X-direction ($\theta = 90°$,$\varphi = 0°$) the polarisation state is vertical linear and the value of the ellipticity is $\chi = 0°$, i.e. also linear, and correct.
- P3: In the Y-direction ($\theta = 90°$,$\varphi = 90°$) the ellipticity is $\chi = 45°$, circular, correct once again.

The values of ellipticity are confirmed in the prediction directions. The vertical or horizontal linear polarisation can be determined. On the trajectory chart, if the segment is horizontal, it is oriented along the angle variation θ and the state is vertical. If the segment is vertical, it is oriented along the angle variation of φ and the state is horizontal. For ($\theta = 0°$,$\forall\varphi$), the polarisation state changes from linear horizontal to linear vertical which have no physical sense as $\theta = 0°$ points towards only one direction, there is therefore only one polarisation state possible.

For a given array, the polarisation state in directions where the directivity is low compared to the maximum does not matter. In low directivity directions, the signal may not be amplified enough to be considered as useful and in a tracking application, the target is assumed close to the main lobe where the directivity is high. As a conclusion, cumulating both ellipticity and field amplitude information is convenient for that purpose. It is the aim of the trajectory chart that offers at a glance the polarisation state deviation and the directivity level as well. Finally, if qualitative results are required, the ellipticity can be displayed. Those two plots are complementary to each other.

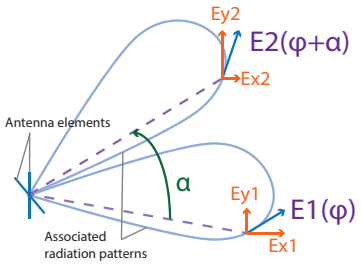

Figure 3.9: Scheme of the rotation

3.2.4 The rotation step

3.2.4.1 The rotation of the field

The second Matlab tool imports the radiation pattern of an element to compute the electric field of the array. The array design can involve elements with different orientations which requires a rotation function.

The rotation of an antenna element is carried out in two steps. Firstly, the vectors of the radiation pattern are rotated and secondly their location is changed. This two step rotation is illustrated in Figure 3.9. A vector E_1 tangent to an element antenna radiation pattern is assumed. This antenna element is rotated by an angle α, it also rotates the radiation pattern and the vector becomes E_2. Hence, once rotated, the components (E_{x1}, E_{y1}) of the original vector E_1 become (E_{x2}, E_{y2}). Secondly, the position of the vector is changed, in this example, it is rotated from the angle φ to the angle $\varphi + \alpha$.

Mathematically, the first step is achieved by multiplying the 3 components of the field, E_x, E_y, E_z, by a rotation matrix M to obtain the new components: E_{xrot}, E_{yrot}, E_{zrot}.

$$\begin{bmatrix} E_{xrot} \\ E_{yrot} \\ E_{zrot} \end{bmatrix} = M \begin{bmatrix} E_x \\ E_y \\ E_z \end{bmatrix} \tag{3.23}$$

The second step consists of moving the location of the vectors from the direction (θ_i, φ_i) to the direction (θ_j, φ_j).

3.2.4.2 Mathematical rotation

The first step projection of the vectors is realised using two rotation matrices as shown in equations 3.24 to 3.26. The elevation rotation matrix M_θ produces a rotation around any vector $[x_{rot}\ y_{rot}\ 0]^T$ contained in the plane xOz and the azimuthal rotation matrix M_φ realises a rotation around the axis Z. The vectors are projected from the local coordinate system E_x, E_y, E_z into the global coordinate system $E_{xrot}, E_{yrot}, E_{zrot}$.

$$\begin{bmatrix} E_{xrot} \\ E_{yrot} \\ E_{zrot} \end{bmatrix} = M_\theta M_\varphi \begin{bmatrix} E_x \\ E_y \\ E_z \end{bmatrix} \tag{3.24}$$

with

$$M_\theta = \begin{bmatrix} x_{rot}^2 + (1 - x_{rot}^2)\cos\theta & x_{rot}y_{rot}(1 - \cos\theta) & -y_{rot}\sin\theta \\ x_{rot}y_{rot}(1 - \cos\theta) & y_{rot}^2 + (1 - y_{rot}^2)\cos\theta & x_{rot}\sin\theta \\ y_{rot}\sin\theta & -x\sin\theta & \cos\theta \end{bmatrix} \tag{3.25}$$

and

$$M_\varphi = \begin{bmatrix} \cos\varphi & \sin\varphi & 0 \\ -\sin\varphi & \cos\varphi & 0 \\ 0 & 0 & 1 \end{bmatrix} \tag{3.26}$$

Depending on the radiating element, the rotation differs. For HZ dipoles, since it has an invariance, it is simpler than for a patch element. For an imported Z-oriented HZ dipole, any orientation can be reached by applying the elevation rotation M_θ only. For a patch antenna, the rotation requires more degrees of freedom. To reach all orientations, both elevation and azimuthal rotations are required.

3.2.4.3 The second step of the rotation

The second step consists in orienting the pattern of each component in the correct direction. An angle $(\theta_{rot}, \varphi_{rot})$ is applied to the component patterns.

$$\begin{bmatrix} E_{xrot} \\ E_{yrot} \\ E_{zrot} \end{bmatrix} (\theta, \varphi) = M_\theta M_\varphi \begin{bmatrix} E_x \\ E_y \\ E_z \end{bmatrix} (\theta_i + \theta_{rot}, \varphi_i + \varphi_{rot}) \tag{3.27}$$

3.2.5 Verification of the program

The accuracy of the program is controlled by comparing its results to the software HFSS©. Different cases are studied to understand the limitations of the proposed Matlab program. Each of them involves a planar hexagonal array. The scenarios are comprising:

- Case 1: Axial arrangement, Hertzian dipoles for HFSS and the Matlab program
- Case 2: Anti-tangent arrangement, Hertzian dipoles for HFSS and the Matlab program

- Case 3: Anti-tangent arrangement, Hertzian dipoles coupled to an infinite ground plane for HFSS and a truncated Hertzian dipole the Matlab program
- Case 4: Anti-tangent arrangement, Hertzian dipoles coupled to an infinite ground plane for HFSS and a truncated Hertzian dipole for the Matlab program, the beam is steered in the direction $\theta = 60°, \varphi = 90°$

The Hertzian dipoles are simulated in HFSS by using an incident Hertzian dipole wave. The choice of truncating the Hertzian dipole in the Matlab program is explained in section 3.3.3.1.

Hertzian dipoles do not have coupling effect and all the elements have the same orientation, therefore, the case 1 verifies the accuracy of the array factor simulation. The calculations realised with the proposed matlab program match with HFSS simulations, as shown in Figure 3.10.

In the case 2, the arrangement of the elements is anti-tangent (Figure 3.28e), where each element has a different orientation. Therefore, this comparison verifies that the rotation of the electromagnetic field is correct. The simulations with HFSS and the Matlab program match perfectly, as shown in Figure 3.11 and 3.12.

The case 3 assesses whether the infinite ground plane is well simulated in the Matlab program. As a result, the results start diverging for elevation angles between 50° and 90°, as shown in Figure 3.13. It can be more precisely observed in Figure 3.14, in the same angle range ($> 50°$) simulation curves separate. This is due to the side effects that are not taken into account in the Matlab program.

In the case 4, the beam is steered in the direction ($\theta = 60°, \varphi = 90°$), close from the infinite ground plane direction ($\theta = 90°$). The results between HFSS and the Matlab program have similar behaviour but the amplitude is different. In the main beam, there is a 2.5dB difference. The Matlab program results have a discontinuity in the direction $\theta = 90°$ which should not exist, as shown in Figure 3.16. Those differences are due to the proximity of the ground plane, its effect is not taken into account in the Matlab program.

In conclusion, the simulations between HFSS and the proposed Matlab program validate the calculation of the array factor and the rotation. However for high beam-steering angles, the use of a truncated dipole does not faithfully transpose the effect of an infinite ground plane.

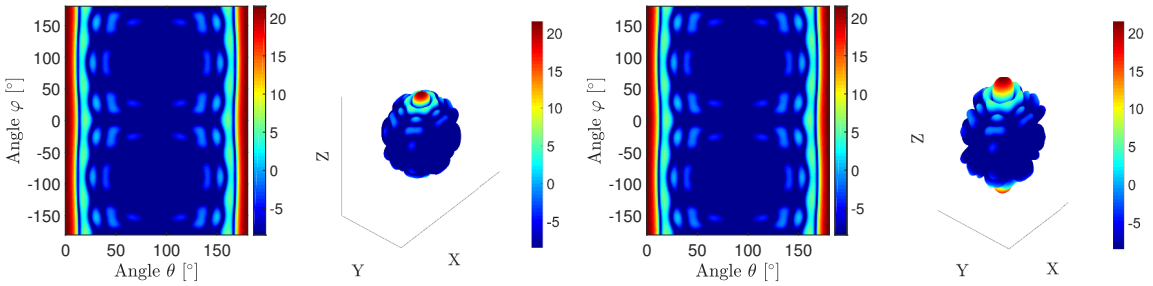

(a) Matlab 2D Dir-Tot (b) Matlab 3D Dir-Tot (c) HFSS 2D Dir-Tot (d) HFSS 3D Dir-Tot

Figure 3.10: Case 1: Comparison HFSS/Matlab program for the planar hexagonal array

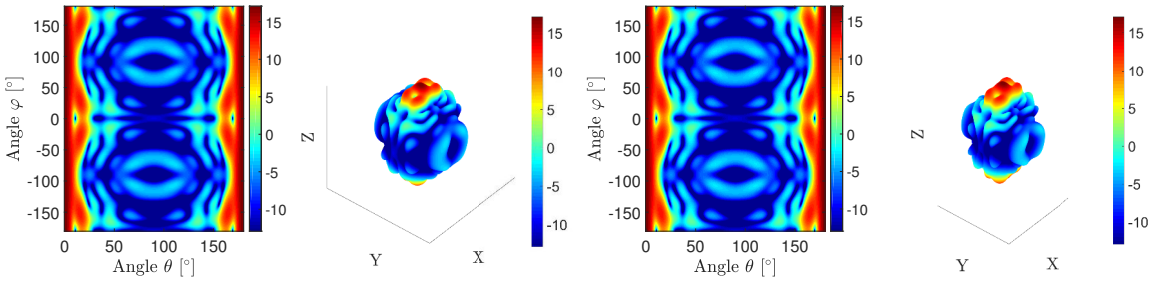

(a) Matlab 2D Dir-Tot (b) Matlab 3D Dir-Tot (c) HFSS 2D Dir-Tot (d) HFSS 3D Dir-Tot

Figure 3.11: Case 2: Comparison HFSS/Matlab program for the planar anti-tangent hexagonal array

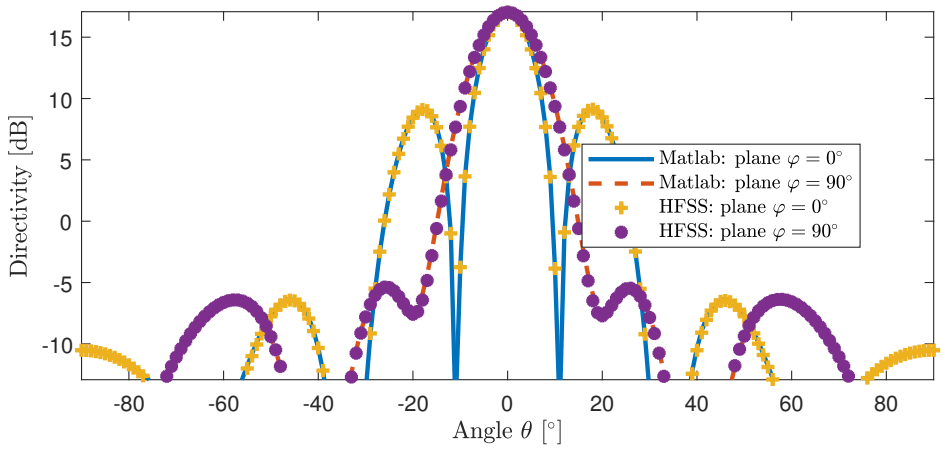

Figure 3.12: Case 2: Comparison HFSS/Matlab for the planar anti-tangent hexagonal array, in the E and H planes

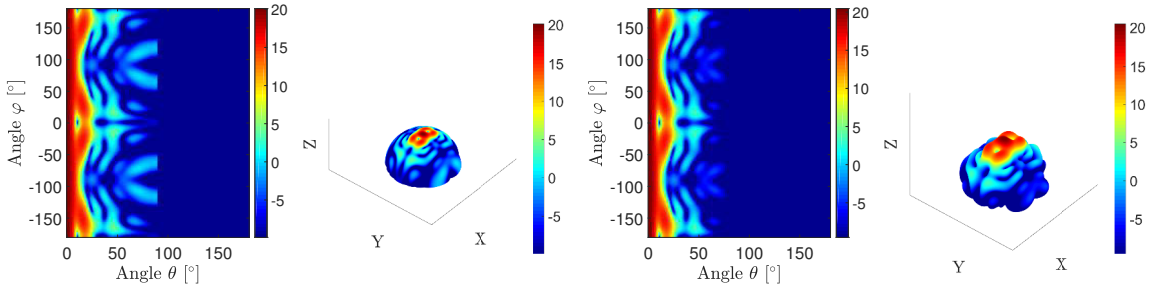

(a) Matlab 2D Dir-Tot (b) Matlab 3D Dir-Tot (c) HFSS 2D Dir-Tot (d) HFSS 3D Dir-Tot

Figure 3.13: Case 3: Comparison HFSS/Matlab program for the planar anti-tangent hexagonal array with an infinite ground plane

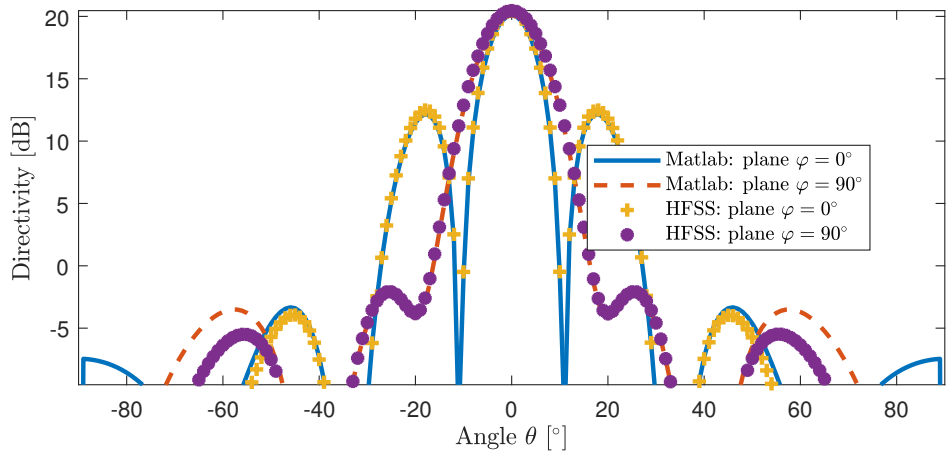

Figure 3.14: Case 3: Comparison HFSS/Matlab for the planar hexagonal array and an infinite ground plane, in the E and H planes

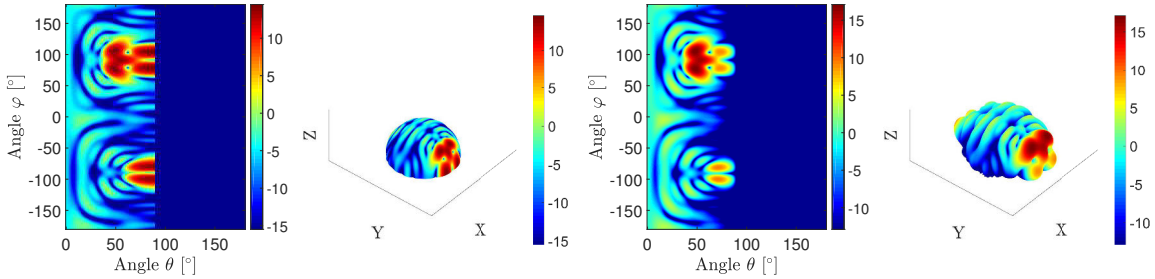

(a) Matlab 2D Dir-Tot (b) Matlab 3D Dir-Tot (c) HFSS 2D Dir-Tot (d) HFSS 3D Dir-Tot

Figure 3.15: Case 4: Comparison HFSS/Matlab program for the planar hexagonal array with a ground plane, steering in the direction $\theta = 60°, \varphi = 90°$

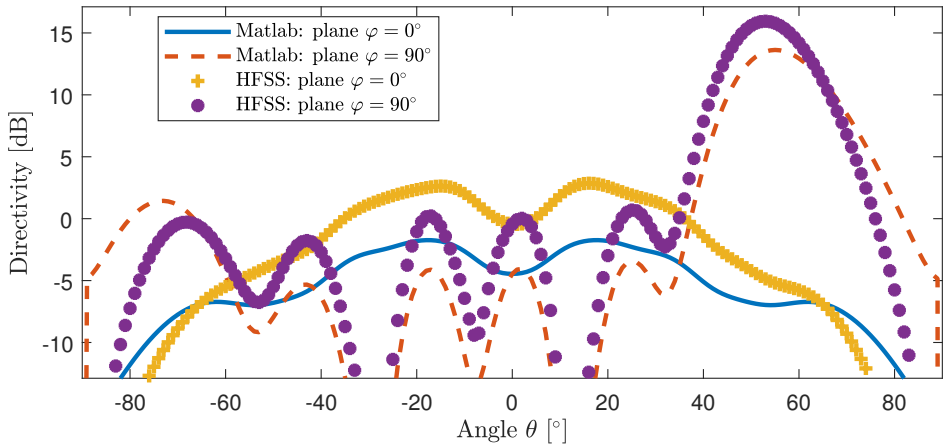

Figure 3.16: Case 4: Comparison HFSS/Matlab for the planar hexagonal array and a ground plane, in the E and H planes, $\theta = 60°, \varphi = 90°$

3.3 Polarisation analysis of planar arrays

The polarisation analysis starts with the study of planar arrays.

3.3.1 Array theory

3.3.1.1 The array factor

When linear arrays are used, the electric field expression includes a factorised element factor term and an array factor term. The generic expression of the total electric field is given in equation 3.20. An $N \times M$ elements rectangle linear array with an inter-element distance d, identical radiating elements $\mathbf{E}_{el}$ and a uniform amplitude low has the simplified total electric field, as given in equation 3.28.

$$\begin{aligned}
\mathbf{E}(\mathbf{r}) &= \|E_{el}\|\mathbf{p}\sum_{n=1}^{N}\sum_{m=1}^{M} e^{-j\frac{2\pi}{\lambda}\mathbf{u}_{n,m}\cdot\mathbf{e}_r} \\
&= \|E_{el}\|\mathbf{p}\sum_{n=1}^{N}\sum_{m=1}^{M} e^{-j\frac{2\pi}{\lambda}(\mathbf{u}_n\mathbf{e}_x+\mathbf{u}_m\mathbf{e}_y)\cdot(\sin\theta\cos\varphi\mathbf{e}_x+\sin\theta\sin\varphi\mathbf{e}_y+\cos\theta\mathbf{e}_z} \\
&= \|E_{el}\|\mathbf{p}\sum_{n=1}^{N}\sum_{m=1}^{M} e^{-j\frac{2\pi}{\lambda}d\sin\theta(n\cos\varphi+m\sin\varphi)} \\
&= \|E_{el}\|\mathbf{p}e^{j\frac{2\pi d}{\lambda}\left((N-1)\frac{\sin\theta\cos\varphi}{2}+(M-1)\frac{\sin\theta\sin\varphi}{2}\right)}\frac{\sin\left(N\frac{2\pi d}{\lambda}\frac{\sin\theta\cos\varphi}{2}\right)}{\sin\left(\frac{2\pi d}{\lambda}\frac{\sin\theta\cos\varphi}{2}\right)}\frac{\sin\left(M\frac{2\pi d}{\lambda}\frac{\sin\theta\sin\varphi}{2}\right)}{\sin\left(\frac{2\pi d}{\lambda}\frac{\sin\theta\sin\varphi}{2}\right)}
\end{aligned} \tag{3.28}$$

To reach the last step of equation 3.28, the phase term is calculated in the general case with $\alpha = \frac{2\pi d}{\lambda}\sin\theta\cos\varphi$ and $\beta = \frac{2\pi d}{\lambda}\sin\theta\sin\varphi$, as given in equation 3.29.

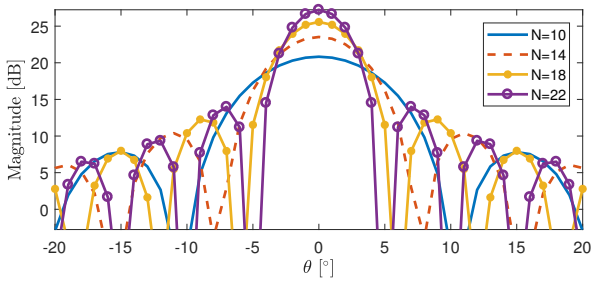

Figure 3.17: Multi size omni-directional linear array

$$\sum_{n=1}^{N}\sum_{n=1}^{M} e^{j(n\alpha+m\beta)} = \sum_{n=1}^{N} e^{jn\alpha}\sum_{n=1}^{M} e^{jm\beta} = \sum_{n=1}^{N} e^{jn\alpha} e^{(M-1)\frac{\beta}{2}} \frac{\sin\left(M\frac{\beta}{2}\right)}{\sin\frac{\beta}{2}}$$
$$= e^{j\left((N-1)\frac{\alpha}{2}+(M-1)\frac{\beta}{2}\right)} \frac{\sin\left(N\frac{\alpha}{2}\right)}{\sin\frac{\alpha}{2}} \frac{\sin\left(M\frac{\beta}{2}\right)}{\sin\frac{\beta}{2}} \tag{3.29}$$

The term $\frac{\sin()}{\sin()}\frac{\sin()}{\sin()}$ is the array factor. The electric field of a single element is factorised, which strongly facilitates the array study. The polarisation of the array is that of the single element.

The array factor follows a ratio of sinus functions, it therefore has multiple cancellations and maxima. The elevation cancellation angle θ_c in the plane $\varphi = 0°$ occurs for $\sin N\frac{\alpha}{2} = 0 \Rightarrow N\frac{\alpha}{2} = n\pi$, where n is an integer. The cancellation angle expression is given in equation 3.30:

$$\theta_c = \text{asin}\,\frac{n\lambda}{Nd} \tag{3.30}$$

For $\theta = 0°$, the norm of the electric field is maximum and equal to $M \times N$. If the number of elements increases, the angle of the first cancellation is smaller and the electric field maximum increases, producing a thinner and higher main beam. This is illustrated in Figure 3.17, where the number of elements is varied and the results are displayed as a function of the angle. Results are calculated for $d = \frac{\lambda}{2}$.

3.3.1.2 Degrees of freedom of the excitation control

The elements of an array can be controlled in amplitude I_n or phase ϕ_{st}. In the previous section, $\forall n\ I_n = 1$ and $\phi_{st} = 0$ were assumed. The amplitude control allows apodisation to be achieved and the phase control ϕ_{st} enables electronic beamsteering, and more rarely apodisation as well [Rocca et al., 2009].

Electronic beamsteering consists of steering the main antenna lobe out of its natural direction by applying a phase delay to the array elements. The phase delay

produces constructive interferences in a new direction. For a linear square array, by applying a phase shift along the X and Y directions, the main lobe reaches all space directions, as shown in Figure 1.15. The angles defining the beamsteering directions are θ_0 and θ_1, as shown in Figure 3.18.

When the beam is steering off its natural direction, the gain decreases. This gain decrease can be compensated for by increasing the power injected in each element. However, in this thesis the antenna study is realised for a given fixed power to keep the same battery size than the mechanically steered planar arrays. The amplitude control is also used for apodisation; it consists of selecting the ideal amplitude to decrease the side lobes [He and Wang, 2006]. This compromises the directivity performance of the main lobe. This degree of freedom has not been explored in this study; it is therefore kept constant.

Decreasing the sidelobes level can be realised using the element phase control [Rocca et al., 2009]. This degree of freedom is also not explored.

Accounting for the beamsteering phase, the new electric field expression is shown in equation 3.31.

$$\begin{aligned}\mathbf{E}(\mathbf{r}) &= \|E_{el}\|\mathbf{p}\sum_{n=1}^{N}\sum_{m=1}^{N} e^{-j\frac{2\pi}{\lambda}\left(\mathbf{u}_{n,m}+\mathbf{u}_{\theta_0,\theta_1}\right)\cdot\mathbf{e}_r} \\ &= \|E_{el}\|\mathbf{p}\sum_{n=1}^{N}\sum_{m=1}^{N} e^{-j\frac{2\pi}{\lambda}\left(\left(\mathbf{u}_n+\mathbf{u}_{\theta_1}\right)\mathbf{e}_x+\left(\mathbf{u}_m+\mathbf{u}_{\theta_2}\right)\mathbf{e}_y\right)\cdot(\sin\theta\cos\varphi\mathbf{e}_x+\sin\theta\sin\varphi\mathbf{e}_y+\cos\theta\mathbf{e}_z)} \\ &= \|E_{el}\|\mathbf{p}\sum_{n=1}^{N}\sum_{m=1}^{N} e^{-j\frac{2\pi d}{\lambda}[\sin\theta(n\cos\varphi+m\sin\varphi)-(n\sin\theta_0+m\sin\theta_1)]}\end{aligned} \tag{3.31}$$

Using equation 3.29, where $\alpha = \frac{2\pi d}{\lambda}(\sin\theta\cos\varphi - \sin\theta_0)$ and $\beta = \frac{2\pi d}{\lambda}(\sin\theta\sin\varphi - \sin\theta_1)$, produces the electric field expression, as shown in equation 3.32.

$$\mathbf{E} = \|E_{el}\|\mathbf{p}e^{j\frac{2\pi d}{\lambda}\left((N-1)\frac{\sin\theta\cos\varphi-\sin\theta_0}{2}+(M-1)\frac{\sin\theta\sin\varphi-\sin\theta_1}{2}\right)}\frac{\sin\left(N\frac{2\pi d}{\lambda}\frac{\sin\theta\cos\varphi-\sin\theta_0}{2}\right)}{\sin\left(\frac{2\pi d}{\lambda}\frac{\sin\theta\cos\varphi-\sin\theta_0}{2}\right)}\frac{\sin\left(M\frac{2\pi d}{\lambda}\frac{\sin\theta\sin\varphi-\sin\theta_1}{2}\right)}{\sin\left(\frac{2\pi d}{\lambda}\frac{\sin\theta\sin\varphi-\sin\theta_1}{2}\right)} \tag{3.32}$$

The beamsteering effect is studied on a linear array of 20 $\frac{\lambda}{2}$-spaced elements, as shown in Figure 3.19. The steering angles considered are 0°, 20°, 40° and 60°.

As the main lobe is steered, the width of the main lobe increases. The beamsteering has no effect on the main lobe maximum of the array factor. However, when the element factor is accounted for, the array factor is multiplied by the amplitude of the element

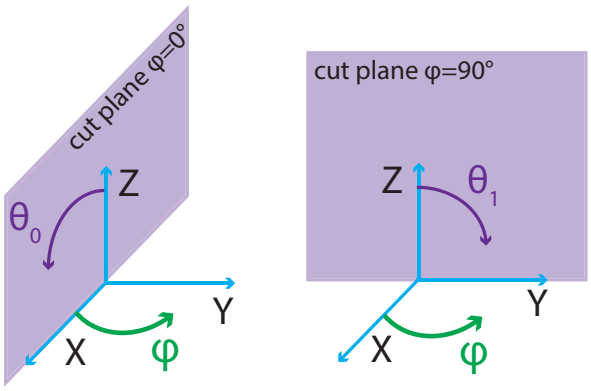

Figure 3.18: θ_0 and θ_1 steering angles

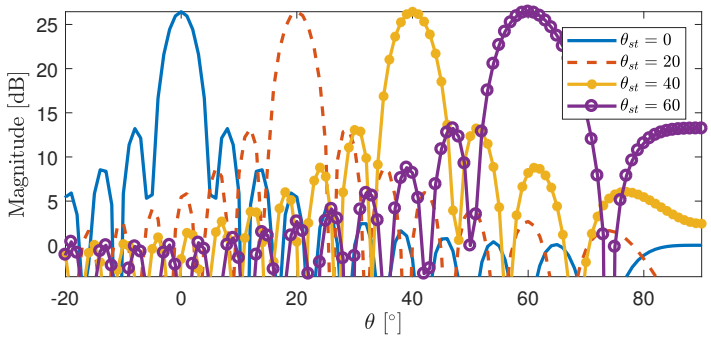

Figure 3.19: Effect of the steering array on the array factor pattern

radiation pattern which changes along the beam direction. This results in changing the maximum of the pattern as a function of the angle.

3.3.2 Array arrangement study

A suitable array arrangement is sought in this section. Omnidirectional elements are used so that only the array factor is accounted. The space between the elements is $\frac{\lambda}{2}$ and the number of element is kept constant and equal to 90, however since symmetry is kept as a priority, the number of elements varies between 89 and 92. The different configurations studied are the square, circular and hexagonal arrays. For the square array, square and triangle meshes are studied and for the circular arrangement, a square and concentric rings meshes are studied. The maximum directivity and the side lobe level are used as figure of merits for comparison.

The radiation patterns are calculated in the $\varphi = 0°$ cut plane sweeping the elevation, as shown in Figure 3.21. All the arrangements have the same maximum directivity although strong differences can be found for the side lobes. The square both with square and triangle meshes produce similar results and high sidelobes compared to other arrangements. The circular arrangement with a square mesh has the low-

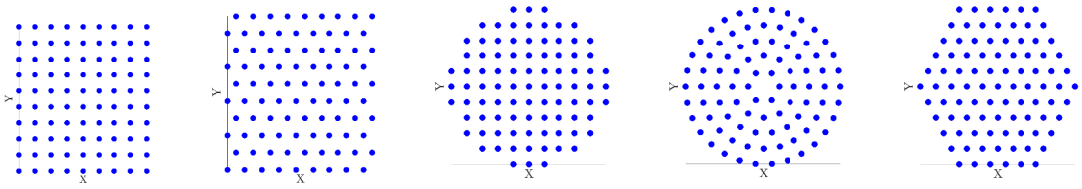

(a) Square array with square cell

(b) Square array with triangle cell

(c) Circular array with square cell

(d) Circular array with concentric rings

(e) Hexagonal array

Figure 3.20: Array arrangements

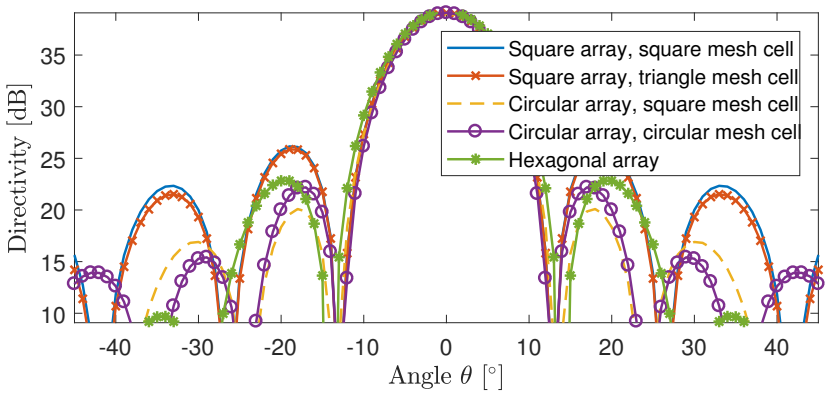

Figure 3.21: Directivity pattern comparison of the omnidirectional arrays in the plane $\varphi = 0°$

est sidelobes. The hexagonal arrangement has average performance. Over the different configurations, the array arrangement changes but also the surface of the array. The array surfaces normalised over the square of the wavelength are shown in Table 3.1. A compromise between the surface covered by the array and the sidelobe level can be observed. The circular array with a square mesh covers the highest surface and has the lowest sidelobes.

Results for all the azimuthal directions are presented for the different arrangements in Figure 3.22. The square arrangements have strong side lobes but only in the orthogonal planes $\varphi = 0°$ and $\varphi = 90°$. The circular arrangements have invariant radiation pattern along the azimuthal angle which also produces constant side lobes level. The hexagonal arrangement has small fluctuations along the azimuth and rather constant sidelobes.

In conclusion, specifications require constant performance which eliminates the square array and selects the circular and the hexagon arrays as suitable arrays for the RF-seeker, they will be used in the next studies.

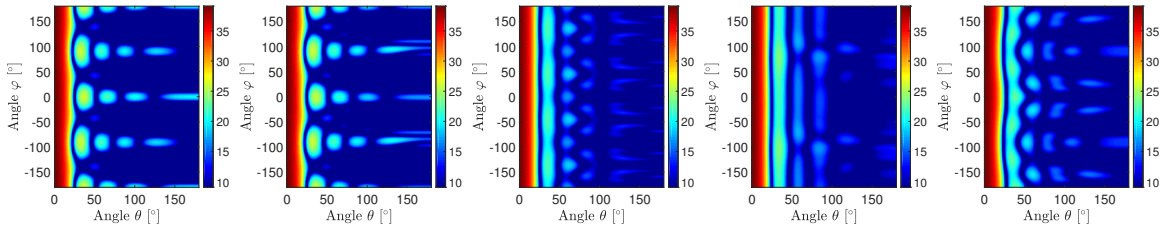

(a) Square array with square cell (b) Square array with triangle cell (c) Circular array with square cell (d) Circular array with concentric ray rings (e) Hexagonal array

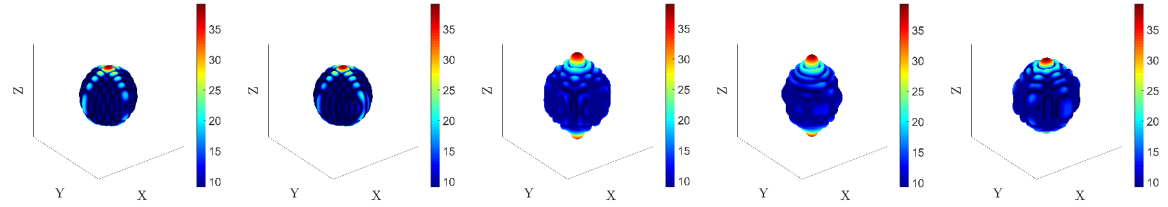

(f) Square array with square cell (g) Square array with triangle cell (h) Circular array with square cell (i) Circular array with concentric rings (j) Hexagonal array

Figure 3.22: 2D and 3D directivity patterns of the omnidirectional arrays

Array	Nbr. elem.	Max. Dir. [dB]	Dir. -3dB [dB]	Sdlobe. lvl. [dB]	Surface/λ^2
Rect, square	90	39.08	11.1	26.15	72
Rect, triangle	90	39.08	11.1	25.87	76.5
Circ, square	89	38.99	11.1	20.09	81.68
Circ, circular	90	39.08	10.68	22.19	78.53
Hexagonal	91	39.18	11.47	22.82	75

Table 3.1: Quantitative comparison of the omnidirectional arrays

3.3.3 Study of element orientation

3.3.3.1 Radiating element design

The radiating element that will be used in the later sections for the arrays studies is discussed. The elements are Hertzian dipoles, they are linked to a reflector ground plane to prevent the radiation from going through the array antenna structure.

The first considered radiating element design is composed of a Hertzian dipole associated to an infinite perfect electric conductor reflector and simulated with HFSS©. The reflector is spaced by a distance $\frac{\lambda}{4}$ to generate constructive interferences.

The resulting radiation pattern is compared to that of a HZ dipole without ground plane, as shown in Figure 3.24.

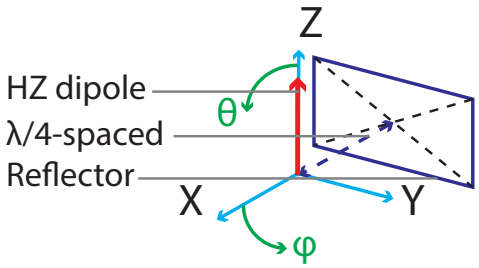

Figure 3.23: HZ dipole and infinite reflector

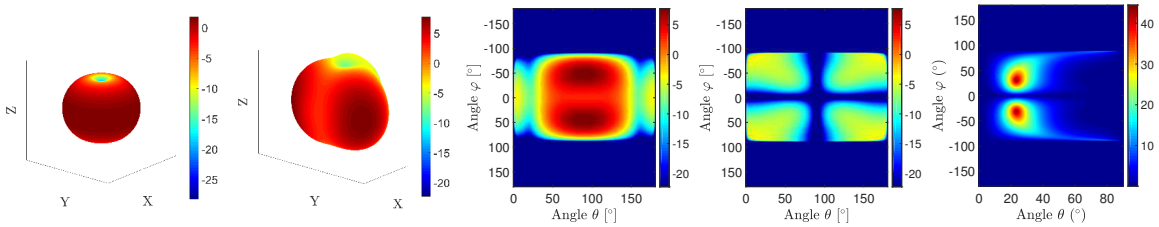

(a) HZ dipole, Dirtot (b) HZ dipole and reflector, DirTot (c) HZ dipole and reflector, Dirθ (d) HZ dipole and reflector, Dirφ (e) HZ dipole and reflector, χ

Figure 3.24: HZ dipole and reflector directivity patterns

The electric field of a vertical Hertzian dipole without ground plane is contained in the θ component of a spherical coordinate system, as shown in appendix A.1. It implies that $DirTot = Dir\theta$ and that the cross-pol component $Dir\phi$ is null which produces a linear polarisation state in all the directions. For a Hertzian dipole with an infinite reflector, the energy is kept in a half-sphere and produces two main lobes in the horizontal plane at $\varphi = \pm 90°$. The presence of the reflector plane generates cross polarisation: $Dir\phi$ is not zero. This is produced by the coupling with the infinite reflector. The limit conditions imposed by the perfect electric conductor is an orthogonal electric field which interferes with the field of the HZ dipole oriented along θ. For small elevation angles, $Dir\phi$ is higher. There is also polarisation deviation from linear. A circular state of polarisation can be found in the direction $(\theta = 24°, \varphi = \pm 31°)$.

Since, the radiating element itself brings cross-polarisation and polarisation deviation, this design is not desirable. Increasing the distance reflector to dipole, reduces the couplings and the cross-pol but does not cancel it and zeros appear in the radiation pattern. One of the objective is to analyse the 3D and conformation effects on the polarisation, therefore an antenna element without cross polarisation is sought. This is why instead a theoretical Hertzian dipole element which radiation pattern is truncated is selected for future simulations. The element pattern used is the same as that of Figure 3.24a where φ is limited to $\pm 90°$.

To facilitate the analysis of future arrays, the electric field of a Y-oriented HZ dipole is briefly studied. In Figure 3.25, the vector field is given. In specific planes, the field

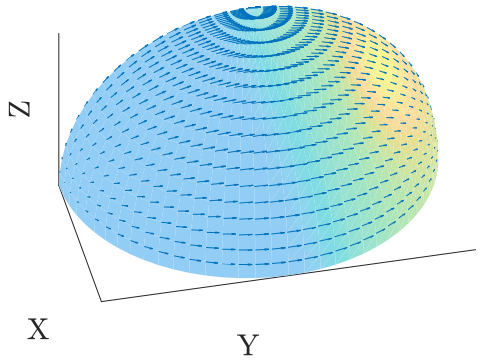

Figure 3.25: Vector field **E** of a Y-oriented HZ dipole

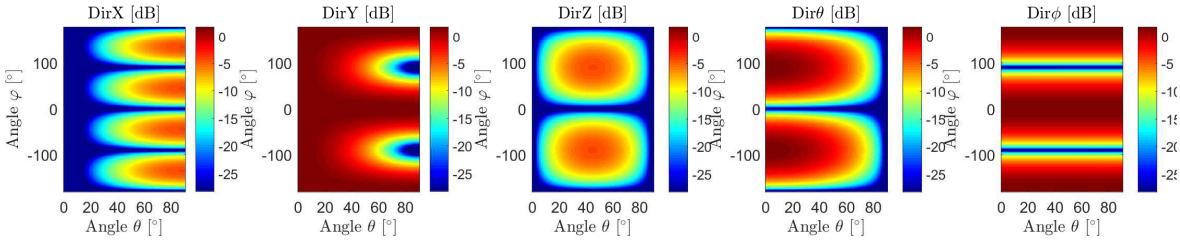

Figure 3.26: Directivity patterns of a Y-oriented HZ dipole

is easy to characterise. In the plane xOz the field is collinear to $\mathbf{e}_y$, in the plane yOz, the field is along $\mathbf{e}_\theta$ and finally in the plane xOy, the field is along $\mathbf{e}_\varphi$.

The field is projected in the Cartesian and spherical bases, the resulting directivity in each component is shown in Figure 3.26. The ideal definition of the polarisation is the Cartesian one, the component $DirY$ hosts most of the energy. The spherical base presents similar amount of energy in both components.

3.3.3.2 Electric field of two HZ dipole elements

Preliminary results are developed in order to better understand the field radiated by more complex arrays. The topology of the two Y-oriented and Y-located Hertzian dipoles is shown in Figure 3.27. The electric field radiated by the element for which the positions $Y < 0$ is $-\cos\theta e^{j\frac{\pi d}{\lambda}\sin\theta}\mathbf{e}_\theta$ and the second element is $\cos\theta e^{-j\frac{\pi d}{\lambda}\sin\theta}\mathbf{e}_\theta$. The resulting electric field is calculated in equation 3.33 for $d = \frac{\lambda}{2}$.

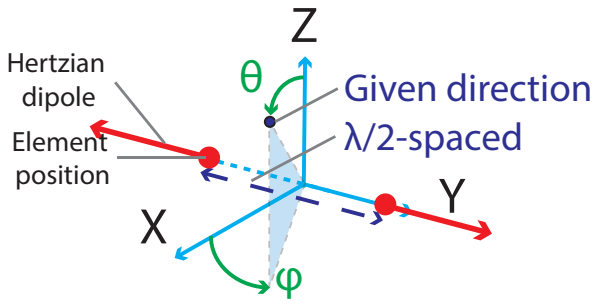

Figure 3.27: Two Y-oriented and Y-located Hertzian dipoles

$$\begin{aligned}
\mathbf{E}\cdot\mathbf{e}_\theta &= \left(-e^{j\frac{2\pi d}{\lambda}\sin\theta} + e^{-j\frac{2\pi d}{\lambda}\sin\theta}\right)\cos\theta \\
&= -2j\sin\left(\frac{\pi d}{\lambda}\sin\theta\right)\cos\theta \\
\|\mathbf{E}\cdot\mathbf{e}_\theta\| &= 2\sin\left(\frac{\pi d}{\lambda}\sin\theta\right)\cos\theta \\
&= 2\sin\left(\frac{\pi}{2}\sin\theta\right)\cos\theta
\end{aligned} \tag{3.33}$$

If $\theta = 0°$ or $\theta = 90°$, then $\|\mathbf{E}\cdot\mathbf{e}_\theta\| = 0$ is found. In the direction $\theta = 0°$ (axis Z), a maximum electric field would be expected, however since the elements have opposite senses, the field cancels in this direction. As the looking direction evolves from $\theta = 0°$ to $\theta = 90°$, the phase shift between the two elements evolves and produces a maximum field amplitude of 1.3 in the direction $\theta = 39°$. To optimise the electric field along the axis Z, a phase shift of 180° would be applied to one of the element, it would produce a maximum field of amplitude 2.

This configuration has been developed to facilitate the understanding of the next sections, where the effect of the elements orientations are studied on the radiation pattern.

3.3.3.3 The planar array design

The hexagonal and circular arrays are considered in this study where different configurations of element orientations are considered: axial, radial, anti-radial, tangent and anti tangent, as shown in Figure 3.28, where the arrows represents the elements orientations and the dots their positions. The element at the origin of the array is removed to keep the symmetry of the designs. In practise the element would have a negligible effect in a large array: the hexagonal array has 90 elements and the circular array has 88 elements.

The total directivity of the axial configuration, as shown in Figures 3.29a and 3.29f, has a strong focused main lobe and the interferences are all constructive which im-

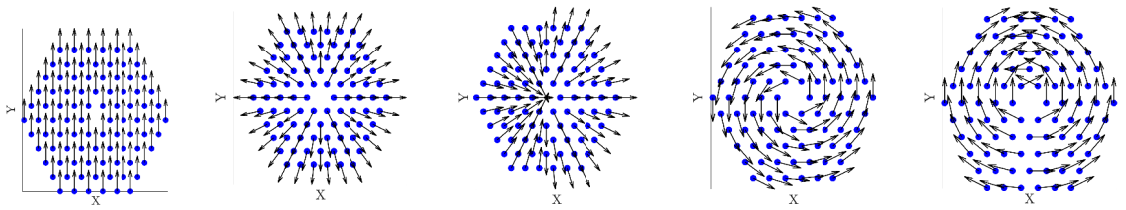

(a) Axial orientation (b) Radial orientation (c) anti-radial orientation (d) Tangent orientation (e) anti-tangent orientation

Figure 3.28: Hexagonal array, orientation of the elements

plies that the directivity is maximised and can be used as a reference for the other configuration, it equals 25.3dB.

The trajectory pattern is shown in Figure 3.30a. For small elevation angles, the trajectory of the field is linear as expected. Then, for higher elevations angles $\theta > 20°$, only dots can be seen which means that the amplitude of the field is too small to observe its trajectory.

For the radial and tangent configurations, the directivity in the Z direction is null. This is due to the symmetry of the structure. Each antenna element has its symmetric around the axis Z which cancels the field along Z as explained in the previous section. The main lobe is located between $\theta = 3°$ and $\theta = 12°$ and is invariant along φ. Those configurations generate a difference pattern with an azimuthal symmetry.

A difference pattern, originally, is generated by carrying out the difference of the signals received by each quadrant of a planar antenna. To realise the monopulse technique for ecartometry, the antenna array is divided into two quadrants that each generate a signal, the ratio of the signal difference over the signal sum is finally carried out. To characterise the performance, the radiation pattern difference is carried out where the difference pattern presents a null in the boresight direction. More generally, in the literature review, some authors mention a difference pattern (Figure 2.23) without mentioning the use of quadrants.

The anti-radial and anti-tangent configurations cancel this symmetry and ensure that the interferences are constructive in Z. The main beam is larger than that of the axial configuration and two nulls can be found in the main lobe, in the xOz plane for both configurations (Figure 3.29c and Figure 3.29e). The anti-radial and anti-tangent configurations can be reached from the radial or tangent configurations using a beam-steering phase shift of 180° applied to the elements of one of the half of the designs. This pattern would be the monopulse sum pattern since a maximum is found in the boresight direction. However this pattern is not azimuth invariant which is limiting.

The ellipticity is null in all the directions for the axial, radial and tangent configura-

tions as shown in Figure 3.30 which respects the requirements. The radial configuration leads to a vertical linear polarisation state (Figure 3.30b) and the tangent configuration leads to a horizontal linear polarisation state (Figure 3.30d). The anti-tangent and anti-radial configurations produce some polarisation state deviation but not in the main lobe region (Figures 3.30c and 3.30e). To investigate that more precisely the ellipticity charts are given in Figure 3.31. On those patterns the region where the directivity is 3dB from the maximum θ_{-3db} is delimited by a white contour. In this area, the maximum ellipticity found is $\chi = 4.45°$ for the anti-radial and $\chi = 4.5°$ for the anti-tangent which remains low and respects the requirements. The hexagonal array encounters less polarisation state deviation in the high directivity area than in other directions.

The directivity patterns of the circular arrays are given in Figure 3.32, they are really similar from that of the hexagonal pattern, for example the maximum directivity is given in Table 3.2 for each arrangement and shows similar values. For the circular array, the trajectory patterns show that for the axial, radial and tangent configurations a linear polarisation state is produced in the direction of the main beam, however for some elevation angles the anti-radial and anti-tangent configurations demonstrate an elliptic polarisation state, as shown in Figure 3.33.

The ellipticity patterns are given in Figure 3.34 for the circular anti-radial and anti-tangent configurations. The circle array gives for the anti-radial $\chi = 11.33°$ and for the anti-tangent $\chi = 11.49°$.

The hexagonal array performs better than the circular array in term of polarisation state deviation although both array performs similarly in term of directivity.

It has been mentioned that the tangent and radial configurations are interesting for their azimuthal invariant difference pattern for ecartometry application. The anti-axial configuration where half of the elements have their sense changed is also studied as it can also produce a difference pattern. The results are shown in Figure 3.35, the difference pattern has very poor performance, there is no azimuth invariance which means that to estimate the elevation angle depending on the plane φ, the characterisation is not the same. On the other hand, thanks to the tangent or radial configuration that are azimuth invariant, potentially, the estimation of the angles θ and φ could be independent.

A tradeoff exists between the axial and radial or tangent configurations. The axial orientation presents a high directivity but a poor different pattern. On the other hand, the radial configuration, from which the anti-radial configuration can be obtained by applying a phase of 180° to change the sense of the elements, offers an azimuth invariant different pattern but a poor sum pattern.

In the next section, the sources of the polarisation deviation are explained.

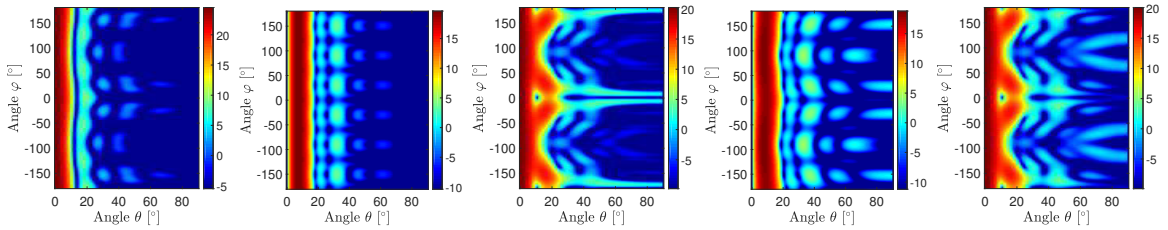

(a) 2D axial orientation (b) 2D radial orientation (c) 2D anti-radial orientation (d) 2D tangent orientation (e) 2D anti-tangent orientation

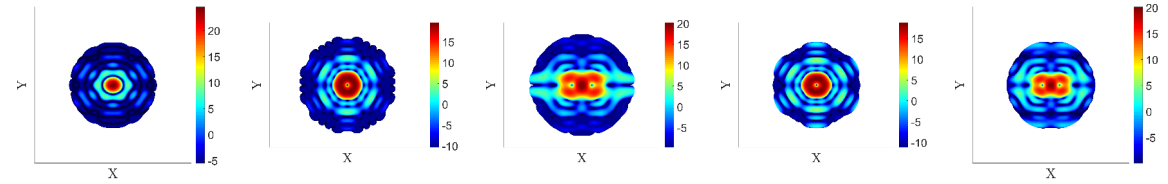

(f) 3D axial orientation (g) 3D radial orientation (h) 3D anti-radial orientation (i) 3D tangent orientation (j) 3D anti-tangent orientation

Figure 3.29: 2D and 3D directivity patterns of the hexagonal arrays

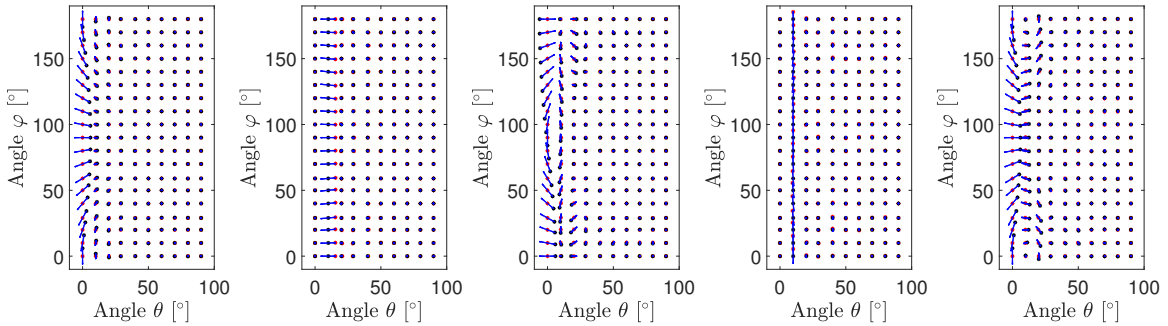

(a) Axial orientation (b) Radial orientation (c) anti-radial orientation (d) Tangent orientation (e) anti-tangent orientation

Figure 3.30: Hexagonal array, study of the trajectory patterns

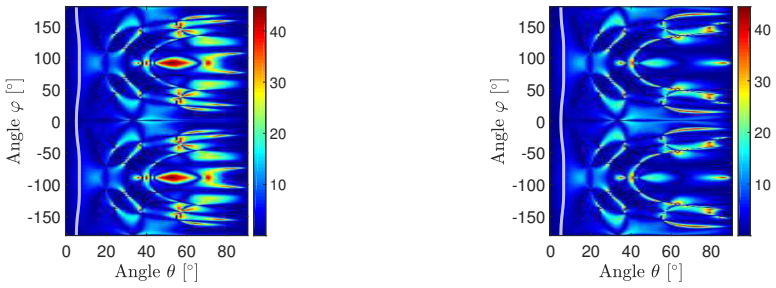

(a) Hexagon: anti-radial orientation (b) Hexagon: anti-tangent orientation

Figure 3.31: Hexagonal arrays, study of the ellipticity

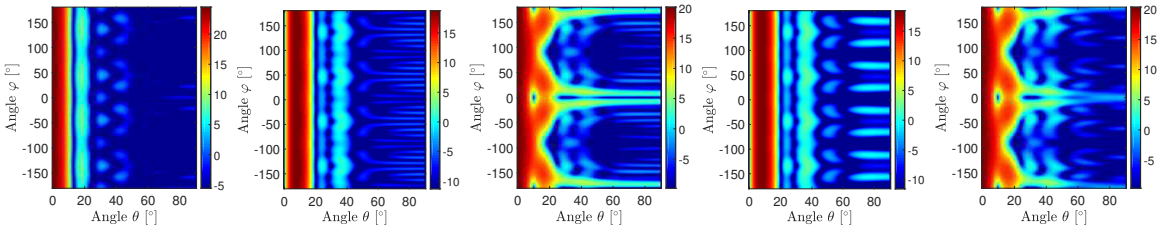

(a) 2D axial orientation (b) 2D radial orientation (c) 2D anti-radial orientation (d) 2D tangent orientation (e) 2D anti-tangent orientation

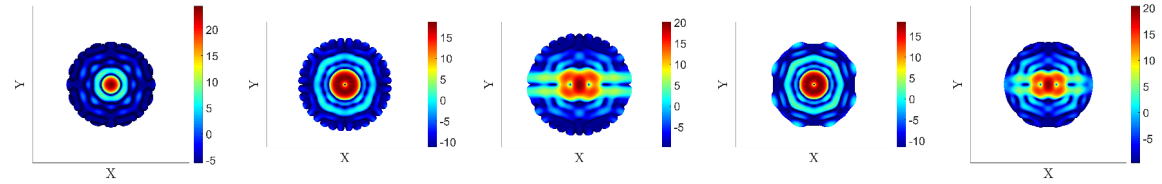

(f) 3D axial orientation (g) 3D radial orientation (h) 3D anti-radial orientation (i) 3D tangent orientation (j) 3D anti-tangent orientation

Figure 3.32: 2D and 3D directivity patterns of the circular arrays

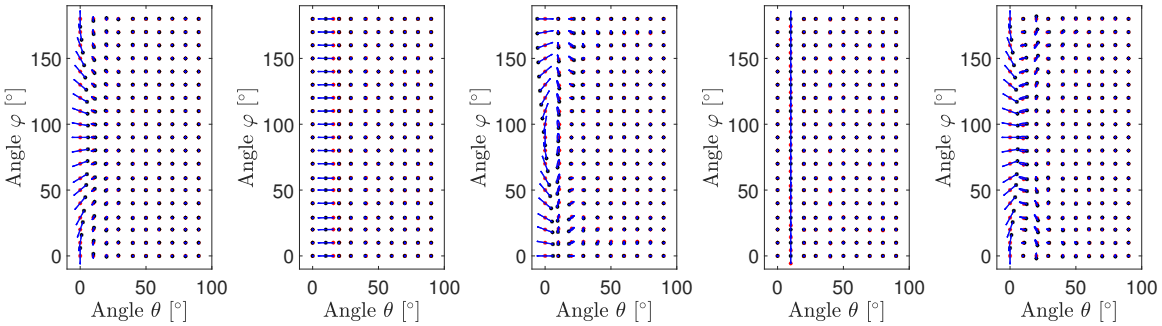

(a) Axial orientation (b) Radial orientation (c) anti-radial orientation (d) Tangent orientation (e) anti-tangent orientation

Figure 3.33: Circular array, study of the trajectory patterns

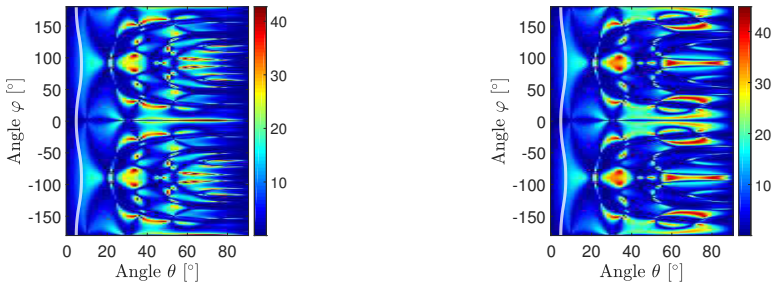

(a) Circular: anti-radial orientation (b) Circular: anti-tangent orientation

Figure 3.34: Circular arrays, study of the ellipticity

Array type	axial	radial	anti-radial	tangent	anti-tangent
Maximum Dir hexagon [dB]	24.52	19.13	20.23	18.8	20.09
Maximum Dir circular [dB]	24.47	18.73	20.15	18.43	20.35

Table 3.2: Quantitative directivity comparison of the different array configurations

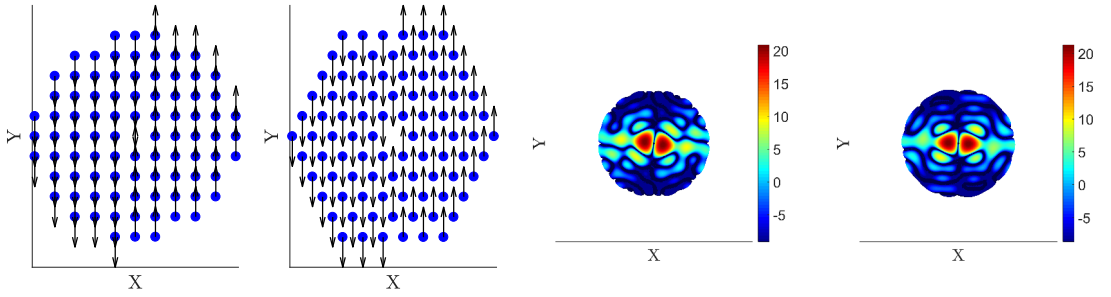

(a) Circular arrangement (b) Hexagonal arrangement (c) Circular directivity pattern (d) Hexagon directivity pattern

Figure 3.35: Anti-axial circular and hexagonal arrays, study of the directivity

The polarisation deviation sources For the radial and tangent configurations, there is no polarisation deviation in all the directions. Those configurations have a perfect symmetry around the axis Z. It is not the case for the anti-radial and anti-tangent configurations. Those latter ones are generated by changing the sense of the radiating elements that are located at $x < 0$. However some elements are located at the limit $x = 0$ which cancels the symmetry. Therefore, the effect of the removal of those elements is observed. The new hexagonal array and the associated trajectory and ellipticity patterns are shown in Figure 3.36.

As a result, the ellipticity is now null in all the directions which is the aim. The maximum directivity increases to 20.42dB against 20.22dB despite the removal of 4

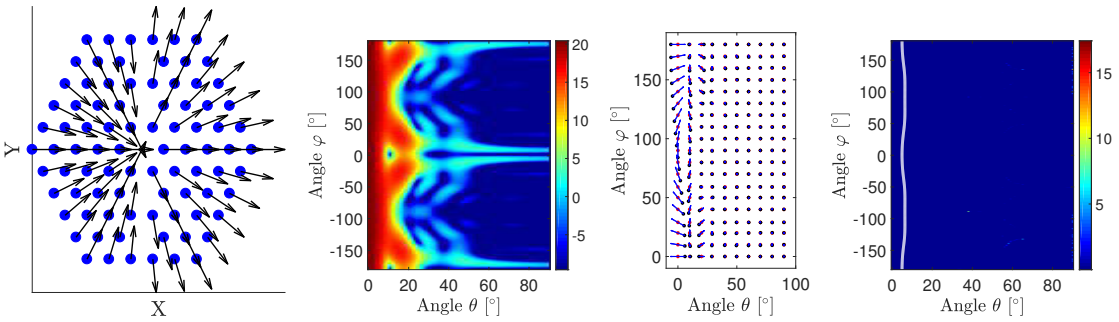

(a) anti-radial orientation (b) Directivity pattern (c) Trajectory pattern (d) Ellipticity pattern

Figure 3.36: Hexagonal arrays and its radiation patterns

elements. This shows the sensitivity of the ellipticity with the array arrangement.

As a conclusion, the hexagonal and circular arrays demonstrate no polarisation deviation for the axial, radial and tangent orientations which is matching with the objectives of low ellipticity. A polarisation state as low as possible is sought to be less affected by hydrometeors. The tangent and radial arrangements present an azimuth invariant pattern with a null in the direction Z which is better to generate a monopulse difference pattern than using the anti-axial configuration that does not lead to an azimuth invariant difference pattern. The anti-radial and anti-tangent patterns do not lead to a neat main lobe which means that the arrangement should be optimised. It also means that it produces a low performing monopulse sum pattern. It has also been observed that the hexagonal array has low polarisation deviation compared to circular arrangement. This deviation is sensitive to the lack of symmetry of the array.

In the following part, the polarisation is studied as a function of the beamsteering. The elements producing polarisation state deviation are maintained for two reasons. The objective is to study the effect of the beamsteering on the polarisation deviation and also since in practise the symmetry may not be ideal due to the manufacturing imperfections.

3.3.4 Beamsteering study

The electric field of the anti-tangent hexagonal and anti-tangent circular arrays are studied for different angles of beamsteering from 0° to 60°. Those configurations are chosen since they present polarisation deviation, as shown in the previous section. The other configurations keep a pure linear polarisation state in all the directions for all the steering angles.

Results for the hexagonal array with the anti-tangent configuration is shown in figure 3.37. As the beamsteering angle increases the main lobe becomes wider, it is particularly clear for steering angles from 20° to 40°. Furthermore, a grating lobe also starts appearing at $\varphi = -90°$ despite the $\frac{\lambda}{2}$ distance between the elements, as shown in Figure 3.37e.

Two phenomena are the cause of the appearing grating lobes. The first cause is illustrated using a linear array made of 11 omnidirectional elements aligned along the Y-axis as well as using the same hexagonal array with omnidirectional elements. 11 is the number of lines of the hexagonal array. Results are shown in Figure 3.45a and 3.45b with a beamsteering of 60° in the plane $\varphi = 90°$. An appearing grating lobe can be observed in both cases. Then, when the tangent or radial orientations with Hertzian dipole are used, due to the symmetry of the arrangement, in the plane $\varphi = -90°$, the electric field is cancelling in the direction of the appearing grating lobe, leading to two

separated lobes. Therefore the first cause of the appearing grating lobes is the array factor.

The second cause of the appearing grating lobe can be found from the verification program section 3.2.5 in Figure 3.15. It is observed from the comparison between the Matlab program and HFSS that the ground plane effect is not correctly taken into account. For high elevation angles, close to $\theta = 90°$, the directivity levels should be much lower than what the Matlab program simulates. Hence, the second cause of the appearing grating lobes is the choice to model a ground plane by a truncated pattern.

The trajectory charts demonstrate that the polarisation state remains linear in all the directions for all the beamsteering angles, as shown in Figure 3.38. For example for a beamsteering of 40°, around the direction $\theta = 40°, \varphi = 90°$ the directivity is strong enough to visualise the field trajectory, as shown in Figure 3.39c. If results are cross checked with the ellipticity pattern, it is found that in high directivity areas (θ_{-3dB} area) the polarisation is strongly linear, it does not overpass an ellipticity of $\chi = 10°$, as shown in Figure 3.39. In other directions, the polarisation state deviates strongly.

The ellipticity χ is studied in some specific directions: for a beamsteering of 0° (Figure 3.39a), $\chi(\theta = 40°, \varphi = 90°) = 30.13°$ and $\chi(\theta = 50°, \varphi = 90°) = 21.20°$. However as the main lobe is steered in those directions, the deviation decreases. For a beamsteering of 40°, $\chi(\theta = 40°, \varphi = 90°) = 0°$ and for a beamsteering of 50°, $\chi(\theta = 50°, \varphi = 90°) = 0°$. For our application it is excellent that as the main lobe is steered in a given direction, the polarisation deviation decreases in this region.

The results for the circular array are given in Figures 3.38, 3.40, 3.41 and 3.42. The comments for the hexagonal array main lobe are also applicable for the circular one. The polarisation state remains close from linear in the areas of high directivity, the ellipticity value does not overpass 10°, which is matching with the antenna objectives.

The beamsteering effect is also investigated as the beam is steered in the plane $\varphi = 0°$, as shown in Figure 3.43. The main lobe is more resilient to the steering in this plane than in the plane $\varphi = 90°$. For a beamsteering of 50°, if the main lobe is compared in both cases using the Figures 3.40d and 3.43d in the plane $\varphi = 90°$ the main lobe is much widened.

It can be noticed that the ellipticity remains very low in the steered direction. In fact for the anti-tangent circular array, in the direction $\varphi = 0°$ the ellipticity is zero due to symmetry, but for very small shift along φ, the ellipticity can be strong, as shown in Figure 3.43. For example $\chi(\theta = 40°, \varphi = 5°) = 21.24°$ and $\chi(\theta = 50°, \varphi = 5°) = 23.21°$ althought when the angle is steered in those directions, for a beamsteering of 40° and 50°, it gives respectively $\chi(\theta = 40°, \varphi = 5°) = 4.1°$ and $\chi(\theta = (50°, \varphi = 5°) = 4.1°$.

A link between the beamsteering and the low ellipticity is suggested in this para-

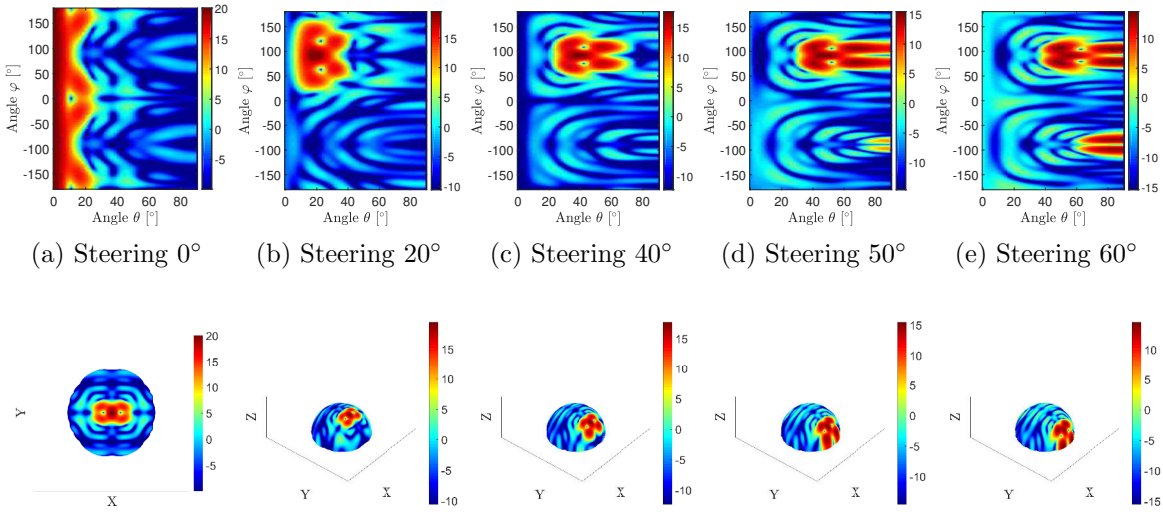

(a) Steering 0° (b) Steering 20° (c) Steering 40° (d) Steering 50° (e) Steering 60°

(f) Steering 0° (g) Steering 20° (h) Steering 40° (i) Steering 50° (j) Steering 60°

Figure 3.37: 2D and 3D directivity patterns of the anti-tangent hexagonal array, steering in the plane $\varphi = 90°$

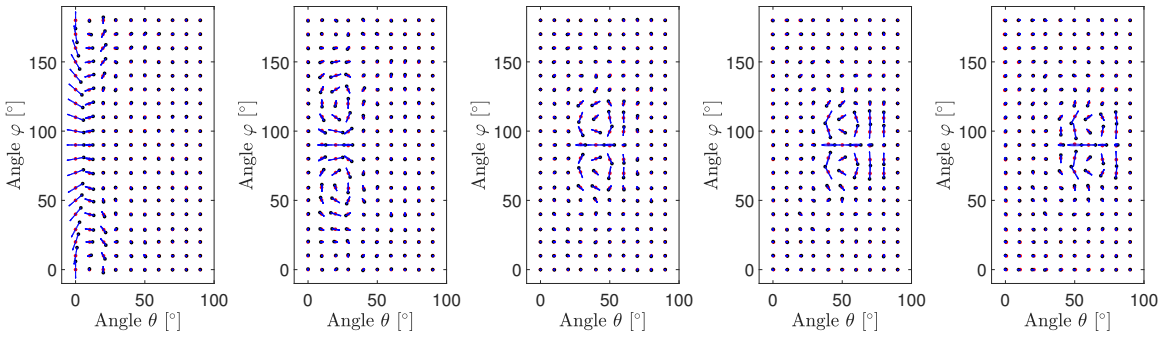

(a) Steering 0° (b) Steering 20° (c) Steering 40° (d) Steering 50° (e) Steering 60°

Figure 3.38: Trajectory chart of the anti-tangent hexagonal array, steering in the plane $\varphi = 90°$

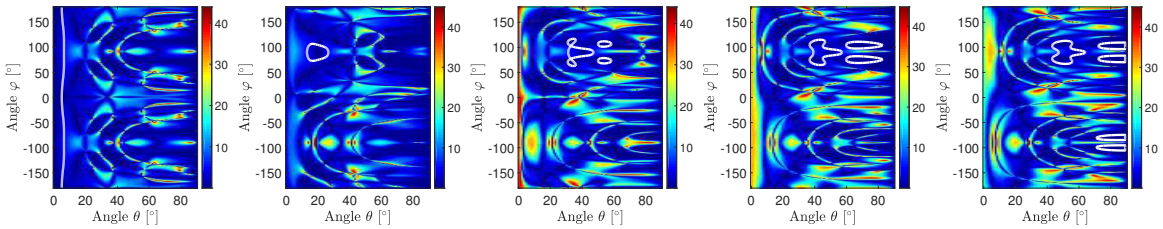

(a) Steering 0° (b) Steering 20° (c) Steering 40° (d) Steering 50° (e) Steering 60°

Figure 3.39: Ellipticity patterns of the anti-tangent hexagonal array, steering in the plane $\varphi = 90°$

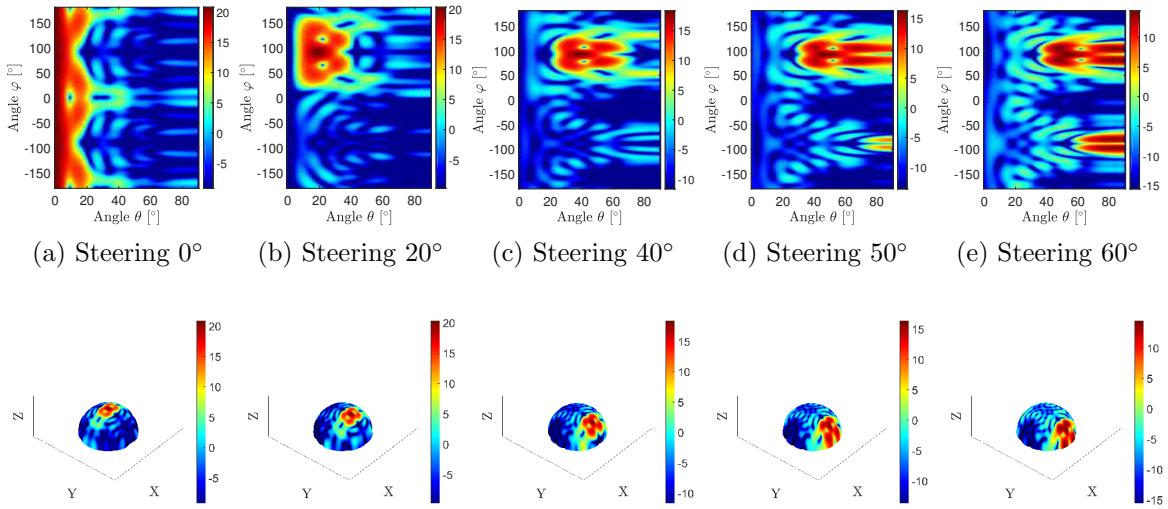

(a) Steering 0° (b) Steering 20° (c) Steering 40° (d) Steering 50° (e) Steering 60°

(f) Steering 0° (g) Steering 20° (h) Steering 40° (i) Steering 50° (j) Steering 60°

Figure 3.40: 2D and 3D directivity patterns of the anti-tangent circular array, steering in the plane $\varphi = 90°$

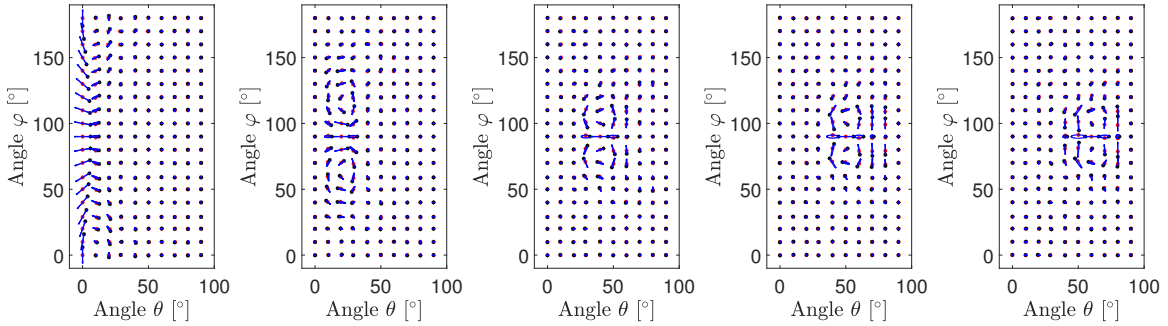

(a) Steering 0° (b) Steering 20° (c) Steering 40° (d) Steering 50° (e) Steering 60°

Figure 3.41: Trajectory chart of the anti-tangent circular array, steering in the plane $\varphi = 90°$

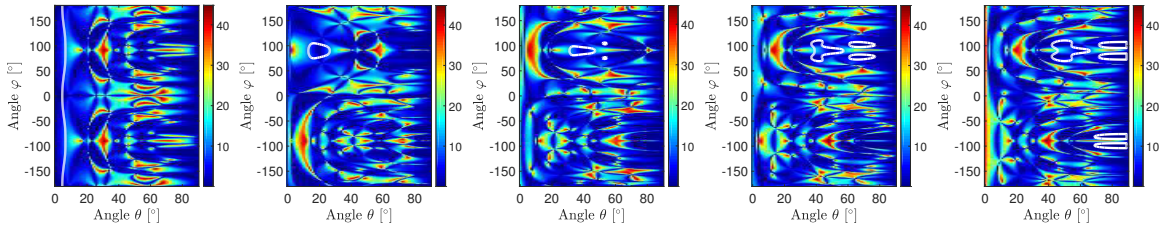

(a) Steering 0° (b) Steering 20° (c) Steering 40° (d) Steering 50° (e) Steering 60°

Figure 3.42: Ellipticity patterns of the anti-tangent circular array, steering in the plane $\varphi = 90°$

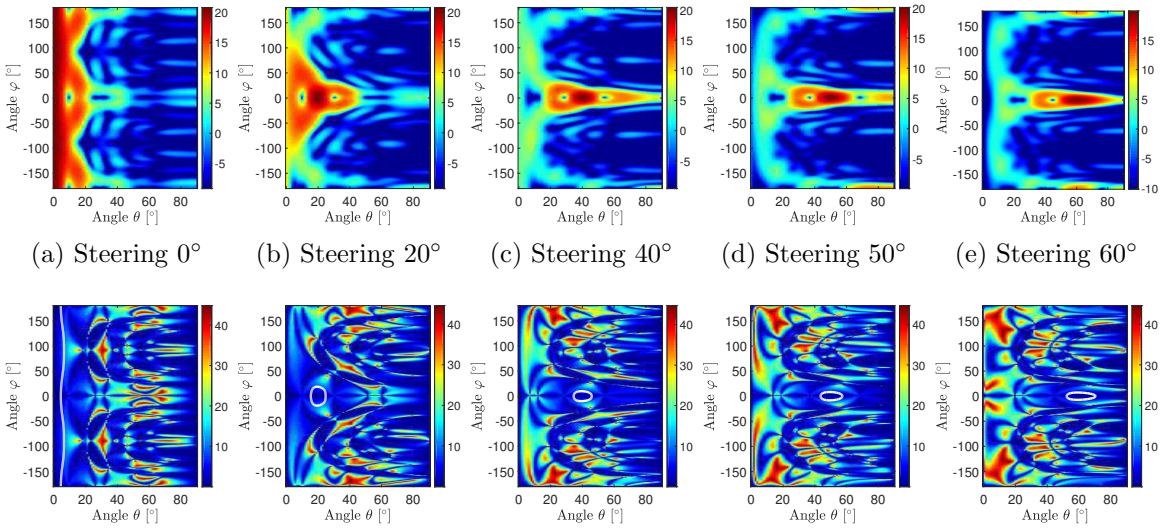

(a) Steering 0° (b) Steering 20° (c) Steering 40° (d) Steering 50° (e) Steering 60°

(f) Steering 0° (g) Steering 20° (h) Steering 40° (i) Steering 50° (j) Steering 60°

Figure 3.43: 2D directivity patterns and ellipticity patterns of the anti-tangent circular array, steering in the plane $\varphi = 0°$

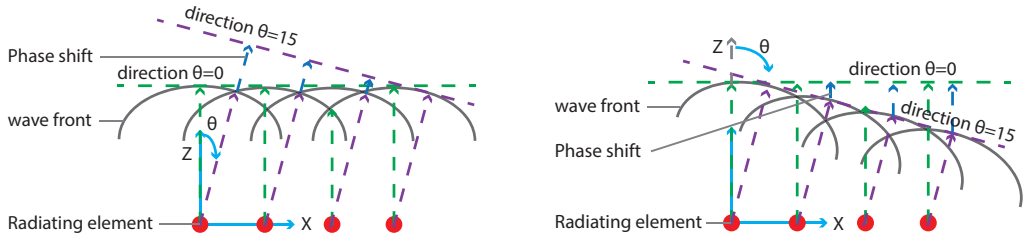

(a) No beamsteering, focus in the direction $\theta = 0°$

(b) Steering in the direction $\theta = 15°$

Figure 3.44: Beamsteering and ellipticity, steering in the plane $\varphi = 0°$

graph. When the beamsteering is carried out, a phase shift is applied to the different elements of the array so that in the steered direction the wave fronts are all in phase. This is illustrated in Figure 3.44. If there is no beamsteering, in the direction $\theta = 0°$, the wave fronts are in phase and the ellipticity is null. However, if the field is studied in the direction $\theta = 15°$ (still no beamsteering), then, a phase shift exists between the elements wave fronts and the polarisation state cannot be predicted and will have any state. For a beamsteering of $\theta = 15°$, the wave fronts are in phase in the steered direction and the ellipticity is null in this direction. This is true even though the elements are emitting in different directions, if the waves are in phase, the resulting field has an ellipticity null. Therefore, the beamsteering cancels the polarisation deviation in the aimed direction and the ellipticity is low closed to the steered direction.

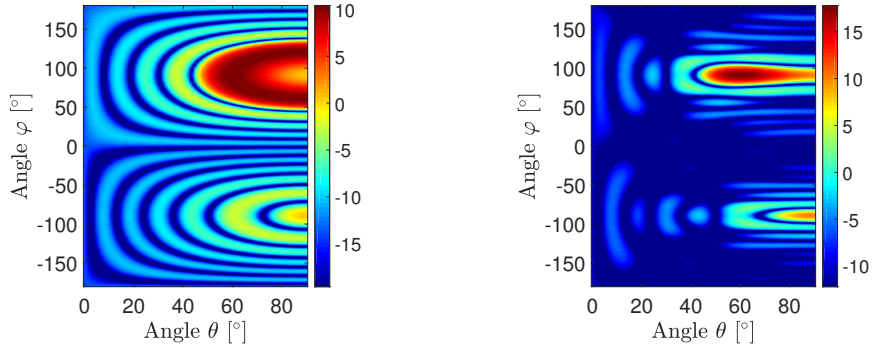

(a) DirTot: Linear array 11 elements

(b) DirTot: Hexagonal array

Figure 3.45: Directivity patterns of the linear and Hexagonal arrays with omnidirectional elements

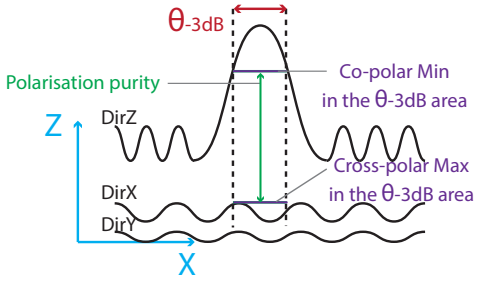

Figure 3.46: Polarisation purity

3.3.5 Beamsteering, polarisation coordinate system and polarisation purity

Usual direction of arrival techniques require a high difference between the directivity of the co-pol and cross-pol components, a personal explanation is proposed in section 4.4. To evaluate this difference, the polarisation purity is used. Hence, firstly, the definition of the polarisation purity is established, secondly, the polarisation of the axial and the anti-tangent configurations of the circular array is studied.

3.3.5.1 Polarisation purity

The polarisation purity is measured by calculating the difference between the co-pol and the cross-pol components. For the Cartesian system, the difference between the two strongest components is measured. Precisely, the purity is measured in the θ_{-3dB} region as the difference between the minimum directivity of the co-pol component and the maximum directivity of the cross-pol component, as illustrated in Figure 3.46. In Cartesian the co-pol and the cross-pol components are the two components that have

the strongest maximum directivity. In spherical, the component that has the strongest directivity is the co-pol and the other one is defined as the cross-pol component.

The polarisation purity characterises the distribution of the energy in the different component. A strong polarisation purity $>$ 10dB means that the energy is mainly focused in one component, if it is low $<$ 10dB, the levels of energy projected in the different component is closer.

3.3.5.2 Analysis of the axial and anti-tangent circular arrays

The polarisation of the axial and the anti-tangent configurations of the circular array is studied, the axial array where the polarisation can be easily predicted is used as a reference and the anti-tangent configuration where the distribution of the energy in the different coordinate system is more difficult to analyse. This study is realised for three elevation steering angles, 0°, 30° and 60° in the plane $\varphi = 90°$.

The axial configuration keeps all the elements with the same orientation. Hence, the total electric field consists in the product of the element array as given in Figure 3.26 with the array factor as given in Figures 3.22e and 3.22j. The array factor magnifies the electric field of the element in the steered direction.

For the single Y-oriented Hertzian dipole element, the Cartesian component of the field that has the strongest directivity values for small elevation angles is $DirY$, as shown in Figure 3.26. Then as the elevation angle increases in the plane $\varphi = 90°$, the Y-field decreases and the Z-field increases, in the direction $\theta = 45°$, their directivity is equal. Finally for $\theta > 45°$ the component Z becomes dominant.

The axial circular array polarisation patterns, as shown in Figure 3.47, when there is no beamsteering, has all its energy in the component $DirY$ as suggested by the single element analysis.

For a beamsteering of 30°, the directivity still has a dominant Y-directivity but not over all the directions and the polarisation purity is eventually low 1.8dB. For a beamsteering of 60°, the dominant component is Z and the polarisation purity is 0.2dB. As a result in Cartesian, as the beamsteering angle increases, the co-pol switches from the Y-component to the Z-component.

For a steering of 30° and 60°, the polarisation purity is much higher in the spherical system than in the Cartesian one. It could therefore be convenient to have a processing system that can choose the coordinate system depending on the steered direction.

The anti-tangent circular array has no dominant component over the different beamsteering angles, as shown in Figure 3.48, this is confirmed by the values given in Table 3.3. It means that a different coordinate system or a different element orientation could be sought so that a dominant component would appear.

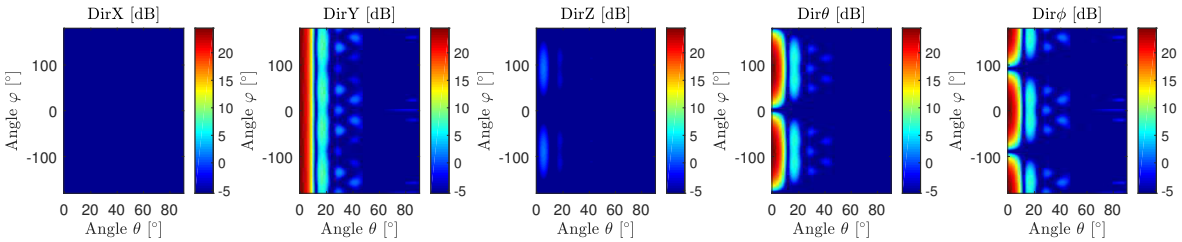

(a) Beamsteering 0°

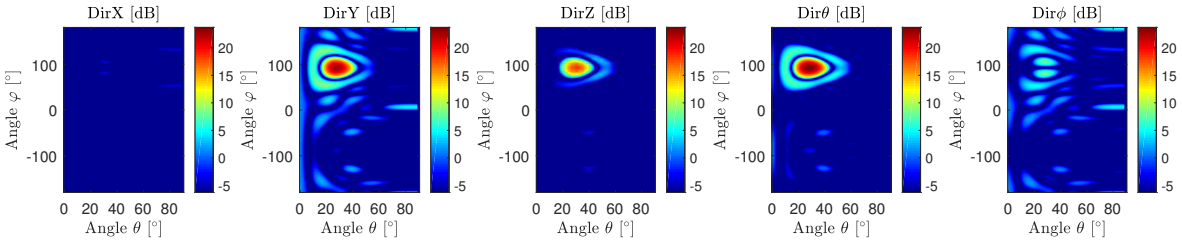

(b) Beamsteering 30°

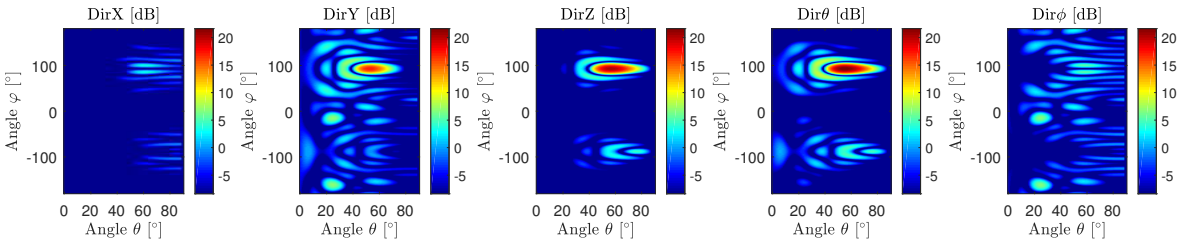

(c) Beamsteering 60°

Figure 3.47: Polarisation patterns of the axial circular array

The details and the polarisation purity for each case are given in Table 3.3. Without beamsteering, the polarisation purity of the Y-oriented elements array is 20.7dB in Cartesian and not applicable in spherical since both co and cross polarisation components are equal, therefore no choice can be made for the co and cross polarisation components.

Those two examples, for the polarisation study of the electric field, show that the polarisation purity is conditioned on the choice of the coordinate system. Therefore a suitable choice of coordinate system for a given array is decisive to have a strong polarisation purity. It also appears that the classic coordinate systems: Cartesian and spherical does not fit to the anti-tangent circular array.

The effect of the elements position and orientation have been investigated on the directivity, ellipticity and polarisation for planar arrays. This study is an intermediate step before studying more complex arrays. In the next section, 3D and conformal arrays are studied.

Array/ Component	*DirX*		*DirY*		*DirZ*		*Dirθ*		*Dirϕ*		Purity	
	Min	Max	Min	Max	Min	Max	Min	Max	Min	Max	Cart	Spher
Axial, str. 0°	-12.1	-9.1	21.9	24.5	-1.7	1.2	21.5	24.5	21.5	24.5	20.7	N/A
Axial, str. 30°	-7.0	-4.0	19.5	22.5	14.8	17.7	20.7	23.7	4.8	7.8	1.8	13.0
Axial, str. 60°	-0.26	2.7	13.9	16.8	17.1	20.1	18.6	21.6	3.5	6.5	0.2	12.2
Anti tg., str. 0°	11.6	14.6	17.4	20.4	-3.4	-0.43	17.4	20.4	17.4	20.4	2.7	N/A
Anti tg., str. 30°	11.6	14.6	14.8	17.8	10.1	13.0	15.9	18.9	-12.0	15.0	0.2	0.9
Anti tg., str. 60°	10.5	13.5	6.8	9.8	9.5	12.5	11.2	14.2	10.7	13.7	-1.9	-2.6

Table 3.3: Beamsteering and partial directivities [dB]

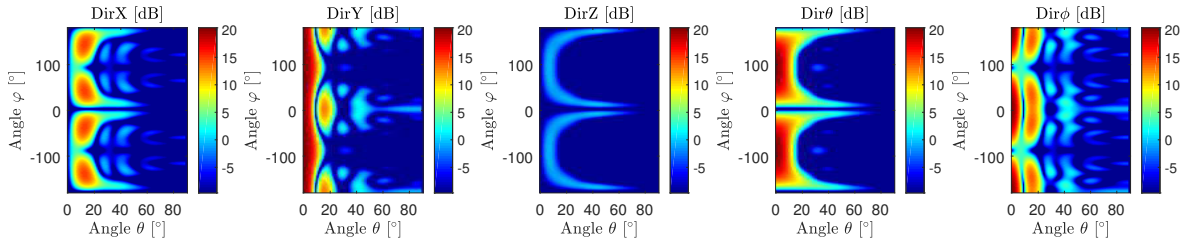

(a) Beamsteering 0°

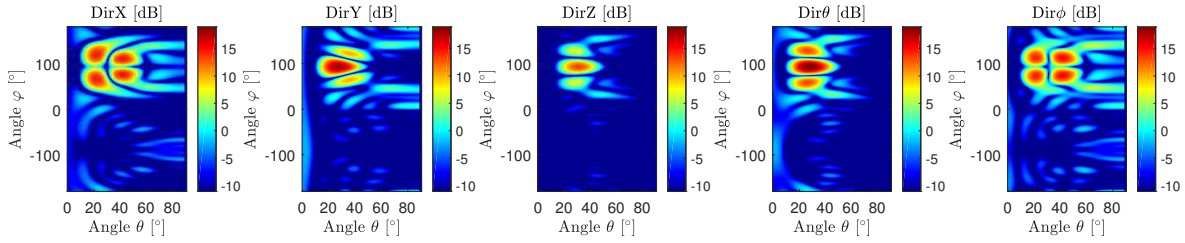

(b) Beamsteering 30°

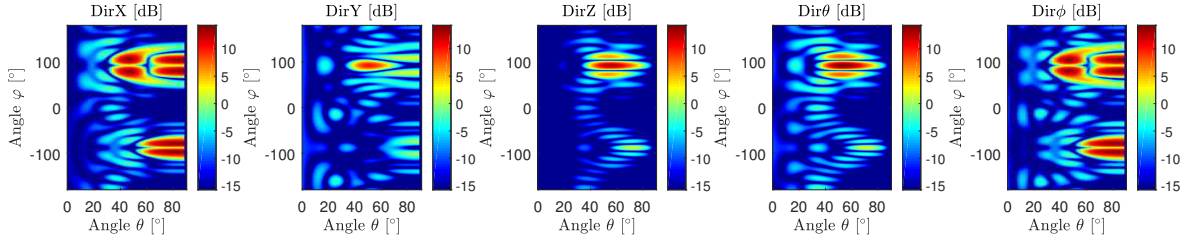

(c) Beamsteering 60°

Figure 3.48: Polarisation patterns of the anti-tangent circular array

3.3.6 Synthesis of the planar array study

A synthesis of the planar array study is proposed in Figure 3.49.

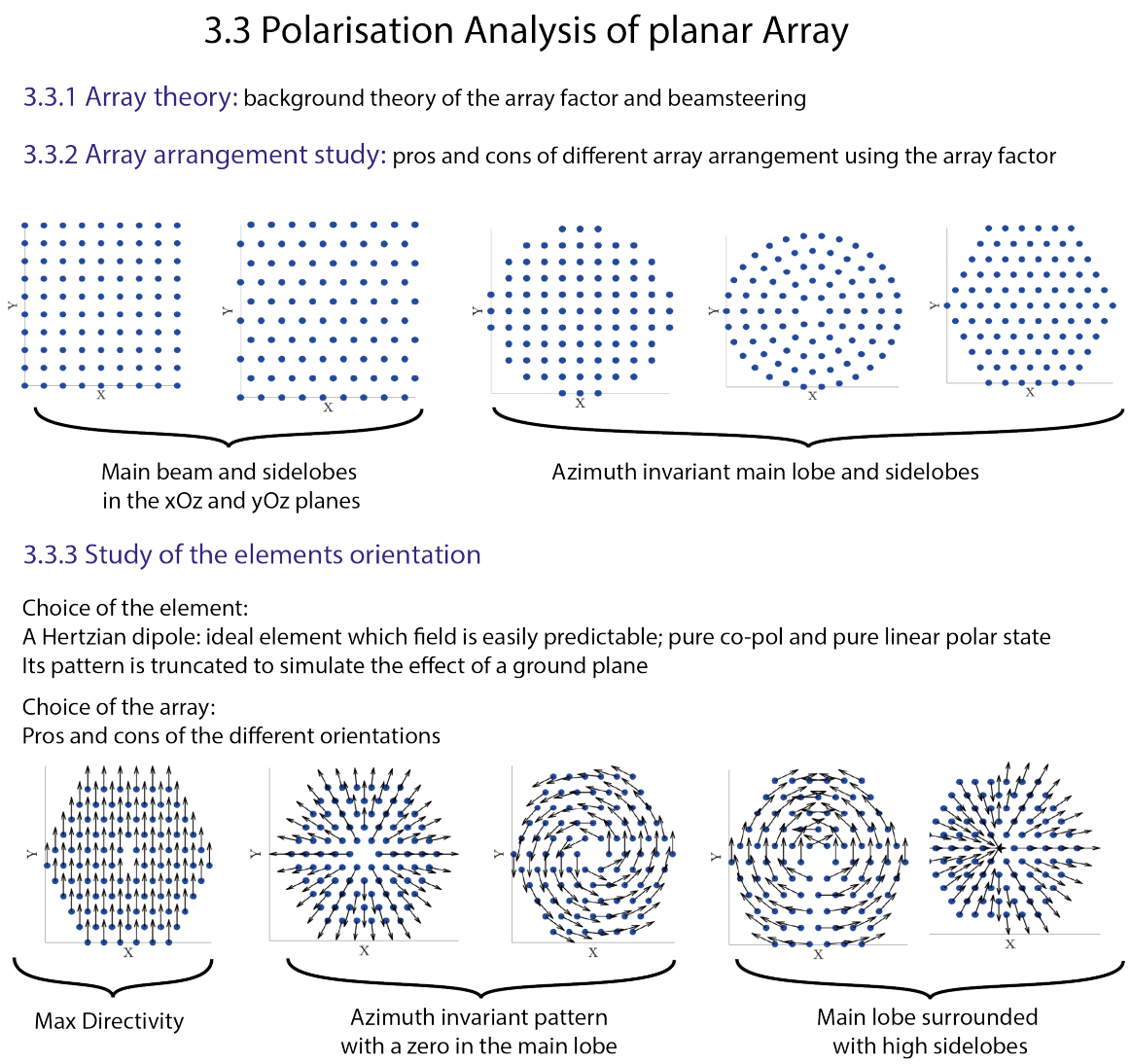

Figure 3.49: Synthesis of the planar array study

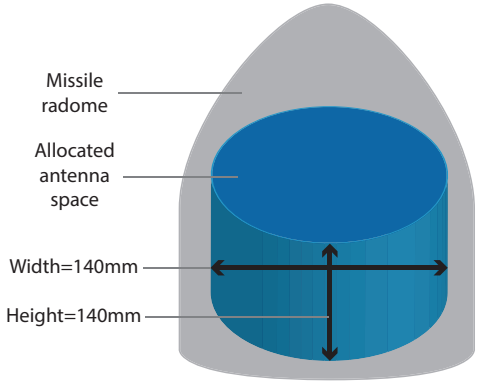

Figure 3.50: Allocated space for the 3D conformal array design

3.4 Polarisation analysis of 3D conformal arrays

3.4.1 3D conformal array topologies

3.4.1.1 The space specifications for the array design

The allocated space for the antenna design below the radome has the shape of a cylinder of 140mm of width by 140mm of height, as shown in Figure 3.50. This shape does not take fully benefits from the space below the radome since its top is flat. This is to facilitate the technology transition since a 3D conformal antenna with a planar top surface would offer similar characteristics to that of the current antenna and would simplify the manufacturing and feeding network design.

3.4.1.2 Simulation of 3D and conformal antennas

Three antennas are considered in this study, as shown in Figure 3.51: a faceted truncated cone, a truncated cone and a half-sphere. The truncated cone and the half-sphere allow to explore respectively the effect of one and two degrees of curvature. The truncated faceted cone and the truncated cone are shapes that fully take benefit from the allocated space below the radome. The half-sphere does not take full benefits of the available space below the radome, its height is only 70mm. Its array is not extended so that the effect of two degrees of curvature can be studied. The half-sphere does not respect the planar top surface, it allows to identify the compromise between the performance gain and a higher fabrication complexity.

For the truncated faceted cone and the truncated cone, the diameter of the top face is 120mm and the diameter of the bottom face is 140mm. Therefore the side faces have an angle of 4.08° with vertical. This angle allows to naturally steer the beam in the front direction Z.

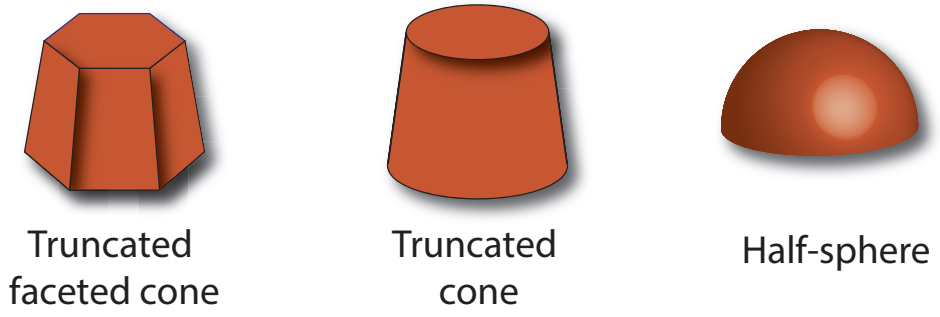

Figure 3.51: The 3D conformal antennas

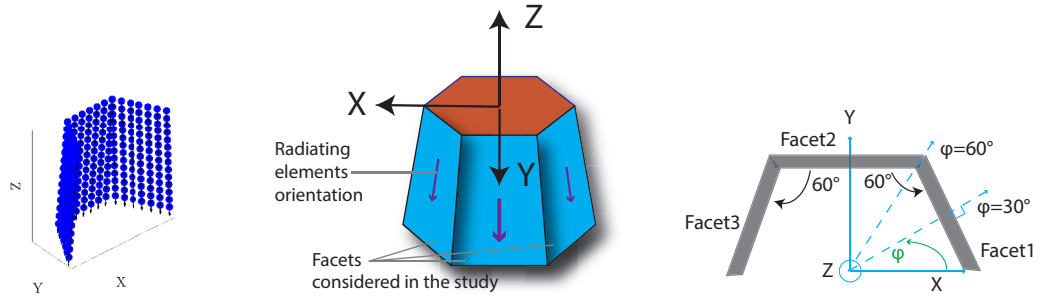

(a) Three quarters view of the active facets of the truncated faceted cone

(b) Elements orientations of the truncated faceted cone

(c) Top view of the truncated faceted cone

Figure 3.52: Truncated faceted array

3.4.2 Study of the lateral facets of the truncated faceted cone

3.4.2.1 Study of the number of active facets and the beamsteering on the total directivity

The impact of the number of active facets and the azimuthal beamsteering angle limit on the array directivity is investigated for the truncated faceted cone. Each lateral facet consists of 98 elements with a square mesh. The study is carried out without elevation steering, in the plane $\theta = 86°$. The Hertzian dipole elements are tangent to the faces and $-Z$-oriented, as shown in Figure 3.52b.

The azimuthal beamsteering angles limits of 30°, 45° and 60° are considered using the lateral faces of the truncated faceted cone. The structure, as illustrated in Figure 3.52c, is $\pi/3$ rotationally symmetric and thanks to the axial symmetry, the radiation pattern can be studied for a $\pi/6$ angle, from $\varphi = 60°$ to $\varphi = 90°$.

The results of the simulations are shown in Figure 3.53, the study is carried out in the plane $\theta = 86°$ with a step angle of $\varphi = 5°$ and the details of the radiating facets for each azimuthal beamsteering angle limits are given:

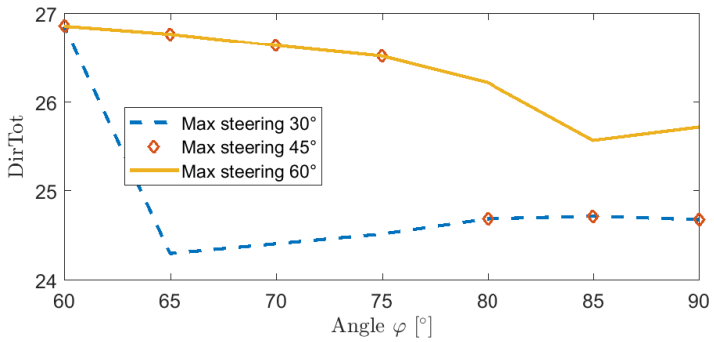

Figure 3.53: Total directivity as a function of the steering angle limits

- For a beamsteering angle limit of 30°
  - For $\varphi = 60°$ Facets 1 and 2 are radiating
  - From $\varphi = 65°$ to $\varphi = 90°$ Facet 2 is radiating
- For a beamsteering angle limit of 45°
  - From $\varphi = 60°$ to $\varphi = 75°$ Facets 1 and 2 are radiating
  - From $\varphi = 80°$ to $\varphi = 90°$ Facet 2 is radiating
- For a beamsteering angle limit of 60°
  - From $\varphi = 60°$ to $\varphi = 85°$ Facets 1 and 2 are radiating
  - For $\varphi = 90°$ Facets 1,2 and 3 are radiating

Results are shown in Figure 3.53. The higher the steering angle limit, the higher the total directivity. The minimum directivity found is 24.3dB over the different steering angle limits. For a steering limit of 30° and 45°, the directivity values have stronger variations than for a steering limit of 60° although the objective is to have a high and constant directivity over the antenna field of view. The highest directivity is also produced by a steering limit of 60°.

A compromise is observed: the increase of complexity that can induce an azimuthal steering limit of 60° instead of 30° increases the minimum directivity by 1.3dB.

3.4.2.2 Study of the polarisation of the lateral faces

Tangent and $-Z$-oriented elements orientation The polarisation patterns of the facet 1 as well as the three facets together (Figure 3.52) are studied. No beamsteering is applied which focuses the beam, respectively, in the directions $(\theta = 86°, \varphi = 30°)$ and $(\theta = 86°, \varphi = 90°)$. The radiating elements of the lateral faces are tangent to the

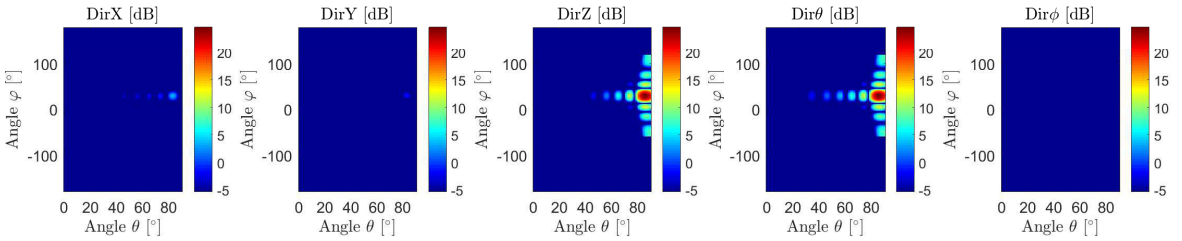

(a) Polarisation pattern of the first facet, focus in direction ($\theta = 86°, \varphi = 30°$)

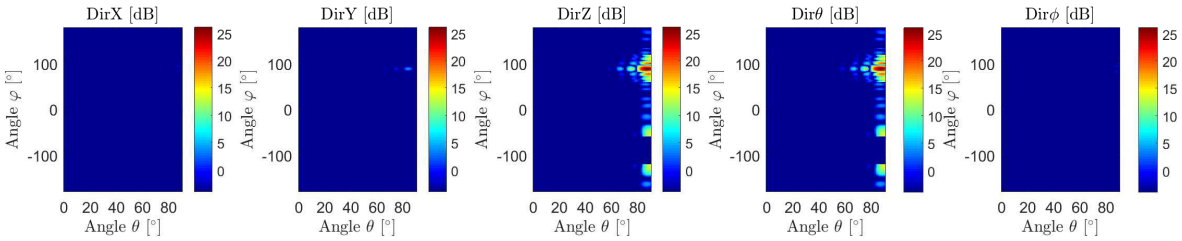

(b) Polarisation pattern of the 3 facets ($\theta = 86°, \varphi = 90°$)

Figure 3.54: Polarisation patterns of the truncated faceted array

face and $-Z$-oriented. As a result, for both cases, without elevation beamsteering, the energy is focused in the components $DirZ$ and $Dir\theta$.

When one facet is radiating, the Cartesian polarisation purity is 18.8dB and the spherical one is 36.8dB. When three facets are radiating the Cartesian purity is 19dB and for the spherical polarisation purity 24.8dB. The polarisation purity remains high in both cases thanks to the symmetry of the structure around the axis Z.

In the plane $\theta = 86°$, the symmetry also induces that the same polarisation purity would occur for each facet independently. The same polarisation purity would also occur for the different combinations of three consecutive facets as well.

Furthermore, a null ellipticity is found for the different configurations.

Tangent and rotated elements orientation Another configuration is tested where the elements of the side facets are rotated depending on the lateral facet. This configuration is illustrated in Figure 3.55a. The choice of the lateral facet elements angle is detailed in section 3.4.3.1.

The polarisation patterns are calculated with one, two and three facets. Results are given in Figure 3.56. When one facet is radiating, the elements have projections along the components X, Y and Z which also produces a field projection in the three components, as shown in Figure 3.56a. Since the elements are rotated by 60°, the stronger component is Y . Then for the two facets 1 and 2, the main component is Z, since the facet 2 contributes mainly in the Z component. Finally for 3 facets, the component Y cancels due to the opposite orientation of the elements in facet 1 and 3.

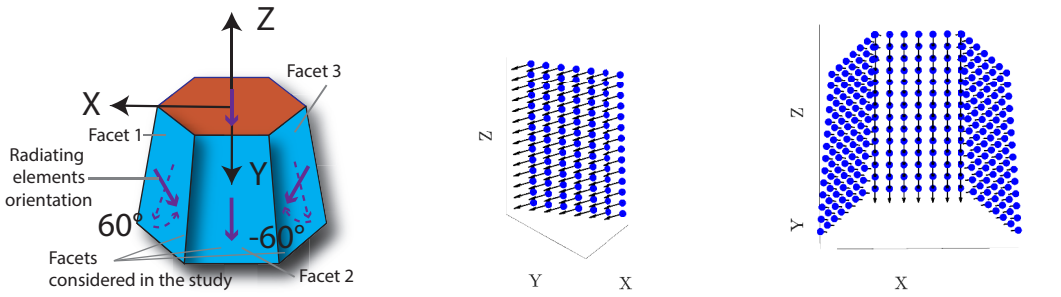

(a) Truncated faceted array and rotated lateral elements

(b) Three quarters view of the facet 1

(c) Three quarters view of the 3 facets

Figure 3.55: Truncated faceted array rotated lateral elements

	Cartesian purity	Spherical purity	Ellipticity purity
$-Z$-oriented radiating elements			
Facet 1	18.8	36.8	0
Facet 1 and 2	19	24.8	0
Rotated radiating elements			
Facet 1	0.79	1.77	0
Facets 1 and 2	4.8	3	26.6
Facets 1,2 and 3	5.4	5.4	25.7

Table 3.4: Polarisation purity in [dB] and maximum ellipticity in high directivity areas in [°]

There is also a cancellation of the field along X but only in the focusing direction not in the side lobe region.

Comparison between the two configurations The quantitative comparison between the $-Z$-oriented elements and the rotated elements is given in Table 3.4. The polarisation and ellipticity purity are much higher when the lateral elements remain vertical.

3.4.3 Polarisation study of the TOP facet and the lateral facet 1

The TOP facet and the lateral facet 1 of the truncated faceted cone are now studied. The suitable elements orientation for the lateral facets is sought to match with the elements of the TOP face. Two cases are considered, first the TOP facet elements orientation is axial, second the orientation is anti-radial. Those two orientations are chosen as the axial has a strong directivity and the anti-radial leads to strong difference

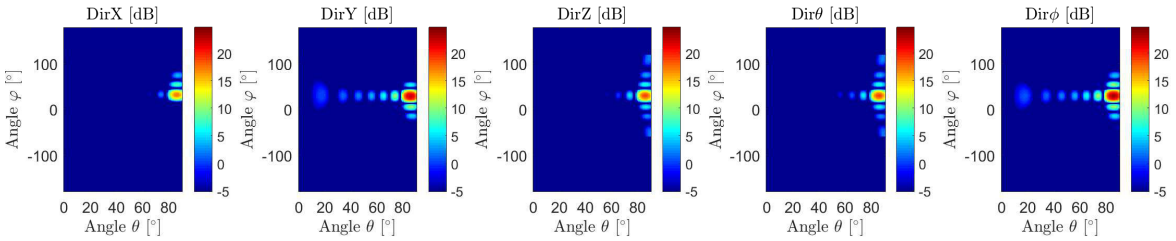

(a) Polarisation pattern of the facet 1 (steering 0°) ($\theta = 86°, \varphi = 30°$)

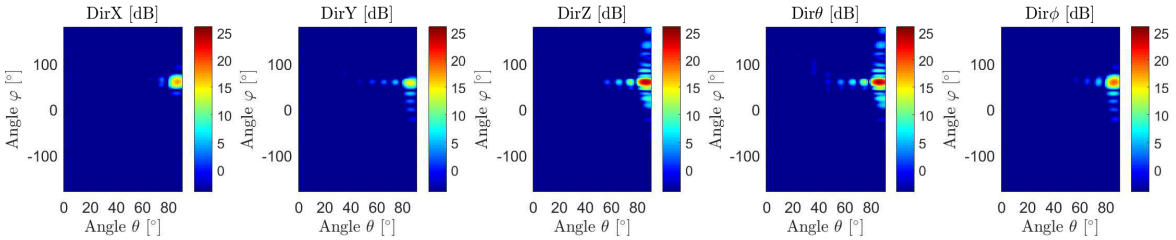

(b) Polarisation pattern of the facet 1 (steering 30°) and 2 (steering −30°) ($\theta = 86°, \varphi = 60°$)

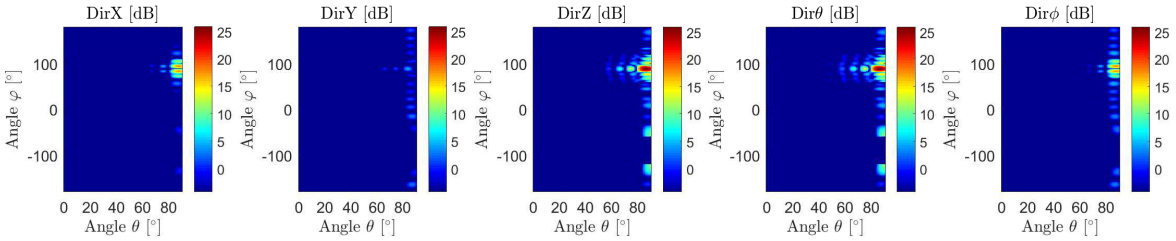

(c) Polarisation pattern of the facet 1 (steering 60°), 2 (steering 0°) and 3 (steering −60°) ($\theta = 86°, \varphi = 90°$)

Figure 3.56: Polarisation patterns of the truncated faceted array with rotated elements

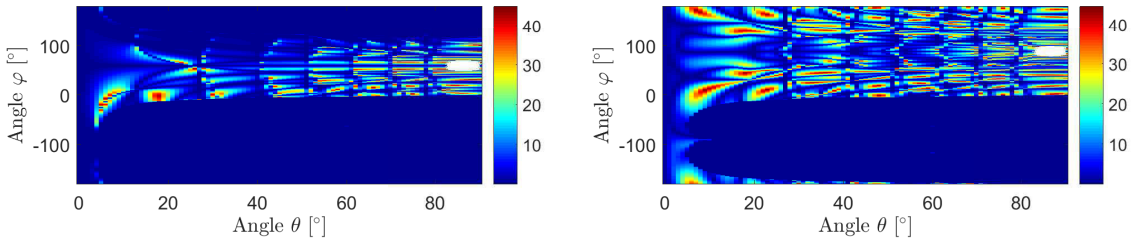

(a) Ellipticity pattern with two facets

(b) Ellipticity pattern with three facets

Figure 3.57: Truncated faceted array ellipticity pattern

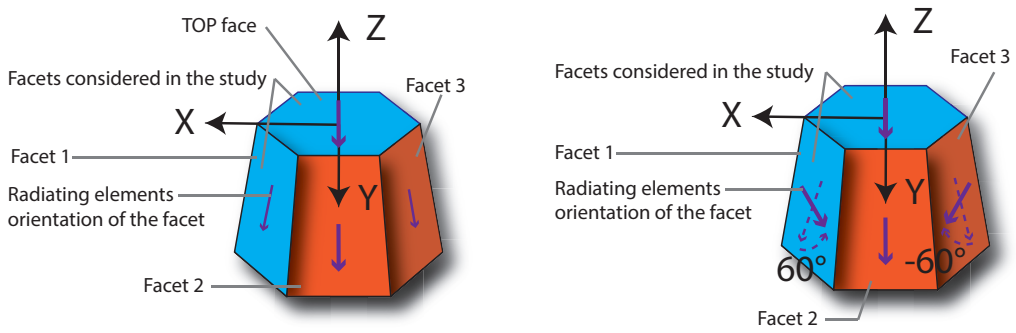

(a) Elements on the facets are $-Z$-oriented

(b) Elements on the facets rotated to match with the TOP

Figure 3.58: Truncated faceted array, axial TOP and the lateral elements orientations

patterns. The TOP facet in both cases has a square mesh and a circular geometry.

3.4.3.1 Axial orientation of the TOP facet

The suitable elements orientation for the lateral facets is sought to match with the axial oriented elements of the TOP facet. The tested lateral elements orientation are first $-Z$-oriented, second, rotated, as shown in Figure 3.58. To find the matching rotation angle, the orientation vector of the TOP facet element is projected on a given facet. When the orientation vector of the TOP facet is projected on the facet 2, it produces a $-Z$ orientation vector. Then, since between the facet 1 and the facet 2, there is an angle of 60° (Figure 3.52c), a rotation angle of 60° is applied to the elements of the facet 2 to match with the TOP facet elements. Hence, the matching rotation angle for the elements of the lateral facets can be found by determining the angle between the given lateral facet and the lateral facet 2. It is the same angle.

An elevation steering is carried out so that the beams of the TOP and lateral facets radiate in the same direction. The steering limit is 60°, therefore a reachable direction should be chosen for the TOP and the side facet. The direction $(\theta = 40°, \varphi = 30°)$ is selected.

Since the polarisation has not been previously studied for a steering in the direction $(\theta = 40°, \varphi = 30°)$, their polarisation patterns are separately investigated, then compared.

Polarisation study of the TOP facet in the direction $(\theta = 40°, \varphi = 30°)$ The polarisation pattern of the TOP facet for a beamsteering in the direction $(\theta = 40°, \varphi = 30°)$ is shown in Figure 3.59. The energy is emitted in the 3 components X, Y and Z, dominantly in the direction Y, as the elements are oriented in the Y direction.

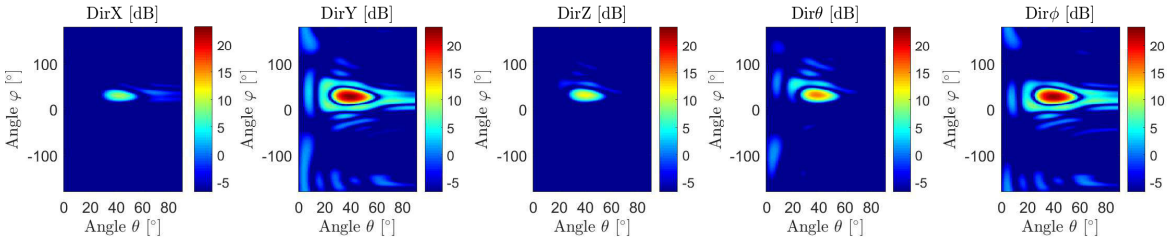

Figure 3.59: Polarisation pattern of the TOP, axial, steering in the direction ($\theta = 40°, \varphi = 30°$)

The polarisation purity in Cartesian is 8.23dB. It is weaker than without beamsteering: 20.7dB, this has been observed in section 3.3.5 (Figure 3.3.5). In spherical with beamsteering the polarisation purity is 3.96dB, without beamsteering, the two components $Dir\theta$ and $Dir\varphi$ are equal therefore, the purity is not applicable in this case.

Polarisation study of the lateral facet 1 in the direction ($\theta = 40°, \varphi = 30°$) The polarisation patterns of the facet 1 are studied with a steering in the direction ($\theta = 40°, \varphi = 30°$). Results are shown in Figure 3.60.

When the lateral elements are $-Z$-oriented, the fields radiate in the three Cartesian components X, Y and Z. Then as the lateral elements are rotated, their projection in the Z direction decreases and the field projection in the Z component decreases as well and goes to the X and Y components. Same is occurring in spherical, as the elements are rotated, their elements projection in the azimuthal component increases and the directivity in the azimuthal component as well.

Results are very different from the field without beamsteering where the field was only radiating in the Z component (Figure 3.54a). The polarisation purity for rotated elements with beamsteering in Cartesian is -2.9dB against 18.8dB without beamsteering. However in spherical the polarisation purity remains high: 32.9dB.

Comparison between the polarisation of the TOP and lateral facet 1 The matching between the TOP and lateral facets can be assessed first by comparison of the polarisation patterns. The polarisation patterns with $-Z$-oriented elements and rotated elements are respectively shown in Figure 3.60a and 3.60b and the TOP facet pattern is shown in Figure 3.59. The configuration that matches the best the TOP facet is the rotated one, it is confirmed by the results given in Table 3.5.

It can be observed that the components Y and Z have the same levels min and max in the θ_{-3dB} area for the TOP and the rotated facet 1. In the direction $\varphi = 30°$ the projection of the element orientation vector of each facet on the Y axis is the same. It explains that the field has the same Y component. The same applies in the direction

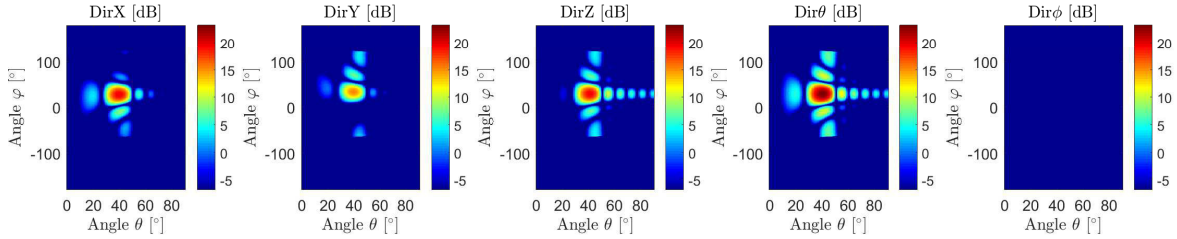

(a) Polarisation pattern of facet 1, $-Z$-oriented elements, steering in direction ($\theta = 40°, \varphi = 30°$)

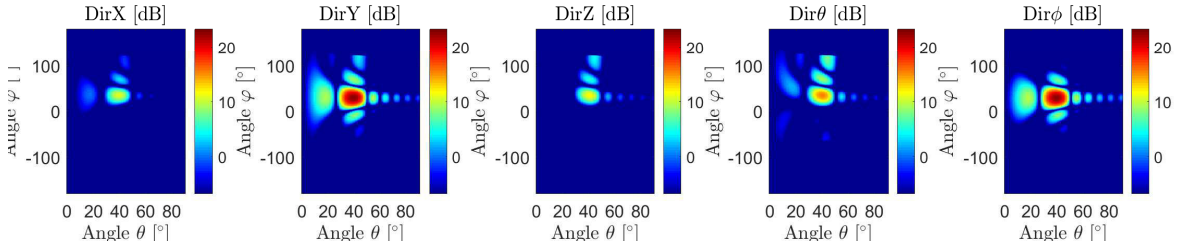

(b) Polarisation pattern of facet 1, rotated elements, steering in direction ($\theta = 40°, \varphi = 30°$)

Figure 3.60: Tr. faceted array, facet 1, polarisation patterns and beamsteering

$\theta = 40°$ for the component Z, the directivity is almost the same since the lateral faces have an angle $\theta = 86°$ from vertical.

Array vs Component	$DirX$		$DirY$		$DirZ$		$Dir\theta$		$Dir\phi$		Purity	
	Min	Max	Min	Max	Min	Max	Min	Max	Min	Max	Cart	Spher
TOP facet	6.15	9.13	19.8	22.8	8.6	11.6	12.7	15.6	19.6	22.6	8.23	3.96
Facet 1, $-Z$-oriented	16.7	19.7	12.4	15.4	16.6	19.6	20.2	23.2	-15.6	-12.7	-2.9	32.9
Facet 1, rotated	7.85	10.8	19.7	22.7	8.76	11.7	12.4	15.4	19.6	22.6	8.0	4.1

Table 3.5: Comparison between the axial TOP and lateral facet in polarisation [dB]

The matching between the TOP facet and the lateral one can be measured by carrying out the scalar product between the field vector of the TOP with the lateral facet when the elements are $-Z$-oriented as well as when the lateral elements are rotated. The scalar product is 0 when the vectors are orthogonal and 1 when they are parallel. The field vectors are normalised prior to the scalar operation. Results are shown in Figure 3.61. Finally in the direction ($\theta = 40°, \varphi = 30°$) the scalar product provides a matching of 0.66 with $-Z$-oriented elements and 1 when the lateral elements are rotated which confirm the matching between the TOP facet and the lateral facet. It can be also noticed that the matching is valid for a wide angle around the steered direction.

The field has been simulated with the TOP and facet 1 together for both cases. The rotated elements of the facet 1 produce a gain of 0.24dB in directivity in the direciton

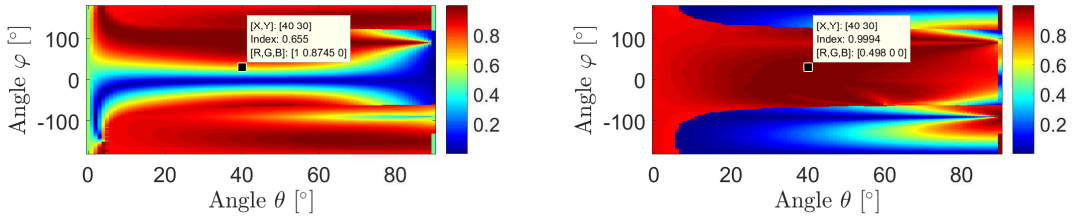

(a) Elements on the facets are $-Z$-oriented, steering in direction $(\theta = 40°, \varphi = 30°)$

(b) Elements on the facets rotated to match with the TOP, steering in direction $(\theta = 40°, \varphi = 30°)$

Figure 3.61: Scalar patterns of the truncated faceted array, TOP axial

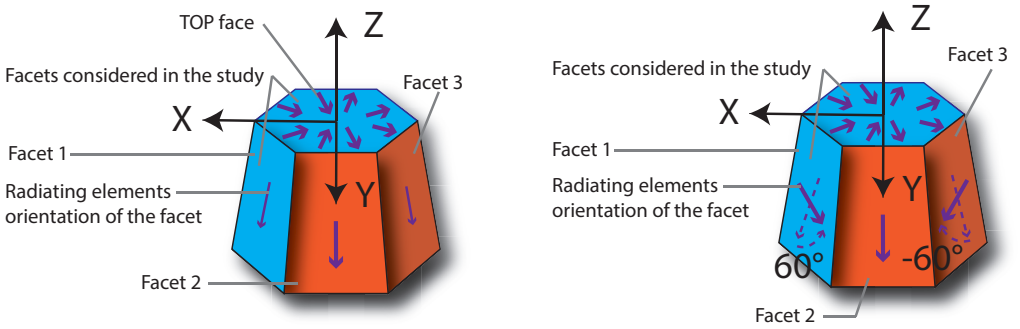

(a) Elements on the facets are $-Z$-oriented

(b) Elements on the facets rotated to match with the TOP

Figure 3.62: Truncated faceted array, anti-radial TOP and the lateral elements orientations

$(\theta = 40°, \varphi = 30°)$, a decrease of 20.7° for the maximum ellipticity and also an increase of polarisation purity of 3.42dB in Cartesian and 7.75dB in spherical.

3.4.3.2 Anti-radial orientation of the TOP facet

The matching between the lateral facet and the TOP with the anti-radial configuration is studied, as shown in Figure 3.62. A beamsteering is applied to focus the beam of the TOP and the facet 1 in the same direction $(\theta = 40°, \varphi = 30°)$.

The polarisation of the anti-radial TOP facet is shown in Figure 3.63. The three field components X, Y and Z are strong, with a dominant component X. By comparison with the polarisation patterns of the lateral facets in Figure 3.60 and with Table 3.6, it can be observed that the $-Z$-oriented configuration matches better than with rotated elements. The Y component has the same directivity for the TOP and facet 1. It is not the case in the Z component, it can be due to the destructive interferences of the TOP facet due to the anti-radial orientation.

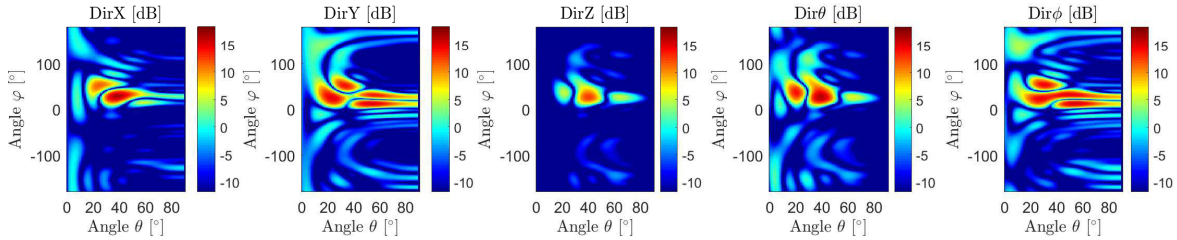

Figure 3.63: Polarisation pattern of the TOP, anti-radial, steering in the direction $(\theta = 40°, \varphi = 30°)$

Array vs Component	*DirX*		*DirY*		*DirZ*		*Dirθ*		*Dirϕ*		Purity	
	Min	Max	Min	Max	Min	Max	Min	Max	Min	Max	Cart	Spher
TOP facet	13.7	16.7	12.4	15.4	9.6	12.6	13.5	16.5	12.7	15.7	-1.6	2.13
Facet 1, $-Z$-oriented	16.7	19.7	12.4	15.4	16.6	19.6	20.2	23.2	-15.6	-12.7	-2.9	32.9
Facet 1, rotated	7.85	10.8	19.7	22.7	8.76	11.7	12.4	15.4	19.6	22.6	8.0	4.1

Table 3.6: Comparison between the anti-radial TOP and lateral facet in polarisation [dB]

The scalar patterns, that provide a quantitative comparison of the two cases, confirm that in the focusing direction $(\theta = 40°, \varphi = 30°)$, the $-Z$-oriented elements have a better match, it gives 0.96 against 0.5. However in this case, the matching is not valid for a wide area.

The field has been simulated with the TOP and facet 1 together for both cases. The rotated elements of the facet 1 produce a gain of 0.69dB in directivity in the direction $(\theta = 40°, \varphi = 30°)$, a decrease of 14.3° for the maximum ellipticity and also an increase of polarisation purity of -0.77dB in Cartesian and 4.52dB in spherical.

As a conclusion, if the TOP array and the lateral one are meant to be used together coherently to process the echo signal, this study has shown the different interest of matching the TOP and lateral elements. It produces an increase of directivity and a

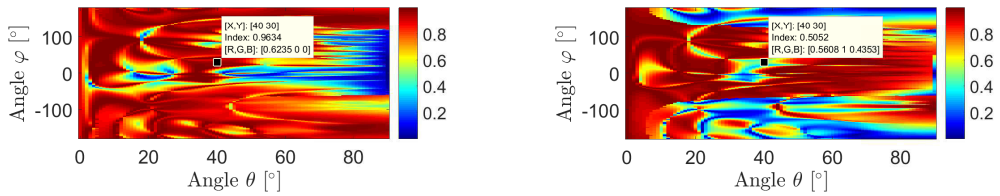

(a) Elements on the facets are $-Z$-oriented

(b) Elements on the facets rotated to match with the TOP

Figure 3.64: Scalar pattern of the truncated faceted array, anti-radial TOP

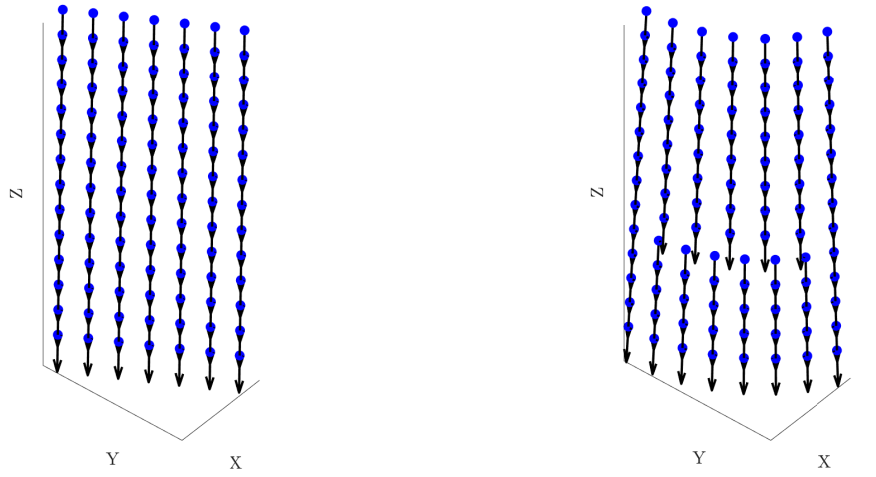

(a) Faceted array

(b) Array with curvature

Figure 3.65: Comparison between the arrays

decrease of ellipticity. Concerning the polarisation, it increases the alignment of the field in the steered direction which means that once expressed in a given coordinate system it produces closer polarisation purity. It only increases the alignment and does not perfectly align the field as shown by the anti-radial TOP case.

3.4.4 Study of the truncated cone

In this section, using the lateral elements of the truncated cone, first the effect of the curvature on the radiation patterns is studied as a function of the elevation beamsteering, then the effect of the number of elements on the radiation patterns is studied. The diameter of the TOP face measures 120mm and that of the bottom 140mm, it produces a lateral array with an angle 4.09° respective to the vertical. The radiating elements are $\frac{\lambda}{2}$-spaced.

3.4.4.1 Comparison of lateral arrays, faceted versus one degree of curvature, study in elevation

The effect of the elevation beamsteering on the faceted truncated cone and the truncated cone is investigated. The faceted truncated cone has a faceted array and the truncated cone has an array with one degree of curvature. Therefore this study has the double interest to explore their performance as a function of the elevation beamsteering and the effect of the curvature. The effect is studied on the directivity,

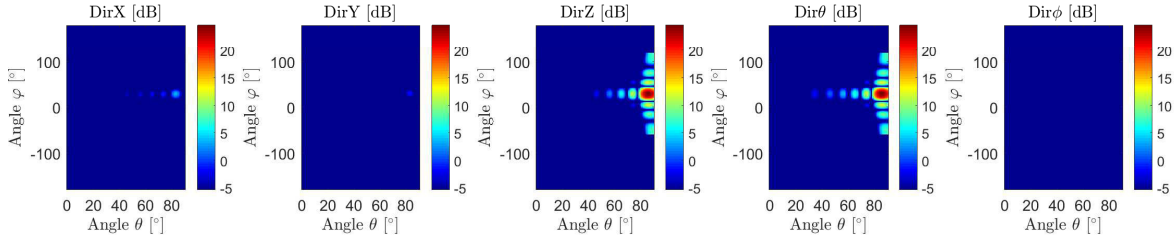

(a) Faceted array, steering in direction ($\theta = 86°, \varphi = 30°$)

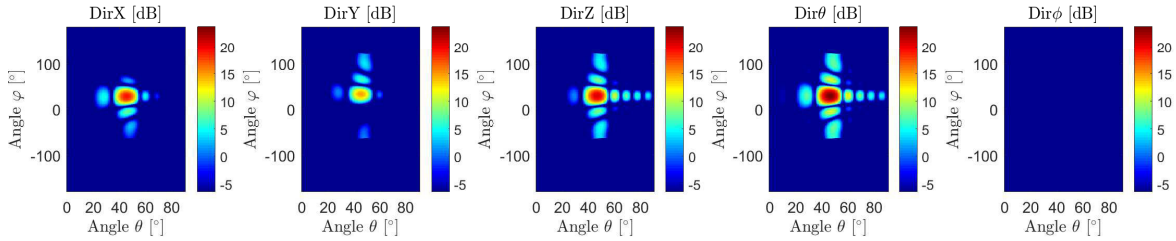

(b) Faceted array, steering in direction ($\theta = 46°, \varphi = 30°$)

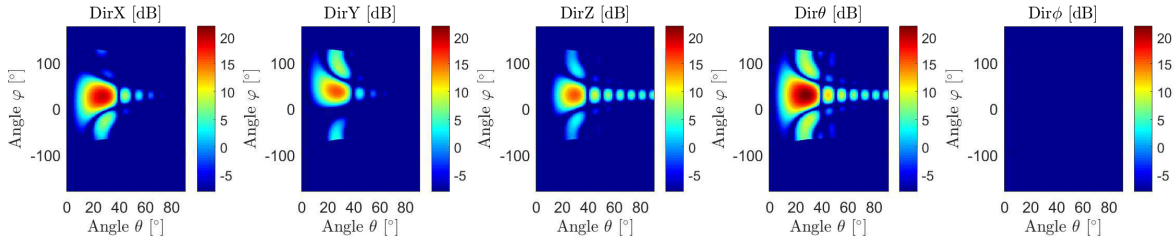

(c) Faceted array, steering in direction ($\theta = 26°, \varphi = 30°$)

Figure 3.66: Polarisation patterns of the faceted array

sidelobes, polarisation and ellipticity.

The faceted array has 98 elements and the curved array has 103 elements. The spacing between the radiating elements is the same and their orientation as well. The array sections are located between $\varphi = 0°$ and $\varphi = 60°$, they are, therefore, centred in the direction $\varphi = 30°$. For the curved array, a beamsteering phase is applied to compensate the curvature, this allows to focus the main lobe. This beamsteering is used wherever the truncated cone is studied. More details are given about the phase applied in section 3.4.5.

Firstly, the beamsteering effect is studied for three elevation beamsteering angles $\theta = 86°$, $\theta = 46°$ and $\theta = 26°$, in the azimuth plane $\varphi = 30°$, which corresponds respectively to a beamsteering of 0°, 40° and 60°. The polarisation patterns results are shown in Figure 3.66 and 3.67. Secondly, the beamsteering effect is studied for the three same elevation beamsteering angles, in the azimuth plane $\varphi = 0°$.

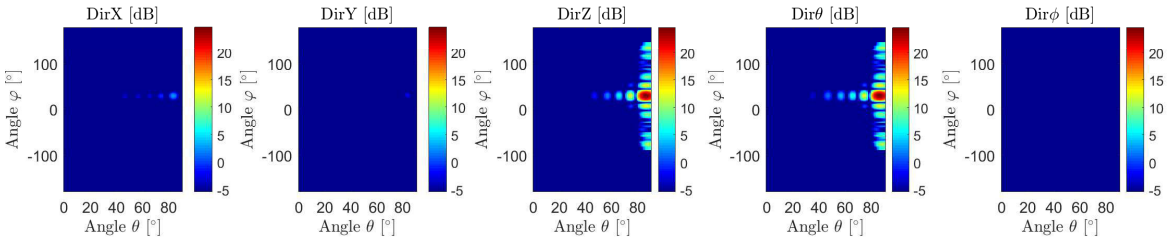

(a) Curved array, steering in direction ($\theta = 86°, \varphi = 30°$)

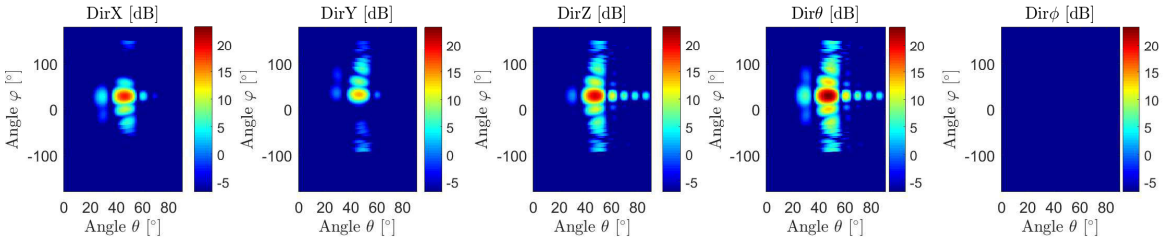

(b) Curved array, steering in direction ($\theta = 46°, \varphi = 30°$)

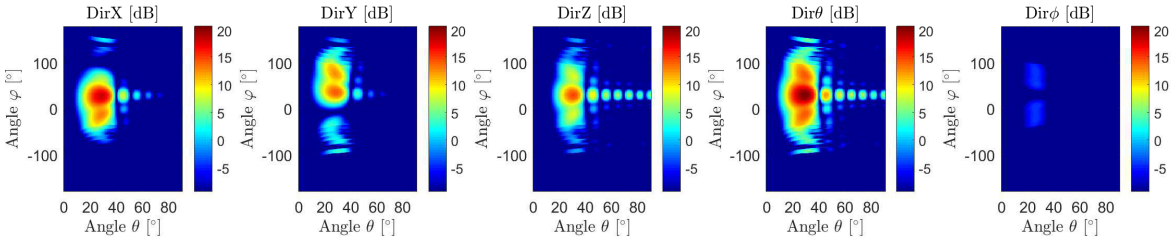

(c) Curved array, steering in direction ($\theta = 26°, \varphi = 30°$)

Figure 3.67: Polarisation patterns of the curved array

Comparison in the plane $\varphi = 30°$ First the observations valid for both arrays are presented. As the elevation beamsteering increases, the faceted and curved arrays have a wider main lobe. For both arrays, the spherical coordinate system keeps a strong polarisation purity although the Cartesian one decreases with the beamsteering angle, as shown in Table 3.7. The ellipticity remains constant and low as a function of beamsteering.

Now, the differences between the arrays are introduced. The curved array has more elements than the faceted array, despite that, the faceted array has a stronger directivity of 0.04dB due to the change of orientation of the elements. The curved array has higher sidelobes than the faceted array as a result of the curvature. For the faceted array the sidelobes remains constant although for the curved array they increase.

As a conclusion, the faceted array has better performance than the curved array in term of directivity, ellipticity, polarisation purity and sidelobes, despite the lower number of elements.

Array type and steering	Max. $DirTot$	Sidelobe level	Purity Cart.	Purity Spher.	Max. χ
Faceted / $\theta = 86°$	24.68	12.0	18.46	36.86	0.0064
Faceted / $\theta = 46°$	23.59	11.86	-1.37	34.03	0.0036
Faceted / $\theta = 26°$	21.71	12.05	1.04	27.25	0.03
Curved / $\theta = 86°$	24.64	12.67	19.2	31.3	1.12
Curved / $\theta = 46°$	23.03	13.13	-1.12	27.69	1.15
Curved / $\theta = 26°$	20.72	14.27	0.66	21.77	1.97

Table 3.7: Comparison between the faceted and curved array, directivity [dB], ellipticity [°], in the direction $\varphi = 30°$

Array type and steering	Max. $DirTot$	Sidelobe level	Purity Cart.	Purity Spher.	Max. χ
Faceted / $\theta = 86°$	23.99	11.35	17.89	25.5	0.0042
Faceted / $\theta = 46°$	23.04	11.21	-2.69	22.8	0.005
Faceted / $\theta = 26°$	21.11	11.7	2.93	16.4	0.0097
Curved / $\theta = 86°$	23.39	14.7	17.2	25.93	1.09
Curved / $\theta = 46°$	22.59	12.74	-2.7	22.29	1.56
Curved / $\theta = 26°$	20.3	13.59	2.74	16.70	2.12

Table 3.8: Comparison between the faceted and curved array, directivity [dB], ellipticity [°], in the direction $\varphi = 0°$

Comparison in the plane $\varphi = 0°$ For the comparison, in the plane $\varphi = 0°$, details about the figure of merit values are given in Table 3.8, the radiation patterns are not provided. Globally, lower performance than in the plane $\varphi = 30°$ can be observed, due to the additional azimuth beamsteering, however, unexpectedly, the sidelobe levels are lower than in the plane $\varphi = 30°$.

The tendencies in the previous comparison are also valid in the plane $\varphi = 0°$. As a conclusion, despite its lower number of elements, the faceted array has better performance than the curved array in term of directivity, sidelobes and ellipticity.

3.4.4.2 Effect of the lateral array size on the directivity and sidelobes

The effect of the number of radiating elements is studied. From 103 elements that covers a section of 60°, to the all structure with 567 elements which covers the 360° as illustrated in Figure 3.68.

The amount of radiating elements have a direct effect on the directivity and the sidelobe level. In each case, the array is steered in the direction ($\theta = 86°, \varphi = 30°$) and

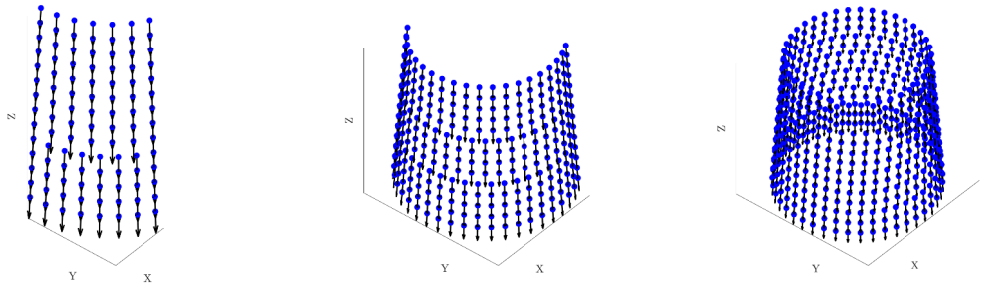

(a) Truncated cone, section of 60° (b) Truncated cone, half array (c) Truncated cone, total array

Figure 3.68: The different sections of the truncated cone

the array is azimuthally centred around the steered direction. It means that for the 60° section of the array, the array starts for $\varphi = 0°$ to $\varphi = 60°$ to be symmetric around the direction $\varphi = 30°$.

Results are shown in Table 3.9, the main lobe directivity is not increasing with the number of elements. Among the particular array size chosen, the best directivity is found for an array with a section 120° wide. The directivity stops decreasing at some point since the added elements are not radiating in the desired direction, their contribution becomes minor and destructive interferences occur.

The stronger difference between the main lobe and the side lobe is reached for the smallest array section 60°. Then as the number of elements increases the difference keeps decreasing.

Thanks to the revolution symmetry of the structure and the elements orientation, those comments are valid for any direction as long as the array is symmetric around the steered direction. The array section of 120° means that the maximum steering applied is 60°, it is the case that brings the best maximum directivity.

As a conclusion, there is a compromise between the number of radiating elements and the total directivity. In case of conformal arrays, increasing the number of elements does not necessarily increases the directivity since the new elements do not radiate in the desired direction. This observation allows to limit the powered elements and therefore focus the power in the most contributing ones and optimise the link budget.

3.4.4.3 Effect of the lateral array size on the polarisation

The elements are tangent to the face and $-Z$-oriented. The dominant coordinate is Z with no beamsteering in elevation. This is confirmed by the polarisation pattern results shown in Figure 3.69. By projection in spherical the θ component is dominant.

Elmts. Nbr. / Array section	Max. *DirTot*	Sidelobe level	Difference
$N = 89$ / 60°	23.94	12.22	11.72
$N = 184$ / 120°	25.78	15.66	10.12
$N = 280$ / 180°	25.75	17.04	8.71
$N = 567$ / 360°	24.03	16.02	8.01

Table 3.9: Truncated cone array size versus directivity max [dB] and sidelobes [dB]

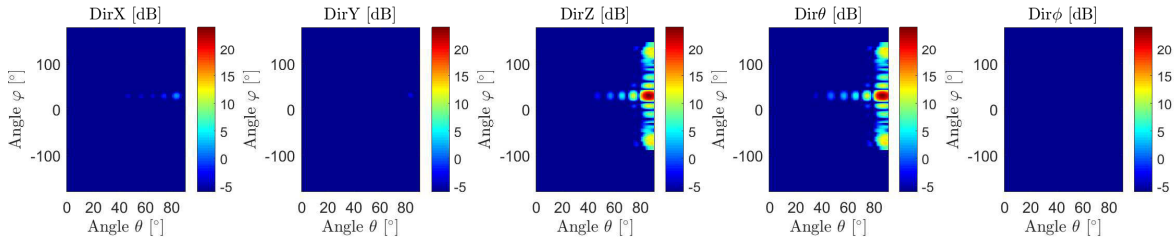

(a) Truncated cone, section of 60°, steering ($\theta = 86°, \varphi = 30°$)

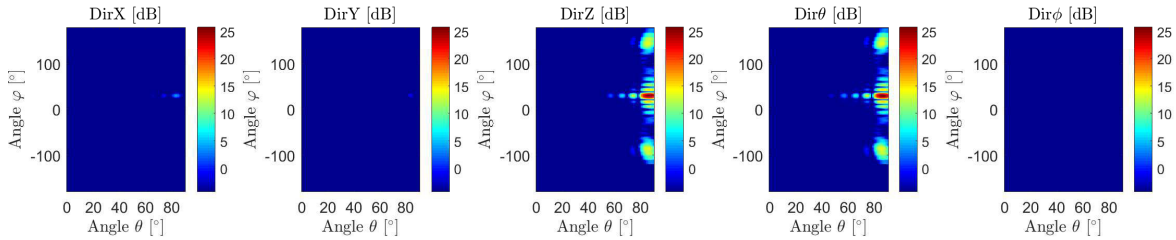

(b) Truncated cone, section of 120°, steering ($\theta = 86°, \varphi = 30°$)

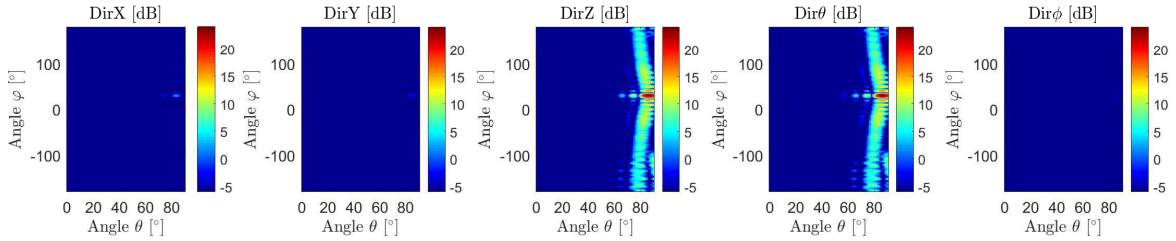

(c) Truncated cone, total array, steering ($\theta = 86°, \varphi = 30°$)

Figure 3.69: The different radiating sections of the truncated cone

Since most of the energy is emitted in the Z component, $DirTot \approx DirZ$ and the sidelobe levels can be analysed thanks to this component. In conclusion, irrespective of the number of active facets, the polarisation purity remains the same.

The sidelobe levels previously discussed are clearly visible and one can notice that for a section of 120° the sidelobes are lower than for the two other illustrated cases.

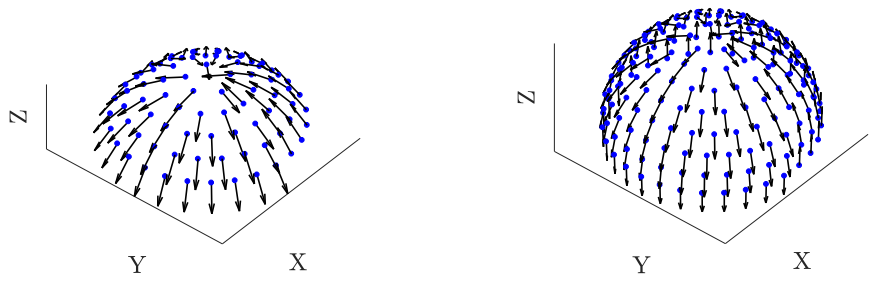

(a) anti-radial half-sphere array, 82 elements

(b) anti-radial half-sphere array, 172 elements

Figure 3.70: Half-sphere array arrangements

3.4.5 The half-sphere array

A half-sphere array is selected for its symmetry. For comparison, the half-sphere array has the same diameter as the circular array: 100mm from section 3.3.3. First, a partial half-sphere array of 82 elements is considered. It is the closest number of elements from the circular array that ensures an azimuthal symmetry. The elements are $\frac{\lambda}{2}$-spaced horizontally and vertically, they are not enough to cover the entire half-sphere array, the base diameter is only 66.65mm. Hence, a full half-sphere of 172 elements is also studied (Figure 3.70). The elements have an anti-radial orientation, they are projected on the half-sphere shape so that they are tangent to its surface.

To focus the energy in a given direction, a beamsteering phase is applied to the elements. For example to steer the beam in the direction Z, the beamsteering phase that aligns the elements wave fronts is proportional to the Z coordinate component of the elements(Figure 3.71a). For other directions, the elements positions are expressed in a rotated coordinate system, as shown in Figure 3.71b. The Z component of the new rotated coordinate system is proportional to the beamsteering phase to steer the direction in this new direction Z. The radiation patterns resulting from the beamsteering are shown in Figure 3.72. For a steering of the beam in the direction $\theta = 0°$, a similar pattern as that of the circular array can be found (Figures 3.72a and 3.32h).

For a beamsteering of 0° and 40°, the anti-radial configuration ensures constructive interferences. However along the anti symmetry plane yOz the anti-radial elements have opposite directions which brings destructive interferences in the direction of the main lobe and decreases the directivity, therefore for a beamsteering of 60°, the radial configuration is selected.

When the beam is steered from 40° to 60° (Figures 3.72b and 3.72c), in the plane $\varphi = 90°$ the main lobe becomes finer and its nulls disappear. The axial orientation is

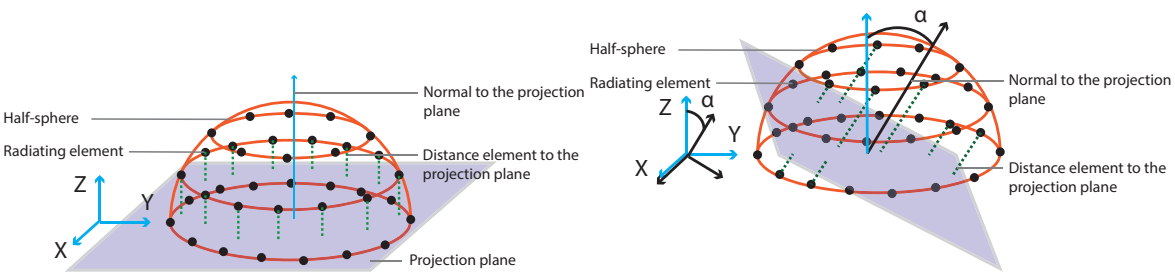

(a) Projection in the direction Z (b) Projection in a given direction

Figure 3.71: Projection of the elements

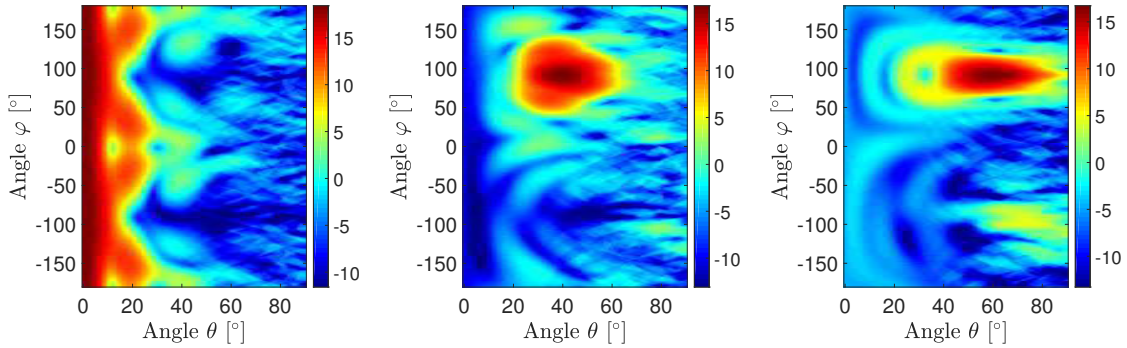

(a) Steering 0°, anti-radial (b) Steering 40°, anti-radial (c) Steering 60°, radial

Figure 3.72: Effect of the beamsteering on the directivity patterns of the partial anti-radial half-sphere array with 82 elements

the reference for a high directivity and a thinner beam. For a beamsteering of 60°, by projection of the orientation vectors in this direction, the most contributing elements have a closer orientation from axial than in the steered direction 0° where elements are anti-radial. First, it explains the enhancement of the main lobe shape, and second, the directivity increase for the half-sphere array of 172 elements for a steering of 60° (Table 3.10).

The number of elements in the half-sphere array impacts the directivity and ellipticity, as shown in Table 3.10. The directivity of the partial half-sphere decreases by 1.7dB with the beamsteering angle from 0° to 60°. For the entire half-sphere, the directivity decreases from 0° to 40° but then increases thanks to the contributions of the side elements. Finally from 0° to 60° the directivity increases by 1.64dB. In both cases, the ellipticity is low for a steering of 0° and then increases with beamsteering.

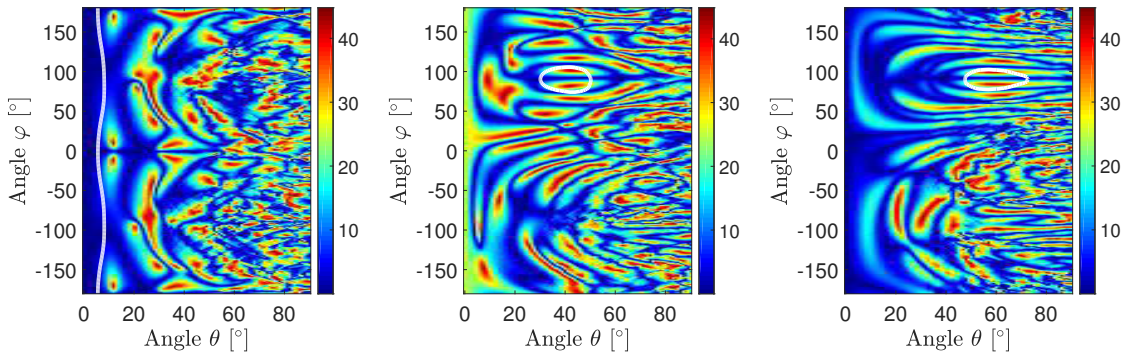

(a) Steering 0°, anti-radial (b) Steering 40°, anti-radial (c) Steering 60°, radial

Figure 3.73: Ellipticity patterns of the partial anti-radial half-sphere array

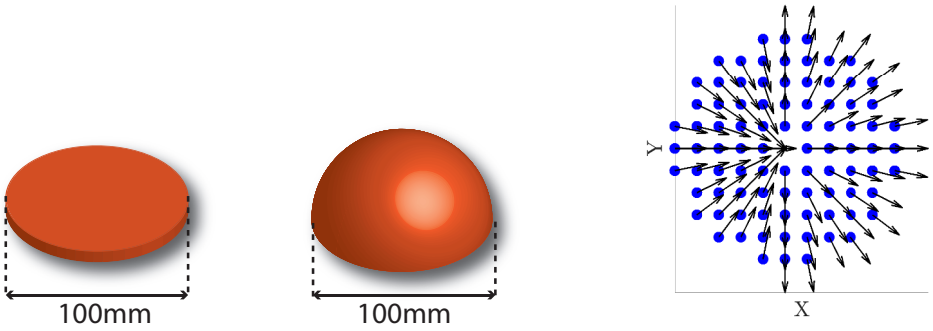

(a) Planar and half-sphere arrays (b) anti-radial circular array, 82 elements

Figure 3.74: The planar and the half-sphere

3.4.6 Comparison between the planar array and the half-sphere array

The comparison between a circular array and a half-sphere array is carried out. Their respective shapes are illustrated in Figure 3.74. This study demonstrates whether the 3D conformal array can overpass the planar array in term of directivity. The beam-steering and ellipticity are also explored.

The planar array with a square mesh and an anti-radial elements orientation from section 3.3.3 is considered, its structure is reminded in Figure 3.35a, it is chosen for its best results over the different arrangements.

The half-sphere arrays have similar ellipticity compared to the planar arrays for a steering of 0°, as shown in Table 3.10. Then for a beamsteering of 40° and 60° (Figure 3.73) the ellipticity increases for the half-sphere arrays although the planar array maintains a low ellipticity. It shows that the ellipticity is more difficult to control

Array / bst* angle	0°	40°	60°
Circle	20.15 / 11.33	20.1 / 9.3	18.5 / 7.74
Half-sphere 82	18.41 / 6.8	16.9 / 44.17	16.7 / 43.33
Half-sphere 172	17.83 / 11.6	17.37 / 43.17	19.47 / 24.77

* bst = beamsteering

Table 3.10: Directivity max [dB] / ellipticity max [°] versus beamsteering

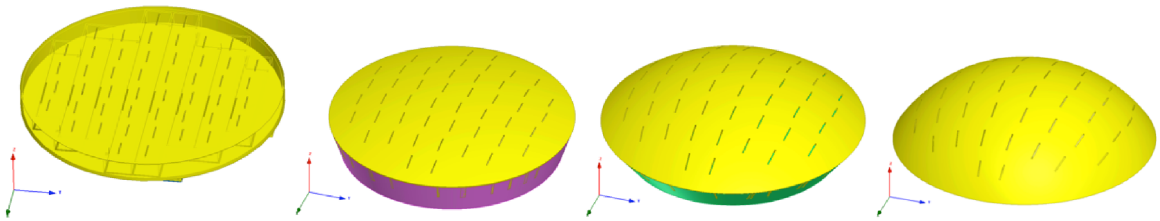

(a) Case 1, planar (b) Case 2, conformal (c) Case 3, conformal (d) Case 4, conformal

Figure 3.75: Planar and conformal topologies

for 3D conformal arrays than for planar arrays for which the ellipticity is low in the θ_{-3dB} directions.

Finally, for a half-sphere array with the same number of elements as the current mechanical planar array, its directivity does not takeover the planar array directivity. However, the entire half-sphere array directivity that can host much more elements overpasses the planar one for high beamsteering angles.

As a conclusion, this study highlights the potential of 3D conformal antennas as the half-sphere array directivity overpasses the circular planar array directivity for a same radius which is also mitigated by the increase of ellipticity.

3.4.7 Effect of the degree of curvature of a 3D conformal antenna simulated on HFSS

The impact of the degree of conformation on the radiation patterns is studied with 4 antenna topologies, as shown in Figure 3.75. The topologies are simulated on HFSS©which accounts for all the coupling effects between the elements. Each antenna has 48 slot antennas and its associated feeding network based on waveguides as illustrated for the planar case in Figure 3.76. The antennas and their feeding network are progressively conformed. The effect of the conformation is therefore studied on the directivity and ellipticity.

The general structure is the same for each array, for the planar one, the exploded

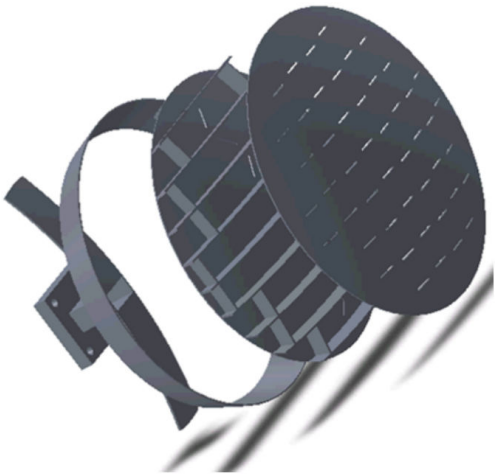

Figure 3.76: Exploded view of the planar array

view of the array associated to its feeding network is shown in Figure 3.76, the parallel slots are fed by a second waveguide which slots are tilted by 45° from the firsts. The conformation bends the waveguides and modifies the spacing between the slots by a few millimetres although the aimed spacing is $\frac{\lambda}{2}$. Nonetheless, the slots position is not corrected since it is conditioned such that the slots are positioned on the maxima of the stationary wave of the waveguides. It ensures that the antenna radiates with a strong gain.

The evolution of the radiation pattern is shown in Figure 3.77. For the planar case, the main lobe is very directive, in the plane $\varphi = 0°$, $\theta_{3dB} = 5.5°$. Then as the degree of conformation increases, as expected, the main lobe widens and its directivity decreases. The planar array has a maximum directivity of 24dB and the topology with the highest degree of curvature has a directivity of 11.4dB. Respectively for the different conformal cases, in the plane $\varphi = 0°$, $\theta_{3dB} = 5.5°$, $\theta_{3dB} = 14.5°$, $\theta_{3dB} = 20.5°$. Sidelobes also appear in the planes $\varphi = \pm 90°$.

Results of the ellipticity are shown in Figure 3.78. The ellipticity remains stable and low as a function of the conformation degree in the area from $\theta = 0°$ to $\theta = 30°$ which includes the θ_{-3dB} areas. In the θ_{-3dB} areas, the maximum ellipticity is respectively 0.42°, 0.15°, 3.5° and 39°. For the highest degree of conformation, the ellipticity goes up to 39°, this is however true only for specific areas.

This antenna design does not allow to carry out beamsteering since all the elements are fed through one port. Irrespective of the degree of conformation, most of the energy is emitted in directions around the axis of symmetry Z. This specific case also demonstrates that the ellipticity is kept low around the axis Z. Those simulations do not allow to predict what would happen with beamsteering, it is investigated in the previous sections

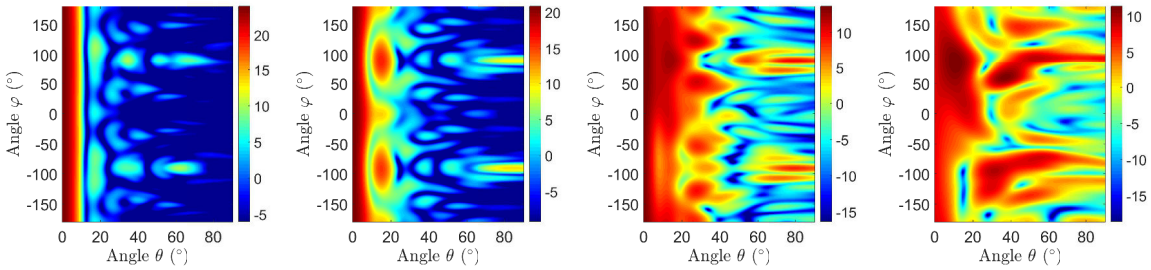

(a) Case 1, planar (b) Case 2, conformal (c) Case 3, conformal (d) Case 4, conformal

Figure 3.77: Directivity patterns of the planar and conformal topologies

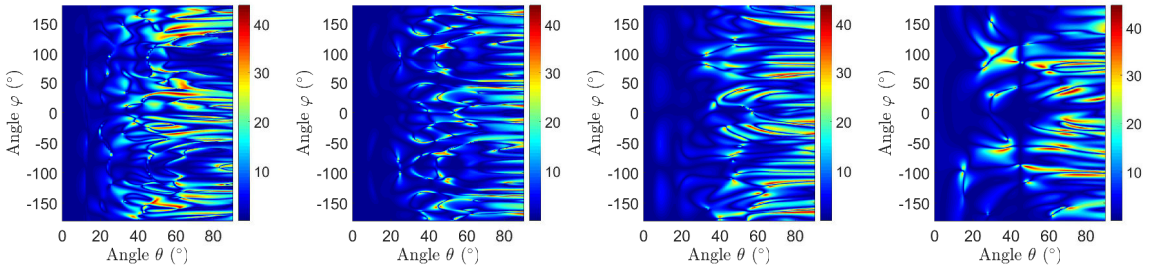

(a) Case 1, planar (b) Case 2, conformal (c) Case 3, conformal (d) Case 4, conformal

Figure 3.78: Ellipticity patterns of the planar and conformal topologies

As a conclusion, after simulation of the slot antenna and its feeding network on HFSS©, the degree of conformation impacts the directivity and the θ_{-3dB} area but does not impact the ellipticity. For the highest degree of conformation, the ellipticity remains low for most directions in the θ_{-3dB} area.

3.4.8 Global comparison of the 3D conformal arrays and the planar array

3.4.8.1 Global comparison of the 3D conformal arrays

The three 3D conformal arrays, as illustrated in Figure 3.79, are compared by calculating their directivity by steering their beam in each direction from $\theta = 0°$ to $\theta = 90°$ and $\varphi = 0°$ to $\varphi = 90°$ with a 5° step angle.

For the truncated faceted cone, the TOP consists in an hexagonal array with a square mesh and for the truncated cone, the TOP is the circular array with a square mesh. In both cases the anti-radial orientation is chosen so that their polarisation matches with that of the lateral facet.

For the truncated faceted cone and the truncated cone, an elevation beamsteering

angle limit of 43° is applied, it is half of the angle between the TOP and lateral facets: 86°.

To facilitate the simulations, an azimuth beamsteering limit of 30° is applied to the truncated faceted cone which means that only one facet radiates at a time except at the corners where there are two: $\varphi = 0°$ and $\varphi = 60°$. One facet covers 60° over the azimuthal angles. Hence, to make the comparison fair, for the truncated cone, the active radiating elements of the lateral face cover a section of 60° for a given direction. The active elements change as the azimuth steering angle varies.

For the half-sphere array, until the elevation angle 25°, the anti-radial configuration is chosen, then the elements are radial oriented. The diameter of the half-sphere is 140mm and there are 322 elements in total. All the elements are active for each steering direction.

As a result, for the three arrays, the field is almost azimuth invariant, as shown in Figure 3.80. For the truncated faceted cone and the truncated cone, until 40° of elevation steering, it is not perfectly invariant since the TOP does not have an azimuthal symmetry due to the anti-radial elements orientation. For the half-sphere array, there is also an anti-symmetry up to 25° since the orientation of the elements is anti-radial.

For the truncated faceted cone and the truncated cone from $\theta = 45°$ to $\theta = 90°$, the directivity increases as the lateral arrays progressively steer the beam in their natural radiating direction. For the truncated faceted cone for $\varphi = 0°$ and $\varphi = 60°$, the directivity is higher as two facets are radiating in this direction.

For the half-sphere array the best directivity is obtained in the directions $\theta = 35°$ to $\theta = 60°$ due to the symmetry of the structure.

The truncated cone has better performance for elevation steering angles below 40° thanks to the circular array. Then for elevation steering angles above 40°, both arrays present very close directivity.

The half-sphere array has a strong potential up to an elevation steering of 60°, its directivity is close to that of the two other arrays and even higher in some directions.

3.4.8.2 Antenna emission and reception scheme

For the 3D and conformal antenna study, different parts of the antenna are used depending on the emission and the reception.

In emission the 3D conformal antenna only uses the TOP facet, which allows to reduce the price of the RF-seeker system by decreasing the feeding network complexity. In reception the whole antenna is used. An illustration is provided in Figure 3.81.

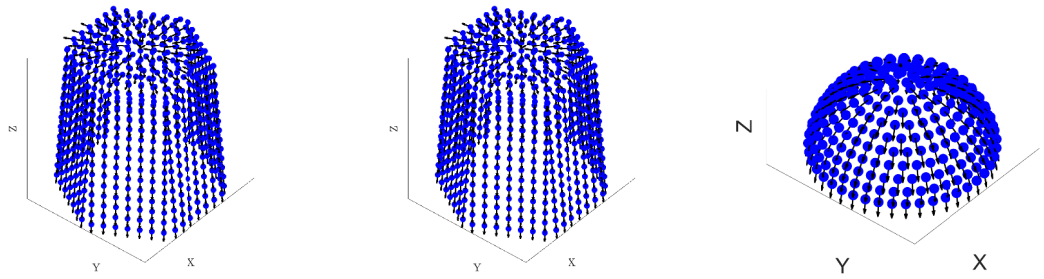

(a) Truncated faceted cone (b) Truncated cone (c) Half-sphere

Figure 3.79: 3D conformal arrays

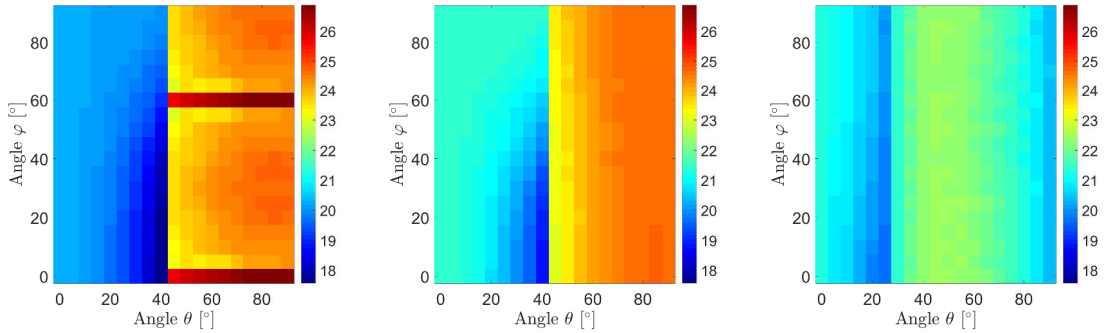

(a) Truncated faceted cone (b) Truncated cone (c) Half-sphere

Figure 3.80: Directivity patterns of the 3D conformal arrays

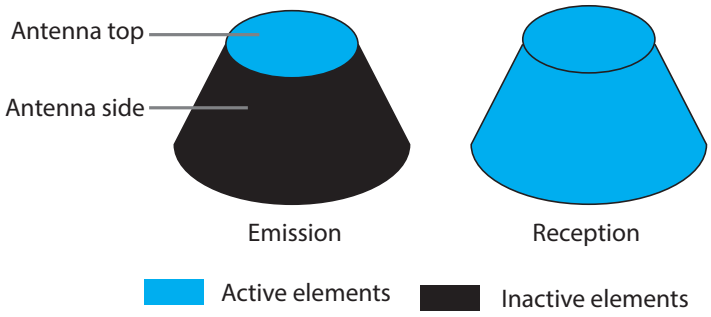

Figure 3.81: Active elements respective to emission or reception

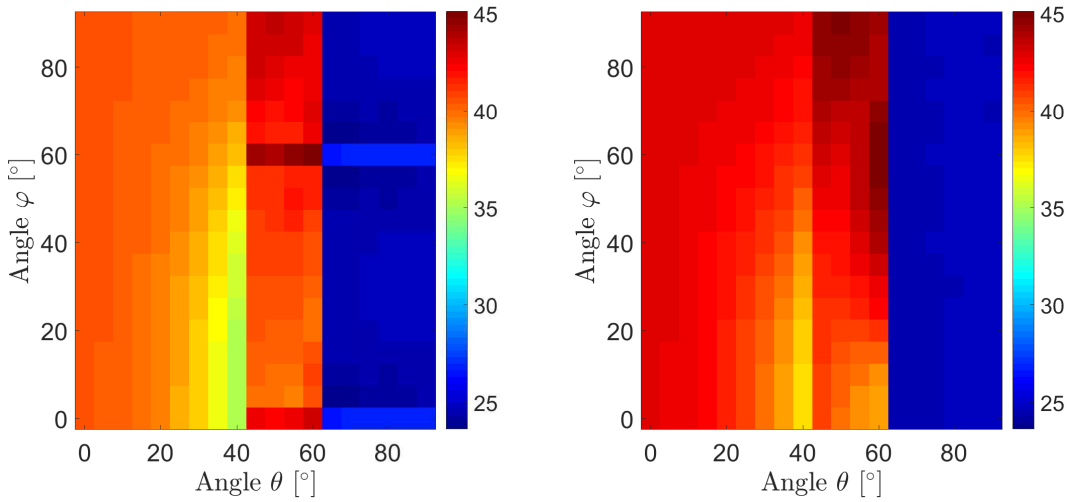

(a) Truncated faceted cone

(b) Truncated cone

Figure 3.82: Emission and reception directivity patterns of the 3D conformal arrays

3.4.8.3 Comparison with the planar mechanically steered array

The directivity of the planar array is estimated to be 25dB (section 3.3.3.3) which gives a directivity product emission and reception of 50dB since the same antenna is used. The mechanically steered antenna array radiates the same energy irrespective of the target direction. It is the directivity that should be reached for the new antenna.

In emission, the TOP can steer the beam up to 60° in elevation. A simple sum is carried out in dB to reach the results shown in Figure 3.82. The truncated faceted cone and the truncated cone are compared, however the half-sphere array is not accounted here since the emission and reception specifications are not applicable.

As a result, up to an elevation steering of 60°, the minimum directivity found is 35dB in the direction $\theta = 40°, \varphi = 0°$ for the truncated faceted cone. The performance are not as good as for the planar mechanically steered case. Performance could be enhanced by use of a higher steering angle. The coverage increase mitigates the lower directivity.

3.4.9 Synthesis of the 3D conformal array study

A synthesis of the 3D conformal arrays study is proposed in Figure 3.83

3.4 Polarisation Analysis of 3D Conformal Arrays

3.4.1 3D Conformal array topologies

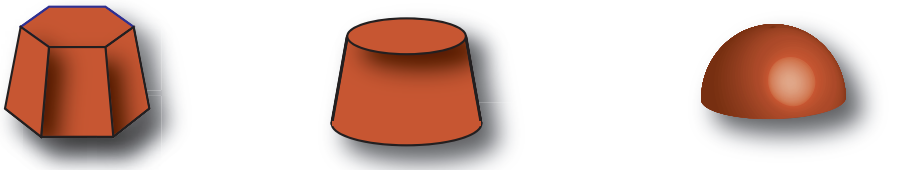

Faceted | 1 degree of curvature | 2 degrees of curvature

The antenna arrays performance will demonstrate whether it is worth to increase the manufacturing complexity

3.4.2 Study of the lateral facets of the truncated faceted cone

A beamsteering angle limit increase from 30deg to 60deg increases the minimum directivity by 1.3dB

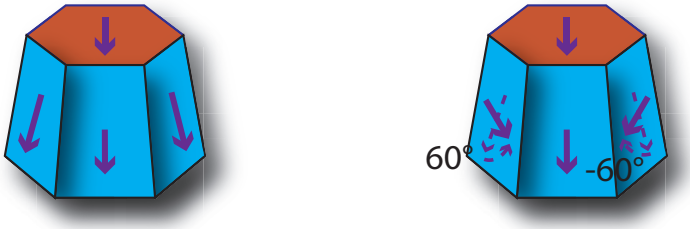

Polarisation purity and ellipticity remain much higher when the lateral elements remain vertical

3.4.3 Polarisation study of the TOP facet and the lateral facet 1

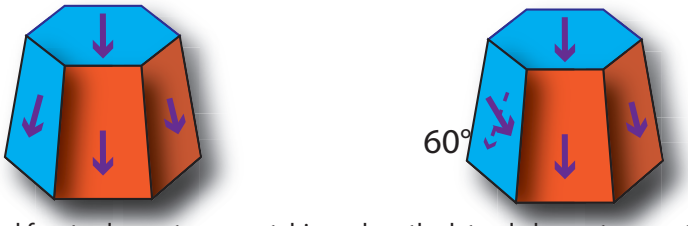

TOP and lateral facets elements are matching when the lateral elements are rotated.
A gain increase in directivity and polarisation purity have been measured as well as an ellipticity decrease.

3.4.4 Study of the truncated cone

A study with a planar array and a curved array has shown that the faceted array performs better, despite a lower number of elements, in terms of directivity, ellipticity, polarisation purity and sidelobes.

Using different section of the lateral face of the truncated cone: 60deg, 120deg and 360deg, it has been shown that an optimal section size offers a better directivity and sidelobe level. This size is close to 120deg.

3.4.6 Comparison between the planar array and the half-sphere array

A half-sphere covered of elements performs worse for low elevation angles (<30deg) but better for high elevation angles (>30deg) than a planar array with the same radius.

3.4.8 Global comparison of the 3D conformal arrays and the planar array

The half-sphere presents an almost constant directivity over its field of view. Similar directivity performance for the 3 arrays suggest that increasing the manufacturing complexity is not worth.
The study of the directivity in emission and reception has shown that the truncated faceted cone and the faceted cone do not reach the 50dB of the mechanically steered planar array. Up to 60deg of elevation, the arrays present an average directivity of 40dB.

Figure 3.83: Synthesis of the 3D conformal array study

3.5 Conclusion

A progressive and methodical study has been carried out to investigate the potential of 3D conformal arrays for RF-seekers. No comparable work could be found by the author in the literature search.

The study starts by considering planar arrays; in order to understand the effect of the position and orientation of the radiating elements on the directivity, polarisation and ellipticity.

- A circular array with a square mesh offers azimuth invariant sidelobes.
- The radial or tangent radiating elements orientations can respectively produce an anti-radial or anti-tangent orientation using 180° phase. These can be an alternative to the use of an axially oriented top array since they offer an azimuth invariant difference pattern.
- The polarisation analysis has demonstrated the low purity of the anti-tangent or anti-radial patterns which may therefore give on advantage to the axial configuration. However, as the beam is steered, this advantage fades since the polarisation purity decreases in both cases.
- The choice of the polarisation definition alters the polarisation purity. Hence, being able to switch from one coordinate system to another could result in a high purity over the steering angle which could alleviate the previous point.
- The anti-symmetry among the elements orientation can be a source of polarisation state deviation. Conversely, the beamsteering produces a linear polarisation state by aligning the elements wavefronts in the main beam region.

The study of planar arrays has the double benefit of facilitating the understanding of the position and orientation of the elements on the electric field and also to allow for the study of faceted arrays.

The mechanical system removal offers space for the design of a 3D conformal antenna. Some conclusions are given below.

- As expected, using more elements increases the global directivity. A directivity increase of 1.3dB is found after increasing the steering limit from 30° to 60°.
- If the TOP array and the lateral one are used coherently together to process the echo signal, the benefit of matching the TOP and lateral elements has been shown. It produces an increase in directivity and polarisation purity and a decrease in ellipticity.

- In that regard, if the anti-radial orientation is used for the TOP array, the matching orientation of the lateral elements is tangential and $-Z$-oriented. This, in the same time, maintains a high polarisation purity for the lateral facets.

- Despite the larger number of elements that can offer the truncated cone with one degree of curvature, the faceted array presents better performance, as a function of the elevation steering in terms of directivity, ellipticity, polarisation purity and sidelobes.

- The truncated cone that presents a revolution symmetry has a specific number of elements that should be active so that the directivity and the sidelobe level may be optimised. An active section of about 120° is recommended.

- The half-sphere with two degrees of curvature has also been studied and compared to the planar array. If a planar array is conformed on a half-sphere array with the same diameter, where a constant distance is kept between the elements (the half-sphere would be partially covered), the planar array has better performance than the conformed array. However if the half-sphere is entirely covered, as it can host many more elements, for a high steering angle, it offers a better directivity. This enhanced directivity is mitigated by an increased polarisation deviation in the θ_{-3dB} area.

- Without beamsteering, it has been shown with a slot antenna simulated on HFSS that, as the degree of conformation increases, the directivity decreases, along with the beamwidth. On the other hand, the polarisation remains linear in the θ_{-3dB} area.

- Finally a global comparison has shown that the truncated faceted cone and the truncated cone both present similar levels of performance. The half-sphere also presents comparable results, except for elevation steering angles above 70° where it performs lower. The half-sphere directivity has the smallest variations as a function of the steering angle.

- The truncated faceted cone and the truncated cone arrays have an average reception/emission directivity product of 40dB, for an elevation steering angle between 0° and 60°. Then, the minimum directivity is 25dB up to 90°. It does not reach the 50dB of the mechanically steered array. This is partially due to the choice of an anti-radial arrangement for the TOP facet.

Chapter 4 Direction of arrival techniques for 3D and conformal arrays

Once launched towards a target, the missile needs to update its trajectory. The RF-seeker system embedded below the missile radome calculates the new angular positions of the target so that the missile can be steered accordingly. Various perturbations alter the signal sent towards the target as explained in section 1.1.3. For this reason, the amount of information extracted at each scan should be maximised. Chapter 3 focused on the study of the beam and how its performance in directivity and polarisation can be enhanced to maximise signal to noise ratio and detection performance. Chapter 4 focuses on the estimation of the target position in angle. Suitable direction of arrival estimation technique for 3D and conformal antennas are investigated as well as the design of the antenna in order to minimise the estimation error.

The objectives of this chapter are:

- Developing models to evaluate the array estimation performance.
- Assess whether 3D conformal antennas can improve the direction of arrival estimation.
- Study how the classic phase monopulse can be adapted to 3D conformal antennas, and determine the suitable monopulse quadrants for a steep monopulse slope.

In this study, the signal is studied after the Low Noise Amplifier (LNA), filter, mixer and matched filter, as shown in Figure 4.1. The signal is considered complex and in baseband.

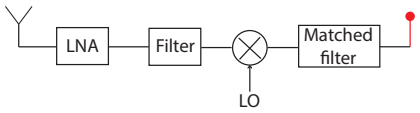

Figure 4.1: The reception chain

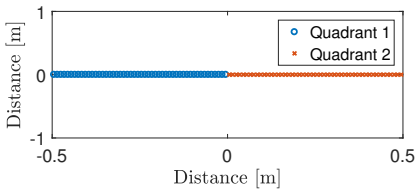

(a) Array quadrants, 50 elements each

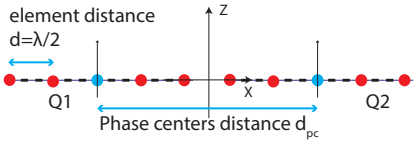

(b) Detail of the array quadrant

Figure 4.2: The omnidirectional antenna element linear array

4.1 Comparison of the CRLB, ML and monopulse estimators for a 1D array

The Maximum Likelihood (ML) estimator, the phase monopulse estimator and their theoretical bound are derived for a theoretical example consisting of a linear array with omnidirectional elements to identify the strengths and weaknesses of each.

4.1.1 Scenario

Let us consider a radar operating at a carrier frequency of $f_0 = 15$GHz or a wavelength of $\lambda = \frac{c}{f_0} = 0.02$m. The linear array consists of $N = 100$ omnidirectional elements spaced of $d = \frac{\lambda}{2} = 0.01$m. The total length of the 1D array is 1m and the geometry is as shown in Figure 4.2a. To process the phase estimation the array is divided into two quadrants of 50 elements each. The quadrants are arranged symmetrically and regularly around the vertical axis, as shown in Figure 4.2b.

The different target positions are as shown in Figure 2.32. The target is located at constant distance and for different angles from $\theta = -90°$ to $\theta = 90°$. The target is considered fixed. The simulations assume that the target is an ideal point reflector, and hence neither glints are accounted nor scintillations. It is assumed that there are neither jammer nor correlated noise from the local oscillator, hence noise remains uncorrelated.

The simulations are carried out in the complex domain. Each element receives a complex signal, as shown in equation 4.1.

$$s_n = Ae^{-j2\pi f_0 t_n} + w_I(0,\sigma^2) + jw_Q(0,\sigma^2) \tag{4.1}$$

Where A is the element amplitude, f_0 is the carrier frequency and t_n is the time delay from the target to the n-th element. The two components w_I and w_Q of the noise are as defined in section 2.4.1.

4.1.2 Definition of the Signal to Noise Ratio SNR

The performance can be assessed as a function of the array signal to noise ratio SNR_{Ar} of the sum channel or the element signal to noise ratio SNR_{elem}. Their expressions are given in equation 4.2 and 4.3 for a planar array of omnidirectional elements.

$$\begin{aligned} SNR_{Ar} &= \frac{\|S\|^2}{\|N\|^2} = \frac{\left\|A\sum_n e^{-j2\pi f_0 t_n}\right\|^2}{E\{\|\sum_n w_I(0,\sigma^2) + jw_Q(0,\sigma^2)\|^2\}} = \frac{\left\|A\sum_n e^{-j2\pi f_0 t_n}\right\|^2}{2N\sigma^2} \\ &= A^2\frac{\|AF\|^2}{2N\sigma^2} \end{aligned} \tag{4.2}$$

Where $E\{\}$ is the expectation and where AF is the array factor. It depends on the array factor, consequently it depends on the target angle as well.

$$SNR_{elem} = \frac{A^2}{2\sigma^2} \tag{4.3}$$

The relation between the array signal to noise ratio SNR_{Ar} of a linear array of N elements and the element signal to noise ratio SNR_{elem} is given in equation 4.4.

$$SNR_{AR} = \frac{\|AF\|^2}{N} SNR_{elem} \tag{4.4}$$

If the array is not planar, the array factor may not be calculated in a closed form and the SNR can be expressed as a function of the total antenna gain G, the free space impedance Z_0, the feeding antenna power P_{in} and the distance antenna phase centre to target r, as shown in equation 4.5.

$$SNR_{Ar} = \frac{\|S\|^2}{2N\sigma^2} = \frac{GZ_0P_{in}}{2\pi r^2}\frac{1}{2N\sigma^2} \tag{4.5}$$

4.1.3 Phase monopulse

4.1.3.1 The phase monopulse patterns

The phase monopulse estimator consists in calculating the imaginary part of the ratio of the sum over the difference of the signals received by the two quadrants, as

$$\mathrm{Im}\left(\frac{\Delta}{\Sigma}\right) = \mathrm{Im}\left(\frac{s_{Q1} - s_{Q2}}{s_{Q1} + s_{Q2}}\right) \tag{4.6}$$

Where s_{Q1} and s_{Q2} are the signals received by the first and second quadrant, respectively, as illustrated in Figure 4.2. The signal received by each quadrant expressed in its own coordinate system is $s_Q = Ae^{-j2\pi f_0 t_0} \sum_{n=\frac{-N}{4}}^{\frac{N}{4}-1} e^{-jn\phi_e}$, where A is the amplitude, ϕ_e is the phase shift between two consecutive elements, $N/2$ is the number of element of each quadrant and t_0 is the delay from target to phase centre. Each quadrant is modelled as a phase centre receiving a delayed version of the echo signal s. Now carrying out sum $s_1 + s_2$ and difference $s_1 - s_2$, a phase ϕ_{pc} is applied to the received signal to take into account the distance between the two quadrant phase centres d_{pc}.

$$\begin{aligned}
s_{Q1} + s_{Q2} &= s_Q + s_Q e^{-j\phi_{pc}} = se^{-j\frac{\phi_{pc}}{2}}\left(e^{j\frac{\phi_{pc}}{2}} + e^{-j\frac{\phi_{pc}}{2}}\right) = 2se^{-j\frac{\phi_{pc}}{2}}\cos\frac{\phi_{pc}}{2} \\
s_{Q1} - s_{Q2} &= 2se^{-j\frac{\phi_{pc}}{2}}\sin\frac{\phi_{pc}}{2} \\
\frac{s_{Q1} - s_{Q2}}{s_{Q1} + s_{Q2}} &= j\tan\frac{\phi_{pc}}{2} = j\tan\frac{\pi}{\lambda}d_{pc}\sin\theta
\end{aligned} \tag{4.7}$$

These calculations are based on the assumption that the pattern of the two quadrants are identical which allows to remove the quadrant patterns variable s from the ratio. The results show that, under this assumption, the monopulse ratio does not depend on the number of elements or the shape of the array. It also does not depend on the amplitude of the quadrants or the type of element by generalising, the amplitude would be a function of the angle A_θ. Although the antenna design of each quadrant has a significant effect on the overall coverage, the gain and therefore the SNR which impacts the probabilities of detection and false alarm, the noise free monopulse ratio only depends on the distance between the phase centres of the two quadrants. This result is essential for the study of the phase monopulse in 2D or 3D. The global monopulse slope is $\frac{\pi d_{pc}}{\lambda}$, hence the higher d_{pc}, the steepest the slope.

Figure 4.3a and Figure 4.3b illustrate respectively the sum, difference patterns and the imaginary part of the ratio using the scenario previously described. The resultant ratio is periodic due to the periodicity of the phase ϕ_{pc} and tangent function. It yields to an ambiguity beyond a certain angle. The range without ambiguity can be calculated by finding the first asymptote angle: $2\theta_{asympt} = 2\arcsin\frac{\lambda}{2d_{pc}} = 2.29°$. This calculation

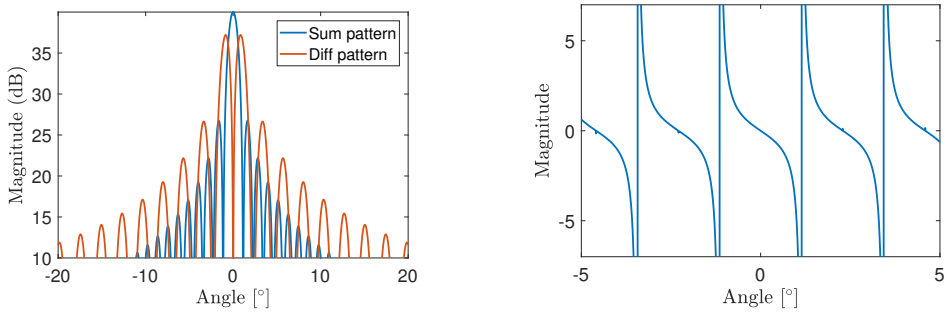

(a) Sum and difference monopulse patterns

(b) Imaginary monopulse pattern

Figure 4.3: 2D and 3D ellipticity patterns of the anti tangent circular array

is based on the result from the equation 4.7. The higher d_{pc}, the higher the ambiguity produced.

A compromise exists between the monopulse slope factor and the angular range without ambiguity.

The period of the phase monopulse estimator is the same as that of the sum array, as shown in equation 3.28. The periodicity of the estimator limits the estimation to a certain range but in reality outside this range the antenna cannot receive the signal where the antenna gain is small or the signal can be received in the side lobe region which would produce an estimation error. Consequently the signal can only be received in the region of the main beam.

To assess the estimation performance of the phase monopulse estimator, uncorrelated complex white Gaussian noise is added to the signals received at both quadrants. The noise variance at each element is $2\sigma^2$. The signal angle of arrival is estimated using $\hat{\theta} = \arcsin \frac{\phi_{pc}\lambda}{2\pi d}$. The resulting angle $\hat{\theta}$ is calculating after estimating the phase ϕ_{pc}. 10000 Monte-Carlo simulations are carried out for each SNR value to have a steady Root Mean Square Error (RMSE) of the estimator. The calculations are relative to one pulse and results are presented in section 4.1.3.3 where they are compared to the Kanter model.

4.1.3.2 Phase monopulse estimation model

A model is provided by Dr. Kanter [Kanter, 1977] to formulate the expression of the bias and the RMSE of the amplitude monopulse. Below, the bias is given and the derivation of the RMSE of the phase monopulse is carried out. The bias model is valid for any SNR whereas for the RMSE, it only works at high SNR. One of the characteristic of the model for the RMSE is the use of the monopulse slope.

Bias model

The complex monopulse ratio error ϵ_c and the phase monopulse error ϵ_{Im} are defined as given in equation 4.8.

$$\begin{aligned} \epsilon_c &= \frac{\Delta'}{\Sigma'} - \frac{\Delta}{\Sigma} \\ \epsilon_{Im} &= \mathrm{Im}\left(\frac{\Delta'}{\Sigma'} - \frac{\Delta}{\Sigma}\right) \end{aligned} \tag{4.8}$$

Where $\frac{\Delta}{\Sigma}$ is the noise free monopulse ratio and $\frac{\Delta'}{\Sigma'}$ is the ratio in the presence of noise.

The model for the bias of the phase monopulse is valid for any SNR_{Ar}. The only assumption here is the need for uncorrelated noise between the sum and difference channels. The expression of the bias is [Kanter, 1977]

$$E\{\epsilon_{Im}\} = E\left\{\mathrm{Im}\left(\frac{\Delta'}{\Sigma'} - \frac{\Delta}{\Sigma}\right)\right\} = -\mathrm{Im}\left(\frac{\Delta}{\Sigma}\right) e^{-SNR_{Ar}} \tag{4.9}$$

The equation shows that the mean value of the error is not zero when SNR_{Ar} is small, the phase monopulse estimator is therefore biased. When SNR_{Ar} is large the equation is such that $E\left\{\mathrm{Im}\left(\frac{\Delta'}{\Sigma'}\right)\right\} = \mathrm{Im}\left\{\frac{\Delta}{\Sigma}\right\}$ and the estimator is unbiased.

RMSE model

The monopulse error model is given in equation 4.10.

$$\begin{aligned} \epsilon_c &= \frac{\Delta'}{\Sigma'} - \frac{\Delta}{\Sigma} = \frac{\Delta + n_\Delta}{\Sigma + n_\Sigma} - \frac{\Delta}{\Sigma} = \frac{\Delta}{\Sigma + n_\Sigma} + \frac{n_\Delta}{\Sigma + n_\Sigma} - \frac{\Delta}{\Sigma} \\ &= \frac{n_\Delta}{\Sigma + n_\Sigma} + \frac{\Delta\Sigma - \Delta\Sigma - \Delta n_\Sigma}{(\Sigma + n_\Sigma)\Sigma} = \frac{n_\Delta}{\Sigma + n_\Sigma} - \frac{\Delta n_\Sigma}{(\Sigma + n_\Sigma)\Sigma} = \frac{n_\Delta - \frac{\Delta}{\Sigma} n_\Sigma}{\Sigma + n_\Sigma} = \frac{\frac{n_\Delta}{\Sigma} - \frac{\Delta}{\Sigma}\frac{n_\Sigma}{\Sigma}}{1 + \frac{n_\Sigma}{\Sigma}} \end{aligned} \tag{4.10}$$

Where n_Δ is the noise of the difference channel and n_Σ is the noise of the sum channel.

If $SNR_{Ar} >> 1$ and because the sum channel noise has zero mean, it gives $\frac{n_\Sigma}{\Sigma} << 1$ and the equation reduces to

$$\epsilon_c = \frac{n_\Delta}{\Sigma} - \frac{\Delta}{\Sigma}\frac{n_\Sigma}{\Sigma} \tag{4.11}$$

Now the MSE (Mean Square Error) is calculated by taking the imaginary part and the expectation of the square of the error ϵ_I^2.

$$\begin{aligned} E\left\{\epsilon_{Im}^2\right\} &= E\left\{\mathrm{Im}\left(\frac{n_\Delta}{\Sigma} - \frac{\Delta}{\Sigma}\frac{n_\Sigma}{\Sigma}\right)^2\right\} \\ &= E\left\{\mathrm{Im}\left(\frac{n_\Delta}{\Sigma}\right)^2 + \mathrm{Im}\left(\frac{\Delta}{\Sigma}\frac{n_\Sigma}{\Sigma}\right)^2 - 2\mathrm{Im}\left(\frac{n_\Delta}{\Sigma}\right)\mathrm{Im}\left(\frac{\Delta}{\Sigma}\frac{n_\Sigma}{\Sigma}\right)\right\} \end{aligned}$$

The third term can be developed:

$$2\mathrm{Im}\left(Z_1\right)\mathrm{Im}\left(Z_2\right) = \mathrm{Re}\left(Z_1 Z_2^*\right) - \mathrm{Re}\left(Z_1 Z_2\right)$$

$$2\mathrm{Im}\left(\frac{n_\Delta}{\Sigma}\right)\mathrm{Im}\left(\frac{\Delta}{\Sigma}\frac{n_\Sigma}{\Sigma}\right) = \mathrm{Re}\left(\frac{n_\Delta}{\Sigma}\frac{\Delta^*}{\Sigma^*}\frac{n_\Sigma^*}{\Sigma^*}\right) - \mathrm{Re}\left(\frac{n_\Delta}{\Sigma}\frac{\Delta}{\Sigma}\frac{n_\Sigma}{\Sigma}\right)$$

The resolution of this term does not contribute to the sum as $E\left\{\mathrm{Re}\left(n_\Sigma^* n_\Delta\right)\right\} = 0$ and $E\left\{\mathrm{Re}\left(n_\Sigma n_\Delta\right)\right\} = 0$. The MSE is then:

$$E\left\{\epsilon_{Im}^2\right\} = E\left\{\mathrm{Im}\left(\frac{n_\Delta}{\Sigma}\right)^2 + \mathrm{Im}\left(\frac{\Delta}{\Sigma}\frac{n_\Sigma}{\Sigma}\right)^2\right\} \tag{4.12}$$

The first term is developed here:

$$\begin{aligned} \mathrm{Im}\left(\frac{n_\Delta}{\Sigma}\right) = \mathrm{Im}\left(\frac{n_\Delta \Sigma^*}{\|\Sigma\|^2}\right) &= \frac{n_\Delta \Sigma^* - n_\Delta^* \Sigma}{2j\|\Sigma\|^2} \\ &= \frac{\left(n_{\Delta I} + jn_{\Delta Q}\right)\Sigma^* - \left(n_{\Delta I} - jn_{\Delta Q}\right)\Sigma}{2j\|\Sigma\|^2} \\ &= \frac{n_{\Delta I}\Sigma^* + jn_{\Delta Q}\Sigma^* - n_{\Delta I}\Sigma + jn_{\Delta Q}\Sigma}{2j\|\Sigma\|^2} \end{aligned} \tag{4.13}$$

Let us first calculate the square product of the numerator and then the cross product.

$$\begin{aligned} Num_1^2 &= \left(n_{\Delta I}\Sigma^*\right)^2 + \left(n_{\Delta I}\Sigma\right)^2 - \left(n_{\Delta Q}\Sigma^*\right)^2 - \left(n_{\Delta Q}\Sigma^*\right)^2 \\ E\left\{Num_1^2\right\} &= \sigma^2\left(\Sigma^*\right)^2 + \sigma^2\left(\Sigma\right)^2 - \sigma^2\left(\Sigma^*\right)^2 - \sigma^2\left(\Sigma\right)^2 \\ &= 0 \\ Num_2^2 &= 2jn_{\Delta I}n_{\Delta Q}(\Sigma^*)^2 - 2n_{\Delta I}^2\Sigma^*\Sigma + 2jn_{\Delta I}n_{\Delta Q}\Sigma^*\Sigma \\ &\quad - 2jn_{\Delta I}n_{\Delta Q}\Sigma^*\Sigma - 2n_{\Delta Q}^2\Sigma^*\Sigma - 2jn_{\Delta I}n_{\Delta Q}\Sigma^2 \\ E\{Num_2^2\} &= E\{-2n_{\Delta I}^2\Sigma^*\Sigma - 2n_{\Delta Q}^2\Sigma^*\Sigma\} \\ &= -4\sigma_\Delta^2\|\Sigma\|^2 \end{aligned}$$

Finally, this reduces to:

$$E\left\{\mathrm{Im}\left(\frac{n_\Delta}{\Sigma}\right)^2\right\} = \frac{-4\sigma_\Delta^2 \|\Sigma\|^{2\,2}}{(2j\|\Sigma\|^2)^2} = \frac{\sigma_\Delta^2}{\|\Sigma\|^2} \tag{4.14}$$

The same is accomplished with the second term in equation 4.12.

$$E\left\{\mathrm{Im}\left(\frac{\Delta}{\Sigma}\frac{n_\Sigma}{\Sigma}\right)^2\right\} = \frac{-4\sigma_\Sigma^2 \|\Sigma\|^2}{\left(2j\|\Sigma\|^2\right)^2} = \frac{\sigma_\Sigma^2}{\|\Sigma\|^2}\left\|\frac{\Delta}{\Sigma}\right\|^2 \tag{4.15}$$

Finally, using the results of equations 4.14 and 4.15, the variance of the error becomes:

$$E\left\{\epsilon_{Im}^2\right\} = \frac{\sigma_\Delta^2}{\|\Sigma\|^2} + \frac{\sigma_\Sigma^2}{\|\Sigma\|^2}\left\|\frac{\Delta}{\Sigma}\right\|^2$$

It is assumed that the noise power received in each channel is the same $\sigma_\Sigma = \sigma_\Delta = \sigma$

$$\begin{aligned} E\left\{\epsilon_{Im}^2\right\} &= \frac{1}{\frac{\|\Sigma\|^2}{\sigma^2}}\left(1 + \left\|\frac{\Delta}{\Sigma}\right\|^2\right) \\ &= \frac{1}{2SNR_{Ar}}\left(1 + \left\|\frac{\Delta}{\Sigma}\right\|^2\right) \end{aligned} \tag{4.16}$$

From this expression, the standard deviation of the error can be calculated

$$\sigma_{\frac{\Delta}{\Sigma}} = \frac{1}{\sqrt{2SNR_{Ar}}}\left(1 + \left\|\frac{\Delta}{\Sigma}\right\|^2\right)^{\frac{1}{2}} \tag{4.17}$$

From there, to reach the standard deviation of the angle, the monopulse slope is used $\mathrm{Im}\left(\frac{\Delta}{\Sigma}\right) = k_m \frac{\theta}{\theta_{bw}}$. It introduces the approximation that the target is close from boresight.

$$\boxed{\sigma_{\hat{\theta}} = \frac{\theta_{bw}}{k_m\sqrt{2SNR_{Ar}}}\left(1 + \left(k_m\frac{\theta}{\theta_{bw}}\right)^2\right)^{\frac{1}{2}}} \tag{4.18}$$

Where θ_{bw} is the bandwidth of the total array and k_m is the normalised monopulse slope such as $k_m = \mathrm{Im}\left(\frac{\partial\frac{\Delta}{\Sigma}}{\partial\theta}\right)\cdot\theta_{bw}\Big|_{\theta=0}$. The approximations and conditions that lead to this result are given here:

- Target is a point (no glint nor scintillation).
- No error when the processor takes the imaginary part.

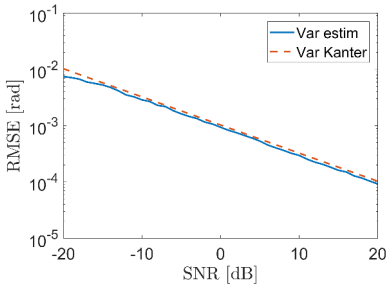

(a) Estimator versus RMSE model , target angle 0.25°

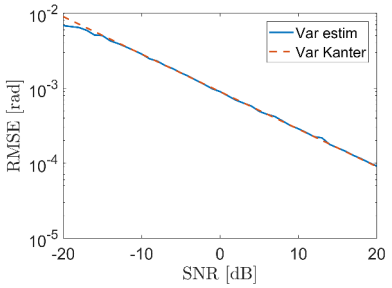

(b) Estimator versus RMSE model, target angle 0°

Figure 4.4: Comparison between the phase monopulse estimator and its model

- Noise from sum and difference channels are independent and with equal power
- Neither jammer nor local oscillator leading to any correlated noise
- Target is close to bore sight, where the linear approximation produces a very small error.
- The noise is only thermal, coming from the receiver. This noise is white and Gaussian.

The expression can be simplified further by assuming that the target is really close to the antenna boresight such as $\left(k_m \frac{\theta}{\theta_{bw}}\right)^2 << 1$, the Woodward law [Woodward, 1953], as shown in equation 4.19.

$$\sigma_{\hat{\theta}} = \frac{\theta_{bw}}{k_m \sqrt{2SNR_{Ar}}} \tag{4.19}$$

This model gives a closed form expression for the phase monopulse performance in term of RMSE for any array. The model for the RMSE of the phase monopulse is a contribution as Kanter was only giving the result for the amplitude monopulse. This model has been calculated using the monopulse slope approximation.

4.1.3.3 Comparison between the phase monopulse estimator and its model

Results are computed with a target located at a distance of 10 km and at an angle of $\theta = 0°$ and $\theta = 0.25°$ so that it remains within the bijective range of the monopulse ratio and it also remains close to the antenna array bore sight. Results are shown in Figure 4.4.

A slight shift of 0.1dB can be observed when the target is at $\theta = 0.25°$ which does not exist when the target is at $\theta = 0°$. It is due to the monopulse slope approximation in the model. Hence the closer to the boresight, the smaller this error.

For low values of the SNR, around -20dB, the RMSE of the phase monopulse separates from the model. This effect is more obvious in Figure 4.6 due to the scale. The RMSE of the phase monopulse flattens since the values of the estimator are sought within a specific window. This window corresponds to the range without ambiguity. Therefore as the SNR decreases, the noise increases but the estimator values are limited, as a result the RMSE separates from the model.

4.1.4 Cramer-Rao lower Bound (CRLB)

4.1.4.1 Deterministic unknown angle and known amplitude and phase

The CRLB provides the theoretical minimum variance of any unbiased estimator; it is derived here from equation 4.1. The signal model as a function of the parameter θ is shown in equation 4.20.

This expression emphasises the physical phenomenon that allows the array to sense the direction of the signal. It comes from the phase shift from one element to the other, this phase shift being proportional to the sinus of the angle.

$$s_n = Ae^{-j(2\pi f_0(t_0-\frac{d}{c}n\sin(\theta)))} + w_I + jw_Q \tag{4.20}$$

The CRLB expression is derived from the noise PDF. To calculate the PDF the signal is split into its real and imaginary parts: $s_n = x_n + jy_n$. The PDF expression of the signal embedded in noise is given in equation 4.21.

$$p(x,y;\theta) = \frac{1}{(2\pi\sigma^2)^N} e^{-\frac{1}{2\sigma^2}\sum_n (x_n - A\cos\left(2\pi f_0(t_0-\frac{d}{c}n\sin\theta)\right))^2 + (y_n + A\sin\left(2\pi f_0(t_0-\frac{d}{c}n\sin\theta)\right))^2} \tag{4.21}$$

The CRLB and the estimator presented later in this report are used to estimate the direction of a signal. In reality, noise not only affects the angle but also the phase $2\pi f_0 t_0$ and amplitude A. Here we assume that phase and amplitude are known in order to simplify the calculations. The effect of using such a hypothesis is a better CRLB performance.

Using equation 2.8 and $s_I(n;\theta) = A\cos\left(2\pi f_0(t_0 - \frac{d}{c}n\sin\theta)\right)$ and $s_Q(n;\theta) = -A\sin\left(2\pi f_0(t_0 - \frac{d}{c}n\sin\theta)\right)$:

$$var(\hat{\theta}) \geq \frac{6\sigma^2}{4\pi^2 A^2 N(N-1)(2N-1)} \frac{\lambda^2}{d^2\cos(\theta)^2} \tag{4.22}$$

$$\geq \frac{3}{4\pi^2 SNR_{elem} \times N(N-1)(2N-1)} \frac{\lambda^2}{d^2\cos(\theta)^2} \tag{4.23}$$

Figure 4.5: CRLB scheme principle

The CRLB strongly depends on the number of array elements; it is inversely proportional to N^3. The more elements the lower the variance. The least variance is obtained when the target is on bore sight at 0° as it maximises the term $\cos\theta$ at the denominator. The term $4\pi\left(\frac{d\cos\theta}{\lambda}\right)^2$ can also be related to the theoretical antenna gain taken from its projected surface in a given direction $G = \frac{4\pi A_{eq}^2}{\lambda^2}$, with A_{eq} the equivalent surface. Thus the variance is inversely proportional to the gain, being better when the target is close to boresight. This equation allows us to make a link between the detection (gain and SNR) and estimation (variance) performance of the antenna. It also depends on the ratio $\frac{\lambda}{d}$ which is required to be small. The CRLB is independent of t_0 which means that the minimum variance does not depend on the reference element from which the phase is calculated.

As a result, the CRLB takes as input the array parameters and provides the minimum error for this given configuration in all directions.

4.1.4.2 Deterministic unknown angle and deterministic unknown amplitude and phase

The effect of deterministic unknown amplitude A and phase ϕ on the lower bound is investigated. To simplify the calculations, the model is slightly modified, as shown in equation 4.24.

$$s_n = Ae^{j(2\pi\frac{d}{\lambda}n\sin\theta+\phi)} + w_I + jw_Q \tag{4.24}$$

By generalising the results from equation 2.8, the new Fisher information matrix is:

$$FIM = \begin{bmatrix} FIM_{\theta\theta} & FIM_{\theta\phi} & FIM_{\theta A} \\ FIM_{\theta\phi} & FIM_{\phi\phi} & FIM_{\phi A} \\ FIM_{\theta A} & FIM_{\phi A} & FIM_{AA} \end{bmatrix} = \frac{1}{\sigma^2}\cdot$$
$$\begin{bmatrix} \sum_n \left[\left(\frac{\partial s_I}{\partial \theta}\right)^2 + \left(\frac{\partial s_Q}{\partial \theta}\right)^2 \right] & \sum_n \left[\left(\frac{\partial s_I}{\partial \phi}\frac{\partial s_I}{\partial \theta}\right) + \left(\frac{\partial s_Q}{\partial \phi}\frac{\partial s_Q}{\partial \theta}\right) \right] & \sum_n \left[\left(\frac{\partial s_I}{\partial A}\frac{\partial s_I}{\partial \theta}\right) + \left(\frac{\partial s_Q}{\partial A}\frac{\partial s_Q}{\partial \theta}\right) \right] \\ \sum_n \left[\left(\frac{\partial s_I}{\partial \phi}\frac{\partial s_I}{\partial \theta}\right) + \left(\frac{\partial s_Q}{\partial \phi}\frac{\partial s_Q}{\partial \theta}\right) \right] & \sum_n \left[\left(\frac{\partial s_I}{\partial \phi}\right)^2 + \left(\frac{\partial s_Q}{\partial \phi}\right)^2 \right] & \sum_n \left[\left(\frac{\partial s_I}{\partial \phi}\frac{\partial s_I}{\partial A}\right) + \left(\frac{\partial s_Q}{\partial \phi}\frac{\partial s_Q}{\partial A}\right) \right] \\ \sum_n \left[\left(\frac{\partial s_I}{\partial A}\frac{\partial s_I}{\partial \theta}\right) + \left(\frac{\partial s_Q}{\partial A}\frac{\partial s_Q}{\partial \theta}\right) \right] & \sum_n \left[\left(\frac{\partial s_I}{\partial \phi}\frac{\partial s_I}{\partial A}\right) + \left(\frac{\partial s_Q}{\partial \phi}\frac{\partial s_Q}{\partial A}\right) \right] & \sum_n \left[\left(\frac{\partial s_I}{\partial A}\right)^2 + \left(\frac{\partial s_Q}{\partial A}\right)^2 \right] \end{bmatrix} \tag{4.25}$$

Using $s_I = \cos\left(2\pi\frac{d}{\lambda}n\sin\theta + \phi\right)$ and $s_Q = \sin\left(2\pi\frac{d}{\lambda}n\sin\theta + \phi\right)$, the results of the FIM is:

$$FIM = \frac{1}{\sigma^2}\begin{bmatrix} \left(A2\pi\frac{d}{\lambda}\cos\theta\right)^2 \frac{N}{6}(N-1)(2N-1) & A^2 2\pi\frac{d}{\lambda}\cos\theta\frac{N}{2}(N-1) & 0 \\ A^2 2\pi\frac{d}{\lambda}\cos\theta\frac{N}{2}(N-1) & A^2(N-1) & 0 \\ 0 & 0 & N-1 \end{bmatrix} \tag{4.26}$$

The matrix is diagonal by square. The determinant of the 2×2 matrix is:

$$\mid FIM \mid = \frac{1}{\sigma^4}A^4\left(2\pi\frac{d}{\lambda}\cos\theta\right)^2\frac{N}{6}(N-1)^2(2N-1) \tag{4.27}$$

The minimum variance is therefore:

$$\begin{aligned} CRLB_{\theta\theta} &= \frac{12\sigma^2}{A^2\left(2\pi\frac{d}{\lambda}\cos\theta\right)^2 N(N-1)(N-2)} \\ CRLB_{\phi\phi} &= \frac{\sigma^2(2N-1)}{A^2(N-1)(\frac{N}{2}-1)} \\ CRLB_{AA} &= \frac{\sigma^2}{N-1} \end{aligned} \tag{4.28}$$

The minimum variance increases as the number of unknowns increases. In this case, if the expressions of the $CRLB_{\theta\theta}$ in equation 4.28 is compared to that of the previous section in equation 4.22 and if they are both approximated for high values of N, then the minimum variance for the angle θ is 4 times higher. When amplitude and phase are unknown, the lower bound increases by $\log_{10}(4) = 0.6$dB.

The minimum variance of the different unkowns do not depend on the phase ϕ. Furthermore, the minimum variance of A do not also depend on θ.

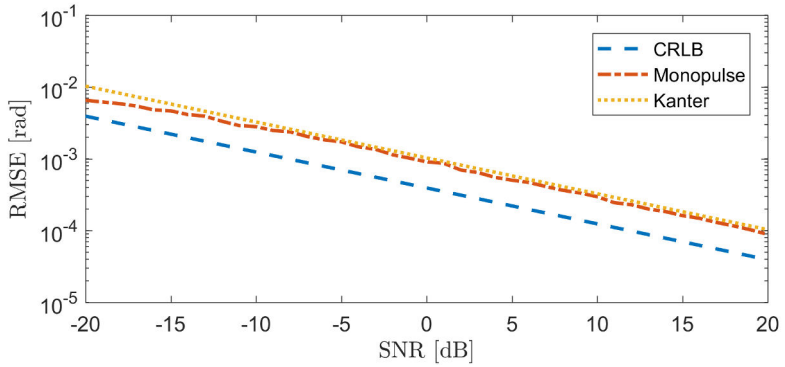

Figure 4.6: CRLB versus the phase monopulse estimator and its model

4.1.4.3 Comparison with the phase estimator

To carry out this comparison, simulations are carried out for $N = 100$ elements and a distance of $\frac{\lambda}{2}$ between two consecutive elements at the frequency $f_0 = 15$GHz. The target is located at an angle $\theta = 0.25°$, as presented in the scenario in section 4.1.1. Figure 4.6 shows the RMSE of the phase monopulse estimator, together with the RMSE from the model derived from Kanter and the CRLB. It may be observed that in the linear part of the RMSE of the phase estimator, the CRLB is lower by about 8dB. This means that the phase estimator is statistically not efficient.

4.1.5 The Maximum Likelihood (ML) estimator

The estimation of the bearing direction of a complex signal embedded in noise is sought. The model is as before, $s(n) = Ae^{-j(2\pi f_0(t_0 - \frac{d}{c}n\sin(\theta)))} + w_I + jw_Q$, with the same linear array, where A and $2\pi f_0 t_0$ are known. The PDF given in equation 4.21 is used for the derivation.

The PDF is convex and its maximum occurs for the most likely value of the signal mean. The noise has zero mean hence, over a large number of iterations, the signal mean true value can be found by average and from that the true value of θ can be found. The first step is to find the value that maximises the PDF. This is equal to the minimum of this expression:

$$\begin{aligned} L(x, y; \theta) = &\sum_{n=0}^{N-1} \left(x_n - A\cos\left(2\pi f_0 \left(t_0 - \frac{d}{c} n \sin\theta\right)\right)\right)^2 \\ &+ \left(y_n + A\sin\left(2\pi f_0 \left(t_0 - \frac{d}{c} n \sin\theta\right)\right)\right)^2 \end{aligned} \tag{4.29}$$

To minimize this function, the derivation is carried out with respect to θ.

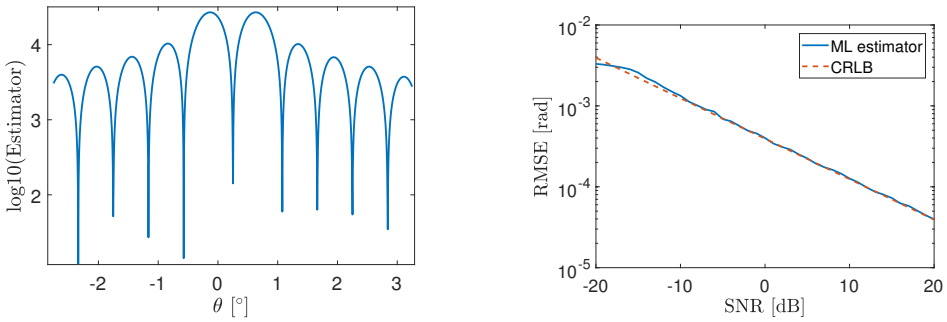

(a) ML estimator for one drawing, $\theta = 0.25°$

(b) ML estimator versus CRLB, $\theta = 0.25°$

Figure 4.7: ML estimator

$$
\begin{aligned}
&\frac{\partial L(x,y;\theta)}{\partial \theta} = \\
&2\sum_n \left[-2\pi f_0 A \frac{d}{c} n \cos\theta \sin\left(2\pi f_0\left(t_0 - \frac{d}{c} n \sin\theta\right)\right)\left(x_n - A\cos\left(2\pi f_0\left(t_0 - \frac{d}{c} n \sin\theta\right)\right)\right)\right. \\
&\quad \left. -2\pi f_0 A \frac{d}{c} n \cos\theta \cos\left(2\pi f_0\left(t_0 - \frac{d}{c} n \sin\theta\right)\right)\left(y_n + A\sin\left(2\pi f_0\left(t_0 - \frac{d}{c} n \sin\theta\right)\right)\right)\right] \\
&= -4\pi f_0 A \frac{d}{c}\cos\theta \sum_n n \left[x_n \sin\left(2\pi f_0\left(t_0 - \frac{d}{c} n \sin\theta\right)\right) + y_n \cos\left(2\pi f_0\left(t_0 - \frac{d}{c} n \sin\theta\right)\right)\right. \\
&\quad \left. -\frac{A}{2}\sin\left(4\pi f_0\left(t_0 - \frac{d}{c} n \sin\theta\right)\right) + \frac{A}{2}\sin\left(4\pi f_0\left(t_0 - \frac{d}{c} n \sin\theta\right)\right)\right] \\
&= -4\pi f_0 A \frac{d}{c}\cos\theta \sum_n n \left[x_n \sin\left(2\pi f_0\left(t_0 - \frac{d}{c} n \sin\theta\right)\right) + y_n \cos\left(2\pi f_0\left(t_0 - \frac{d}{c} n \sin\theta\right)\right)\right]
\end{aligned}
\tag{4.30}
$$

This final result cannot be expressed in a closed form and therefore this ML estimate is found by computation. This expression is calculated using the scenario presented in section 4.1.1 to calculate the bearing direction estimation for a target located at 0.25°. The result is shown in Figure 4.7a for $A = 1$ and $t_0 = r/c$ where $r = 10$ km is the target to phase reference element distance and c is the speed of light.

Figure 4.7a shows the log of the final equation 4.30. To find the minimum of the expression, the target direction parameter is swept. This example has been derived without noise to clearly see its variations. A minimum is observed at the true value angle of the target. The minimum is local which means that the search has to be limited to an interval around the true target angle. Hence the ideal angle range is two times the angle between the true angle and the next local minimum. As the target moves, the curve minimum moves which means that the target should be estimated at any angle with a prior knowledge of the target direction imposed by the estimator periodicity.

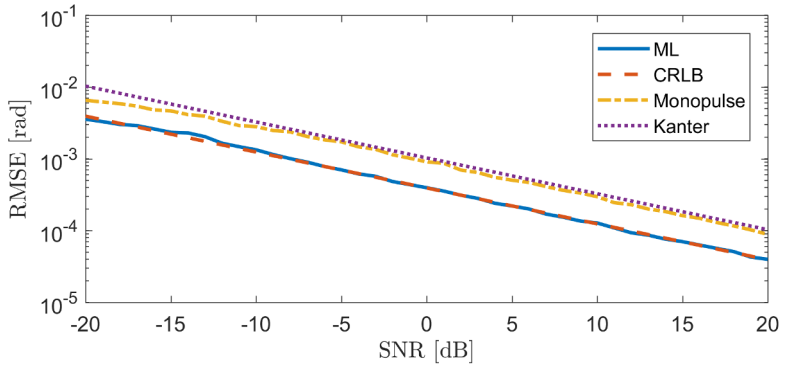

Figure 4.8: Global comparison, $\theta = 0.25°$

In this example, the ML estimator range free from ambiguity is 0.82°. Therefore, to calculate the ML estimator variance for different SNR values, the minimum is sought between $0.25° - 0.82/2$ to $0.25° + 0.82/2$. This choice of limiting the search range also limits the range of the RMSE. As a result, as shown in Figure 4.7b, at low SNR, the ML estimator is not linear anymore and goes below the CRLB, this part of the results is not statistically relevant. Finally, as the SNR increases, the ML estimator matches with the bound. Therefore, the ML estimator is an asymptotically efficient estimator.

4.1.6 Global comparison and conclusion

Again, using the scenario described in section 4.1.1 with a hundred omnidirectional elements and a target located at $\theta = 0.25°$, the global comparison is carried out between the estimators, the minimum bound and the phase monopulse model, as shown in Figure 4.8.

Different observations can be realised from the results:

- The ML estimator is asymptotically efficient.
- The ML estimator is better than the phase estimator. The monopulse requires a higher SNR of 7dB to equalise the ML estimator for a given value of the RMSE.
- The phase and amplitude (A, t_0) of the target are assumed to be known, if not the minimum variance increases by 0.6dB which reduces the gap to 6.4dB. This has been approximated for a high number of elements. The ML estimator would have asymptotically the same behaviour, i.e. for a high SNR.
- The phase monopulse does not need prior estimation of the amplitude and phase (A, t_0) of the signal.
- The developed phase monopulse estimator does not use the monopulse slope approximation but the exact mathematical expression.

- The phase monopulse requires much less processing than the ML estimator. The ML estimator requires a minimum value to be found over a range which is subject to some error.

- The phase estimator model deviates from simulation since it uses the monopulse slope, in this case the model matches with the simulated phase monopulse only when the target is on boresight axis.

- The periodicity of the estimators constrains, respectively, the find the estimations of the ML estimator and the phase monopulse in an angle range of 0.82° and 2.29°. This means that the signal is assumed to be impinging in the main beam. To verify that, the null to null main lobe range can be calculated using the first cancellation of the array patterns: 2.3° (equation 3.30).

As a conclusion, although the ML estimator is statistically more efficient than the monopulse, this improved performance requires additional signal processing. Furthermore, both estimators present ambiguity due to their periodicity. The ambiguity of the ML estimator is higher than the monopulse, meaning that it requires a finer prior knowledge of the target direction.

4.1.7 Generalisation of the comparison for different array size and for different target directions

The previous section has been developed for an array of $N = 100$ elements and a target located at $\theta = 0.25°$ where a difference of 7dB has been found between the phase monopulse estimator and the ML estimator. In this section, the performance comparison is carried out for different array sizes and different target directions for a constant $SNR_{elem} = 20$dB.

To carry out this comparison, the CRLB is used instead of the ML estimator which means that it is assumed that the number of drawing is high enough to have an asymptotic and efficient ML estimator. The Kanter model cannot be used since it is only accurate when the target is on boresight.

Firstly the behaviour of the CRLB and phase monopulse are both explored as a function of the target angle and number of elements, as shown in Figure 4.9.

The CRLB expression is given in equation 4.23, it is a function of $\frac{1}{\cos^2\theta}$ and of $\frac{1}{N^3}$. The minimum variance is optimum for $\theta = 0°$ and the RMSE increases as θ increases. The curves seem constant due to the small range of angles and the small variations of $\frac{1}{\cos^2\theta}$ for small angles. The results also show that the higher the number of elements, the lower the bound. For $\theta = 0°$, respectively for $N =$

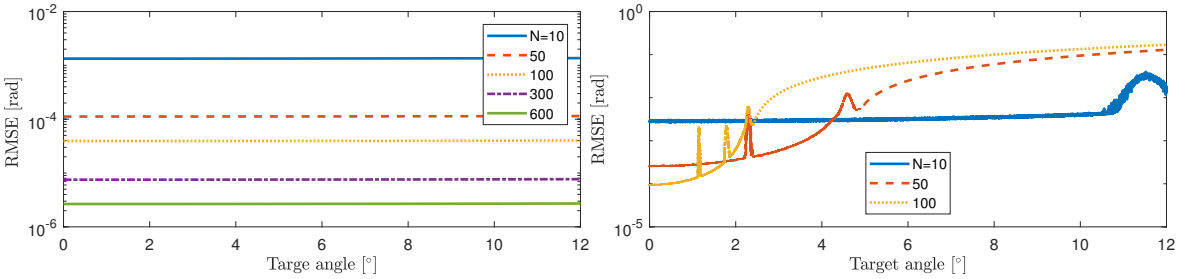

(a) CRLB (b) Phase monopulse estimator

Figure 4.9: CRLB and phase monopulse comparison

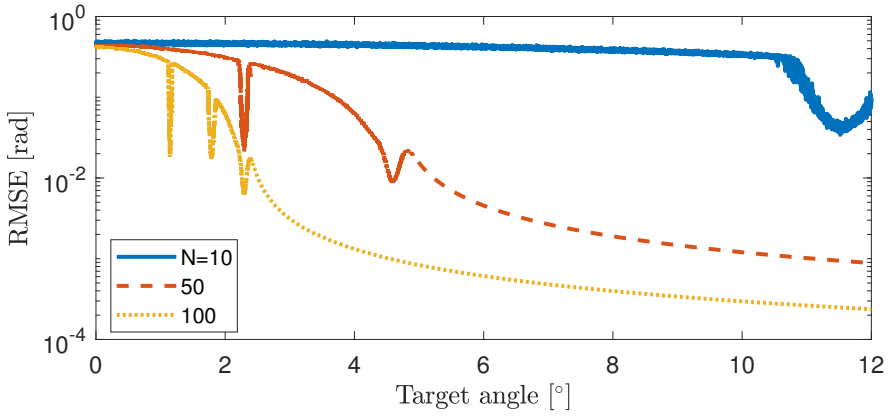

Figure 4.10: CRLB to phase monopulse variance ratio

$10, 50, 100, 300, 600$, the CRLB can be calculated from equation 4.23 which equals to $RMSE = 1.3e^{-3}, 1.12e^{-4}, 3.92e^{-5}, 7.52e^{-6}, 2.66e^{-6}$ $[rad]$, as confirmed in Figure 4.9a.

For the phase monopulse, the part of each curve that is relevant goes from $\theta = 0°$ until the first peak, at the peak angle the target is on the asymptote of the estimator which produces an undefined point. This angle range corresponds to the bijective angle range of the estimator due to its periodicity. As mentioned in section 4.1.3.1, the periodicity is $\theta_{asympt} = \arcsin \frac{\lambda}{2d_{pc}}$ and equal to $\theta_{asympt} = 11.5°, 2.3°, 1.15°$ for each number of elements, as confirmed in Figure 4.9b.

The CRLB is used instead of the ML estimator to simplify the simulations. The ratio of the CRLB over the phase monopulse variance is carried out to evaluate which of the ML and phase monopulse is more efficient as a function of the angle and the number of elements. The simulation result is shown in Figure 4.10.

For each number of elements, the part of the curve that is relevant is from $\theta = 0°$ until the first local minimum. Within this range, the ratio decreases, meaning that the CRLB at the numerator decreases and/or the phase monopulse variance at the denominator increases. As a conclusion, the ML estimator represented here by the CRLB is better than the phase monopulse and the gap increases as the target angle

increases. For $N = 100$ elements and for a target at $\theta = 0.25°$, the gap is 0.84dB (measured vertically) between both estimator and the gap increases to 1.031dB for a target at $\theta = 1°$.

For the target direction $\theta = 0°$, the simplified expression for the Kanter model given in equation 4.19 can be used to analytically verify the results shown in Figure 4.10 and leads to equation 4.31.

$$\begin{aligned} k_m &= \pi \frac{d_{pc}}{\lambda} \theta_{bw} = \pi \frac{Nd}{2\lambda} \theta_{bw} \\ var(\theta)_{Kanter} &= \frac{\theta_{bw}^2}{k_m^2 2SNR_{Ar}} = \frac{2\lambda^2}{\pi^2 N^2 d^2 SNR_{Ar}} \end{aligned} \tag{4.31}$$

The expression of the CRLB using SNR_{Ar} is given in equation 4.32 where $\|AF\| = N$.

$$\begin{aligned} CRLB &= \frac{3\|AF\|^2}{4\pi^2 SNR_{Ar} N^2 (N-1)(2N-1)} \frac{\lambda^2}{d^2 \cos^2\theta} \\ &= \frac{3}{4\pi^2 SNR_{Ar} (N-1)(2N-1)} \frac{\lambda^2}{d^2 \cos^2\theta} \end{aligned} \tag{4.32}$$

The ratio of the variances is finally given in equation 4.33 and the difference for an array of $N = 100$ elements gives 0.727dB, which is also the value obtained from Figure 4.10.

$$\frac{CRLB}{var(\theta)_{Kanter}} = \frac{3N^2}{8(N-1)(2N-1)} = \frac{3}{16} = -0.727dB \tag{4.33}$$

4.2 Phase monopulse from planar to 3D conformal antennas

4.2.1 The optimal choice for the quadrant size

When the monopulse is carried out for planar arrays, the quadrants are identical. For 3D conformal arrays, the quadrants cannot be identic as the elements covering a conformal shape are looking towards different directions, as shown in Figure 1.25. Therefore the effect of non identical quadrants are priorly discussed for the case of a planar array.

The array has two quadrants with respective complex signals of Q_1 and Q_2; the phase shift between the quadrants phase centres is ϕ_{PC}. The quadrant ratio is $\frac{Q_2}{Q_1} = ae^{-j\phi_r}$. The general monopulse ratio is given in equation 4.34.

$$\begin{aligned}\frac{\Delta}{\Sigma} &= \frac{Q_1 - Q_2 e^{-j\phi_{PC}}}{Q_1 + Q_2 e^{-j\phi_{PC}}} = \frac{Q_1(1 - \frac{Q_2}{Q_1}e^{-j\phi_{PC}})}{Q_1(1 + \frac{Q_2}{Q_1}e^{-j\phi_{PC}})} = \frac{1 - ae^{-j(\phi_{PC}+\phi_r)}}{1 + ae^{-j(\phi_{PC}+\phi_r)}} \\ &= \frac{(1 - ae^{-j(\phi_{PC}+\phi_r)})(1 + ae^{j(\phi_{PC}+\phi_r)})}{(1 + ae^{-j(\phi_{PC}+\phi_r)})(1 + ae^{j(\phi_{PC}+\phi_r)})} = \frac{1 - a^2 + 2ja\sin(\phi_{PC} + \phi_r)}{1 + a^2 + 2a\cos(\phi_{PC} + \phi_r)}\end{aligned} \tag{4.34}$$

If the quadrants are identical, $\frac{Q_2}{Q_1} = 1$ and the result goes back to the normal monopulse ratio $j\tan(\frac{\phi_{PC}}{2})$. The more unbalanced the quadrants, the lower is a, which decreases the imaginary part and increases the real part of the ratio. The real and imaginary parts of the ratio are given in equation 4.35.

$$\begin{aligned}\mathrm{Re}(\frac{\Delta}{\Sigma}) &= \frac{1 - a^2}{1 + a^2 + 2a\cos(\phi_{PC} + \phi_r)} \\ \mathrm{Im}(\frac{\Delta}{\Sigma}) &= \frac{2a\sin(\phi_{PC} + \phi_r)}{1 + a^2 + 2a\cos(\phi_{PC} + \phi_r)}\end{aligned} \tag{4.35}$$

Assuming that the coordinate centre of each quadrant is taken at the phase centre, then the phase of each signal is zero and $\phi_r = 0$. The derivative of the imaginary part of the monopulse ratio is derived respective to ϕ_{PC}. ϕ_{PC} is the phase, it is therefore a function of the angle. The slope is finally calculated for $\phi_{PC} = 0$.

$$\begin{aligned}\frac{\partial \mathrm{Im}(\frac{\Delta}{\Sigma})}{\partial \phi_{PC}} &= \frac{2a\cos\phi_{PC}(1 + a^2 + 2a\cos\phi_{PC}) + 4a^2\sin\phi_{PC}\sin\phi_{PC}}{(1 + a^2 + 2a\cos\phi_{PC})^2} \\ &= \frac{2a\cos\phi_{PC}(1 + a^2) + 4a^2\cos^2\phi_1 + 4a^2\sin^2\phi_{PC}}{(1 + a^2 + 2a\cos\phi_{PC})^2} \\ &= \frac{2a\cos\phi_{PC}(1 + a^2) + 4a^2}{(1 + a^2 + 2a\cos\phi_{PC})^2} \\ \left.\frac{\partial \mathrm{Im}(\frac{\Delta}{\Sigma})}{\partial \phi_{PC}}\right|_{\phi_{PC}=0} &= \frac{2a(1 + 2a + a^2)}{(1 + a)^4} = \frac{2a(1 + a)^2}{(1 + a)^4} = \frac{2a}{(1 + a)^2}\end{aligned} \tag{4.36}$$

Now the value that maximises the monopulse slope is sought by differentiating with respect to a.

$$\frac{\partial \frac{2a}{(1+a)^2}}{\partial a} = \frac{2(1 + a)^2 - 4a(1 + a)}{(1 + a)^4} = \frac{2(1 - a^2)}{(1 + a)^4} \tag{4.37}$$

The derivate cancels out for $a = 1$ and the convexity of the function ensures that it is a maximum. Finally the best monopulse slope is reached for $Q_1 = Q_2$.

The strength of the phase monopulse method comes from the linearity between the target angle and the voltage ratio for small angles. The steeper the slope, the

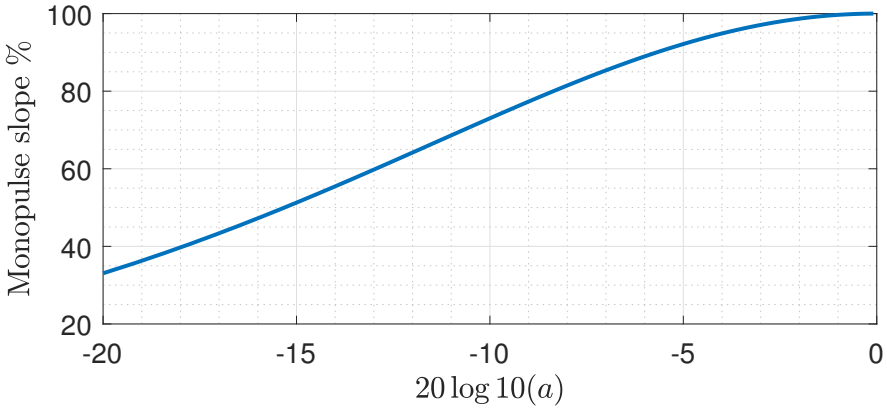

Figure 4.11: Monopulse slope as a function of the quadrant ratio

better the antenna discriminates the signal direction of arrival when embedded in the noise. Furthermore, the bigger the difference between the gains of each quadrant the stronger the real part which decreases the slope. Therefore there is a compromise between the phase monopulse slope and how different are the gains of each quadrant. This is shown in Figure 4.11. The phase monopulse slope is approximated for small angles so that a Taylor approximation of the first order is applied and assuming that the phase $\phi_r = 0$: $\frac{\partial \mathrm{Im}(\frac{\Delta}{\Sigma})}{\partial \theta} = \frac{2a}{(1+a)^2} 2\pi \frac{d_{pc}}{\lambda}$. The curve is normalised over the maximum slope factor which removes the dependency on d, λ and d_{pc} and the results are finally displayed in percentage. The classic phase monopulse curve verifies that the steepest slope is produced when the quadrants are identical. The performance reduction can be calculated as a function of the difference in gain of the quadrants, e.g. a performance reduction of 20% is produced by a quadrant difference of 8dB.

4.2.2 Discussion on the phase monopulse estimation processing

The classic phase monopulse expression is $j \tan\left(\frac{\phi_{PC}}{2}\right)$ and by inversing the tangent, the phase is calculated and the angle is estimated. The expression of the monopulse ratio for unequal quadrants gives an imaginary part proportional to the sinus of the phase in which the target angle is embedded, as shown in equation 4.35. This shows the limitations of the classic phase monopulse for 3D and conformal arrays. As a result the phase monopulse should be updated for non identical quadrants.

However, even though the phase cannot be calculated, a monopulse slope still exists for arrays with non-equal quadrants. This poses the question of the monopulse processing in the RF-seeker. Currently, the antenna is planar with identical quadrants, therefore the processing can be carried out using the tangent inversion. (This is poor as it is not resilient to multi target processing). The second possibility would be the cal-

culation of the target angle using a look-up table that corresponds with the monopulse ratio. For seeker radars, the target direction is close to boresight, therefore storing the monopulse slope may be sufficient.

Based on the assumption that the monopulse slope is the only factor necessary for the calculation of the target angle, the quadrant choice is optimised using the monopulse slope factor for 3D conformal arrays.

4.2.3 Optimisation of quadrants for the phase monopulse slope

This section investigates the potential of linear and conformal arrays from the point of view of the monopulse slope.

The quadrant choice is optimised using the normalised monopulse slope $k_m = \theta_{bw}\mathrm{Im}\left(\frac{\partial\frac{\Delta}{\Sigma}}{\partial\theta}\right)$ as a figure of merit. This is realised for different shapes: a linear array, a half-sphere and a linear faceted array.

The study is realised for steering angles from $\theta = -60°$ to $\theta = 0°$. The beamsteering technique is used to reach the different directions and each element is only emitting in a half-plane tangent to the surface in order to simulate the effect of a ground plane.

The study is performed in 2D in a cut plane to simplify the problem. In this thesis, it is the only optimisation carried out. The diameter of the space below the radome is 0.14 m and at 15 GHz with a $\frac{\lambda}{2}$ spacing between the elements, 15 elements can be hosted. In the first study, this number of elements is fixed for each array. The elements are Hertzian dipoles and they are uniformly distributed, their orientations are shown in Figure 4.12. The half-sphere has a diameter equal to the length of the linear array. For the linear faceted array, 6 of the elements are tilted by 30°, 3 on the left side and three on the right side.

The second study is realised as it can be noticed that the half-sphere array can host more elements by keeping the elements spaced by $\frac{\lambda}{2}$. The perimeter is $7\pi = 21.99$ which allows to host 22 elements. For the linear faceted shape, the tilting angle of the sides is increased to 60° which permits 6 elements on each side and thus a total of 21 elements.

4.2.3.1 Comparison of the monopulse slope for the 3 arrays

Every 10°, all the combinations of quadrants are reviewed. The best set of quadrant is the one that produces the highest monopulse slope factor. The phase shift applied is the same for each combination. The monopulse slope is calculated at the angle of the sum pattern maximum which means that the highest monopulse slope can occur in a

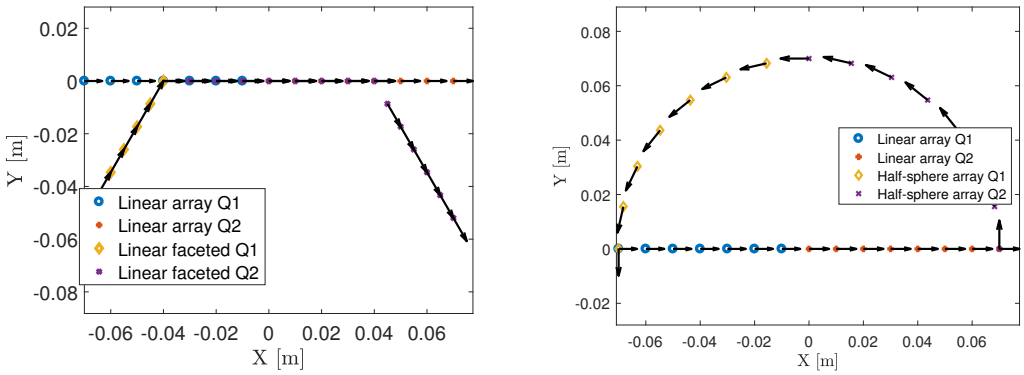

(a) Linear vs linear faceted arrays (b) Linear vs half-sphere arrays

Figure 4.12: Array configurations

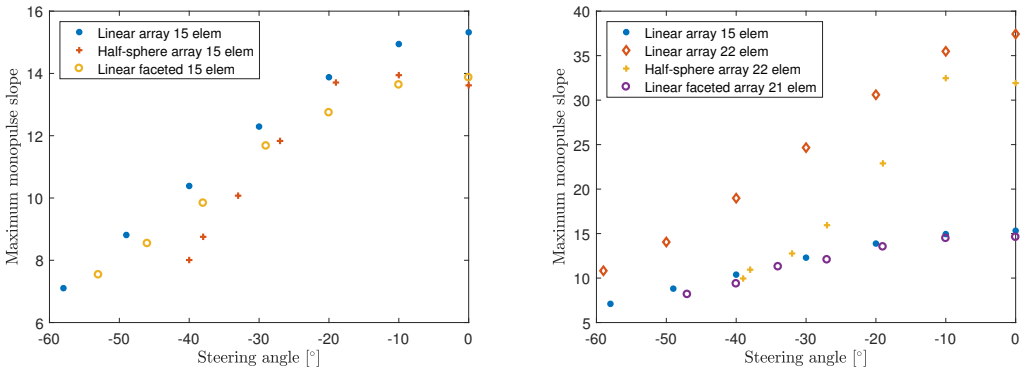

(a) Fixed number of elements (b) Number of elements that take advantage of 3D

Figure 4.13: Monopulse optimisation results

direction different from the aimed beamsteering direction.

For a fixed number of elements for each array, results are shown in Figure 4.13a. The linear array has the best performance as a function of the steering angle. As the beam is steered, all its elements keep contributing, on the contrary, for the two other arrays, the number of contributing elements decreases with the beamsteering angle although some elements rest in the shadow due to the ground plane of the structure. From $0°$ to $-20°$ the half-sphere has a constant monopulse slope and performs better than the linear faceted array. From $-30°$ to $-60°$ the linear faceted array performs better than the half-sphere array. For high beamsteering angles, the maximum of the half-sphere sum pattern does not steer, despite a phase shift of $60°$ and the maximum of the sum pattern appears at $-40°$. This is due to the low number of elements contributing in a given direction.

The results of the half-sphere and the linear faceted arrays with an enhanced number

of elements are shown in Figure 4.13b. The monopulse slope performance of the linear array with 22 elements is indicative. The half-sphere made of 22 elements performs better than the linear array of 15 elements up to 30°; afterwards the results are similar. The linear faceted array with an extended number of elements has performance very similar to the linear array, meaning that, with more elements on the sides, the slope could be improved for high beamsteering angles.

As a conclusion, the conformal arrays with the drawback of shadowed elements not contributing in all directions is counteracted by the increase of the number of elements. For beamsteering angles between −60° and −35°, the monopulse slope does not reach the aimed direction, this limits the coverage of the antenna. However, for steering angles between −35° and 0°, first, results have shown that the conformal arrays have a better monopulse slope than the linear array and secondly, that the conformal array would also have a better slope than the mechanically rotating array (its slope is constant over the field of view).

Those are first conclusions carried out using the assumption that a truncated pattern models a ground plane. This model also takes into account the shadowing effect: elements in one side of the structure are not contributing to the other side. Therefore, a more robust model should be build to more finely take into account the effects of a ground plane and finally give more realistic estimations of the monopulse slope.

4.2.3.2 Details of the optimisation

In order to more deeply understand the results of the monopulse slope, further simulations are carried out. Firstly, the comparison between the linear array and the linear faceted array is realised and, secondly, the comparison between the linear array and the half-sphere array is carried out. In both cases, the study is sampled for three beamsteering angles 0°, −30° and −60°. Each figure displays the array with the indication of the elements for each quadrant, the patterns produced by each quadrant and finally the sum and difference patterns.

Comparison between the linear array and the linear faceted array On the first hand, it can be noticed that for the three beamsteering angles, as shown in Figures 4.14, 4.15 and 4.16, the linear array uses all its elements, and the quadrant choice that produces the best slope is always the same, half of the total array for each quadrant. This is coherent with the study carried out in section 4.2.1.

On the other hand, for the linear faceted array, all the elements are contributing for a steering of 0° but as the beam is steered, it changes, as shown in Figures 4.17, 4.18 and 4.19. The elements from the right facets appear in the shadow although the beam is steered in the direction −30°. As a result, 15 elements only are contributing in

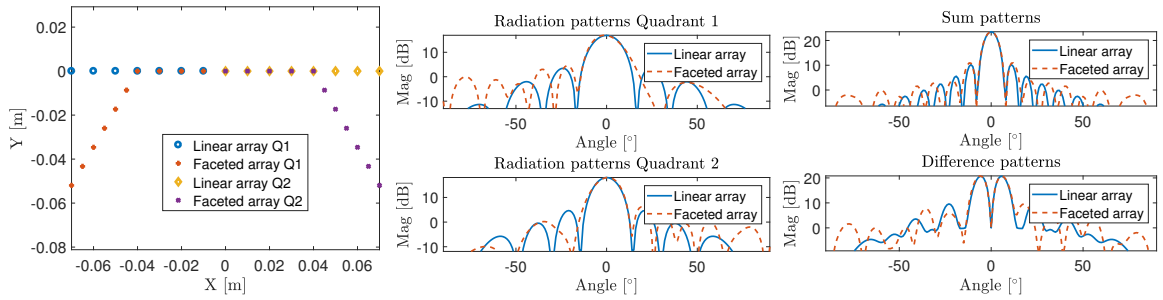

(a) Array (b) Patterns Q_1 and Q_2 (c) Sum and difference patterns

Figure 4.14: Monopulse optimisation, 15 and 21 elements for the linear and linear faceted array, steering $\theta = 0°$

this direction, same number as for the planar array. In this direction, the first quadrant elements of the linear faceted array covers the left facet and the horizontal part as well. This produces a main beam that does not focus precisely in the direction $-30°$. As a result, the maximum of the sum pattern and the local minimum of the difference pattern are not focused at $-30°$ and the monopulse ratio also follows this behaviour. Those comments are even more easily observable for a steering in the direction $-60°$.

As the beam is steered for the linear array, the main beam of the quadrants patterns become wider with a lower maximum gain. Consequently, the sum and difference patterns become less sharp which finally produces a decreasing monopulse slope factor.

Comparison between the linear array and the half-sphere array Each array has 22 elements in total. For a beamsteering of 0°, all the elements contribute in both cases. For the half-sphere, a phase shift is applied to focus the beam which gives quadrants patterns with a lower main beam than for the planar array 4.14b. Furthermore, the comments about the behaviour of the patterns for the linear faceted array are also applicable to the half-sphere array: as the beam is steered, the main beam of the quadrants patterns do not focus in the aim direction which lowers the monopulse slope. The linear array with 22 elements is indicative, in reality, the elements would not be spaced so closely.

In conclusion, the linear faceted array with 21 elements and the half-sphere array with 22 elements do not focus the main beam in the steering directions lower than $-35°$. This produces a monopulse slope which is not focused in the aimed direction, as a result, it limits the angular coverage of estimation. This could be counteracted by using arrays with more elements on the lateral faces.

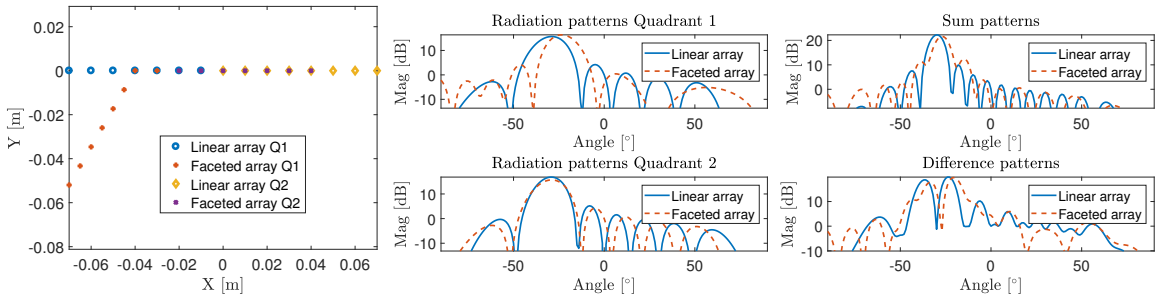

(a) Array (b) Patterns Q_1 and Q_2 (c) Sum and difference patterns

Figure 4.15: Monopulse optimisation, 15 and 21 elements for the linear and linear faceted array, steering $\theta = -30°$

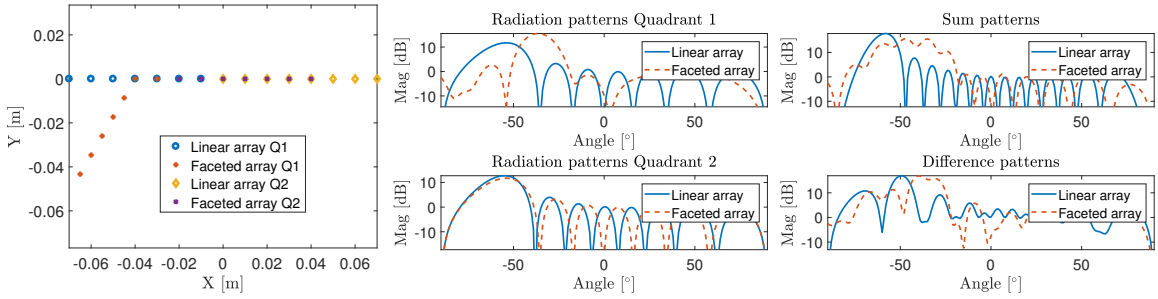

(a) Array (b) Patterns Q_1 and Q_2 (c) Sum and difference patterns

Figure 4.16: Monopulse optimisation, 15 and 21 elements for the linear and linear faceted array, steering $\theta = -60°$

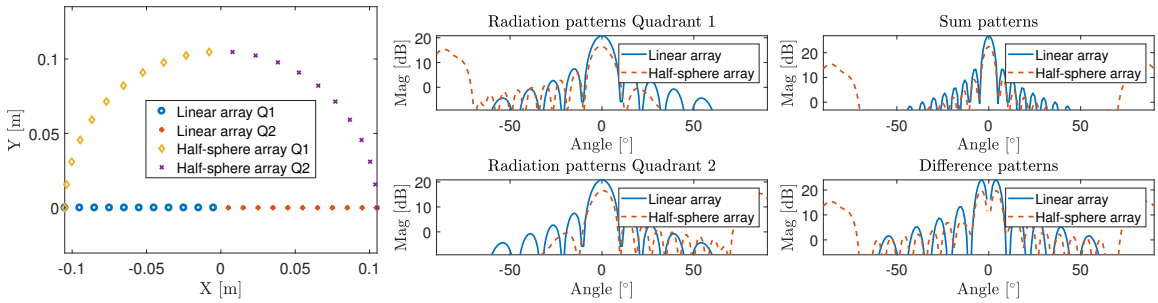

(a) Array (b) Patterns Q_1 and Q_2 (c) Sum and difference patterns

Figure 4.17: Monopulse optimisation details, 22 elements, steering $\theta = 0°$

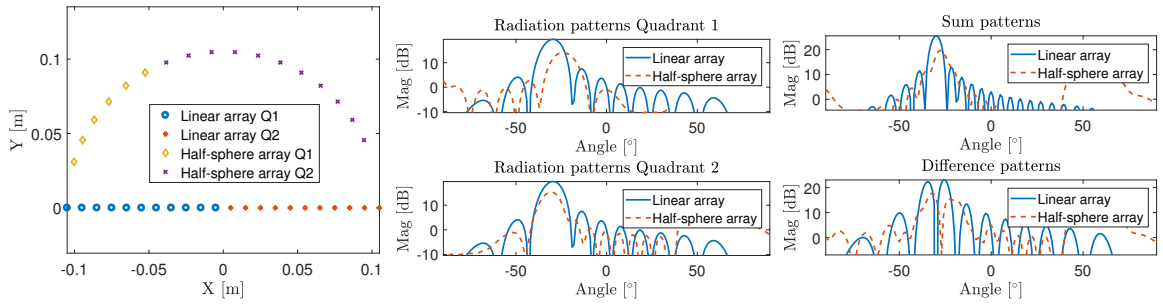

(a) Array (b) Patterns Q_1 and Q_2 (c) Sum and difference patterns

Figure 4.18: Monopulse optimisation details, 22 elements, steering $\theta = -30°$

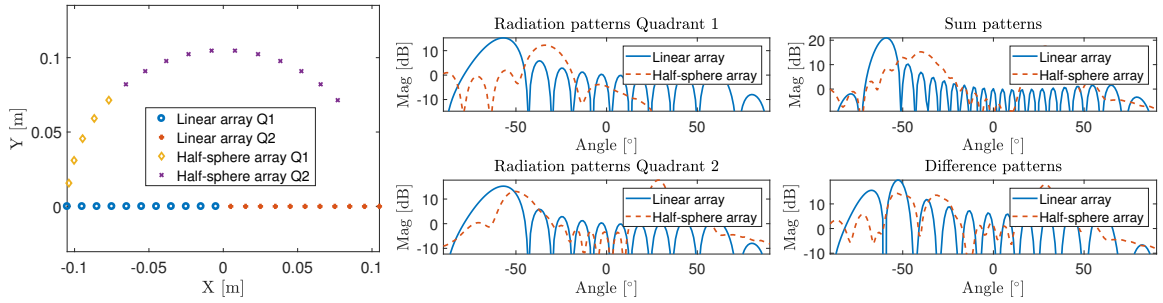

(a) Array (b) Patterns Q_1 and Q_2 (c) Sum and difference patterns

Figure 4.19: Monopulse optimisation details, 22 elements, steering $\theta = -60°$

4.3 CRLB for 3D arrays

This section investigates the effects of the conformation and 3D arrays on the estimation. Firstly, a physical model is developed for the estimation of the direction of arrival (DOA) of a polarised signal impinging on an arbitrary antenna field vector. Secondly, the CRLB for directive elements for 3D geometries, taking into account the polarisation of the impinging signal, is derived. Thirdly, the CRLB is fully analytically addressed for different array configurations composed of ideal Hertzian dipoles and the interest of the orientation and position diversities on the DOA estimation are shown. For more realistic studies, the effect of known and unkown cross-pol phases on the DOA is also explored. In the fourth part, the monopulse estimator is derived using the exposed model; its limitations are shown and an alternative monopulse is presented.

4.3.1 General reception model

Pulse reception is studied to estimate the direction of arrival of an incoming signal from the far field with an antenna array, as shown in Figure 4.20a. The direction of arrival in a spherical coordinate system is identified by the elevation angle θ and the

azimuth angle φ, as shown in Figure 4.20.

The baseband signal received at the n_{th} element of the array after Doppler treatment and the matched filter is modelled as the sum between the free-noise signal s_n and the thermal noise w_n. The thermal noise has been defined previously in section 2.4.1.

The received electromagnetic field $\mathbf{E}$ at the array phase centre, that can represent a target echo or the signal from a co-operative or non-cooperative transmitter is expressed using the Jones notation [Jones, 1941] in the spherical coordinate system $\mathbf{E} = E_\theta \mathbf{e}_\theta + E_\varphi \mathbf{e}_\varphi$, where E_θ and E_φ are the complex components of the electric field along the θ and φ directions, respectively. This notation enables the analytical treatment of an incident signal with any type of polarisation.

At each element, the incident electric field is decomposed into a co-polarisation component and a cross-polarisation component by projecting a replica of the electric field $\mathbf{E}$, delayed with respect to the antenna array phase centre, on two orthogonal complex unit vectors $\mathbf{e_{C_n}}$ and $\mathbf{e_{X_n}}$ that respectively identify the co-pol and cross-pol components of the field at each element. The use of complex unit vectors allows for the projection of the incoming $\mathbf{E}$-field over any elliptical and orthogonal polarisation components. The result of the projection is the extraction of the co-pol component E_{C_n} and the cross-pol component E_{X_n} as

$$\begin{aligned} E_{C_n} &= \langle E_\theta \mathbf{e}_\theta + E_\varphi \mathbf{e}_\varphi | \mathbf{e_{C_n}} \rangle \, e^{j\frac{2\pi}{\lambda}\mathbf{r}_n \cdot \mathbf{e}_r} \\ E_{X_n} &= \langle E_\theta \mathbf{e}_\theta + E_\varphi \mathbf{e}_\varphi | \mathbf{e_{X_n}} \rangle \, e^{j\frac{2\pi}{\lambda}\mathbf{r}_n \cdot \mathbf{e}_r} \end{aligned} \tag{4.38}$$

The term $e^{j\frac{2\pi}{\lambda}\mathbf{r}_n \cdot \mathbf{e}_r}$ is a phase delay accounting for the path difference between elements and is expressed with respect to the phase centre of the array, where $\mathbf{r}_n$ is the position vector of the n-th element phase centre and $\mathbf{e}_r = [\sin\theta\cos\varphi, \sin\theta\sin\varphi, \cos\theta]$ is the unit vector of the spherical coordinate system that identifies the direction (θ,φ), as shown in figure 4.20.

For an ideal antenna, the signal received by a channel is only a function of the component of the field E_{C_n} and the co-pol antenna gain G_{C_n}. However, real antennas suffer from cross-polarisation limitations resulting from inevitable technological imperfections and the use of radomes; such factors must be taken into account.

The antenna is modelled as a transducer that transforms the electromagnetic field into a voltage signal. Analytically, this operation can be described as [Sinclair, 1950].

A general model of the antenna includes two possible feeding ports (e.g. patch antenna) and is shown in equation 4.39. This corresponds to a co-channel and a cross-channel, as shown in Figure 4.20b which produces two output voltages:

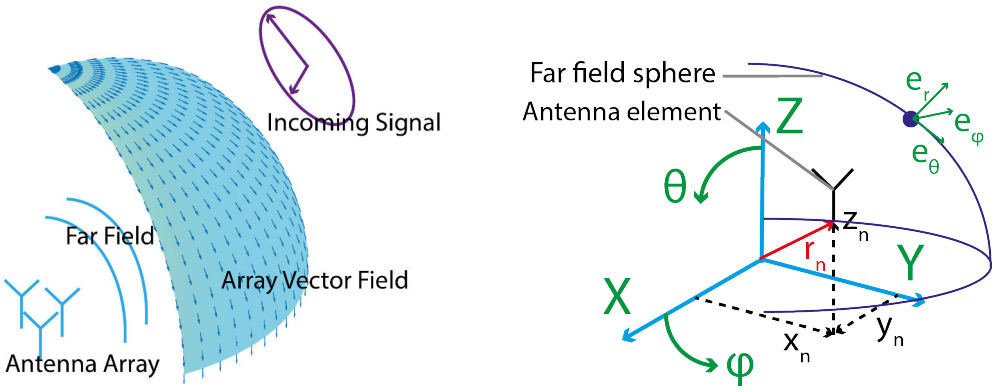

(a) Projection of the incoming signal on the antenna radiated field

(b) Coordinate system and position vector

Figure 4.20: Illustrations for the model

$$\begin{bmatrix} V_{C_n} \\ V_{X_n} \end{bmatrix} = \begin{bmatrix} \sqrt{G_{C_n}(\theta,\varphi)} & \sqrt{G_{X_n}(\theta,\varphi)}e^{j\phi_{c_n}} \\ \sqrt{GX_{C_n}(\theta,\varphi)}e^{j\phi_{x_n}} & \sqrt{GX_{X_n}(\theta,\varphi)} \end{bmatrix} \begin{bmatrix} E_{C_n} \\ E_{X_n} \end{bmatrix} \tag{4.39}$$

The received voltage at the co-channel is indicated with V_{C_n} and that at the cross channel with V_{X_n}. In reception, the incident signal in the co-channel is affected by the square root of the co-pol gain G_{C_n} and the cross-pol gain G_{X_n} where a phase difference $e^{j\phi_{c_n}}$ is also induced between the two components. Similar phenomena are occuring in the antenna cross-channel, where the co-pol gain is GX_{C_n}, the cross-pol gain is GX_{X_n} and the phase between the components $e^{j\phi_{x_n}}$. The problem is that, whilst antenna elements are fabricated to ensure that the co-channel gains are the same for all elements, current fabrication techniques are such that the cross-channel gains may significantly differ from element to element.

In this thesis, the study is limited to the case where only the co-channel is used to estimate the direction of arrival to investigate advantages and disadvantages of using 3D shape, along with limitations resulting from antenna imperfections with respect to estimation performance. The signal received at each element can therefore be indicated as $V_{C_n} = (\sqrt{G_{C_n}}E_{C_n} + \sqrt{G_{X_n}}e^{j\phi_{c_n}}E_{X_n})$. Finally the voltage induced in the receiving channel of the antenna is:

$$V_{C_n} + w_n = (\sqrt{G_{C_n}}E_{C_n} + \sqrt{G_{X_n}}e^{j\phi_{c_n}}E_{X_n}) + w_n \tag{4.40}$$

4.3.2 General derivation of the CRLB

The signal model previously set is now used to derive the expression of the CRLB. The final expression provides an understanding of the physical phenomena affecting

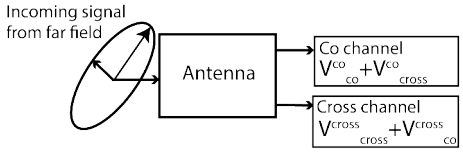

Figure 4.21: General dual channel antenna model

the bound and the parameters which would lower it.

The DOA estimation relies both on the amplitude ρ_n and the phase of the incident signal. Since the phase delay between elements $\frac{2\pi}{\lambda}\mathbf{r}_n \cdot \mathbf{e}_r$ has a strong impact on the estimation, it is separated from the cross-pol phase and the incident signal phase ϕ_n.

$$\sqrt{G_{C_n}}E_{C_n} + \sqrt{G_{X_n}}e^{j\phi_{c_n}}E_{X_n} = \rho_n e^{j\phi_n}e^{j\frac{2\pi}{\lambda}\mathbf{r}_n\cdot\mathbf{e}_r} \tag{4.41}$$

The resulting probability density function is:

$$PDF(\theta,\varphi) = \frac{1}{(2\pi\sigma^2)^N}e^{\frac{-1}{2\sigma^2}\sum_n\left[\left(s_{In}-\rho_n\cos\left(\frac{2\pi}{\lambda}\mathbf{r}_n\cdot\mathbf{e}_r+\phi_n\right)\right)^2+\left(s_{Qn}-\rho_n\sin\left(\frac{2\pi}{\lambda}\mathbf{r}_n\cdot\mathbf{e}_r+\phi_n\right)\right)^2\right]} \tag{4.42}$$

where s_{In} is the real part of the signal in equation 4.41 and s_{Qn} its imaginary part.

The CRLB expression is obtained from the Fisher Information Matrix (FIM). Its expression is given in equation 4.43 [Kay, 1993b].

$$FIM = \begin{bmatrix} -E\left[\frac{\partial^2}{\partial\theta^2}\ln PDF(\theta,\varphi)\right] & -E\left[\frac{\partial^2}{\partial\theta\partial\varphi}\ln PDF(\theta,\varphi)\right] \\ -E\left[\frac{\partial^2}{\partial\theta\partial\varphi}\ln PDF(\theta,\varphi)\right] & -E\left[\frac{\partial^2}{\partial\varphi^2}\ln PDF(\theta,\varphi)\right] \end{bmatrix} \tag{4.43}$$

The result of each term is given in equation 4.44. More detailed calculations can be found in B.

$$\begin{aligned}
FIM_{\theta\theta} &= -E\left[\frac{\partial^2}{\partial\theta^2}\ln PDF(\theta,\varphi)\right] = \frac{1}{\sigma^2}\sum_{n=1}^{N}\left[\left(\frac{\partial\rho_n}{\partial\theta}\right)^2 + \rho_n^2\left(\frac{2\pi}{\lambda}\frac{\partial\mathbf{r}_n\cdot\mathbf{e}_r}{\partial\theta}+\frac{\partial\phi_n}{\partial\theta}\right)^2\right] \\
FIM_{\varphi\varphi} &= -E\left[\frac{\partial^2}{\partial\varphi^2}\ln PDF(\theta,\varphi)\right] = \frac{1}{\sigma^2}\sum_{n=1}^{N}\left[\left(\frac{\partial\rho_n}{\partial\varphi}\right)^2 + \rho_n^2\left(\frac{2\pi}{\lambda}\frac{\partial\mathbf{r}_n\cdot\mathbf{e}_r}{\partial\varphi}+\frac{\partial\phi_n}{\partial\varphi}\right)^2\right] \\
FIM_{\theta\varphi} &= -E\left[\frac{\partial^2}{\partial\theta\partial\varphi}\ln PDF(\theta,\varphi)\right] \\
&= \frac{1}{\sigma^2}\sum_{n=1}^{N}\left[\frac{\partial\rho_n}{\partial\theta}\frac{\partial\rho_n}{\partial\varphi} + \rho_n^2\left(\left(\frac{2\pi}{\lambda}\frac{\partial\mathbf{r}_n\cdot\mathbf{e}_r}{\partial\theta}+\frac{\partial\phi_n}{\partial\theta}\right)\left(\frac{2\pi}{\lambda}\frac{\partial\mathbf{r}_n\cdot\mathbf{e}_r}{\partial\varphi}+\frac{\partial\phi_n}{\partial\varphi}\right)\right)\right]
\end{aligned} \tag{4.44}$$

The last step required to reach the CRLB consists of carrying out the inverse of the FIM: $CRLB = FIM^{-1}$. For that, its determinant has to be derived, as shown in equation 4.45.

$$\begin{aligned}|FIM| &= E\left[\frac{\partial^2}{\partial\theta^2}\ln PDF(\theta,\varphi)\right]E\left[\frac{\partial^2}{\partial\varphi^2}\ln PDF(\theta,\varphi)\right] - E\left[\frac{\partial^2}{\partial\theta\partial\varphi}\ln PDF(\theta,\varphi)\right]^2 \\ &= \frac{1}{\sigma^4}\sum_{i=1}^{N}\sum_{j=1}^{N}\left(\frac{\partial\rho_i}{\partial\theta}\right)^2\left(\rho_j\frac{\partial}{\partial\varphi}\left(\frac{2\pi}{\lambda}\mathbf{r}_j\cdot\mathbf{U}+\phi_n\right)\right)^2 \\ &+ \sum_{i=1}^{N}\sum_{j=1}^{N}\left(\frac{\partial\rho_i}{\partial\varphi}\right)^2\left(\rho_j\frac{\partial}{\partial\theta}\left(\frac{2\pi}{\lambda}\mathbf{r}_j\cdot\mathbf{U}+\phi_n\right)\right)^2 \\ &- \frac{1}{\sigma^4}2\sum_{i=1}^{N}\sum_{j=1}^{N}\frac{\partial\rho_i}{\partial\theta}\frac{\partial\rho_i}{\partial\varphi}\rho_j^2\frac{\partial}{\partial\theta}\left(\frac{2\pi}{\lambda}\mathbf{r}_j\cdot\mathbf{U}+\phi_n\right)\frac{\partial}{\partial\varphi}\left(\frac{2\pi d}{\lambda}\mathbf{r}_j\cdot\mathbf{U}+\phi_n\right)\end{aligned} \tag{4.45}$$

Finally

$$CRLB = \begin{bmatrix} CRLB_{\theta\theta} & CRLB_{\theta\varphi} \\ CRLB_{\theta\varphi} & CRLB_{\varphi\varphi}\end{bmatrix} = \sigma^2\cdot$$
$$\begin{bmatrix} \frac{\sum_{n=1}^{N}\left[\left(\frac{\partial\rho_n}{\partial\varphi}\right)^2+\rho_n^2\left(\frac{2\pi}{\lambda}\frac{\partial\mathbf{r}_n\cdot\mathbf{e}_r}{\partial\varphi}+\frac{\partial\phi_n}{\partial\varphi}\right)^2\right]}{|FIM|} & -\frac{\sum_{n=1}^{N}\left[\frac{\partial\rho_n}{\partial\theta}\frac{\partial\rho_n}{\partial\varphi}+\rho_n^2\left(\left(\frac{2\pi}{\lambda}\frac{\partial\mathbf{r}_n\cdot\mathbf{e}_r}{\partial\theta}+\frac{\partial\phi_n}{\partial\theta}\right)\left(\frac{2\pi}{\lambda}\frac{\partial\mathbf{r}_n\cdot\mathbf{e}_r}{\partial\varphi}+\frac{\partial\phi_n}{\partial\varphi}\right)\right)\right]}{|FIM|} \\ -\frac{\sum_{n=1}^{N}\left[\frac{\partial\rho_n}{\partial\theta}\frac{\partial\rho_n}{\partial\varphi}+\rho_n^2\left(\left(\frac{2\pi}{\lambda}\frac{\partial\mathbf{r}_n\cdot\mathbf{e}_r}{\partial\theta}+\frac{\partial\phi_n}{\partial\theta}\right)\left(\frac{2\pi}{\lambda}\frac{\partial\mathbf{r}_n\cdot\mathbf{e}_r}{\partial\varphi}+\frac{\partial\phi_n}{\partial\varphi}\right)\right)\right]}{|FIM|} & \frac{\sum_{n=1}^{N}\left[\left(\frac{\partial\rho_n}{\partial\theta}\right)^2+\rho_n^2\left(\frac{2\pi}{\lambda}\frac{\partial\mathbf{r}_n\cdot\mathbf{e}_r}{\partial\theta}+\frac{\partial\phi_n}{\partial\theta}\right)^2\right]}{|FIM|}\end{bmatrix} \tag{4.46}$$

4.3.3 Effect of 3D and conformation for omnidirectional and DOA decoupled arrays

In this section, a planar array and a 3D array are compared, whereby elements are shifted over the axis Z. To simplify the CRLB expression, different conditions are applied to the array, as shown in equation 4.47, where x_n,y_n and z_n are the Cartesian coordinates of the n-th element. Firstly, it is derived in the specific case of decoupled elevation and azimuthal angles [Nielsen, 1994] is desired resulting in cancelling out the off-diagonal terms. Secondly, omnidirectional elements are considered with a constant amplitude ρ_0 and phase ϕ_0.

$$\begin{aligned}
&\sum_{n=1}^{N}(x_n-\bar{x})(y_n-\bar{y})=\sum_{n=1}^{N}(x_n-\bar{x})(z_n-\bar{z})=\sum_{n=1}^{N}(y_n-\bar{y})(z_n-\bar{z})=0\\
&\sum_{n=1}^{N}(x_n-\bar{x})^2=\sum_{n=1}^{N}(y_n-\bar{y})^2\\
&\bar{x}=\sum_{n=1}^{N}x_n\quad;\quad\bar{y}=\sum_{n=1}^{N}y_n\quad;\quad\bar{z}=\sum_{n=1}^{N}z_n\\
&\rho_n=\rho_0\qquad\phi_n=\phi_0
\end{aligned}\tag{4.47}$$

The new expression of the determinant of the FIM is given in equation 4.48.

$$\begin{aligned}
&E\left[\frac{\partial^2}{\partial\theta\partial\varphi}\ln PDF\,(\theta,\varphi)\right]=0\\
&|FIM|=E\left[\frac{\partial^2}{\partial\theta^2}\ln PDF\,(\theta,\varphi)\right]E\left[\frac{\partial^2}{\partial\varphi^2}\ln PDF(\theta,\varphi)\right]
\end{aligned}\tag{4.48}$$

The coordinate system is chosen such as $\bar{x}=\bar{y}=\bar{z}=0$. Finally the simplified expression of the CRLB is given in equation 4.49.

$$\begin{aligned}
\begin{bmatrix}CRLB_{\theta\theta} & CRLB_{\theta\varphi}\\ CRLB_{\theta\varphi} & CRLB_{\varphi\varphi}\end{bmatrix}&=\begin{bmatrix}\frac{1}{-E\left[\frac{\partial^2}{\partial\theta^2}\ln PDF(\theta,\varphi)\right]} & 0\\ 0 & \frac{1}{-E\left[\frac{\partial^2}{\partial\varphi^2}\ln PDF(\theta,\varphi)\right]}\end{bmatrix}\\
&=\sigma^2\cdot\begin{bmatrix}\frac{1}{\frac{2\pi\rho_0}{\lambda}\sum_{n=1}^{N}\left(\frac{\partial\mathbf{r}_n\cdot\mathbf{e}_r}{\partial\theta}\right)^2} & 0\\ 0 & \frac{1}{\frac{2\pi\rho_0}{\lambda}\sum_{n=1}^{N}\left(\frac{\partial\mathbf{r}_n\cdot\mathbf{e}_r}{\partial\varphi}\right)^2}\end{bmatrix}
\end{aligned}\tag{4.49}$$

For a planar array in the plane $z=0$, the scalar product $\mathbf{r}_n\cdot\mathbf{e}_r=\sin\theta(x_n\cos\varphi+y_n\sin\varphi)$ has a derivate with respect to the angles given in equation 4.50, producing CRLB expressions, as shown in equation 4.51.

$$\begin{aligned}
\frac{\partial\mathbf{r}_n\cdot\mathbf{e}_r}{\partial\theta}&=\cos\theta(x_n\cos\varphi+y_n\sin\varphi)\\
\frac{\partial\mathbf{r}_n\cdot\mathbf{e}_r}{\partial\varphi}&=\sin\theta(-x_n\sin\varphi+y_n\cos\varphi)
\end{aligned}\tag{4.50}$$

$$\begin{aligned}
CRLB_{\theta\theta z=0}&=\frac{\sigma^2}{\frac{2\pi\rho_0}{\lambda}\cos\theta\sum_{n=1}^{N}(x_n\cos\varphi+y_n\sin\varphi)^2}\\
CRLB_{\varphi\varphi z=0}&=\frac{\sigma^2}{\frac{2\pi\rho_0}{\lambda}\sin\theta\sum_{n=1}^{N}(-x_n\sin\varphi+y_n\cos\varphi)^2}
\end{aligned}\tag{4.51}$$

For an array where elements are shifted along the axis Z, the z term appears in the scalar product $\mathbf{r}_n \cdot \mathbf{e}_r = \sin\theta(x_n \cos\varphi + y_n \sin\varphi) + z_n \cos\theta$ and its derivate with respect to the angles is given in equation 4.52, leading to CRLB expressions, as shown in equation 4.53.

$$\begin{aligned} \frac{\partial \mathbf{r}_n \cdot \mathbf{e}_r}{\partial \theta} &= \cos\theta(x_n \cos\varphi + y_n \sin\varphi) - z_n \sin\theta \\ \frac{\partial \mathbf{r}_n \cdot \mathbf{e}_r}{\partial \varphi} &= \sin\theta(-x_n \sin\varphi + y_n \cos\varphi) \end{aligned} \tag{4.52}$$

The derivate respective to φ remains unchanged when elements are shifted along the axis Z. This also has no effect on estimation performance along the azimuthal angle: $CRLB_{\varphi\varphi z=0} = CRLB_{\varphi\varphi 3D}$.

$$CRLB_{\theta\theta 3D} = \frac{\sigma^2}{\frac{2\pi\rho_0}{\lambda} \sum_{n=1}^{N} \left(\cos\theta \left(x_n \cos\varphi + y_n \sin\varphi\right) - z_n \sin\theta\right)^2} \tag{4.53}$$

$CRLB_{\theta\theta 3D}$ thus has no effect on performance. The denominator is therefore expanded, as shown in equation 4.54.

$$\begin{aligned} &\sum_{n=1}^{N} \left(\cos\theta \left(x_n \cos\varphi + y_n \sin\varphi\right) - z_n \sin\theta\right)^2 \\ &= \sum_{n=1}^{N} \left[\left(\cos\theta \left(x_n \cos\varphi + y_n \sin\varphi\right)\right)^2 + \left(z_n \sin\theta\right)^2 - 2\left(\cos\theta \left(x_n \cos\varphi + y_n \sin\varphi\right)\right)\left(z_n \sin\theta\right)\right] \\ &= \sum_{n=1}^{N} \left[\left(\cos\theta \left(x_n \cos\varphi + y_n \sin\varphi\right)\right)^2 + \left(z_n \sin\theta\right)^2\right] - 2\cos\theta\sin\theta \left(\cos\varphi \sum_{n=1}^{N} x_n z_n + \sin\varphi \sum_{n=1}^{N} y_n z_n\right) \\ &= \sum_{n=1}^{N} \left[\left(\cos\theta \left(x_n \cos\varphi + y_n \sin\varphi\right)\right)^2 + \left(z_n \sin\theta\right)^2\right] \end{aligned} \tag{4.54}$$

The square cross term cancels out using the hypothesis given in equation 4.47 to decouple the estimation along the azimuthal and elevation angles. The final expression of $CRLB_{\theta\theta 3D}$ is given in equation 4.55.

$$CRLB_{\theta\theta 3D} = \frac{\sigma^2}{\sum_{n=1}^{N} \left[\left(\frac{2\pi}{\lambda}\rho_0\right)^2 \left(\left(\cos\theta \left(x_n \cos\varphi + y_n \sin\varphi\right)\right)^2 + \left(z_n \sin\theta\right)^2\right)\right]} \tag{4.55}$$

As a result, for $\theta \neq 0$ $CRLB_{\theta\theta z=0} > CRLB_{\theta\theta 3D}$ and the equality happens for $\theta = 0$. This shows that a 3D conformal array made of omnidirectional elements performs better than a planar array. Here, the array uncoupling conditions cancel out the covariance terms. This confirms and generalises the results obtained in [Moriya et al., 2012].

4.3.4 Illustration of 3D and conformation interest for directive elements

In this section, 3D arrays composed of Hertzian dipoles will be used to illustrate the interest of 3D and conformal arrays using the model described in section 4.3.1. Firstly, to calculate the bound, the voltage expression of a Hertzian dipole is derived in the generalised case for any orientation and without cross-polarisation. Then, the CRLB is derived and the computed results are presented. For a more realistic study, the model is finally enhanced to a signal in the presence of cross-polarisation.

4.3.4.1 General voltage expression for a Hertzian dipole

The derivation of the joint CRLB for any incoming signal impinging on a Hertzian dipole with any orientation starts with the projection of the incident signal vectors on the Hertzian dipole vectors base. This base identifies the co and cross-pol of the element which depends on the element orientation. The incident signal and the element base need to be expressed in the same coordinate system for the projection. The global spherical coordinate system $(\mathbf{e}_r, \mathbf{e}_\theta, \mathbf{e}_\varphi)$ is chosen as a reference.

The orientation of the Hertzian dipole is defined by the vector $V_n = \begin{bmatrix} V_{xn} & V_{yn} & V_{zn} \end{bmatrix}^T$ expressed in Cartesian coordinates, therefore as an intermediate step, the element vectors co and cross-pol base is first derived in the global cartesian coordinate system. The results are shown in equation 4.56.

$$
\begin{aligned}
\mathbf{e}_{\varphi_n\ (\mathbf{e}_x,\mathbf{e}_y,\mathbf{e}_z)} &= \frac{1}{\mid V_n \otimes \mathbf{e}_r \mid} \begin{bmatrix} V_{xn} \\ V_{yn} \\ V_{zn} \end{bmatrix} \otimes \mathbf{e}_r = \frac{1}{\mid V_n \otimes \mathbf{e}_r \mid} \begin{bmatrix} V_{xn} \\ V_{yn} \\ V_{zn} \end{bmatrix} \otimes \begin{bmatrix} \sin\theta\cos\varphi \\ \sin\theta\sin\varphi \\ \cos\theta \end{bmatrix} \\
&= \frac{1}{\mid V_n \otimes \mathbf{e}_r \mid} \begin{bmatrix} V_{yn}\cos\theta - V_{zn}\sin\theta\sin\phi \\ V_{zn}\sin\theta\cos\varphi - V_{xn}\cos\theta \\ V_{xn}\sin\theta\sin\varphi - V_{yn}\sin\theta\cos\varphi \end{bmatrix} \\
\mathbf{e}_{\theta_n\ (\mathbf{e}_x,\mathbf{e}_y,\mathbf{e}_z)} &= \mathbf{e}_{\varphi_n} \otimes \mathbf{e}_r = \frac{1}{\mid V_n \otimes \mathbf{e}_r \mid} \cdot \\
&\begin{bmatrix} (V_{zn}\sin\theta\cos\varphi - V_{xn}\cos\theta)\cos\theta - (V_{xn}\sin\theta\sin\varphi - V_{yn}\sin\theta\cos\varphi)\sin\theta\sin\varphi \\ (V_{xn}\sin\theta\sin\varphi - V_{yn}\sin\theta\cos\varphi)\sin\theta\cos\varphi - (V_{yn}\cos\theta - V_{zn}\sin\theta\sin\varphi)\cos\theta \\ (V_{yn}\cos\theta - V_{zn}\sin\theta\sin\varphi)\sin\theta\sin\varphi - (V_{zn}\sin\theta\cos\varphi - V_{xn}\cos\theta)\sin\theta\cos\varphi \end{bmatrix}
\end{aligned}
\tag{4.56}
$$

The co and cross-pol vectors base is now projected in the global spherical coordinate system $(\mathbf{e}_r, \mathbf{e}_\theta, \mathbf{e}_\varphi)$ [Balanis, 2005]. The result is shown in equation 4.57. The r component is null since the vectors are in a plane orthogonal to the radius.

$$\begin{aligned}
\mathbf{e}_{\varphi_n\ (\mathbf{e}_r,\mathbf{e}_\theta,\mathbf{e}_\varphi)} &= \frac{1}{\mid V_n \otimes \mathbf{e}_r \mid} \begin{bmatrix} 0 \\ -V_{xn}\sin\varphi + V_{yn}\cos\varphi \\ -V_{xn}\cos\theta\cos\varphi - V_{yn}\cos\theta\sin\varphi + V_{zn}\sin\theta \end{bmatrix} \\
\mathbf{e}_{\theta_n\ (\mathbf{e}_r,\mathbf{e}_\theta,\mathbf{e}_\varphi)} &= \frac{1}{\mid V_n \otimes \mathbf{e}_r \mid} \begin{bmatrix} 0 \\ -V_{xn}\cos\theta\cos\varphi - V_{yn}\cos\theta\sin\varphi + V_{zn}\sin\theta \\ V_{xn}\sin\varphi - V_{yn}\cos\varphi \end{bmatrix}
\end{aligned} \tag{4.57}$$

The final expression of the incoming signal projected in the Hertzian dipole base is given in equation 4.58.

$$\begin{aligned}
E_{C_n} &= \left(E_\theta \frac{1}{\mid V_n \otimes \mathbf{e}_r \mid} (-V_{xn}\cos\theta\cos\varphi - V_{yn}\cos\theta\sin\varphi + V_{zn}\sin\theta) \right. \\
&\quad \left. + E_\varphi e^{j\gamma} \frac{1}{\mid V_n \otimes \mathbf{e}_r \mid} (V_{xn}\sin\varphi - V_{yn}\cos\varphi) \right) e^{j\frac{2\pi}{\lambda}\mathbf{r}_n\cdot\mathbf{e}_r} \\
E_{X_n} &= \left(E_\theta \frac{1}{\mid V_n \otimes \mathbf{e}_r \mid} (-V_{xn}\sin\varphi + V_{yn}\cos\varphi) \right. \\
&\quad \left. + E_\varphi e^{j\gamma} \frac{1}{\mid V_n \otimes \mathbf{e}_r \mid} (-V_{xn}\cos\theta\cos\varphi - V_{yn}\cos\theta\sin\varphi + V_{zn}\sin\theta) \right) e^{j\frac{2\pi}{\lambda}\mathbf{r}_n\cdot\mathbf{e}_r}
\end{aligned} \tag{4.58}$$

The result of equation 4.58 can be inserted into equation 4.40. The Hertzian dipole elements are ideal which removes the cross-pol component $\sqrt{G_{X_n}} = 0$. Finally the equation of the signal model applied to the Hertzian dipole with any orientation is given in equation 4.59.

$$\begin{aligned}
s_n = \frac{\sqrt{G_{C_n}}}{\mid V_n \otimes \mathbf{e}_r \mid} &\left(E_\theta \left(-V_{xn}\cos\theta\cos\varphi - V_{yn}\cos\theta\sin\varphi + V_{zn}\sin\theta\right) \right. \\
&\left. + E_\varphi e^{j\gamma} \left(V_{xn}\sin\varphi - V_{yn}\cos\varphi\right) \right) e^{j\frac{2\pi}{\lambda}\mathbf{r}_n\cdot\mathbf{e}_r}
\end{aligned} \tag{4.59}$$

For ease of calculation, the proportional factors of the gain are not taken into account [Balanis, 2005, p. 159] such as the free space impedance, constant dipole current etc. This leads to the ratio $\frac{\sqrt{G_{C_n}}}{\mid V_n \otimes \mathbf{e}_r \mid}$ being cancelled; as an example, a HZ dipole oriented along z would have a gain $G_C = \sin^2\theta$ and, using equation 4.57, $\mid Z_n \otimes \mathbf{e}_r \mid = \mid \sin\theta \mid$. The simplified signal model is given in equation 4.60.

$$s_n = \left(E_\theta \left(-V_{xn}\cos\theta\cos\varphi - V_{yn}\cos\theta\sin\varphi + V_{zn}\sin\theta\right) + E_\varphi e^{j\gamma} \left(V_{xn}\sin\varphi - V_{yn}\cos\varphi\right) \right) e^{j\frac{2\pi}{\lambda}\mathbf{r}_n\cdot\mathbf{e}_r} \tag{4.60}$$

The signal to noise ratio (SNR) is defined as the power of the incident signal over the noise in the receiver $SNR = \frac{\mathbf{E}^2}{2\sigma^2}$.

In the next part, the signal model will be used in a specific configuration with 4 Hertzian dipoles, following the steps exposed in section 4.3.2.

4.3.4.2 Application to 4 HZ dipoles

Three arrangements are used to study a 3D array. The phase centres of the first arrangement are in a square; a similar arrangement can be found in [Moriya et al., 2012], limited to omni-directional elements. However, for the phase term of the CRLB where the same results would be expected, different expressions are obtained since the CRLB expression in [Moriya et al., 2012] uses the results from [Stoica and Nehorai, 1989] where the signal model considers unknown phase and amplitude. They are assumed to be known in this study. Nevertheless, the study goes further by exploring the effect of directive elements and cross-polarisation.
Case 1: The elements are arranged vertically in a square pattern.
Case 2: The Z-coordinate of two of the four elements is changed to form a 3D array.
Case 3: The orientations of the elements in the plane $z = 0$ are changed.
These different configurations are illustrated in figure 4.22. The signal expressions of each element are derived using equation 4.60. For those calculations, the phase between the components of the incident signal is $\gamma = 0$. To facilitate the calculations, the angle range is reduced to $0° < \theta < 90°$ and $0° < \varphi < 90°$ and the incident signal amplitudes E_θ and E_φ remain positive.

For cases 1 and 2:

All elements are vertical therefore for $n = 1$ to 4, the axis is $[V_{xn}\ V_{yn}\ V_{zn}]^{-1} = [0\ 0\ 1]^{-1}$. The signal expression can be addressed for each element using equation 4.60. Results are given in equation 4.61, in the case 1, $d_z = 0$ and in the case 2 $d_z \neq 0$.

$$\begin{aligned} s_1 &= E_\theta \sin\theta \qquad s_2 = E_\theta \sin\theta e^{j\frac{2\pi d}{\lambda}(\sin\theta\sin\varphi + \frac{d_z}{d}\cos\theta)} \\ s_3 &= E_\theta \sin\theta e^{j\frac{2\pi d}{\lambda}\sin\theta\cos\varphi} \qquad s_4 = E_\theta \sin\theta e^{j\frac{2\pi d}{\lambda}\left(\sin\theta\cos\varphi + \sin\theta\sin\varphi + \frac{d_z}{d}\cos\theta\right)} \end{aligned} \tag{4.61}$$

For case 3:

The first element is oriented along the x-axis $[V_{x1}\ V_{y1}\ V_{z1}]^{-1} = [1\ 0\ 0]^{-1}$ and the fourth element is oriented along the y-axis $[V_{x4}\ V_{y4}\ V_{z4}]^{-1} = [0\ 1\ 0]^{-1}$. The resulting signals are given in equation 4.62.

$$s_1 = -E_\theta \cos\theta \cos\varphi + E_\varphi \sin\varphi \qquad s_2 = E_\theta \sin\theta e^{j\frac{2\pi d}{\lambda}(\sin\theta\sin\varphi + \frac{d_z}{d}\cos\theta)}$$
$$s_3 = E_\theta \sin\theta e^{j\frac{2\pi d}{\lambda}\sin\theta\cos\varphi} \qquad s_4 = -(E_\theta \cos\theta \sin\varphi + E_\varphi \cos\varphi) e^{j\frac{2\pi d}{\lambda}(\sin\theta\cos\varphi + \sin\theta\sin\varphi + \frac{d_z}{d}\cos\theta)} \tag{4.62}$$

To reach the FIM expression, the norm and derivation of those expressions have to be calculated using the model given in equation 4.41. The phase is given directly in the FIM expression.

For cases 1 and 2:

$$\rho_1 = E_\theta \sin\theta = \rho_2 = \rho_3 = \rho_4 \tag{4.63}$$

The derivatives of the signals follow:

$$\begin{aligned} \frac{\partial\rho_1}{\partial\theta} &= E_\theta \cos\theta = \frac{\partial\rho_2}{\partial\theta} = \frac{\partial\rho_3}{\partial\theta} = \frac{\partial\rho_4}{\partial\theta} \\ \frac{\partial\rho_1}{\partial\varphi} &= 0 = \frac{\partial\rho_2}{\partial\varphi} = \frac{\partial\rho_3}{\partial\varphi} = \frac{\partial\rho_4}{\partial\varphi} \end{aligned} \tag{4.64}$$

For case 3: Depending on the incident signal direction, the expression of the absolute value (signal is real) is different, depending on the sign of the expression.

$$\begin{aligned} \rho_1 &= -E_\theta \cos\theta\cos\varphi + E_\varphi \sin\varphi \ \text{IF} \ -E_\theta \cos\theta\cos\varphi + E_\varphi \sin\varphi > 0 \\ \rho_1 &= -(-E_\theta \cos\theta\cos\varphi + E_\varphi \sin\varphi) \ \text{IF} \ -E_\theta \cos\theta\cos\varphi + E_\varphi \sin\varphi < 0 \\ \rho_2 &= E_\theta \sin\theta = \rho_3 \\ \rho_4 &= E_\theta \cos\theta \sin\varphi + E_\varphi \cos\varphi \end{aligned} \tag{4.65}$$

The derivatives of the signals follow.

$$\begin{aligned} &\frac{\partial\rho_1}{\partial\theta} = E_\theta \sin\theta\cos\varphi \quad \frac{\partial\rho_1}{\partial\varphi} = (E_\theta \cos\theta\sin\varphi + E_\varphi\cos\varphi) \ \text{IF} \ -E_\theta\cos\theta\cos\varphi + E_\varphi\sin\varphi > 0 \\ &\frac{\partial\rho_1}{\partial\theta} = -E_\theta \sin\theta\cos\varphi \quad \frac{\partial\rho_1}{\partial\varphi} = -(E_\theta \cos\theta\sin\varphi + E_\varphi\cos\varphi) \ \text{IF} \ -E_\theta\cos\theta\cos\varphi + E_\varphi\sin\varphi < 0 \\ &\frac{\partial\rho_2}{\partial\theta} = E_\theta\cos\theta = \frac{\partial\rho_3}{\partial\theta} \quad \frac{\partial\rho_2}{\partial\varphi} = 0 = \frac{\partial\rho_3}{\partial\varphi} \\ &\frac{\partial\rho_4}{\partial\theta} = -E_\theta \sin\theta\sin\varphi \quad \frac{\partial\rho_4}{\partial\varphi} = (E_\theta\cos\theta\cos\varphi - E_\varphi\sin\varphi) \end{aligned} \tag{4.66}$$

The absolute values in equation 4.66 cancel in the covariance term $FIM_{\theta\varphi}$ with the product $\frac{\partial|s_1|}{\partial\theta}\frac{\partial|s_1|}{\partial\varphi}$ as well as in the variance terms $FIM_{\theta\theta}$ and $FIM_{\varphi\varphi}$ due to the square.

This results in removing the cases for the following calculations. The FIM results for each case follow in equations 4.67, 4.68 and 4.69:

For case 1:

$$\begin{aligned} FIM_{\theta\theta} &= \frac{1}{\sigma^2}\left[4\left(E_\theta \cos\theta\right)^2 + \left(\frac{2\pi d}{\lambda} E_\theta \sin\theta\cos\theta\right)^2 \left(1 + \left(\cos\varphi + \sin\varphi\right)^2\right)\right] \\ FIM_{\varphi\varphi} &= \frac{1}{\sigma^2}\left(E_\theta \sin^2\theta \frac{2\pi d}{\lambda}\right)^2 \left(1 + \left(\cos\varphi - \sin\varphi\right)^2\right) \\ FIM_{\theta\varphi} &= \frac{1}{\sigma^2}\left(E_\theta \sin\theta\right)^2 \left(\frac{2\pi d}{\lambda}\right)^2 \cos\theta\sin\theta\left(\cos^2\varphi - \sin^2\varphi\right) \end{aligned} \tag{4.67}$$

For case 2:

$$\begin{aligned} FIM_{\theta\theta} &= \frac{1}{\sigma^2}\left[4\left(E_\theta \cos\theta\right)^2 + \left(E_\theta \sin\theta \frac{2\pi d}{\lambda}\right)^2 \left(\left(\cos\theta\sin\varphi - \frac{d_z}{d}\sin\theta\right)^2 \right.\right. \\ &\quad \left.\left. + \left(\cos\theta\cos\varphi - \frac{d_z}{d}\sin\theta\right)^2 + \left(\cos\theta\left(\cos\varphi + \sin\varphi\right)\right)^2\right)\right] \\ FIM_{\varphi\varphi} &= \frac{1}{\sigma^2}\left[\left(E_\theta \sin^2\theta \frac{2\pi d}{\lambda}\right)^2 \left(1 + \left(\cos\varphi - \sin\varphi\right)^2\right)\right] \\ FIM_{\theta\varphi} &= \frac{1}{\sigma^2}\left[\left(E_\theta \sin\theta \frac{2\pi d}{\lambda}\right)^2 \left(\left(\cos\theta\sin\varphi - \frac{d_z}{d}\sin\theta\right)\sin\theta\cos\varphi \right.\right. \\ &\quad \left.\left. - \left(\cos\theta\cos\varphi - \frac{d_z}{d}\sin\theta\right)\sin\theta\sin\varphi + \cos\theta\sin\theta\left(\cos^2\varphi - \sin^2\varphi\right)\right)\right] \end{aligned} \tag{4.68}$$

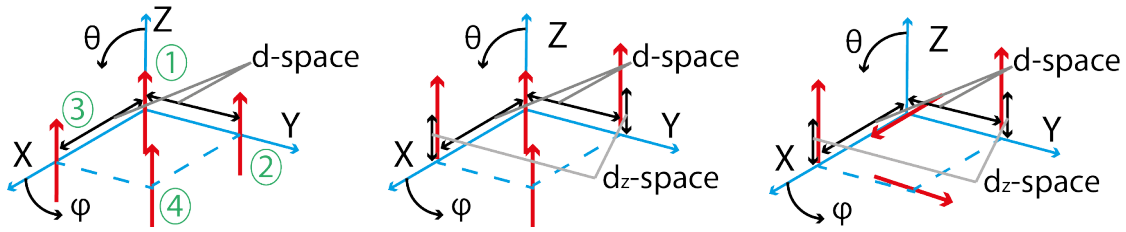

(a) Case 1 (b) Case 2 (c) Case 3

Figure 4.22: The 3 array arrangements

For case 3:

$$
\begin{aligned}
FIM_{\theta\theta} = \frac{1}{\sigma^2}\Bigg[& \left(E_\theta \sin\theta\cos\varphi\right)^2 + 2\left(E_\theta\cos\theta\right)^2 + \left(E_\theta\sin\theta\sin\varphi\right)^2 \\
& + \left(E_\theta\sin\theta\right)^2\left(2\pi\frac{d}{\lambda}\right)^2\left(\left(\cos\theta\sin\varphi - \frac{d_z}{d}\sin\theta\right)^2 + \left(\cos\theta\cos\varphi - \frac{d_z}{d}\sin\theta\right)^2\right) \\
& + \left(E_\theta\cos\theta\sin\varphi + E_\varphi\sin\varphi\right)^2\left(2\pi\frac{d}{\lambda}\right)^2\cos^2\theta\left(\cos\varphi + \sin\varphi\right)^2\Bigg] \\
FIM_{\varphi\varphi} = \frac{1}{\sigma^2}\Bigg[& \left(E_\theta\cos\theta\sin\varphi + E_\varphi\cos\varphi\right)^2 + \left(E_\theta\cos\theta\cos\varphi - E_\varphi\sin\varphi\right)^2 \\
& + \left(E_\theta\sin\theta\right)^2\left(2\pi\frac{d}{\lambda}\right)^2\sin^2\theta + \left(E_\theta\cos\theta\sin\varphi + E_\varphi\cos\varphi\right)^2\left(2\pi\frac{d}{\lambda}\sin\theta\right)^2\left(\cos\varphi - \sin\varphi\right)^2\Bigg] \\
FIM_{\theta\varphi} = \frac{1}{\sigma^2}\Bigg[& E_\theta\sin\theta\cos\varphi\left(E_\theta\cos\theta\sin\varphi + E_\varphi\cos\varphi\right) - E_\theta\sin\theta\sin\varphi\left(E_\theta\cos\theta\cos\varphi - E_\varphi\sin\varphi\right) \\
& + \left(E_\theta\sin\theta\right)^2\left(2\pi\frac{d}{\lambda}\right)^2\left(\left(\cos\theta\sin\varphi - \frac{d_z}{d}\sin\theta\right)\sin\theta\cos\varphi - \left(\cos\theta\cos\varphi - \frac{d_z}{d}\sin\theta\right)\sin\theta\sin\varphi\right) \\
& + \left(E_\theta\cos\theta\sin\varphi + E_\varphi\cos\varphi\right)^2\left(2\pi\frac{d}{\lambda}\right)^2\cos\theta\sin\theta\left(\cos^2\varphi - \sin^2\varphi\right)\Bigg]
\end{aligned}
\tag{4.69}
$$

Finally, the expression of the CRLB is obtained by inverting the FIM matrix, as given in equation 4.70. The full expression is not derived since no simplification results.

$$
\begin{aligned}
CRLB_{\varphi\varphi} &= \frac{FIM_{\theta\theta}}{FIM_{\theta\theta}FIM_{\varphi\varphi} - FIM_{\theta\varphi}^2} \\
CRLB_{\theta\theta} &= \frac{FIM_{\varphi\varphi}}{FIM_{\theta\theta}FIM_{\varphi\varphi} - FIM_{\theta\varphi}^2}
\end{aligned}
\tag{4.70}
$$

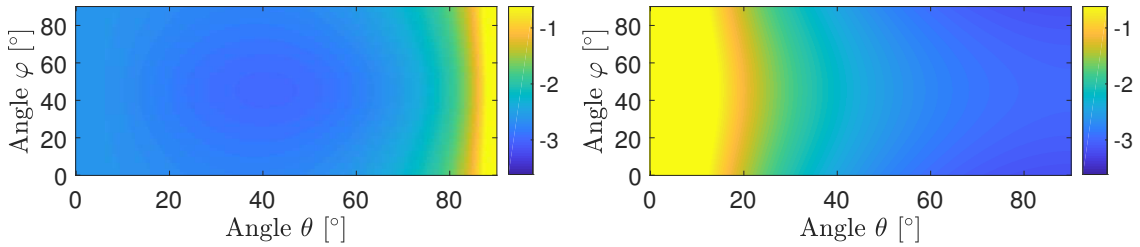

(a) $CRLB_{\theta\theta}$ (b) $CRLB_{\varphi\varphi}$

Figure 4.23: CRLB matrixes, $SNR = 20$dB, case 1

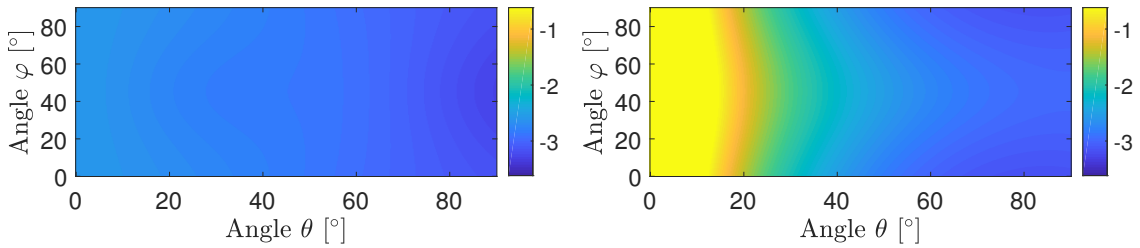

(a) $CRLB_{\theta\theta}$ (b) $CRLB_{\varphi\varphi}$

Figure 4.24: CRLB matrixes, $SNR = 20$dB, case 2

4.3.4.3 Results

Simulations are executed with incident signal components $E_\theta = E_\varphi = 1/\sqrt{2}$ and $\gamma = 0$, so that the incident polarisation is linear with a 45° angle and $SNR = 20$dB. The results of the configuration 1, 2 and 3 are shown respectively in Figures 4.23, 4.24 and 4.25. The lower limit of the colour scales is the minimum over all the configurations; the scales have a 3dB span. In first configuration, it is difficult to estimate the θ angle from $\theta = 80°$ to $\theta = 90°$ and the φ angle from $\theta = 0°$ to $\theta = 25°$. As a first step, moving some elements over to the axis Z (case 2) increases the elevation estimation performance while maintaining the elevation performance. From $\theta = 80°$ to $\theta = 90°$ the bound decreases by 3dB although the bound remains constant along all other

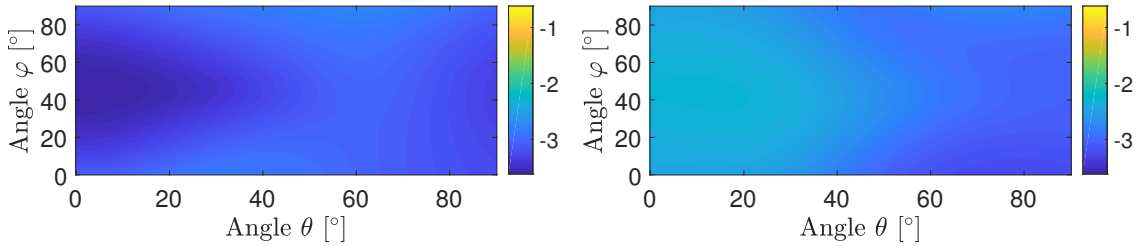

(a) $CRLB_{\theta\theta}$ (b) $CRLB_{\varphi\varphi}$

Figure 4.25: CRLB matrixes, $SNR = 20$dB, case 3

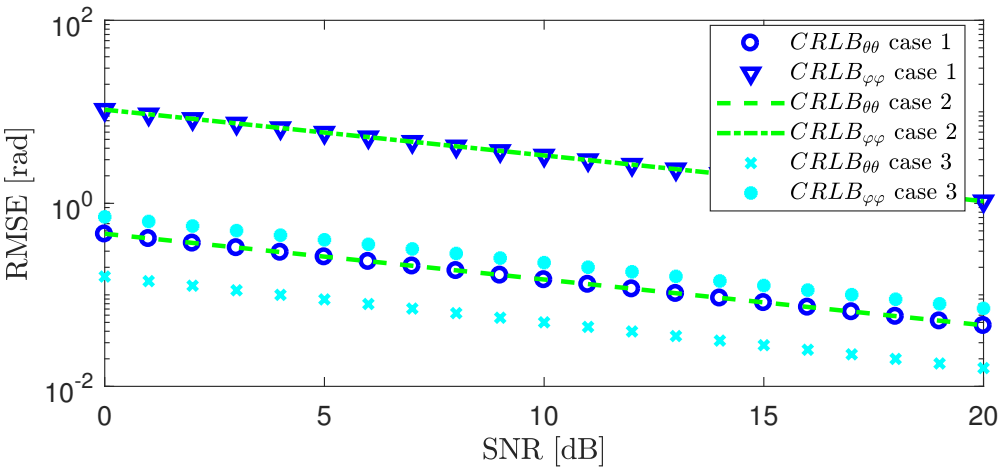

Figure 4.26: CRLB, sweep over the SNR ($\theta = 30°, \varphi = 45°$)

directions. Finally, bringing orientation diversity for the elements (case 3) lowers the bound for the θ angle while strongly lowering the bound for the φ angle: at least 3dB from $\theta = 0°$ to $\theta = 6°$ and at least 1dB from $\theta = 6°$ to $\theta = 20°$.

In the same conditions, the signal direction is fixed and the SNR is swept: $SNR =$ 0dB to $SNR = 20$dB. Results are given in Fig. 4.26. Again, the $CRLB_{\theta\theta}$ is better than $CRLB_{\varphi\varphi}$. The bound is inversely proportional to the SNR (scales are in log). This comes from the equations which could be written as $CRLB = \sigma^2 \cdot f(\theta, \varphi) = \frac{\mathbf{E^2}}{2SNR} \cdot f(\theta, \varphi)$.

These results confirm the interest of 3D and conformal arrays over 2D arrays. In this first approach which does not consider cross-polarisation, orientation diversity has been demonstrated to increase the DOA performance of the array. The modelling of the estimation of antenna also goes one step further by taking into account the incident signal and the element radiation pattern. In the following sections, the cross-polarisation is considered and its effect on the estimation performance of the antenna is studied.

4.3.4.4 Effect of the deterministic known cross-polarisation phase

So far, in this thesis, the Hertzian dipole has been studied with $\sqrt{G_{X_n}} = 0$. However, the cross-polarisation effect is intrinsic to antennas, therefore a better model should take it into account. The effect of the cross-pol phase ϕ_{c_n} on the estimation performance is explored. Firstly the cross-pol phase is considered to be deterministic known and secondly it is considered as deterministic unknown.

In both cases, the cross-polarisation phase is constant over all the directions and it is only added to the first element, the cross-pol gain is set to $\sqrt{G_{X_n}} = 1$ in all the directions. The new signal model for s_1 is given in equation 4.58, s_2, s_3 and s_4 remain

unchanged.

$$s_1 = E_\theta \sin\theta + E_\varphi e^{j\phi_{c_n}} \tag{4.71}$$

The signal is transformed into its module and phase, as shown in equation 4.41. The expression of ρ_1 and ϕ_1 are given in equation 4.72.

$$\rho_1 = \sqrt{(E_\theta \sin\theta + E_\varphi \cos\phi_{c_n})^2 + (E_\varphi \sin\phi_{c_n})^2} \quad \phi_1 = \arctan \frac{E_\varphi \sin\phi_{c_n}}{E_\theta \sin\theta + E_\varphi \cos\phi_{c_n}} \tag{4.72}$$

To obtain the FIM, the terms along θ and φ are derived; the results are given in equation 4.73.

$$\begin{aligned} \frac{\partial\rho_1}{\partial\theta} &= \frac{E_\theta \cos\theta(E_\theta \sin\theta + E_\varphi \cos\phi_{c_n})}{\rho_1} \quad \frac{\partial\rho_1}{\partial\varphi} = 0 \\ \frac{\partial\phi_1}{\partial\theta} &= \frac{-E_\varphi \sin\phi_{c_n} E_\theta \cos\theta}{\rho_1^2} \quad \frac{\partial\phi_1}{\partial\varphi} = 0 \end{aligned} \tag{4.73}$$

The calculation of $FIM_{\theta\theta}$ is shown in Appendix B and as a result the same expression is found as without cross polarisation phase (equation 4.67). $FIM_{\varphi\varphi}$ and $FIM_{\theta\varphi}$ remain unchanged since the derivative respective to φ cancels, as shown in equation 4.73. As a conclusion, since the FIM matrix does not change, the CRLB expression also remains unchanged, which means that, for this configuration, cross-polarisation does not affect the estimation performance.

4.3.4.5 Effect of the deterministic unknown cross-polarisation phase

A more realistic model would take into account the need to estimate the cross-polarisation phase; therefore it is now considered as deterministic unknown. This changes the FIM into a 3x3 matrix, as shown in equation 4.74.

$$FIM = -E\begin{bmatrix} \frac{\partial^2}{\partial\theta^2}\ln PDF(\theta,\varphi,\phi_{c_n}) & \frac{\partial^2}{\partial\theta\partial\varphi}\ln PDF(\theta,\varphi,\phi_{c_n}) & \frac{\partial^2}{\partial\theta\partial\phi_{c_n}}\ln PDF(\theta,\varphi,\phi_{c_n}) \\ \frac{\partial^2}{\partial\varphi\partial\theta}\ln PDF(\theta,\varphi,\phi_{c_n}) & \frac{\partial^2}{\partial\varphi^2}\ln PDF(\theta,\varphi,\phi_{c_n}) & \frac{\partial^2}{\partial\varphi\partial\phi_{c_n}}\ln PDF(\theta,\varphi,\phi_{c_n}) \\ \frac{\partial^2}{\partial\phi_{c_n}\partial\theta}\ln PDF(\theta,\varphi,\phi_{c_n}) & \frac{\partial^2}{\partial\phi_{c_n}\partial\varphi}\ln PDF(\theta,\varphi,\phi_{c_n}) & \frac{\partial^2}{\partial\phi_{c_n}^2}\ln PDF(\theta,\varphi,\phi_{c_n}) \end{bmatrix} \tag{4.74}$$

The terms FIM_{11}, FIM_{12}, FIM_{21} and FIM_{22} remain unchanged, as shown previsouly with the deterministic known phase. The new terms are found with the model given in equation 4.44; results are shown in equation 4.75.

$$
\begin{aligned}
FIM_{\theta\phi_{c_n}} &= -E\left[\frac{\partial^2}{\partial\theta\partial\phi_{c_n}}\ln PDF(\theta,\varphi,\phi_{c_n})\right] \\
&= \frac{1}{\sigma^2}\sum_n\left[\frac{\partial\rho_n}{\partial\theta}\frac{\partial\rho_n}{\partial\phi_{c_n}} + \rho_n^2\frac{\partial\frac{2\pi}{\lambda}\mathbf{r}_n\cdot\mathbf{e}_r+\phi_n}{\partial\theta}\frac{\partial\frac{2\pi}{\lambda}\mathbf{r}_n\cdot\mathbf{e}_r+\phi_n}{\partial\phi_{c_n}}\right] \\
FIM_{\varphi\phi_{c_n}} &= -E\left[\frac{\partial^2}{\partial\varphi\partial\phi_{c_n}}\ln PDF(\theta,\varphi,\phi_{c_n})\right] \\
&= \frac{1}{\sigma^2}\sum_n\left[\frac{\partial\rho_n}{\partial\varphi}\frac{\partial\rho_n}{\partial\phi_{c_n}} + \rho_n^2\frac{\partial\frac{2\pi}{\lambda}\mathbf{r}_n\cdot\mathbf{e}_r+\phi_n}{\partial\varphi}\frac{\partial\frac{2\pi}{\lambda}\mathbf{r}_n\cdot\mathbf{e}_r+\phi_n}{\partial\phi_{c_n}}\right] \\
FIM_{\phi_{c_n}\phi_{c_n}} &= -E\left[\frac{\partial^2}{\partial\phi_{c_n}^2}\ln PDF(\theta,\varphi,\phi_{c_n})\right] = \frac{1}{\sigma^2}\sum_n\left[\left(\frac{\partial\rho_1}{\partial\phi_{c_n}}\right)^2 + \left(\rho_n\frac{\partial\frac{2\pi}{\lambda}\mathbf{r}_n\cdot\mathbf{e}_r+\phi_n}{\partial\phi_{c_n}}\right)^2\right]
\end{aligned}
\tag{4.75}
$$

To calculate those terms, the derivatives of the signal norm and phase with respect to ϕ_{c_n} are required; their expressions are shown in equation 4.76.

$$
\frac{\partial\rho_1}{\partial\phi_{c_n}} = \frac{-E_\theta\sin(\theta)E_\varphi\sin\phi_{c_n}}{\rho_1} \quad \frac{\partial\phi_1}{\partial\phi_{c_n}} = \frac{E_\varphi\cos(\phi_{c_n})E_\theta\sin\theta + E_\varphi^2}{\rho_1^2} \tag{4.76}
$$

As shown in equation 4.73, the derivation of the signal norm along φ cancels and since the phase delay does not depend on ϕ_{c_n} its derivate cancels the phase term which then cancels the $FIM_{\varphi\phi_{c_n}}$. The expressions of $FIM_{\theta\phi_{c_n}}$ and $FIM_{\phi_{c_n}\phi_{c_n}}$ are given in equation 4.77.

$$
\begin{aligned}
FIM_{\phi_{c_n}\phi_{c_n}} &= \frac{1}{\sigma^2}\frac{1}{\rho_1^2}\left[\left(E_\theta\sin\theta E_\varphi\sin\phi_{c_n}\right)^2 + \left(E_\varphi\cos\phi_{c_n}E_\theta\sin\theta + E_\varphi^2\right)^2\right] \\
FIM_{\theta\phi_{c_n}} &= \frac{-1}{\sigma^2}\frac{1}{\rho_1^2}\left(E_\theta\cos\theta E_\varphi\sin\phi_{c_n}\right)\left[E_\theta\sin\theta\left(E_\theta\sin\theta + E_\varphi\cos\phi_{c_n}\right)\right. \\
&\quad \left. + \left(E_\varphi\cos\phi_{c_n}E_\theta\sin\theta + E_\varphi^2\right)\right]
\end{aligned}
\tag{4.77}
$$

Major simplifications may be preferred for the expression of both the determinant of the FIM and for the CRLB, as shown in equation 4.78.

$$
\begin{aligned}
|\,FIM\,| &= FIM_{\varphi\varphi}(FIM_{\theta\theta}FIM_{\phi_{c_n}\phi_{C_n}} - FIM_{\theta\phi_{c_n}}^2) \\
CRLB_{\theta\theta} &= \frac{1}{FIM_{\theta\theta} - \frac{FIM_{\theta\phi_{c_n}}^2}{FIM_{\phi_{c_n}\phi_{C_n}}}} \\
CRLB_{\varphi\varphi} &= \frac{1}{FIM_{\varphi\varphi}}
\end{aligned}
\tag{4.78}
$$

As a result, the estimation performance of the angle φ does not depend on the cross-polarisation phase ϕ_{c_n}. When $\phi_{c_n} = 0°$ or $\phi_{c_n} = 180°$ which cancels $FIM_{\theta\phi_{c_n}}$, the

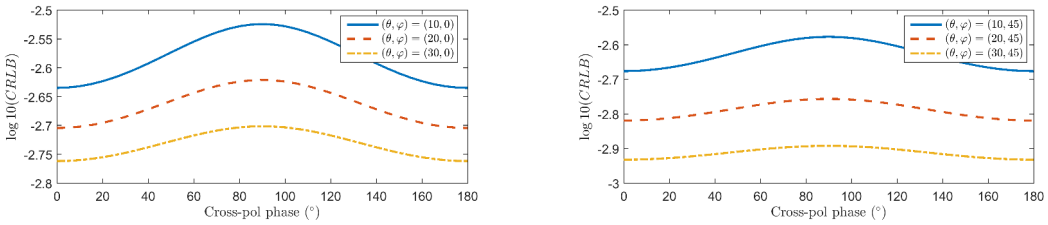

(a) Direction $(\theta = X, \varphi = 0)$ (b) Direction $(\theta = X, \varphi = 45)$

Figure 4.27: $CRLB_{\theta\theta}$ with cross-pol phase, $SNR = 20$dB

$CRLB_{\theta\theta}$ is minimized. The variations of $CRLB_{\theta\theta}$ are shown in Figure 4.27; as expected a minimum is obtained for $\phi_{c_n} = 0°$. The incident signal polarisation is linear, slanted at 45° with a null phase and when the antenna polarisation is null too ($\phi_{c_n} = 0°$) the estimation performance is the best. For the cross-pol phase, however, the estimation performance decreases. The effect of the cross-polarisation phase decreases as the θ angle increases. In figure 4.27, for $\varphi = 0°$, the amplitude of the variations in the direction $\theta = 10°$ is 0.11dB and in direction $\theta = 30°$ it gives 0.06dB.

4.4 Phase monopulse limitations and polarisation purity

4.4.1 Phase monopulse and polarisation purity

A strong polarisation purity is sought for both planar and 3D conformal arrays, as shown in the literature review. In this section, an explanation related to the monopulse is proposed, using the model previously discussed.

Three cases are considered to understand the effect of the cross-pol component. First, for a planar array with a high polarisation purity; second with a 3D conformal array with a high polarisation purity and third with a 3D conformal array with a low polarisation purity.

The expression of the signal received by each quadrant of an array consisting of N elements is shown in equation 4.79. Each quadrant has $\frac{N}{2}$ elements. The radiating elements are considered with single access and the noise is not taken into account.

Equation 4.79 relates the signal received at each element to the signal received at each quadrant. The first quadrant resulting signal has a co-pol and cross-pol complex component S_{Q1C}, S_{Q1X}; those signals have a phase ϕ_{C1}. This quadrant phase centre is referenced from the antenna phase centre, represented by a phase $e^{j\phi_{Q1}}$. Same notations are used for the second quadrant.

$$
\begin{aligned}
V_{c1} &= \sum_{n=1}^{\frac{N}{2}} \left(\sqrt{G_{C_n}} E_{C_n} + \sqrt{GX_{C_n}} E_{X_n} e^{j\phi_{c_n}} \right) = \left(S_{Q1C} + S_{Q1X} e^{j\phi_{C1}} \right) e^{j\phi_{Q1}} \\
V_{c2} &= \sum_{\frac{N}{2}+1}^{N} \left(\sqrt{G_{C_n}} E_{C_n} + \sqrt{GX_{C_n}} E_{X_n} e^{j\phi_{c_n}} \right) = \left(S_{Q2C} + S_{Q2X} e^{j\phi_{C2}} \right) e^{j\phi_{Q2}}
\end{aligned}
\tag{4.79}
$$

4.4.1.1 Case 1

The quadrants are part of a planar array with a high polarisation purity $G_{C_n} >> G_{X_n}$ and the voltage signals are $V_{c1} = S_{Q1C} e^{\phi_{Q1}}$ and $V_{c2} = S_{Q2C} e^{\phi_{Q2}}$.

For planar arrays, the complex amplitude signal received by each quadrant is the same $S_{Q1C} = S_{Q2C}$ which produces the monopulse ratio, as shown in equation 4.80, from which the target angle can be estimated.

$$
\frac{V_{c1} - V_{c2}}{V_{c1} + V_{c2}} = \frac{S_{Q1C} e^{j\phi_{Q1}} - S_{Q2C} e^{j\phi_{Q2}}}{S_{Q1C} e^{j\phi_{Q1}} + S_{Q2C} e^{j\phi_{Q2}}} = \frac{e^{j\phi_{Q1}} - e^{j\phi_{Q2}}}{e^{j\phi_{Q1}} + e^{j\phi_{Q2}}} \tag{4.80}
$$

4.4.1.2 Case 2

If the array has a 3D conformal shape and a high polarisation purity, the monopulse ratio cannot simplify and its expression is shown in equation 4.81.

$$
\frac{V_{c1} - V_{c2}}{V_{c1} + V_{c2}} = \frac{S_{Q1C} e^{j\phi_{Q1}} - S_{Q2C} e^{j\phi_{Q2}}}{S_{Q1C} e^{j\phi_{Q1}} + S_{Q2C} e^{j\phi_{Q2}}} \tag{4.81}
$$

Using the monopulse slope approximation, the target angle can again be estimated. In the next section, a method to overcome this limitation is proposed.

4.4.1.3 Case 3

If the array has a 3D conformal shape and a low polarisation purity, its expression is shown in equation 4.82.

$$
\frac{V_{c1} - V_{c2}}{V_{c1} + V_{c2}} = \frac{\left(S_{Q1C} + S_{Q1X} e^{j\phi_{C1}} \right) e^{j\phi_{Q1}} - \left(S_{Q2C} + S_{Q2X} e^{j\phi_{C2}} \right) e^{j\phi_{Q2}}}{\left(S_{Q1C} + S_{Q1X} e^{j\phi_{C1}} \right) e^{j\phi_{Q1}} + \left(S_{Q2C} + S_{Q2X} e^{j\phi_{C2}} \right) e^{j\phi_{Q2}}} \tag{4.82}
$$

The co-pol and the cross-pol components have similar amplitude levels, furthermore the quadrants have different amplitudes, therefore no simplification occurs. The estimation performance may be degraded compared to the planar case for different reasons.

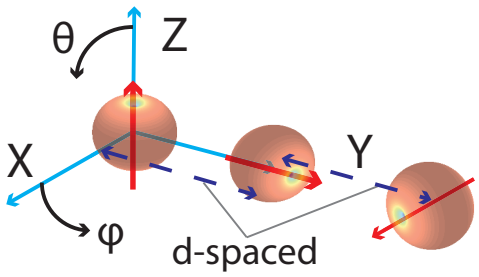

Figure 4.28: Configuration of the 3 orthogonal Hertzian dipoles

- The co-pol and cross-pol components can interfere with and degrade each other if they are not in phase.
- The cross-pol component has variations of amplitude from one element to another which makes the modelling difficult and would impact upon the monopulse slope.
- The radome affects differently the co-pol and the cross-pol components; this also complicates the modelling of the monopulse slope.

RF-seekers today have high polarisation purity. Therefore, to ease the change of antenna technology, a strong polarisation purity is preferred. As shown in this section, a low polarisation purity complicates the modelling and therefore the robustness of the estimator and its measurements.

In the next section, the limitations of the phase monopulse using an analytical expression for non-identical quadrants is shown and a solution is proposed.

4.4.2 Hybrid phase amplitude monopulse

In this section, the limitations of the well-known phase monopulse estimator for direction of arrival are detailed when applied to non-identical quadrants. Different beams for each quadrant appear when a 3D and conformal antenna design is used leading to difficulties in calculating the bearing direction of a signal. Therefore an alternative is explored: a hybrid monopulse. In this section, an array made of 3 Hertzian dipoles illustrates the abilities of such a new estimator.

The phase monopulse is a target angle estimator often used for direction of arrival as an approximation of the maximum likelihood estimator [Nickel, 2006]. This method requires one pulse to determine a signal direction of arrival. In emission, the array sends a pulse on to a target. In reception the array is divided into two quadrants Q_1 and Q_2; each of them processes the target echo. The phase delay between the two signals allows the incoming signal direction to be estimated.

The phase monopulse is carried out by taking the imaginary part of the ratio of the signal difference Δ over the signal sum Σ. In this method the quadrant beams

are parallel. As a result when the target is centred on the quadrants beam, the signal received by each quadrant is the same and the ratio cancels. This estimator is usually carried out with identical quadrants and planar arrays. Equation 4.83 shows that the phase is reached from the signal ratio by calculating the inverse of the tangent.

$$\frac{\Delta}{\Sigma} = \frac{Q_1 - Q_1 e^{j\varphi_0}}{Q_1 + Q_1 e^{j\varphi_0}} = \frac{1 - e^{j\varphi_0}}{1 + e^{j\varphi_0}} = \frac{e^{-j\frac{\varphi_0}{2}} - e^{j\frac{\varphi_0}{2}}}{e^{-j\frac{\varphi_0}{2}} + e^{j\frac{\varphi_0}{2}}} = -j\tan\left(\frac{\varphi_0}{2}\right) \tag{4.83}$$

Where Q_1 is the quadrant amplitude and φ_0 is the phase delay between the quadrants.

The limits of the phase monopulse are reached when used for 3D and conformal antennas since it will induce non identical quadrants. The phase delay cannot be reached anymore and therefore the angle cannot be estimated directly from the imaginary part, as shown in equation 4.84.

$$\begin{gathered}\frac{\Delta}{\Sigma} = \frac{Q_1 - Q_2 e^{j(\varphi_0+\varphi_1)}}{Q_1 + Q_2 e^{j(\varphi_0+\varphi_1)}} = \frac{Q_1(1 - \frac{Q_2}{Q_1}e^{j(\varphi_0+\varphi_1)})}{Q_1(1 + \frac{Q_2}{Q_1}e^{j(\varphi_0+\varphi_1)})} = \frac{1 - ae^{j(\varphi_0+\varphi_1)}}{1 + ae^{j(\varphi_0+\varphi_1)}} = \frac{1 - 2ja\sin(\varphi_0+\varphi_1) - a^2}{1 + a^2 + 2a\cos(\varphi_0+\varphi_1)} \\ Re\left(\frac{\Delta}{\Sigma}\right) = \frac{1 - a^2}{1 + a^2 + 2a\cos(\varphi_0+\varphi_1)} \quad Im\left(\frac{\Delta}{\Sigma}\right) = \frac{-2a\sin(\varphi_0+\varphi_1)}{1 + a^2 + 2a\cos(\varphi_0+\varphi_1)}\end{gathered} \tag{4.84}$$

Where $a = \left\|\frac{Q_2}{Q_1}\right\|$ and $\varphi_1 = \arg(\frac{Q_2}{Q_1})$.

As a verification, when the quadrants are identical ($a = 1$), the real part cancels out. To counteract the limitations of the phase monopulse for 3D and conformal arrays, a new method consists of carrying out the ratio of the imaginary part over the real part of the ratio.

$$\frac{Im\left(\frac{\Delta}{\Sigma}\right)}{Re\left(\frac{\Delta}{\Sigma}\right)} = \frac{-2a}{1 - a^2}\sin(\varphi_0 + \varphi_1) \tag{4.85}$$

This method is tested on the 3 orthogonal dipoles, as shown in Figure 4.28. The first quadrant includes the Z-oriented and Y-oriented dipoles, the second one is made of the X-oriented element. The voltage signals as a function of the angles are given in equation 4.61. The scenario where the angle $\varphi = 90°$ is studied and the angle θ is estimated to be a true value, fixed to $\theta = 5°$. The $CRLB_{\theta\theta}$ is calculated by inversion of the term FIM_{11} in equation 4.43. A sweep over the SNR is performed, for each SNR value 10 000 Monte-Carlo simulations are executed in order to have a precise variance.

The results are shown in Figure 4.29. The phase monopulse is unable to determine the angle of arrival, as shown by the constant variance of the estimator. However, the hybrid monopulse can perform this calculation since the variance of the estimator decreases as a function of the SNR.

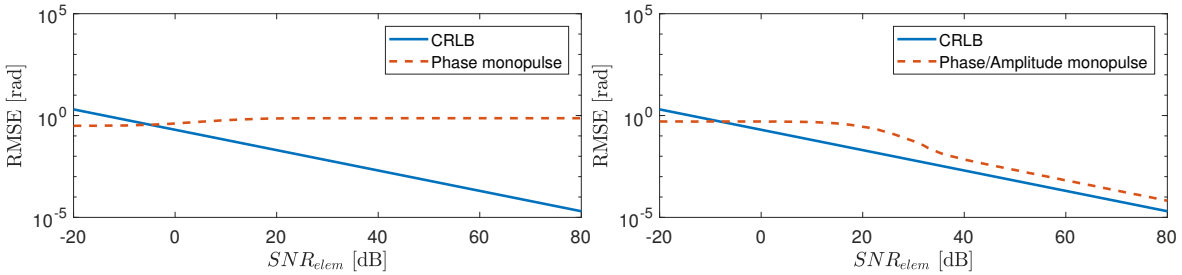

(a) Phase monopulse (b) Hybrid monopulse

Figure 4.29: Phase Monopulse and the Hybrid monopulse alternative

4.5 Conclusion

A model has been developed to study the variance of the phase monopulse for the estimation of the elevation angle for any given array. This model uses the monopulse approximation and is valid at high SNR. This model shows the limitations of the monopulse slope approximation; it has been shown that an RF-sekeer that uses the analytical expression of the phase monopulse ratio would provide a more accurate estimation.

The phase monopulse estimator uses the signal coming from the two quadrant phase centres. This estimator is compared to the maximum likelihood estimator that uses the signal coming from each element. As a result, the monopulse estimator is statistically less efficient than the ML estimator. This trend increases with an increasing number of elements and an increasing target angle.

The monopulse for 3D conformal arrays has been demonstrated for a theoretical array made of Hertzian dipoles where their phase centres are arranged in a semi-circle and linear faceted shapes. An optimisation procedure is performed to find the best quadrant configuration and maximise the monopulse slope factor. Finally the 3D conformal shapes have a better slope factor than the planar array as the former can take benefit of the mechanical removal to have more elements. Nevertheless, the 3D conformal arrays can not use all of their elements, depending on the direction, as some elements radiate away from the aimed direction.

The advantage of 3D conformal arrays is theoretically shown using omnidirectional elements. The variance of the elevation angles is lower for 3D conformal arrays than for planar arrays while the azimuthal angle variance is constant. A model is developed for any array and a polarised incident signal in the presence of thermal noise. This model is applied to specific cases consisting of 4 Hertzian dipoles and confirms the interests of 3D conformal arrays and elements orientation diversity.

The effect of the cross-polarisation phase is investigated. In a specific case, it is

observed that if the antenna cross-polarisation phase is matching with that of the incident signal, the variance is at its lowest. Otherwise, the variance increases and is the highest when phases are 90° shifted.

Finally, the limitations of the classic phase monopulse estimator has been shown where the analytical expression of the monopulse ratio is used. Instead, the previously mentioned optimisation, using the monopulse slope, shows its robustness for 3D conformal arrays. Furthermore, it has been shown that a new estimator which makes use of the amplitude and phase monopulse can overcome the phase monopulse limitations for a theoretical case.

General conclusion and perspectives

4.6 Conclusion

AESA antennas are mature today for planar arrays and naturally, antenna manufacturers are looking at AESA for conformal arrays. This thesis focuses on RF-seeker applications, nonetheless, some results remain true for other applications. The effect of 3D and conformation has been investigated, firstly on the electric field properties, and secondly on the direction of arrival estimation.

To realise a progression of antenna technology from the current generation of planar antennas to future 3D conformal antennas, antenna designs made of a planar TOP facet have been studied. A half-sphere antenna has also been considered. To realise all the studies, a Matlab program has been developed to compute fast simulations of complex arrays.

The study considers the position and the orientation of the radiating elements. Their effects on the sidelobes, directivity, ellipticity and polarisation purity have been investigated. The tradeoffs between axially oriented elements and radially oriented elements have been addressed: the axial array has a difference pattern that is not azimuth invariant, however, it has the interest to have a high polarisation purity. The radial or tangent oriented array has an opposite set of characteristics, azimuth invariance and low polarisation purity.

It has been shown that when an antenna array steers its beam by applying a phase shift on the elements excitations, it maintains an almost linear polarisation state in the θ_{-3dB} area. It has also been shown that by projecting the electric field in different coordinate systems depending on the steering angle, it would maintain a high polarisation purity.

If different parts of an array are meant to work coherently, it has been demonstrated that by matching their elements orientation, it improves the polarisation purity, the directivity and the ellipticity.

A half-sphere array has better performance than a fixed planar array with the same diameter and a better coverage. The enhanced directivity is mitigated by an increasing polarisation deviation in the θ_{-3dB} area.

A global comparison has shown that the truncated faceted cone and the truncated cone both present similar performance levels. The half-sphere also presents comparable results, except, for elevation steering angles above 70° which could be counteracted by coupling the half-sphere with a cylinder below. The half-sphere has the smallest variations in directivity as a function of the steering angle. Those comments suggest that the increased manufacturing complexity may not be worth although the curved arrays would not bring an enhanced performance.

The emission/reception directivity product of the truncated faceted cone and the truncated cone is in average 40dB up to a steering angle of 60° which does not reach the 50dB required. The chosen anti-radial orientation for the TOP facet can turn into a radial orientation which presents an invariant monopulse difference pattern and a poor sum pattern. Instead, the selection of an axial orientation would produce a higher directivity and an invariant sum pattern but in the same time, a poor difference pattern.

The direction of arrival estimation for conformal arrays has shown promising results, compared to planar arrays, using simple theoretical array examples, some of them could be derived analytically.

It has been shown that the phase monopulse estimator is not statistically efficient and that the gap between the monopulse and the minimum variance given by the CRLB increases as the target angle or the number of elements increases.

The phase monopulse estimator for 3D conformal arrays has been explored in two forms: using the monopulse slope and using the analytical monopulse ratio. First with the monopulse slope, a model for the RMSE expression has been developed, it is valid for any array. It has also been shown that for 3D conformal arrays made of Hertzian dipoles, the monopulse slope is better than for planar arrays, since the 3D conformal arrays can host more elements thanks to the mechanical system removal. Conversely, some elements may not be radiating since they are away from the aimed direction. Secondly, with the analytical monopulse ratio, it has been shown that it cannot be used to estimate an impinging signal direction with non-identical quadrants, as it would occur with 3D conformal arrays.

The interest of 3D conformal arrays is theoretically shown using omnidirectional elements. The variance of the elevation angles is lower for 3D conformal arrays than for planar arrays, while the azimuthal angle variance is constant. Furthermore, their interest is shown for specific cases, using a model developed for any array and a polarised incident signal in presence of thermal noise. The specific case consists of 4 Hertzian dipoles and confirms the interest of 3D conformal arrays and element orientation diver-

sity. The effect of the cross-polarisation phase is also investigated, the lowest variance is obtained when the incident signal phase and the cross polarisation phase are matching.

4.7 Perspectives

This work presents some results and indications on the preferable antenna array shape and elements orientations in the RF-seeker context. Those results open to new questions and can be extended.

The 3D conformal study has been carried out using theoretical Hertzian dipoles to simplify the study. To go further, dipoles elements could be simulated, and accounting for mutual couplings would also give more realistic results. The simulation of patch element would also be interesting since they can host two access points. Therefore, it would increase the electric field control and allow more flexibility for digital beamsteering. The simulations results should be confirmed by realising experiments.

The direction of arrival estimation study has been addressed in the general case for omnidirectional elements and applied to Hertzian dipoles. Again, this can be improved by developing results using more realistic elements as well as more complex arrays. Furthermore, the proposed hybrid amplitude/phase estimator should be verified by carrying out experiments.

Next challenges for the construction of a 3D conformal antenna will appear with the design of the feeding network and T/R modules. The feeding network needs to be integrated, robust and precisely manufactured and the T/R modules will require an efficient cooling as the density of the active components will increase with the number of elements.

Appendix A

The electric field radiated by a Hertzian dipole and a patch antenna

A.1 The Hertzian dipole

The Hertzian dipole is an ideal and theoretical radiating element, it has a radius null and an infinitesimal length d where $d << \lambda$. This condition keeps the current constant along the dipole as a function of time. It also produces an electric field which is analytically solvable.

The dipole is along the axis Z of a Cartesian coordinate system of which a spherical coordinate system $(\mathbf{e}_r, \mathbf{e}_\theta, \mathbf{e}_\varphi)$ is associated as shown in Figure A.1. From the electrostatic theory, the electric field in far field is contained in the symmetry planes $(\mathbf{e}_r, \mathbf{e}_\theta)$. The plane wave theory assesses that the field is orthogonal to the propagation direction, therefore $\mathbf{E} = E \cdot \mathbf{e}_\theta$. This coincides with the expression of the electric field as shown in equation A.1 [Balanis, 2005, p. 159].

$$\begin{aligned} E_\theta &\simeq j\eta \frac{kI_0 l e^{-jkr}}{4\pi r} \sin\theta \\ E_r &\simeq E_\varphi \simeq 0 \end{aligned} \tag{A.1}$$

The electric field follows a sin law along the θ angle and there is no variations along the φ angle, this is imposed by the symmetry of the element. The sin variation of the field is confirmed by the projection of the dipole length in the different directions.

The directivity can be calculated in a few steps.

$$D = \frac{4\pi \sin^2\theta}{\int_\varphi \int_\theta \sin^3\theta d\theta d\varphi} = \frac{3}{2}\sin^2\theta \tag{A.2}$$

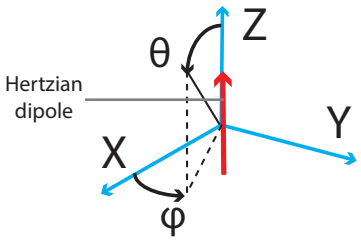

Figure A.1: Hertzian dipole modelised by the arrow

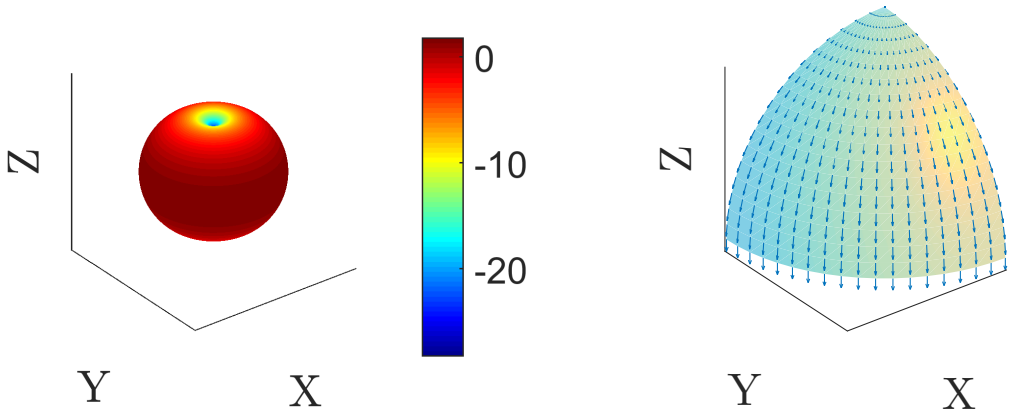

(a) Total directivity [dB]

(b) Vector field **E**

Figure A.2: Radiation pattern of the Hertzian pattern

For $\theta = 0°$ the directivity is null and in $\theta = 90°$ the directivity is maximum and worth 3/2 in linear and 1.76 in dB as shown in Figure A.2a. The field vectors are collinear with the $\mathbf{e}_\theta$ component of the spherical coordinate system which allows to conclude that the polarisation is linear in all the directions as shown in Figure A.2b.

A.2 The patch antenna

The patch antenna is a micro-strip antenna, it has the advantage to be low profile, light, cheap, easy to manufacture and it can be easily conformed. Although it is a simple element, models are required to express its electric field. Two models are known: the cavity and the transmission line model. The transmission line model does not give any physical insight for that reason it is not described here. The cavity model considers the top and bottom metallised layers as two perfect electric conductors (PEC) and the four sides as perfect magnetic conductors (PMC). The two metallised layers behave like a capacity. The electrostatic theory in the cartesian coordinate system as shown in Figure A.3 keeps the electric field in the symmetry planes $(\mathbf{e}_x, \mathbf{e}_y)$ and $(\mathbf{e}_x, \mathbf{e}_z)$. Consequently the electric field is $\mathbf{E} = E\mathbf{e}_x$, it is orthogonal to the metallised layers. The height h is small in front of the width W which guarantees a constant electric field

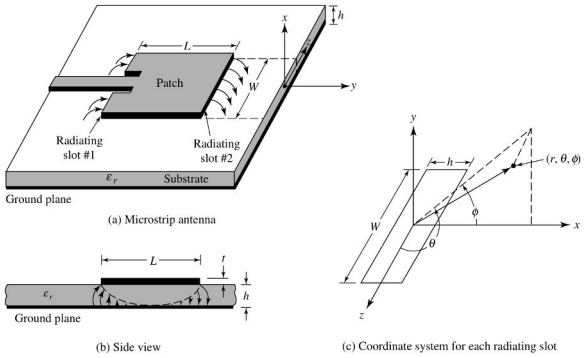

Figure A.3: Patch antenna, cavity and transmission line models

along x. Therefore the resonating mode is the TM^x_{xyz} where the superscript indicates the propagation direction and the subscript the axis along which the modes resonate. Following the cavity model, the fundamental resonates along the smallest patch length, however in practise the feeding probe position imposes the resonance. The probe of the rectangular patch is bonded to the width W and the other patch side is called length L. The length L has a $\frac{\lambda}{2}$ size and in order to have a good impedance matching the width W equals λ. If the length would have the same size as that of the width, the same mode would resonate along both directions which would strengthen the radiation pattern, nonetheless it would also decrease the impedance matching, this is therefore a compromise adaptation versus directivity. Still a square patch is used for circular polarisation with two feeding ports $\frac{\pi}{2}$ out of phase.

The standing wave below the patch travels back and forth along the length and gives a constant electric field along the width. The cavity model considers the two of the four PMC along the width where the electric field is constant as radiating slots and the two left as non radiating slots. This theoretical perfect structure does not radiate, to introduce radiations a loss has to be accounted. Finally, from the radiating slots considered as an array of two apertures, an analytical expression of the electric field can be found in [Balanis, 2005, p. 835].

$$\begin{aligned} E_{\mathbf{r}} &\approx E_\theta \approx 0 \\ E_\varphi &= j\frac{k_0 h W E_0 e^{-jk_0 r}}{2\pi r}\sin\theta\frac{\sin X}{X}\frac{\sin Z}{Z} \\ X &= \frac{k_0 h}{2}\sin\theta\cos\varphi \\ Z &= \frac{k_0 W}{2}\cos\theta \end{aligned} \tag{A.3}$$

The orientation chosen by Dr. Balanis allows to express the field in a single component. In practise, the E_θ component is not null.

The resulting radiation pattern is given in Figure A.4a and A.4b. The flat radiation

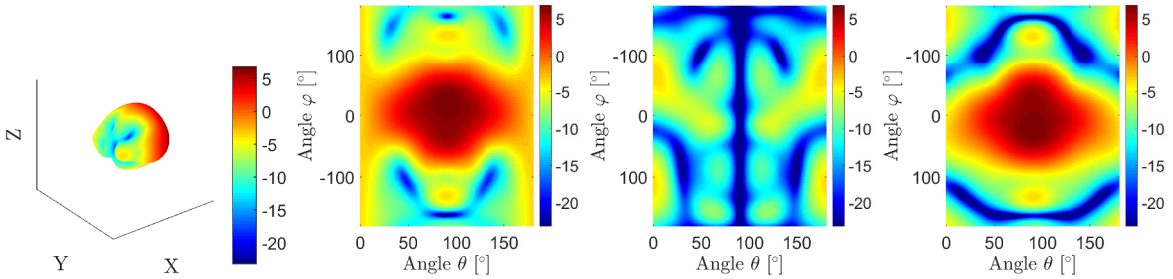

(a) 3D Dir-Total [dB] (b) 2D Dir-Total [dB] (c) Dir-Theta [dB] (d) Dir-Phi [dB]

Figure A.4: Patch patterns

pattern has the maximum energy radiated in the X-axis direction or ($\theta = 90°, \varphi = 0°$). The flat representation is convenient to see all the directions in one glance. All the patterns have the same scale, the directivity maximum over all the directions is 6.8dB, same maximum exists for the phi component of the directivity (Dir-Phi) and the maximum of the theta component of the directivity (Dir-Theta) is -3.5dB which is more than 10dB below.

Appendix B
Cramer-Rao lower bound expression

Details of the FIM_{11} calculation is given, result for FIM_{22} follows the same scheme.

$$
\begin{aligned}
PDF(\theta,\varphi) &= \frac{1}{(2\pi\sigma^2)^N} e^{\frac{-1}{2\sigma^2}\sum_{n=1}^{N}\left[\left(x_n-\rho_n\cos\left(\frac{2\pi}{\lambda}\mathbf{r}_n\cdot\mathbf{e}_r+\phi_n\right)\right)^2+\left(y_n-\rho_n\sin\left(\frac{2\pi}{\lambda}\mathbf{r}_n\cdot\mathbf{e}_r+\phi_n\right)\right)^2\right]} \\
\frac{\partial}{\partial\theta}\ln PDF(\theta,\varphi) &= \frac{-1}{2\sigma^2}\sum_{n=1}^{N}\Bigg[2(-1)\left(\frac{\partial\rho_n}{\partial\theta}\cos\left(\frac{2\pi}{\lambda}\mathbf{r}_n\cdot\mathbf{e}_r+\phi_n\right)\right. \\
&\quad \left.-\rho_n\frac{\partial\frac{2\pi}{\lambda}\mathbf{r}_n\cdot\mathbf{e}_r+\phi_n}{\partial\theta}\sin\left(\frac{2\pi}{\lambda}\mathbf{r}_n\cdot\mathbf{e}_r+\phi_n\right)\right)\cdot\left(x_n-\rho_n\cos\left(\frac{2\pi}{\lambda}\mathbf{r}_n\cdot\mathbf{e}_r+\phi_n\right)\right) \\
&\quad +2(-1)\left(\frac{\partial\rho_n}{\partial\theta}\sin\left(\frac{2\pi}{\lambda}\mathbf{r}_n\cdot\mathbf{e}_r+\phi_n\right)+\rho_n\frac{\partial\frac{2\pi}{\lambda}\mathbf{r}_n\cdot\mathbf{e}_r+\phi_n}{\partial\theta}\cos\left(\frac{2\pi}{\lambda}\mathbf{r}_n\cdot\mathbf{e}_r+\phi_n\right)\right) \\
&\quad \cdot\left(y_n-\rho_n\sin\left(\frac{2\pi}{\lambda}\mathbf{r}_n\cdot\mathbf{e}_r+\phi_n\right)\right)\Bigg]
\end{aligned}
\tag{B.1}
$$

$$
\begin{aligned}
E[\frac{\partial^2}{\partial\theta^2}\ln PDF(\theta,\varphi)] &= \frac{-1}{\sigma^2}\sum_{n=1}^{N}\Bigg[\left(\frac{\partial\rho_n}{\partial\theta}\cos\left(\frac{2\pi}{\lambda}\mathbf{r}_n\cdot\mathbf{e}_r+\phi_n\right)\right. \\
&\quad \left.-\rho_n\frac{\partial\frac{2\pi}{\lambda}\mathbf{r}_n\cdot\mathbf{e}_r+\phi_n}{\partial\theta}\sin\left(\frac{2\pi}{\lambda}\mathbf{r}_n\cdot\mathbf{e}_r+\phi_n\right)\right)^2 \\
&\quad +\left(\frac{\partial\rho_n}{\partial\theta}\sin\left(\frac{2\pi}{\lambda}\mathbf{r}_n\cdot\mathbf{e}_r+\phi_n\right)+\rho_n\frac{\partial\frac{2\pi}{\lambda}\mathbf{r}_n\cdot\mathbf{e}_r+\phi_n}{\partial\theta}\cos\left(\frac{2\pi}{\lambda}\mathbf{r}_n\cdot\mathbf{e}_r+\phi_n\right)\right)^2\Bigg] \\
&= \frac{-1}{\sigma^2}\sum_{n=1}^{N}\left[\left(\frac{\partial\rho_n}{\partial\theta}\right)^2+\rho_n^2\left(\frac{2\pi}{\lambda}\frac{\partial\mathbf{r}_n\cdot\mathbf{e}_r}{\partial\theta}+\frac{\partial\phi_n}{\partial\theta}\right)^2\right] \\
E[\frac{\partial^2}{\partial\varphi^2}\ln PDF(\theta,\varphi)] &= \frac{-1}{\sigma^2}\sum_{n=1}^{N}\left[\left(\frac{\partial\rho_n}{\partial\varphi}\right)^2+\rho_n^2\left(\frac{2\pi}{\lambda}\frac{\partial\mathbf{r}_n\cdot\mathbf{e}_r}{\partial\varphi}+\frac{\partial\phi_n}{\partial\varphi}\right)^2\right]
\end{aligned}
\tag{B.2}
$$

Details of the FIM_{12} is given here, then $FIM_{21} = FIM_{12}$.

$$
\begin{aligned}
E[\frac{\partial^2}{\partial\theta\partial\varphi}\ln PDF(\theta,\varphi)] = \frac{-1}{\sigma^2}\sum_{n=1}^{N}\Bigg[&\left(\frac{\partial\rho_n}{\partial\theta}\cos\left(\frac{2\pi}{\lambda}\mathbf{r}_n\cdot\mathbf{e}_r+\phi_n\right)\right.\\
&\left.-\rho_n\frac{\partial\frac{2\pi}{\lambda}\mathbf{r}_n\cdot\mathbf{e}_r+\phi_n}{\partial\theta}\sin\left(\frac{2\pi}{\lambda}\mathbf{r}_n\cdot\mathbf{e}_r+\phi_n\right)\right)\\
&\cdot\left(\frac{\partial\rho_n}{\partial\varphi}\cos\left(\frac{2\pi}{\lambda}\mathbf{r}_n\cdot\mathbf{e}_r+\phi_n\right)-\rho_n\frac{\partial\frac{2\pi}{\lambda}\mathbf{r}_n\cdot\mathbf{e}_r+\phi_n}{\partial\varphi}\sin\left(\frac{2\pi}{\lambda}\mathbf{r}_n\cdot\mathbf{e}_r+\phi_n\right)\right)\\
&+\left(\frac{\partial\rho_n}{\partial\theta}\sin\left(\frac{2\pi}{\lambda}\mathbf{r}_n\cdot\mathbf{e}_r+\phi_n\right)+\rho_n\frac{\partial\frac{2\pi}{\lambda}\mathbf{r}_n\cdot\mathbf{e}_r+\phi_n}{\partial\theta}\cos\left(\frac{2\pi}{\lambda}\mathbf{r}_n\cdot\mathbf{e}_r+\phi_n\right)\right)\\
&\cdot\left(\frac{\partial\rho_n}{\partial\varphi}\sin\left(\frac{2\pi}{\lambda}\mathbf{r}_n\cdot\mathbf{e}_r+\phi_n\right)+\rho_n\frac{\partial\frac{2\pi}{\lambda}\mathbf{r}_n\cdot\mathbf{e}_r+\phi_n}{\partial\varphi}\cos\left(\frac{2\pi}{\lambda}\mathbf{r}_n\cdot\mathbf{e}_r+\phi_n\right)\right)\Bigg]\\
= \frac{-1}{\sigma^2}\sum_{n=1}^{N}&\left[\frac{\partial\rho_n}{\partial\theta}\frac{\partial\rho_n}{\partial\varphi}+\rho_n^2\left(\left(\frac{2\pi}{\lambda}\frac{\partial\mathbf{r}_n\cdot\mathbf{e}_r}{\partial\theta}+\frac{\partial\phi_n}{\partial\theta}\right)\left(\frac{2\pi}{\lambda}\frac{\partial\mathbf{r}_n\cdot\mathbf{e}_r}{\partial\varphi}+\frac{\partial\phi_n}{\partial\varphi}\right)\right)\right]
\end{aligned}
\tag{B.3}
$$

The determimant of the FIM:

$$
\begin{aligned}
|FIM| &= E\left[\frac{\partial^2}{\partial\theta^2}\ln PDF(\theta,\varphi)\right]E\left[\frac{\partial^2}{\partial\varphi^2}\ln PDF(\theta,\varphi)\right]-E\left[\frac{\partial^2}{\partial\theta\partial\varphi}\ln PDF(\theta,\varphi)\right]^2\\
&=\left\{\frac{1}{\sigma^2}\sum_n\left[\left(\frac{\partial\rho_n}{\partial\theta}\right)^2+\left(\rho_n\frac{\partial\frac{2\pi}{\lambda}\mathbf{r}_n\cdot\mathbf{e}_r+\phi_n}{\partial\theta}\right)^2\right]\right\}\\
&\left\{\frac{-1}{\sigma^2}\sum_n\left[\left(\frac{\partial\rho_n}{\partial\varphi}\right)^2+\left(\rho_n\frac{\partial\frac{2\pi}{\lambda}\mathbf{r}_n\cdot\mathbf{e}_r+\phi_n}{\partial\varphi}\right)^2\right]\right\}\\
&-\left\{\frac{1}{\sigma^2}\sum_n\left[\frac{\partial\rho_n}{\partial\theta}\frac{\partial\rho_n}{\partial\varphi}+\rho_n^2\frac{\partial\frac{2\pi}{\lambda}\mathbf{r}_n\cdot\mathbf{e}_r+\phi_n}{\partial\theta}\frac{\partial\frac{2\pi}{\lambda}\mathbf{r}_n\cdot\mathbf{e}_r+\phi_n}{\partial\varphi}\right]\right\}^2\\
&=\frac{1}{\sigma^4}\sum_{i=1}^{N}\sum_{j=1}^{N}\left(\frac{\partial\rho_i}{\partial\theta}\right)^2\left(\rho_j\frac{\partial}{\partial\varphi}\left(\frac{2\pi}{\lambda}\mathbf{r}_j\cdot\mathbf{U}+\phi_n\right)\right)^2\\
&+\sum_{i=1}^{N}\sum_{j=1}^{N}\left(\frac{\partial\rho_i}{\partial\varphi}\right)^2\left(\rho_j\frac{\partial}{\partial\theta}\left(\frac{2\pi}{\lambda}\mathbf{r}_j\cdot\mathbf{U}+\phi_n\right)\right)^2\\
&-\frac{1}{\sigma^4}2\sum_{i=1}^{N}\sum_{j=1}^{N}\frac{\partial\rho_i}{\partial\theta}\frac{\partial\rho_i}{\partial\varphi}\rho_j^2\frac{\partial}{\partial\theta}\left(\frac{2\pi}{\lambda}\mathbf{r}_j\cdot\mathbf{U}+\varphi\right)\frac{\partial}{\partial\varphi}\left(\frac{2\pi d}{\lambda}\mathbf{r}_j\cdot\mathbf{U}+\phi_n\right)
\end{aligned}
\tag{B.4}
$$

The calculation of the $FIM_{\theta\theta}$ in case of cross-polarisation

$$
\begin{aligned}
FIM_{\theta\theta} &= \frac{1}{\sigma^2}\sum_{n=1}^{N}\left[\left(\frac{\partial\rho_n}{\partial\theta}\right)^2+\left(\rho_n\frac{\partial\frac{2\pi}{\lambda}\mathbf{r}_n\cdot\mathbf{e}_r+\phi_n}{\partial\theta}\right)^2\right] \\
&= \frac{1}{\sigma^2}\left[\frac{1}{\rho_1^2}\left(E_\theta\sin\theta\cos\theta(E_\theta\sin\theta+E_\varphi\cos\phi_{C_n})\right)^2+3(E_\theta\cos\theta)^2+\frac{1}{\rho_1^2}\left(E_\varphi\sin\phi_{c_n}E_\theta\cos\theta\right)^2\right. \\
&\quad \left.+\left(\frac{2\pi d}{\lambda}E_\theta\sin\theta\cos\theta\right)^2\left(1+(\cos\varphi+\sin\varphi)^2\right)\right] \\
&= \frac{1}{\sigma^2}\left[\frac{(E_\theta\cos\theta)^2}{\rho_1^2}\left(\left(E_\theta\sin\theta+E_\varphi\cos\phi_{C_n}\right)^2+\left(E_\varphi\sin\phi_{c_n}E_\theta\cos\theta\right)\right)^2\right. \\
&\quad \left.+3(E_\theta\cos\theta)^2+\left(\frac{2\pi d}{\lambda}E_\theta\sin\theta\cos\theta\right)^2\left(1+(\cos\varphi+\sin\varphi)^2\right)\right] \\
&= \frac{1}{\sigma^2}\left[4\left(E_\theta\cos\theta\right)^2+\left(\frac{2\pi d}{\lambda}E_\theta\sin\theta\cos\theta\right)^2\left(1+(\cos\varphi+\sin\varphi)^2\right)\right]
\end{aligned}
\tag{B.5}
$$

Bibliography

[Ahn et al., 2010] Ahn, H., Tomasic, B., and Liu, S. (2010). Digital beamforming in a large conformal phased array antenna for satellite operations support; architecture, design, and development. In *2010 IEEE International Symposium on Phased Array Systems and Technology*, pages 423–431.

[Airbus Defense and Space, 2017] Airbus Defense and Space (2017). Trs-4d (aesa technology) multi-mode naval radar. http://northamerica.airbus-group.com/north-america/usa/Airbus-Defense-and-Space/TRS-4D/Overview.html.

[Anguera et al., 2001] Anguera, J., Puente, C., Borja, C., Montero, R., and Soler, J. (2001). Small and high-directivity bow-tie patch antenna based on the sierpinski fractal. *Microwave and Optical Technology Letters*, 31(3):239–241.

[Antennas and Society, 2013] Antennas, I. and Society, P. (2013). Ieee standard for definitions of terms for antennas. http://www.engr.mun.ca/~eldarymli/ENGI_7811/materials/relevant_additional_materials/IEEE_Standard_for_Definitions_of_Terms_for_Antennas.pdf.

[Balanis, 2005] Balanis, C. A. (2005). *Antenna Theory: Analysis and Design*. Wiley-Interscience.

[Banach and Cunningham, 1988] Banach, M. and Cunningham, J. (1988). Synthesis of arbitrary and conformal arrays using non-linear optimization techniques. In *Radar Conference, 1988., Proceedings of the 1988 IEEE National*, pages 38–43.

[Baviskar et al., 2016] Baviskar, J., Mulla, A., Baviskar, A., and Pawar, S. (2016). Metamaterial lens incorporated enhanced gain omnidirectional conformal patch antenna. In *2016 IEEE Aerospace Conference*, pages 1–7.

[Baysal and Moses, 2003] Baysal, U. and Moses, R. L. (2003). On the geometry of isotropic arrays. *IEEE Transactions on Signal Processing*, 51(6):1469–1478.

[Bertuch et al., 2010] Bertuch, T., Knott, P., Wilden, H., and Peters, O. (2010). Sar experiments using a conformal antenna array radar demonstrator. In *8th European Conference on Synthetic Aperture Radar*, pages 1–4.

[Bil and Holpp, 2015] Bil, R. and Holpp, W. (2015). Naval radar trends: A look back - a look forward. In *2015 16th International Radar Symposium (IRS)*, pages 13–19.

[Bilotti and Vegni, 2010] Bilotti, F. and Vegni, C. (2010). Design of high-performing microstrip receiving gps antennas with multiple feeds. *IEEE Antennas and Wireless Propagation Letters*, 9:248–251.

[Borja et al., 2000] Borja, C., Font, G., Blanch, S., and Romeu, J. (2000). High directivity fractal boundary microstrip patch antenna. *Electronics Letters*, 36(9):778–779.

[Boutayeb et al., 2010] Boutayeb, H., Djerafi, T., and Wu, K. (2010). Gain enhancement of a circularly polarized microstrip patch antenna surrounded by a circular mushroom-like substrate. In *The 3rd European Wireless Technology Conference*, pages 257–260.

[Briheche et al., 2016] Briheche, Y., Barbaresco, F., Bennis, F., and Chablad, D. (2016). Optimization of radar search patterns for multiple scanning missions in localized clutter. In *2016 IEEE Conference on Antenna Measurements Applications (CAMA)*, pages 1–4.

[Brookner, 2008] Brookner, E. (2008). Phased-array and radar astounding breakthroughs - an update. In *2008 IEEE Radar Conference*, pages 1–6.

[Caille et al., 2002] Caille, G., Vourch, E., Martin, M. J., Mosig, J. R., and Polegre, M. (2002). Conformal array antenna for observation platforms in low earth orbit. *IEEE Antennas and Propagation Magazine*, 44(3):103–104.

[Cision PR Newswire, 2017] Cision PR Newswire (2017). The global missiles and missile defense systems market 2017-2027. website. http://www.prnewswire.com/news-releases/the-global-missiles-and-missile-defense-systems-market-2017-2027-300434684.html.

[Coccioli et al., 1999] Coccioli, R., Yang, F.-R., Ma, K.-P., and Itoh, T. (1999). Aperture-coupled patch antenna on uc-pbg substrate. *IEEE Transactions on Microwave Theory and Techniques*, 47(11):2123–2130.

[Comisso and Vescovo, 2013] Comisso, M. and Vescovo, R. (2013). Fast co-polar and cross-polar 3d pattern synthesis with dynamic range ratio reduction for conformal antenna arrays. *Antennas and Propagation, IEEE Transactions on*, 61(2):614–626.

[Costa et al., 2012] Costa, M., Richter, A., and Koivunen, V. (2012). Doa and polarization estimation for arbitrary array configurations. *IEEE Transactions on Signal Processing*, 60(5):2330–2343.

[Darricau, 1993] Darricau, J. (1993). *Physique et Theorie du Radar*. Societe Deniaud Freres; 3rd edition (1993).

[de Mingo et al., 2012] de Mingo, J., Roncal, C., and Carro, P. L. (2012). 3-d conformal spiral antenna on elliptical cylinder surfaces for automotive applications. *IEEE Antennas and Wireless Propagation Letters*, 11:148–151.

[Deepti Das et al., 2008] Deepti Das, K., Gopikrishna, M., Aanandan, C. K., Mohanan, P., and Vasudevan, K. (2008). Compact dual band slot loaded circular microstrip antenna with a superstrate. *Progress In Electromagnetics Research*.

[Dinnichert, 2000] Dinnichert, M. (2000). Full polarimetric pattern synthesis for an active conformal array. In *Phased Array Systems and Technology, 2000. Proceedings. 2000 IEEE International Conference on*, pages 415–419.

[Dogandzic and Nehorai, 2001] Dogandzic, A. and Nehorai, A. (2001). Cramer-rao bounds for estimating range, velocity, and direction with an active array. *IEEE Transactions on Signal Processing*, 49(6):1122–1137.

[Dohmen et al., 2007] Dohmen, C., Odendaal, J., and Joubert, J. (2007). Synthesis of conformal arrays with optimized polarization. *Antennas and Propagation, IEEE Transactions on*, 55(10):2922–2925.

[Fei-lin and Jun, 2011] Fei-lin, Q. and Jun, L. (2011). Polarization selectivity and optimization of thinned array for millimeter wave radar seeker with conformal phased array. In *Proceedings of 2011 IEEE CIE International Conference on Radar*, volume 1, pages 198–201.

[Ferreira and Ares, 1997] Ferreira, J. and Ares, F. (1997). Pattern synthesis of conformal arrays by the simulated annealing technique. *Electronics Letters*, 33(14):1187–1189.

[Filik and Tuncer, 2008] Filik, T. and Tuncer, T. E. (2008). Uniform and nonuniform v-shaped isotropic planar arrays. In *2008 5th IEEE Sensor Array and Multichannel Signal Processing Workshop*, pages 99–103.

[Gazzah and Abed-Meraim, 2009] Gazzah, H. and Abed-Meraim, K. (2009). Optimum ambiguity-free directional and omnidirectional planar antenna arrays for doa estimation. *IEEE Transactions on Signal Processing*, 57(10):3942–3953.

[Geng et al., 2009] Geng, J. P., Li, J. J., Jin, R. H., Ye, S., Liang, X. L., and Li, M. Z. (2009). The development of curved microstrip antenna with defected ground structure. In *Progress In Electromagnetics Research*.

[Ghosh et al., 2015] Ghosh, A., Chattopadhyay, S., Paul, A., Shivani, S., Sengupta, S., Banik, S., Kumari, S., and Chakraborty, S. (2015). Rectangular microstrip antenna with defected patch surface for improved polarization purity. In *Computer, Communication, Control and Information Technology (C3IT), 2015 Third International Conference on*, pages 1–5.

[Guennou-Martin et al., 2016] Guennou-Martin, A., Quere, Y., Rius, E., Fourtinon, L., Person, C., Lesueur, G., and Merlet, T. (2016). Design and manufacturing of a 3-d conformal slotted waveguide antenna array in ku-band based on direct metal laser sintering. In *2016 IEEE Conference on Antenna Measurements Applications (CAMA)*, pages 1–4.

[He and Wang, 2006] He, Q. and Wang, B. (2006). Design of a low sidelobe planar array antennas. In *2006 7th International Symposium on Antennas, Propagation EM Theory*, pages 1–4.

[Häge and Oispuu, 2011] Häge, M. and Oispuu, M. (2011). Doa and polarization accuracy study for an imperfect dual-polarized antenna array. In *2011 19th European Signal Processing Conference*, pages 599–603.

[Ho and Vicente, 2008] Ho, K. C. and Vicente, L. M. (2008). Sensor allocation for source localization with decoupled range and bearing estimation. *IEEE Transactions on Signal Processing*, 56(12):5773–5789.

[Hommel and Feldle, 2005] Hommel, H. and Feldle, H. P. (2005). Current status of airborne active phased array (aesa) radar systems and future trends. In *IEEE MTT-S International Microwave Symposium Digest, 2005.*, pages 4 pp.–.

[Hushkit, 2015] Hushkit (2015). The indomitable squall: Rafale cutting edge rada. https://hushkit.net/2015/06/07/the-indomitable-squall-rafales-cutting-edge-radar/.

[Jackson et al., 2015] Jackson, B. R., Rajan, S., Liao, B. J., and Wang, S. (2015). Direction of arrival estimation using directive antennas in uniform circular arrays. *IEEE Transactions on Antennas and Propagation*, 63(2):736–747.

[Jane's by IHS Markit, 2014] Jane's by IHS Markit (2014). The missile and precision guided weapon market - a 10 year outlook. https://www.youtube.com/watch?v=ircSdYF69nQ.

[Jones, 1941] Jones, R. C. (1941). A new calculus for the treatment of optical systemsi. description and discussion of the calculus. *J. Opt. Soc. Am.*, 31(7):488–493.

[Josefsson and Persson, 2006] Josefsson, L. and Persson, P. (2006). *Conformal Array Antenna Theory and Design*. IEEE Press Series on Electromagnetic Wave Theory. Wiley.

[Kanno et al., 1996] Kanno, M., Hashimura, T., Katada, T., Sato, M., Fukutani, K., and Suzuki, A. (1996). Digital beam forming for conformal active array antenna. In *Proceedings of International Symposium on Phased Array Systems and Technology*, pages 37–40.

[Kanter, 1977] Kanter, I. (1977). The probability density function of the monopulse ratio for n looks at a combination of constant and rayleigh targets. *IEEE Transactions on Information Theory*, 23(5):643–648.

[Kay, 1993a] Kay, S. M. (1993a). *Fundamentals of Statistical Signal Processing: Estimation Theory*. Prentice-Hall, Inc., Upper Saddle River, NJ, USA.

[Kay, 1993b] Kay, S. M. (1993b). *Fundamentals of Statistical Signal Processing: Estimation Theory*. Prentice-Hall, Inc., Upper Saddle River, NJ, USA.

[Kemkemian and Nouvel-Fiani, 2010] Kemkemian, S. and Nouvel-Fiani, M. (2010). Toward common radar amp; ew multifunction active arrays. In *2010 IEEE International Symposium on Phased Array Systems and Technology*, pages 777–784.

[Kinghorn et al., 2016] Kinghorn, T., Scott, I., and Totten, E. (2016). Recent advances in airborne phased array radar systems. In *2016 IEEE International Symposium on Phased Array Systems and Technology (PAST)*, pages 1–7.

[Knittel, 1973] Knittel, G. (1973). Comments on "the definition of cross polarization". *Antennas and Propagation, IEEE Transactions on*, 21(6):917–918.

[Koffman, 1966] Koffman, I. (1966). Feed polarization for parallel currents in reflectors generated by conic sections. *Antennas and Propagation, IEEE Transactions on*, 14(1):37–40.

[Kumar and Guha, 2014] Kumar, C. and Guha, D. (2014). Defected ground structure (dgs)-integrated rectangular microstrip patch for improved polarisation purity with wide impedance bandwidth. *Microwaves, Antennas Propagation, IET*, 8(8):589–596.

[Kummer, 1974] Kummer, W. H. (1974). Preface of the special issue on conformal arrays. *IEEE Transactions on Antennas and Propagations*, 1.

[Lacomme, 2003] Lacomme, P. (2003). New trends in airborne phased array radars. In *IEEE International Symposium on Phased Array Systems and Technology, 2003.*, pages 17–22.

[Li et al., 2004] Li, P., Lai, H., Luk, K., and Lau, K. (2004). A wideband patch antenna with cross-polarization suppression. *Antennas and Wireless Propagation Letters, IEEE*, 3(1):211–214.

[Liang and Xin, 2014] Liang, M. and Xin, H. (2014). *Three-Dimensionally Printed/Additive Manufactured Antennas*, pages 1–30. Springer Singapore, Singapore.

[Liu et al., 2014] Liu, F., Li, H., Xia, W., and Wang, Y. (2014). A doa and polarization estimation method using a spatially non-collocated vector sensor array. In *Signal and Information Processing (ChinaSIP), 2014 IEEE China Summit International Conference on*, pages 763–767.

[Liu et al., 2008] Liu, X. F., Jiao, Y. C., and Zhang, F. S. (2008). Conformal array antenna design using modified particle swarm optimization. *Journal of Electromagnetic Waves and Applications*, 22(2-3):207–218.

[Liu et al., 2012] Liu, Z. Q., Zhang, Y. S., Qian, Z., Han, Z. P., and Ni, W. (2012). A novel broad beamwidth conformal antenna on unmanned aerial vehicle. *IEEE Antennas and Wireless Propagation Letters*, 11:196–199.

[Ludwig, 1973] Ludwig, A. (1973). The definition of cross polarization. *Antennas and Propagation, IEEE Transactions on*, 21(1):116–119.

[Luk et al., 1998] Luk, K., Mak, C., Chow, Y., and Lee, K. (1998). Broadband microstrip patch antenna. *Electronics Letters*, 34(15):1442–1443.

[Mahmoud and Al-Ajmi, 2008] Mahmoud, S. F. and Al-Ajmi, A. R. (2008). A novel microstrip patch antenna with reduced surface wave excitation. *Progress In Electromagnetics Research*, 86:71–86.

[Mahmud and Dey, 2012] Mahmud, M. S. and Dey, S. (2012). Design and performance analysis of a compact and conformal super wide band textile antenna for wearable body area applications. In *2012 6th European Conference on Antennas and Propagation (EUCAP)*, pages 1–5.

[Mailloux, 2005] Mailloux, R. (2005). *Phased Array Antenna Handbook*. Artech House.

[Mancuso and Renard, 2014] Mancuso, Y. and Renard, C. (2014). New developments and trends for active antennas and tr modules. In *2014 International Radar Conference*, pages 1–3.

[Manikas et al., 1994] Manikas, A., Karimi, H. R., and Dacos, I. (1994). Study of the detection and resolution capabilities of a one-dimensional array of sensors by using differential geometry. *IEE Proceedings - Radar, Sonar and Navigation*, 141(2):83–92.

[Mao et al., 2016] Mao, C. X., Gao, S., Wang, Y., Wang, Z., Qin, F., Sanz-Izquierdo, B., and Chu, Q. X. (2016). An integrated filtering antenna array with high selectivity and harmonics suppression. *IEEE Transactions on Microwave Theory and Techniques*, 64(6):1798–1805.

[Mastrangeli et al., 2013] Mastrangeli, F., De Luca, A., Valerio, G., and Galli, A. (2013). Low-cost dual-polarized printed antenna for multifunction phased-array radar. *Microwave and Optical Technology Letters*, 54(3):697–702.

[Mazzarella and Panariello, 1993] Mazzarella, G. and Panariello, G. (1993). Pattern synthesis of conformal arrays. In *Antennas and Propagation Society International Symposium, 1993. AP-S. Digest*, pages 1054–1057 vol.2.

[Mirkin and Sibul, 1991] Mirkin, A. N. and Sibul, L. H. (1991). Cramer-rao bounds on angle estimation with a two-dimensional array. *IEEE Transactions on Signal Processing*, 39(2):515–517.

[Moriya et al., 2012] Moriya, H., Ichige, K., Arai, H., Hayashi, T., Matsuno, H., and Nakano, M. (2012). Novel 3-d array configuration based on crlb formulation for high-resolution doa estimation. In *Antennas and Propagation (ISAP), 2012 International Symposium on*, pages 1140–1143.

[Morton and Pasala, 2004] Morton, T. and Pasala, K. (2004). Pattern synthesis of conformal arrays for airborne vehicles. In *Aerospace Conference, 2004. Proceedings. 2004 IEEE*, volume 2, pages 1030–1039 Vol.2.

[Nickel, 2006] Nickel, U. (2006). Overview of generalized monopulse estimation. *IEEE Aerospace and Electronic Systems Magazine*, 21(6):27–56.

[Nielsen, 1994] Nielsen, R. O. (1994). Azimuth and elevation angle estimation with a three-dimensional array. *IEEE Journal of Oceanic Engineering*, 19(1):84–86.

[Ouyang et al., 2010] Ouyang, J., Yang, F., Zhou, H., Nie, Z., and Zhao, Z. (2010). Conformal antenna optimization with space mapping. *Journal of Electromagnetic Waves and Applications*, 24(2-3):251–260.

[Pozar and Schaubert, 1984] Pozar, D. and Schaubert, D. (1984). Scan blindness in infinite phased arrays of printed dipoles. *IEEE Transactions on Antennas and Propagation*, 32(6):602–610.

[Q. Wang, 1974] Q. Wang, Q.-Q. H. (1974). An arbitrary conformal array pattern synthesis method that includes mutual coupling and platform effects. *Progress In Electromagnetics Research*, 22:12–16.

[Qiu and He, 2001] Qiu, M. and He, S. (2001). High-directivity patch antenna with both photonic bandgap substrate and photonic bandgap cover. *Microwave and Optical Technology Letters*, 30(1):41–44.

[Rocca et al., 2009] Rocca, P., Haupt, R. L., and Massa, A. (2009). Sidelobe reduction through element phase control in uniform subarrayed array antennas. *IEEE Antennas and Wireless Propagation Letters*, 8:437–440.

[Schulz and Thomae, 2015] Schulz, D. and Thomae, R. S. (2015). Cramer-rao lower bounds for polarimetric 2d direction of arrival estimation. In *WSA 2015; 19th International ITG Workshop on Smart Antennas*, pages 1–8.

[Sherman and Barton, 2011] Sherman, S. and Barton, D. (2011). *Monopulse Principles and Techniques*. Artech House radar library. Artech House.

[Sinclair, 1950] Sinclair, G. (1950). The transmission and reception of elliptically polarized waves. *Proceedings of the IRE*, 38(2):148–151.

[Siouris, 2004] Siouris, G. (2004). *Missile Guidance and Control Systems*. Springer.

[Skolnik, 2008] Skolnik, M. (2008). *Radar Handbook, Third Edition*. Electronics electrical engineering. McGraw-Hill Education.

[Song, 2008] Song, Y. (2008). Study on radiation characteristics of a conical conformal phased array. *Progress In Electromagnetics Research Symposium Cambridge*.

[Stoica et al., 2001] Stoica, P., Larsson, E. G., and Gershman, A. B. (2001). The stochastic crb for array processing: a textbook derivation. *IEEE Signal Processing Letters*, 8(5):148–150.

[Stoica and Nehorai, 1989] Stoica, P. and Nehorai, A. (1989). Music, maximum likelihood, and cramer-rao bound. *IEEE Transactions on Acoustics, Speech, and Signal Processing*, 37(5):720–741.

[Stoica and Nehorai, 1990] Stoica, P. and Nehorai, A. (1990). Performance study of conditional and unconditional direction-of-arrival estimation. *IEEE Transactions on Acoustics, Speech, and Signal Processing*, 38(10):1783–1795.

[Swaisaenyakorn et al., 2016] Swaisaenyakorn, S., Cole, A. J., Ng, C. C. H., and Young, P. R. (2016). Conformal switched beam antenna. In *2016 Loughborough Antennas Propagation Conference (LAPC)*, pages 1–4.

[Tan et al., 1996] Tan, K.-C., Goh, S. S., and Tan, E.-C. (1996). A study of the rank-ambiguity issues in direction-of-arrival estimation. *IEEE Transactions on Signal Processing*, 44(4):880–887.

[Tsao et al., 1988] Tsao, C., Hwang, Y., Kilburg, F., and Dietrich, F. (1988). Aperture-coupled patch antennas with wide-bandwidth and dual-polarization capabilities. In *Antennas and Propagation Society International Symposium, 1988. AP-S. Digest*, pages 936–939 vol.3.

[Van Trees, 2004] Van Trees, H. (2004). *Detection, Estimation, and Modulation Theory*, volume ptie. 1. Wiley.

[Vaskelainen, 1997a] Vaskelainen, L. (1997a). Iterative least-squares synthesis methods for conformal array antennas with optimized polarization and frequency properties. *Antennas and Propagation, IEEE Transactions on*, 45(7):1179–1185.

[Vaskelainen, 1997b] Vaskelainen, L. (1997b). Iterative least-squares synthesis methods for conformal array antennas with optimized polarization and frequency properties. *Antennas and Propagation, IEEE Transactions on*, 45(7):1179–1185.

[Wan et al., 2014] Wan, L., Si, W., Liu, L., Tian, Z., and Feng, N. (2014). High accuracy 2d-doa estimation for conformal array using parafac. *International Journal of Antennas and Propagation*.

[Wang et al., 2009] Wang, Z., Fang, S., Fu, S., and Lu, S. (2009). Dual-band probe-fed stacked patch antenna for gnss applications. *IEEE Antennas and Wireless Propagation Letters*, 8:100–103.

[Werner et al., 2016] Werner, J., Wang, J., Hakkarainen, A., Cabric, D., and Valkama, M. (2016). Performance and cramer rao bounds for doa/rss estimation and transmitter localization using sectorized antennas. *IEEE Transactions on Vehicular Technology*, 65(5):3255–3270.

[Woodward, 1953] Woodward, P. (1953). Discussion on mr. p.m. woodward's paper on theory of radar information. *Transactions of the IRE Professional Group on Information Theory*, 1(1):182–186.

[Yang et al., 2010] Yang, P., Yang, F., Nie, Z.-P., Li, B., and Tang, X. (2010). Robust adaptive beamformer using interpolation technique for conformal antenna array. *Progress In Electromagnetics Research*, 23:215–228.

[Zhou and Ingram, 1999] Zhou, P. Y. and Ingram, M.-A. (1999). Pattern synthesis for arbitrary arrays using an adaptive array method. *Antennas and Propagation, IEEE Transactions on*, 47(5):862–869.

N° d'ordre : 2017IMTA0060

IMT Atlantique
Bretagne-Pays de la Loire
École Mines-Télécom

IMT Atlantique Bretagne-Pays de la Loire - www.imt-atlantique.fr

Campus de Brest
Technopôle Brest-Iroise
CS 83818
29238 Brest Cedex 03
T +33 (0)2 29 00 11 11
F +33 (0)2 29 00 10 00

Campus de Nantes
4, rue Alfred Kastler - La Chantrerie
CS 20722
44307 Nantes Cedex 3
T +33 (0)2 51 85 81 00
F +33 (0)2 51 85 81 99

Campus de Rennes
2, rue de la Châtaigneraie
CS 17607
35576 Cesson Sévigné Cedex
T +33 (0)2 99 12 70 00
F +33 (0)2 99 12 70 08

Résumé

Embarqué sous le radôme du missile, les autodirecteurs existants utilisent une rotation mécanique du plan d'antenne pour balayer le faisceau en direction d'une cible. Les recherches actuelles examinent le remplacement des composantes mécaniques de rotation de l'antenne par un nouveau réseau d'antennes 3D conformes à balayage électronique. Les antennes 3D conformes pourraient offrir des avantages significatifs, tels qu'un balayage plus rapide et une meilleure couverture angulaire mais qui pourraient aussi offrir de nouveaux challenges résultant d'un diagramme de rayonnement plus complexes en 3D qu'en 2D.

Le nouvel autodirecteur s'affranchit du système mécanique de rotation ce qui libère de l'espace pour le design d'une nouvelle antenne 3D conforme. Pour tirer le meilleur parti de cet espace, différentes formes de réseaux sont étudiées, ainsi l'impact de la position, de l'orientation et de la conformation des éléments est établi sur les performances de l'antenne, en termes de directivité, ellipticité et de polarisation. Pour faciliter cette étude de réseaux 3D conformes, un programme Matlab a été développé, il permet de générer rapidement le diagramme de rayonnement en polarisation d'un réseau donné dans toutes les directions.

L'une des tâches de l'autodirecteur consiste à estimer la position d'une cible donnée afin de corriger la trajectoire du missile. Ainsi, l'impact de la forme du réseau sur l'erreur entre la direction d'arrivée mesurée de l'écho de la cible et sa vraie valeur est analysé. La borne inférieure de Cramer-Rao est utilisée pour calculer l'erreur minimum théorique. Ce modèle suppose que chaque élément est alimenté séparément et permet ainsi d'évaluer le potentiel des réseaux 3D conformes actifs. Finalement, l'estimateur du monopulse en phase est étudié pour des réseaux 3D conformes dont les quadrants n'auraient pas les mêmes caractéristiques. Un nouvel estimateur, plus adapté à des quadrants non identiques, est aussi proposé.

Mots-clés : antenne conforme, antenne réseau à commande de phase, polarisation, polarisation croisée, ellipticité, monopulse, maximum de vraisemblance, borne inférieure de Cramer-Rao

Abstract

Embedded below the radome of a missile, existing RF-seekers use a mechanical rotating antenna to steer the radiating beam in the direction of a target. Latest research is looking at replacing the mechanical antenna components of the RF-seeker with a novel 3D conformal antenna array that can steer the beam electronically. 3D antennas may offer significant advantages, such as faster beamsteering and better coverage but, at the same time, introduce new challenges resulting from a much more complex radiation pattern than that of 2D antennas.

Thanks to the mechanical system removal, the new RF-seeker has a wider available space for the design of a new 3D conformal antenna. To take best benefits of this space, different array shapes are studied, hence the impact of the position, orientation and conformation of the elements is assessed on the antenna performance in terms of directivity, ellipticity and polarisation. To facilitate this study of 3D conformal arrays, a Matlab program has been developed to compute the polarisation pattern of a given array in all directions.

One of the task of the RF-seeker consists in estimating the position of a given target to correct the missile trajectory accordingly. Thus, the impact of the array shape on the error between the measured direction of arrival of the target echo and its true value is addressed. The Cramer-Rao lower bound is used to evaluate the theoretical minimum error. The model assumes that each element receives independently and allows therefore to analyse the potential of active 3D conformal arrays. Finally, the phase monopulse estimator is studied for 3D conformal arrays whose quadrants do not have the same characteristics. A new estimator more adapted to non-identical quadrants is also proposed.

Keywords: conformal, 3D, phased arrays, AESA, polarisation, cross-polarisation, ellipticity, monopulse, maximum likelihood estimator, Cramer-Rao lower bound

N° d'ordre : 2017IMTA0060

IMT Atlantique Bretagne-Pays de la Loire - www.imt-atlantique.fr

IMT Atlantique
Bretagne-Pays de la Loire
École Mines-Télécom

Campus de Brest
Technopôle Brest-Iroise
CS 83818
29238 Brest Cedex 03
T +33 (0)2 29 00 11 11
F +33 (0)2 29 00 10 00

Campus de Nantes
4, rue Alfred Kastler - La Chantrerie
CS 20722
44307 Nantes Cedex 3
T +33 (0)2 51 85 81 00
F +33 (0)2 51 85 81 99

Campus de Rennes
2, rue de la Châtaigneraie
CS 17607
35576 Cesson Sévigné Cedex
T +33 (0)2 99 12 70 00
F +33 (0)2 99 12 70 08